The Resolved Stellar Populations in Nearby Star-forming Galaxies: M83, NGC 4214, and CGCG 269-049

by

Hwihyun Kim

A Dissertation Presented in Partial Fulfillment
of the Requirements for the Degree
Doctor of Philosophy

Approved November 2012 by the
Graduate Supervisory Committee:

Rogier Windhorst, Chair
Rolf Jansen
James Rhoads
Evan Scannapieco
Patrick Young

ARIZONA STATE UNIVERSITY

December 2012

ABSTRACT

Understanding the properties and formation histories of individual stars in galaxies remains one of the most important areas in astrophysics. The impact of the *Hubble Space Telescope* (*HST*) has been revolutionary, providing deep observations of nearby galaxies at high resolution and unprecedented sensitivity over a wavelength range from near-ultraviolet to near-infrared. In this study, I use deep *HST* imaging observations of three nearby star-forming galaxies (M83, NGC 4214, and CGCG 269-049) to construct color-magnitude and color-color diagrams of their resolved stellar populations. First, I select 50 regions in the spiral arm and inter-arm areas of M83, and determine the age distribution of the luminous stellar populations in each region. I developed an innovative method of star-by-star correction for internal extinction to improve stellar age and mass estimates. I compare the extinction-corrected ages of the 50 regions with those determined from several independent methods. The young stars are much more likely to be found in concentrated aggregates along spiral arms, while older stars are more dispersed. These results are consistent with a scenario where star formation is associated with the spiral arms, and stars form primarily in star clusters before dispersing on short timescales to form the field population. I address the effects of spatial resolution on the measured colors, magnitudes, and age estimates. While individual stars can occasionally show measurable differences in the colors and magnitudes, the age estimates for entire regions are only slightly affected. The same procedure is applied to nearby starbursting dwarf NGC 4214 to study the distributions of young and old stellar populations. Lastly, I describe the analysis of the *HST* and *Spitzer Space Telescope* observations of the extremely metal-poor dwarf galaxy (XMPG) CGCG 269-049 at a distance of 4.96 Mpc. This galaxy is one of the most metal-poor known with 12+log(O/H)=7.43. I find clear

evidence for the presence of an old stellar population in CGCG 269-049, ruling out the possibility that this galaxy is forming its first generation of stars, as originally proposed for XMPGs. This comprehensive study of resolved stellar populations in three nearby galaxies provides detailed view of the current state of star formation and evolution of galaxies.

To my family, who always believes in me.

ACKNOWLEDGEMENTS

I cannot thank enough to my collaborators, family, and friends for their support and encouragement. Without them, my dissertation and I would have not reached to this point.

First I thank my adviser, Rogier Windhorst for his encouragement and the financial support during the past few years. I also thank Bradley Whitmore and Rupali Chandar for their guidance and comments for my main dissertation project on M83 and NGC 4214. I would like to thank Robert O'Connell, Abi Saha, Bruce Balick, Max Mutchler, and Daniela Calzetti for their insightful comments. I thank Rolf Jansen for the help and support on the CGCG 269-049 project and also for teaching me how to write a proposal. I would like to thank Seth Cohen for helping me solve scientific and technical problems, and also for so many delightful discussions. I would like to thank my dissertation committee members James Rhoads, Evan Scannapieco, and Patrick Young for their support and helpful comments during the comprehensive exam, and the annual meetings.

I would like to express my gratitude to my fellow ASU graduate students in Rogier's research group including Drs. Russell Ryan, Amber Straughn, Nimish Hathi, Kaz Tamura, Robert Morgan, and Matt Mechtley, Michael Rutkowski, Teresa Ashcraft. I am specially grateful to have Dr. Catherine Kaleida as my friend and collaborator. I cannot even imagine my graduate school life without her. In addition to those who mentioned, I want to thank Drs. Cynthia D'Angelo, Emily McLinden, Carola Ellinger, Rosa Diaz Rivas, Adam Mott, and Mike Lesniak, Angel Fuentes, and Brian Gleim.

Without friends and professors at Yonsei University, my career in Astrophysics would have not existed. I thank my Master's thesis adviser Prof. Yong-Ik

Byun, Profs. Yong-Cheol Kim and Youngjong Sohn, my friend and sister from another mother Prof. Aeree Chung, Drs. Sangmo Sohn, Junhwan Choi, Soochang Rey, and Changhee Ree.

I would like to express my thanks to Jessie Chang, Jinsung Kim, Jisung Choi, Myoung-Sook Kim for spending many nights listening and giving me good advises. I also thank the TKPC EM members including Pastor Chris Yi, and his wife Grace Kim for their constant prayer and support.

My dissertation was supported by several different grants though NASA. The part of this dissertation project is based on Early Release Science observations (M83 and NGC 4214) made by the WFC3 Science Oversight Committee. I am also grateful to Matt Mountain, the Director of the Space Telescope Science Institute for awarding Director's Discretionary time for this program. Support for program GO/DD #11360 and AR #12137 was provided by NASA through a grant from Space Telescope Science Institute, which is operated by the Association of Universities for Research in Astronomy, Inc., under NASA contract NAS 5-26555. The work on CGCG 269-049 was supported by NASA under Hubble Space Telescope grant GO-10843.04-A, AR #11258, and Spitzer Space Telescope grant RSA1281759 to the United States Naval Observatory and Arizona State University. This research has used the NASA Extragalactic Database (NED), which is operated by the Jet Propulsion Laboratory of the California Institute of Technology, under contract with NASA. I also thank ASU Graduate Professional Student Association (GPSA) for the travel grant.

Last but not least, I can't thank enough to my family: Mom, Dad, my sister, and brother. Without their prayer, support, patience, and unconditional love, I am nothing a whining child. Thank you God for keeping me on track. Without you, I get lost.

TABLE OF CONTENTS

Page

TABLE OF CONTENTS vi

LIST OF TABLES ix

LIST OF FIGURES x

CHAPTER

1 INTRODUCTION 1

1.1 Stellar Population Studies in Nearby Galaxies 1

1.1.1 Studies of Local Group Galaxies 2

1.1.2 Galaxies Beyond the Local Group 5

1.2 Dissertation Goals 6

2 THE RESOLVED STELLAR POPULATIONS IN 50 REGIONS OF M83 10

2.1 Overview 10

2.2 *HST* WFC3 Observations 13

2.2.1 The WFC3/UVIS Data 13

2.2.2 Photometry and Artificial Star Tests 14

2.2.3 CMDs and Color–Color Diagrams in M83 16

2.2.4 Extinction Corrections 18

2.3 Age-dating Populations in M83 21

2.3.1 Age-dating the Resolved Stellar Population Using Color–Magnitude Diagrams 21

2.3.3 Comparison between $\mathrm{Age}_{\mathrm{CMDauto}}$ and Compact Cluster Ages 24

2.3.4 Comparison between $\mathrm{Age}_{\mathrm{CMDauto}}$ and Age Estimates from Integrated Light from the Entire Regions 25

2.4 Comparison between $\mathrm{Age}_{\mathrm{CMDauto}}$ and Other Parameters that Correlate with Age 26

2.4.1 Comparison between $Age_{CMDauto}$ and Number Ratio of Red-to-blue Stars . . . 26
2.4.2 Comparison between $Age_{CMDauto}$ and Morphological Category 27
2.4.3 Comparison between $Age_{CMDauto}$ and Stellar Surface Brightness Fluctuations . . . 27
2.5 Insights into the Star Formation History in M83 Based on Spatial Variations for 50 regions . . . 28
2.6 Using Wolf–Rayet Stars to Check for Consistency with Our Age Estimates . . . 30
2.7 Effect of Spatial Resolution . . . 32
2.8 Summary . . . 35
3 MAPPING THE RESOLVED STELLAR POPULATIONS IN METAL-POOR IRREGULAR NGC 4214 . . . 58
3.1 Overview . . . 58
3.2 WFC3 Observations . . . 60
3.2.1 Data . . . 60
3.2.2 Photometry and Artificial Star Tests . . . 61
3.2.3 Extinction Corrections . . . 63
3.3 Age-Dating Populations in NGC 4214 . . . 64
3.1 CMD Fitting . . . 65
3.2 Stellar SED Fitting . . . 66
3.4 Discussion . . . 67
3.5 Summary . . . 68
4 EXTREMELY METAL-POOR DWARF GALAXY CGCG 269-049 . . 80
4.1 Overview . . . 80
4.2 Observations . . . 82
4.2.1 Spitzer Images and Photometry . . . 82

CHAPTER Page

4.2.2 Estimate of Dust Mass 83

4.2.3 *HST*/ACS Data 84

4.2.4 Photometry from *HST* Images 86

4.3 Results 88

4.3.1 Mass Fraction of Old Stars 88

4.3.2 Evidence of Past Outflows? 90

4.4 Discussion 91

5 CONCLUSION 102

5.1 Summary of Current Work 102

5.2 Future Work 105

REFERENCES 106

A ADDITIONAL FIGURES FOR CHAPTER TWO 113

B SUPPLEMENTARY MATERIAL TO CHAPTER FOUR 161

B.1 Photometric Data Analysis 162

B.2 Construction of the CMD and the Color-color Diagram 163

B.3 Completeness Level in Each Filter 164

B.4 Distance Calculation Using the RGB Tip Magnitude 164

B.5 Estimate of the Mass Fraction for Evolved Stars 165

B.6 Radial Change of Stellar Populations 167

LIST OF TABLES

Table Page

2.1 Properties of the 50 Regions in M83 37

2.2 Wolf-Rayet Star Candidates in M83 40

3.1 Properties of the 38 Regions in NGC 4214 78

4.1 CGCG 269-049 Spitzer Space Telescope and MIPS Fluxes 94

B.1 Mass Fraction of Evolved Stars in CGCG 269-049 166

LIST OF FIGURES

Figure Page

2.1 Color composite of the M83 WFC3 images [Image Credit: Zolt Levay (STScI)]. The F336W image is shown in blue, the F502N ([O III]) image in cyan, the F555W image in green, and the combined F814W and F657N (Hα) image in red. The 50 selected regions are outlined in boxes of three different colors based on the values of $\mathrm{Age}_{\mathrm{CMD\,auto}}$ determined in this paper (see Section 2.3.1 for details). The regions with ages in the range 1–10 Myr are outlined in blue, ages of 10–20 Myr in yellow, and ages greater than 20 Myr in red. 41

2.2 Image cutouts (15.2″×13.9″, 340 pc×310 pc) of Regions 26 and 27 in the F555W (top) and the color-composite images (bottom). Stars circled in red have $(V-I)$ >0.8 mag. The "postage stamp" images on the left are"pseudo" matched candidates, while the images on the right appear to be heavily reddened (see Section 2.2.2 for details). 42

2.3 Top: the color–magnitude diagram (CMD) and color–color diagram of all stars in our M83 image corrected for Galactic foreground extinction but not for internal extinction. Padova isochrones of logτ (age/yr) = 6.55, 6.85, 7.0, 7.2, 7.5, 7.8, and 8.0 for a metallicity of Z=0.03 (1.5 $Z_{\odot}$) are overlaid in both panels. The dashed line in cyan represents the 50% photometric completeness level. The arrow in each panel indicates the direction of the reddening vector with $R_V = 3.1$. Magnitudes are on the Vega scale. The distance modulus $(m-M)_0 = 28.32$ mag is used to calculate the absolute magnitude M_{F814W}. Bottom: histograms of the distribution of ages and masses, as determined from the CMD (see Section 2.3.1 for details). The age quoted in the bottom left panel is the luminosity-weighted mean age. 43

2.4 Top: the CMD and color–color diagram of all stars corrected for the internal extinction determined for each individual star. The blue and two red dotted lines indicate boundaries for the locations of stars in the color–color diagram uncorrected for internal extinction (see Section 2.2.4 for discussion). Two arrows in the color–color diagram show reddening vectors: one with the standard reddening vector ($R_V = 3.1$) and the other with the flatter reddening vector ($R_V = 5.7$) which appears to be more appropriate for some of the data in the green triangle (see Section 2.2.4 for discussion). The dashed line in magenta shows the M_I<−5.5 mag cutoff used for the $\mathrm{Age}_{\mathrm{CMDauto}}$. Bottom: same as described in Figure 2.3. 44

2.5 CMDs, color–color diagrams, and the image cut-outs of Regions 12 and 7. Data points before and after the individual extinction correction are plotted as black crosses (upper: uncorrected) and blue Xs (lower: corrected). The Padova isochrones in these diagrams are the same as the ones plotted in Figure 2.3. See Section 2.2.4 for details. 45

2.6 Same as Figure 2.5 for Regions 29 and 2. 46

2.7 Correlation plots between the ages of the stellar populations in the 50 regions from CMD isochrone fitting. Left: correlation between the manual ages determined by HK and BCW. Right: correlation between the average of manual ages and automatic ages (see Section 2.3.1 for details). The best linear fits are shown in black with the significance of the correlation in unit of σ (i.e., slope/uncertainty) in the top left of each panel. The solid red line is the unity line. 47

2.8 Histograms of the distribution of ages and masses of the individual stars in Regions 12, 7, 29, and 2, as determined by the automated isochrone fitting technique (see Section 2.3.1). The age indicated at the top right in each age histogram is the luminosity-weighted mean age of all stars with $M_I<-5.5$ in each region. 48

2.9 Image cutout (18.3″×16.9″, 410 pc×380 pc) of the area near Region 9 as an example of a "field" region with old red giant stars, and a small population of isolated young blue stars. See Section 2.3.1 for detail. 49

2.10 Top: correlations between the ages of stars ($\mathrm{Age_{CMDauto}}$) and clusters ($\mathrm{Age_{Cl}}$). Bottom: correlation between the ages of stars determined by $\mathrm{Age_{CMDauto}}$ and the integrated light within the region ($\mathrm{Age_{Reg}}$). See Section 2.3.4 for details. The best linear fits are shown in black solid line with 5.4σ (top) and 4.6σ (bottom) correlations. The red line is the unity line. 50

2.11 Correlations between the stellar ages ($\mathrm{Age_{CMDauto}}$) and the number ratio of red-to-blue stars (top), Hα morphology (middle), and pixel-to-pixel fluctuations (bottom) for the 50 selected regions. See Section 2.2.4 for details. The best linear fits are indicated in solid black line with 7.2σ (top), 5.8σ (middle), and 1.1σ (bottom) correlations. . . . 51

2.12 Spatial distribution of stars with ages of 1–10, 15–35, and 40–100 Myr determined in this study. Each panel has the same orientation and scale as Figure 1. The top panel is the youngest group of stars, clearly showing that the stars in these regions are mostly distributed along the active star-forming region (i.e., associated with the strong Hαemission) in the spiral arms. The stars in the middle panel tend to be found slightly downstream of the spiral arms while the older stars are still farther out in the inter-arm regions, as expected. See Section 2.2.5 for details. 52

2.13 Distribution of Wolf–Rayet sources in our *HST* WFC3 M83 images. The color image at the center is the $UBVI$Hα composite and the image cutouts are the Hα(left or *top*) and F814W (right or bottom) images for regions A–E. The top right panel is an original finding chart (Hadfield et al. 2005, λ4684 narrowband FORS2 image) for the region A. Numbers in blue are the IDs of Wolf–Rayet sources identified by Hadfield et al. (2005). 53

2.14 CMD and color–color diagram of Wolf–Rayet sources in M83 marked in Figure 2.13. Three sources (78, 86, 105) circled in both diagrams are identified as clusters in our M83 WFC3 images. A twice solar metallicity BC09 cluster model (Bruzual & Charlot 2009, private communication; see also Bruzual & Charlot 2003) is shown in the right panel (dots), and Padova stellar models (Marigo et al. 2008) are shown in both panels. No correction has been made for internal reddening, which appears to be minimal for all but one object. The arrow indicates the Galactic reddening vector. 54

2.15 *HST*/ACS images (290″×290″, 68 pc×68 pc) of the compact star cluster NGC 2108 in the LMC: a color composite of the F435W, F555W, and F814W ACS images (left), the F555W ACS image (middle), and the degraded F555W ACS image (right) by a factor of 100 (from a distance of ∼50 kpc to a distance of ∼5 Mpc). See Section 2.2.7 for details. 55

2.16 Image cutouts of *HST*/ACS F555W image of NGC 2108. The large circles in yellow show the 300 pixel aperture (corresponding to a ∼3 pixel aperture at the distance of M83) centered at the location determined from the degraded image in Figure 15. The location of the dominant star (used to determine the "truth" value) is shown in red. See Section 2.2.7 for details. 56

2.17 Original CMD of Region 3 in M83 (solid points) with the effect of simulation representing a factor of 100 degradation in spatial resolution (open points). The $\mathrm{Age}_{\mathrm{CMDauto}}$ of this region changes from 21.9 Myr (determined from the solid points) to 23.8 Myr (from the open points). The difference in the age estimates is within $\sim 1\,\sigma$ error listed in Table 1. See Section 2.2.7 for detail. 57

3.1 Color composite of the central 2.9 kpc×2.9 kpc of the NGC 4214 WFC3 images [Image Credit: Zolt Levay (STScI)]. The combined F225W and F336W images are in blue, the F547M in green, and the combined F814W and F657N (Hα) image in red. The 38 adaptive box-grid is outlined in yellow. 70

3.2 Completeness of stellar photometry for WFC3/UVIS images used in this study. Completeness was determined by inserting artificial stars with the magnitude range from 22 to 30 mag in Vega magnitude system. See Section 3.2.2 for more details. 71

3.3 Top: the color–magnitude diagram (CMD) and color–color diagram of all stars in our NGC 4214 image corrected for Galactic foreground extinction. Padova isochrones of age = 5, 10, 30, 50, 100, 500 Myr, and 1, and 5 Gyr for a metallicity of Z=0.006 (0.3 $Z_{\odot}$) are overlaid in both panels. The dashed line in magenta represents the 50% photometric completeness level. The arrow in each panel indicates the direction of the reddening vector with $R_V = 3.1$. All magnitudes are in Vega magnitude system. We use the distance modulus $(m - M)_0 = 27.37$ mag (Dopita et al. 2010) to calculate the absolute magnitude M_{F814W}. Bottom: the CMD and color–color diagram of all stars corrected for the internal extinction determined for each individual star. The blue and two red dotted lines indicate boundaries for the locations of stars in the color–color diagram uncorrected for internal extinction (see Section 2.2.3 for discussion). 72

3.4 Histograms of stellar ages and masses determined from the CMD age-dating method (see Section 3.1 for details). The luminosity-weighted age averaged over all stars is at the top right in the left panel of this figure. 73

3.5 CMDs, color-color diagrams of Regions 6, 14, 35, and 23. Each data point is extinction corrected by the method described in Section 3.2.3. The Padova isochrones in these diagrams are the same as the ones plotted in Figure 3.3. 74

3.6 Histograms of the distribution of ages and masses of the individual stars in Regions 6, 14, 35, and 23, as determined by the automated CMD age-dating method (see Section 3.3.1). The age at the top right in each age histogram is the luminosity-weighted mean age of all stars in each region. 75

3.7 Age$_{CMD}$ distribution of stars in our WFC3 field outlined in grey. Ages are determined using the extinction-corrected CMD and the model isochrones in Figure 3.3. Each panel has the same orientation and scale as Figure 3.1. The top panels are the youngest (age $<$ 10 Myr) and the second youngest (10 $\leq$ age $<$ 35 Myr) groups of stars, clearly showing that the stars in these regions are mostly distributed along the active star-forming region (i.e., associated with the strong Hα emission) in the central bar of the galaxy. The stars in the bottom left panel (35 $\leq$ age $<$ 100 Myr) tend to show less clustered feature and more evenly distributed, except the loosely bound OB associations in the north part of the image. See Sections 3.1 for details. 76

3.8 Spatial distribution of stars with ages determined from the SED fitting method. Due to the smaller number of stars with all five-band photometry used in the SED fitting, fewer objects ($\sim$3500 total) are shown in each panel. Note that we use age ranges different from the ones used in Figure 3.7. The top left panel is the youngest (age $<$ 5 Myr) group of stars, showing the enhancement of stars distributed in the southern part of the central bar and the stars in the star-forming region in the west side of the image. The top right panel is the stars with ages of 5 to 10 Myr, clearly showing that stars in the super star cluster of the center and in the OB association are not far from their birthplace associated with the strong Hα emission. 77

4.1 Optical image of CGCG 269-049 from the Sloan Digital Sky Survey, representing a composite of images in the SDSS g, r, and i bands. The integrated Petrosian g magnitude of the galaxy is 15.75 (Kniazev et al. 2003). 95

4.2 Spitzer Space Telescope IRAC and MIPS images of CGCG 269-049. The galaxy is also detected in the IRAC 4.5 μm and 5.8 μm bands, with an appearance intermediate between that in the 3.6 μm and 8.0 μm bands. 96

4.3 Infrared spectral energy distribution of CGCG 269-049 from the Spitzer IRAC and MIPS fluxes, shown with open circles and solid squares, respectively. The solid line is a Bruzual & Charlot (2003) population synthesis model for an instantaneous burst evolved to an age of 10 Gyr, a Chabrier initial mass function, and a metallicity of 0.02 $Z_{\odot}$. The dashed line is a Draine & Li (2007) thermal dust model for a Large Magellanic Cloud dust composition and a range in the parameter U = 5 – 10^4, where U represents the intensity of the radiation field incident on the dust in units of the ambient radiation field in the solar neighborhood. The dotted line is the sum of the two models. 97

4.4 Color composite of the HST Advanced Camera for Surveys / High Resolution Channel F330W, F550M, and F814W images of CGCG 269-049. The feature at the bottom of the image is the "coronagraphic finger" of the ACS/HRC. 98

4.5 Hα image of CGCG 269-049 obtained in the F658N filter of the Advanced Camera for Surveys / High Resolution Channel. The image is centered on the Central Cluster (see Figures 1 and 4). 99

4.6 (a) Color-magnitude diagram of CGCG 269-049 from the photometry of the F550M and F814W images. Magnitudes are on a Vega scale. Padua isochrones for these filters and for a metallicity of Z = 0.0004 are plotted (see text for details). The dashed line represents the 50% completeness level. (b) Color-color diagram for the stars detected in the F330W, F550M, and F814W filters, with the same isochrones as in 6(a). The roughly linear portions of the isochrones on this plot correspond to the blue horizonal branch loops on 6(a). 100

4.7 Completeness of stellar photometry as a function of magnitude for each of the three filters used, as determined by inserting artificial stars into the images (see text for details). The error bars represent the variance between different simulations, where stars were inserted at different positions in the images. 101

B.1 *HST* ACS/HRC F550M image of CGCG 269-049 with the elliptical annuli used in our analysis overlaid. The ellipticity of the annuli is 0.2608. The cross indicates the flux-weighted center of the galaxy. . . 169

B.2 (a)–(f) CMDs of resolved stars within annuli with the semi-major and -minor axis defined at the top right corner of each panel (also, see Figure B.1). The isochrones and dashed lines of 50% completeness level are the same as in Figure 4.6 (a). 170

B.3 Selection criteria (grey dotted line) of MS, HB, and RGB+AGB stars brighter than 25.5 mag (grey dashed line) in CMD. Data points circled in red are stars with (F330W-F550M)< -1.3. 171

B.4 Distribution of different stellar populations selected based on the criteria in Figure B.3 with the ACS/HRC footprint superposed. The color and the size of each data point are based on the (F550M-F814W) color and the F550M magnitude. 172

Chapter 1

INTRODUCTION

1.1 Stellar Population Studies in Nearby Galaxies

Studying stellar populations of galaxies is similar to what archaeologists do to understand human activity in the past through the recovery and analysis of the cultural and environmental data left behind. Observations of stellar populations in nearby galaxies play a key role in stellar archaeology, since they provide the detailed fossil records of the star formation history and evolution of each galaxy. The color-magnitude diagram (CMD) is the best tool to study and assess the star formation history of a galaxy, since stars occupy a very specific location in the luminosity-temperature plane determined by their mass, age and metallicity. This means that the CMDs can be used to constrain the intrinsic properties of stellar populations. Over the past five decades, stellar evolutionary theory has been applied to understand the CMD of galactic globular and open clusters and explain the distribution of stars in the observed CMDs, in terms of cluster age and chemical abundance. On the observational side, significant advances with *Hubble Space Telescope* (*HST*) observations led to the development of sophisticated CMD fitting techniques to determine these properties of star clusters in galaxies in the Local Group (LG) and beyond. The space-based *HST* is a direct solution to the problem that most ground-based telescopes have to face: the atmospheric distortion of stellar images. The resolving power of *HST* is diffraction-limited with an angular resolution of 0.05 arcseconds at ∼6000Å, which allows us to differentiate between two stars less than 0.1 arcsecond apart on the sky. It is also important to note that *HST* allows us to observe ultraviolet and infrared radiation blocked or partially absorbed by the Earth's atmosphere. In this chapter, I will highlight several stellar population studies of nearby galaxies, primarily focused

on the resolved stellar population studies conducted with *HST* data and the unique insights that this telescope can provide to the study of stellar evolutionary models.

1.1.1 Studies of Local Group Galaxies

Observations of Galactic stars and star clusters provided detailed information of the history of star formation and chemical enrichment in the Milky Way (MW) galaxy and led to our current understanding of different components (bulge, thin disk, thick disk, and halo populations) of the Galaxy and other similar galaxies. We now know the bulge population is similar to that of a typical elliptical galaxy, which is old and metal rich with a large metallicity spread. The thin disk population contains most of the young stars with high metallicity, while the thick disk has older stars with intermediate metallicity. Lastly, the halo population consists mostly of old and metal poor stars. This current understanding of the different stellar populations in our own Galaxy has been fundamental to studies of the stellar contents of galaxies in the LG.

Stellar populations in the Magellanic Clouds are well-observed and studied, not just because they are the nearest extragalactic systems, but also because they offer a unique opportunity to study the detailed history of star formation. Several ground-based studies of the Large Magellanic Cloud (LMC) show that the star formation history (SFH) of the LMC is unlike the SFH of the MW, suggesting the bulk of the star formation occurred in the past few Gyr (Bertelli et al. 1992, and references therein). The age distribution of star clusters in the LMC is known to be unusual, having ages of either 0–3 Gyr or >12 Gyr (Da Costa 1991). Using the *HST*/Wide Field Planetary Camera 2 (WFPC2), Gallagher et al. (1996) constructed a deep CMD of the outer disk in the LMC and found evidence for active star-formation throughout the past 0.1–3 Gyr, confirming previous ground-based

studies. Geha et al. (1998) analyzed the CMDs and stellar luminosity functions (LFs) of three different fields in the LMC using WFPC2 observations. Comparing to previous studies (e.g., Bertelli et al. 1992), they showed a significant increase in star formation over the past 4 Gyr. In contrast, studies of the stellar populations in the inner part (bar) of the LMC (Elson, Gilmore, & Santiago 1997) show evidence of starbursting activities that occurred about 2 Gyr ago. This suggests that the bar formed more recently than the disk. Combining these results, it is apparent that the LMC has undergone different star formation history from that of the MW. One of the recent *HST* observations of the Magellanic Clouds is the Wide Field Camera 3 (WFC3) Early Release Science (ERS) program on the 30 Doradus region. (De Marchi et al. 2011) identified about 1000 pre-main-sequence (PMS) stars and compared the photometry with theoretical PMS evolutionary tracks in the CMD. They determined that the younger PMS populations ($\sim$4 Myr) preferentially occupy the central field of 30 Dor, while older PMS stars ($\sim$30 Myr) are more uniformly distributed across the field. Their study also reveals the presence of dust extinction variations across the central field of 30 Dor.

As the most massive galaxy in the LG, and a similar morphological type to our own MW, M31 is the most well-studied and the most observed extragalactic system. Due to the similarity of the Hubble types (M31: Sb and MW: Sbc), M31 represents the best analog for the properties of stellar populations in the MW and the other similar types of galaxies in the LG and beyond. Ever since Hubble (1929) studied the first CMD of an OB association in the outer part of the M31 disk, the stars in the outer disk have been observed and resolved into individual stars, while the stars in the central region are unresolved. Following work has also focused on the OB associations of the M31 disk since these stars are the brightest and easily resolved with the ground-based observations (van den Bergh 1964, 1966; Massey et al. 1986; Cananzi 1992). The first complete catalog of open

clusters in M31 is provided by Hodge (1979). He used the spatial distribution of the M31 open clusters to constrain the spiral structure of M31 and showed that it is more likely a two-armed structure than a one-armed structure.

At the distance of M31 ($D = 794$ kpc; NASA/IPAC Extragalactic Database), *HST* imaging can reach the horizontal branch ($M_V = 0.82$ mag), which makes possible to study metallicity distributions of the old resolved populations. Rich et al. (1996) obtained *HST* deep imaging of one of the M31 globular clusters G1 and its adjacent halo field. The CMDs of these fields clearly show blue and red horizontal branch stars. They compared the CMDs of G1 and halo field populations to the ones of Galactic globular cluster 47 Tuc and conclude that the properties of the G1 CMD are consistent with those of an old globular cluster with the metallicity of 47 Tuc, while the outer M31 halo consists of stars as metal rich as 47 Tuc. The most interesting result is that the red horizontal branch stars may be the product of a field population younger than the oldest Galactic globular clusters. The same group has observed the nuclear region of M33 with *HST* WFPC2. The giants in this region show very broad dispersion in color, corresponding to a metallicity range between M15 to at least 47 Tuc (Mighell 1995; Mighell et al. 1996).

The new *HST* multi-cycle treasury program, called the "Panchromatic Hubble Andromeda Treasury (PHAT)" survey (Dalcanton et al. 2012), takes full advantage of the new *HST* observing capability, in addition to the wealth of previous work carried out in M31. Dalcanton et al. (2012) describes the details of the PHAT survey, and gives a well-summarized history of M31 resolved stellar population studies. To summarize the results of the PHAT survey obtained over the past two years, the stellar populations of millions of resolved stars in M31 within projected radii from 0 to 20 kpc are studied and their CMDs are analyzed.

The results show the structure of M31's disk derived from the density of red giant branch stars, and reveal the variations in dust extinction from the center to the outer disk of M31. The data products from this survey will be combined with the existing ground- and space-based imaging and spectroscopic data, and will be an invaluable resource to the community for years to come.

1.1.2 Galaxies Beyond the Local Group

Even with *HST*, the distinct age indicators in the CMDs, such as the main-sequence turn-off (MSTO), horizontal branch location, and subgiant branch region, in galaxies beyond the LG, fall below the *HST* detection limit and its angular resolution limit. Observations and studies of the resolved populations in these galaxies are focused on the giant and supergiant populations to investigate the characteristic properties of the massive young populations and the upper-end of initial mass functions (IMFs). Among a large number of *HST* programs designed to study individual stars and parsec-scale structures in nearby galaxies out to several megaparsecs, the Advanced Camera for Surveys (ACS) Nearby Galaxy Survey Treasury (ANGST) survey (Dalcanton et al. 2009) is one of the most noteworthy programs conducted with the *HST*. The images obtained in this program provide uniform multiwavelength observations of resolved stars for a volume-limited sample of 69 galaxies within a distance of 3.5 Mpc. The resulting catalogs of resolved stars and star clusters, which can be used for studies of ancient and recent SFHs, provide millions of measurements of resolved stellar populations using their CMDs, and the distance of each sample galaxy was measured from the tip magnitude of the red giant branch stars (TRGB; Dalcanton et al. 2009; Williams et al. 2009; Weisz et al. 2008).

As briefly discussed above, previous research on resolved stellar populations has provided a wealth of data resources and results. The work presented in this

dissertation builds on previous investigations by extending the methodology and data for the specific scientific goals, which are summarized in the next section and discussed in more detail at the start of each chapter.

1.2 Dissertation Goals

The goal of this dissertation is to present a comprehensive study of the resolved stellar populations in three nearby star-forming galaxies: M83, NGC 4214, and CGCG 269-049. As described in the previous section, studying the resolved populations in these extragalactic systems can be difficult due to their large distances and stellar crowding. The high spatial resolution and sensitivity of *HST* now provides us an ability to obtain photometric measurements of individual stars in these three nearby galaxies. With this precise photometry and unprecedented spatial resolution from ACS and the recently installed WFC3, I have analyzed deep CMDs and color-color diagrams of M83, NGC 4214, and CGCG 269-049.

In Chapter 2, we present a multi-wavelength photometric study of ∼15,000 resolved stars in the nearby spiral galaxy M83 (NGC 5236, $D = 4.61$ Mpc) based on *HST* WFC3 observations using four filters: F336W, F438W, F555W, and F814W. We select 50 regions (an average area size of 260×280 pc) in the spiral arm and inter-arm areas of M83, and determine the age distribution of the luminous stellar populations in each region. This is accomplished by correcting for extinction towards each individual star by comparing its colors with predictions from stellar isochrones (e.g., Padova; Girardi et al. 2002, 2008, 2010). We compare the resulting luminosity-weighted mean ages of the luminous stars in the 50 regions with those determined from several independent methods, including the number ratio of red-to-blue supergiants, morphological appearance of the regions, surface brightness fluctuations, and the ages of clusters in the regions. We find reasonably good agreement between these methods. We find that young stars are much more likely

to be found in concentrated aggregates along spiral arms, while older stars are more dispersed. These results are consistent with the scenario that star formation is physically associated with the spiral arms, and stars form primarily in star clusters and then disperse on short timescales to form the field population. The locations of Wolf-Rayet stars are found to correlate with the positions of many of the youngest regions, providing additional support for our ability to accurately estimate ages. We also address the effects of spatial resolution on the measured colors, magnitudes, and age estimates. While individual stars can occasionally show measurable differences in the colors and magnitudes, the age estimates for entire regions are only slightly affected by over-crowding. This work has been published in *The Astrophysical Journal* (Kim et al. 2012).

In Chapter 3, we present a detailed UV-optical study of the nearby dwarf galaxy NGC 4214 based on *HST* WFC3/UVIS observations using five filters: F225W, F336W, F438W, F547M, and F814W. We divide the central 3 kpc×3 kpc region of NGC 4214 into a 38 box adaptive grid, and determine the age and mass distributions of the resolved stars in each grid-box using their color-magnitude and color-color information. We also estimate the ages and masses of the individual stars from stellar spectral energy distribution (SED) fitting to a set of stellar SED models. These measurements allow us to map the recent star formation histories of the dwarf galaxy NGC 4214 in detail. By mapping the distribution of stellar ages in this galaxy, we have found that the young stars are strongly clustered, while the older stars are more dispersed. This is consistent with a picture where stars form in star clusters and subsequently dissipate on short timescales to form the field population.

In Chapter 4, we present *HST* and *Spitzer Space Telescope* images and photometry of the star-forming dwarf galaxy CGCG 269-049. This galaxy is

extremely metal-poor (12 + log(O/H) = 7.43), and ∼5 Mpc from the MW. The *HST* images were obtained with the ACS High Resolution Channel (HRC) and reveal a large population of red giant and asymptotic giant branch stars, ruling out the possibility that CGCG 269-049 is a young galaxy as had been previously thought. The spectral energy distribution of the galaxy between ∼3.6 μm – 70 μm is best fitted by emission from predominantly ∼10 Gyr old stars, with a component of thermal dust emission having a temperature of 72 ± 10 K. Our ACS/HRC Hα image shows no evidence of a supernova-driven outflow — which would remove metals from the galaxy — nor do we find observational evidence that such outflows occurred in the past. Considering CGCG 269-049's large neutral hydrogen to stellar mass ratio (∼1), these results support recent models in which the metal deficiency of dwarf galaxies results mainly from inefficient star formation, rather than youth or the escape of supernova ejecta. The large fraction of ∼10 Gyr old stars in the galaxy (> 60% by mass) is consistent with simulations in which the star formation rates of isolated dwarf galaxies have significantly decreased near the epoch of reionization by the photoevaporation of baryons from their cold dark matter halos. This work has been published in *The Astrophysical Journal Letters* (Corbin et al. 2008a), with an *Erratum* (Corbin et al. 2008b) on the calculation of the Spitzer MIPS flux. My contribution to this paper consisted of the analysis and interpretation of the *HST* data. I include a more detailed, not previously published, description of this study in Appendix B. The authors of the paper kindly agreed to give me permission to use the whole paper in this dissertation.

This dissertation is outlined as follows: Chapter 2 describes the resolved stellar population study of the 50 selected regions in M83, with an introduction of the CMD fitting age-dating and the internal extinction correction methods developed in this study. Chapter 3 presents the results of the resolved stellar

population study of NGC 4214. The same CMD age-dating and the extinction correction methods used in the M83 study are applied. Chapter 4 shows the results of the photometric study of the dwarf galaxy CGCG 269-049. Chapter 5 summarizes the main results from the studies of M83, NGC 4214, and CGCG 269-049 and discusses plans for future work.

Chapter 2

THE RESOLVED STELLAR POPULATIONS IN 50 REGIONS OF M83

2.1 Overview

Understanding the properties of stars and the history of star formation in galaxies remains one of the most fundamental subjects in astrophysics. The Hubble Space Telescope (HST) provides an important tool for this endeavor, since it enables the detailed study of stars and star clusters, not only in the Milky Way and its nearest neighbors, but in galaxies well beyond the Local Group. The Wide Field Camera 3 (WFC3) provides a particularly valuable new panchromatic imaging capability, with spectral coverage from the near-UV to the near-IR. This capability is especially useful for studying the stellar populations in nearby galaxies where individual stars are resolved.

A good example of a multi-wavelength survey of nearby galaxies which employs resolved stars and star clusters is the ACS Nearby Galaxy Treasury (ANGST) program (Dalcanton et al. 2009). This study includes ∼65 galaxies out to ∼3.5 Mpc, and provides uniform multi-color (BVI) catalogs of tens of thousands of individual stars in each galaxy. Although the ANGST program provides an excellent survey for a wide range of studies, it does not provide observations in the U band since the observations were obtained before WFC3 was installed on HST. The U band is particularly useful for age-dating populations of young stars, which is the focus of the current paper. PHAT (Panchromatic Hubble Andromeda Treasury) is a related study that does take advantage of the new U band capability on WFC3. While nowhere as extensive as the Multiple Cycle Treasury Program PHAT survey, the current study of M83 is complementary in the sense that it provides similar observations of the resolved stellar component of a nearby spiral galaxy, and uses quite different analysis techniques, as will be

discussed in Sections 2.2.2 and 2.2.3. Future observations of M83 (ID:12513, PI: William Blair) will expand the WFC3 dataset available for M83 from 2 to 7 fields.

M83 (NGC 5236), also known as the "Southern Pinwheel" galaxy, is a slightly barred spiral galaxy with a starbursting nucleus located at a distance of 4.61 Mpc, i.e., $(m - M)_0 = 28.32 \pm 0.13$ (Saha et al. 2006). The Hα emission can be used to pinpoint regions of recently formed massive stars along the spiral arms, while red supergiants can be found throughout the galaxy. The color–magnitude diagram (CMD) of resolved stars is a powerful diagnostic tool for understanding the stellar evolution and history of star formation of galaxies in detail. By comparing stellar evolution models to observed CMDs, we are able to determine the ages of the stellar populations in galaxies. However, in active star-forming regions, the stars are often partially obscured by dust. Applying a single extinction correction value for the whole galaxy often results in overestimates or underestimates of the ages of individual stars. If the CMD is the only tool used to determine the ages, the spatial variations of dust extinction in galaxies and their effects on the determined ages are not readily apparent. The additional information available from the color–color diagram can remedy this problem. By using techniques developed in this chapter, we can constrain the variations of dust extinction across M83, and make corrections for individual stars. We also focus on spatial variations in the stellar properties throughout the galaxy.

The *HST* WFC3 observations of M83 were performed in 2009 August as part of the WFC3 Science Oversight Committee Early Release Science (ERS) program (ID:11360, PI: Robert O'Connell). The central region (3.2 kpc×3.2 kpc) of M83 was observed in 2009 August. A second adjacent field to the NNW was observed in 2010 March and will be included in future publications. Details of the WFC3 ERS data calibration and processing are given by Chandar et al. (2010).

In this chapter we present $UBVI$ photometry of resolved stars in M83 and the resulting color–color and color–magnitude diagrams. We use ($F336W-F438W$) versus ($F555W$–$F814W$) color–color diagrams to constrain the variation of dust extinction along the line of sight of each individual star, and correct $F814W$ versus ($F555W-F814W$) CMDs for the extinction of individual stars to determine their ages. The high sensitivity and the superb resolving power in the WFC3 F336W band play a key role in allowing us to develop our extinction correction techniques, and demonstrate the performance of the newly installed WFC3. This results in improved stellar age estimates, and a better understanding of the recent star formation history of M83. Our investigations are focused on the followings.

(1) Do we see spatial variations of stellar ages in M83? If so, can we use these variations to learn more about the evolution of the galaxy and what triggers star formation?

(2) How well do various age estimates correlate (i.e., resolved stars, integrated light, clusters, number ratio of red-to-blue stars, Hα morphology, stellar surface brightness fluctuations, presence of Wolf–Rayet stars)?

This chapter is organized as follows. In Section 2.2, we describe the observations, photometric analysis, and the extinction correction method. CMDs and color–color diagrams of the 50 selected regions are then used to provide stellar age estimates, as described in Section 2.3. Comparisons with other age estimates (i.e., integrated light and star clusters) are also made. In Section 2.4, we compare the stellar ages to a variety of other parameters that correlate with age, including red-to-blue star ratios, Hα morphology, and surface brightness fluctuations. Section 2.5 includes a discussion of how these comparisons can be used as diagnostics, with special attention paid to the question of what spatial variations can tell us

about the star formation history in M83, and on the question of how star clusters might dissolve and populate the field. In Section 2.6, we investigate the locations of sources of Wolf-Rayet stars in our M83 field and discuss the correlation with the positions of young regions. In Section 2.7, we describe how the spatial resolution affects our measured colors and magnitudes, and our age estimates of stars in our M83 field. A summary of our primary results is provided in Section 2.8.

2.2 *HST* WFC3 Observations

2.2.1 The WFC3/UVIS Data

The data were obtained in seven broadband and seven narrowband filters in the WFC3 UVIS and IR channels. Details are described in Dopita et al. (2010) and Chandar et al. (2010). In the current study we use four broadband images. The filters and exposure times are F336W (1890 s), F438W (1880 s), F555W (1203 s), and F814W (1203 s). Although we do not make transformations to the Johnson–Kron–Cousins $UBVI$ system, we will refer to these filters as U, B, V, and I for convenience. Three exposures were taken in each filter at different dithered positions to remove cosmic rays, the intrachip gap, and to partially compensate for the undersampled point-spread function (PSF) of the WFC3/UVIS channel. The raw data were processed using the `MULTIDRIZZLE` software (Koekemoer et al. 2002) with an effective pixel size of $0.0396''$, which corresponds to 0.885 pc pixel^{-1} at the distance of 4.61 Mpc (Saha et al. 2006). The resulting multidrizzled images are combined, cosmic-ray removed, and distortion-corrected. A color composite of the F336W, F555W, F814W (broad bands) and F502N, F657N (narrow bands) images is shown in Figure 2.1. It covers the nuclear region of M83, part of its eastern spiral arm, and the inter-arm region. Stars in the cores of compact star clusters are not resolved at this resolution, but the brighter stars in the outskirts of the star clusters and in the field are generally resolved into individual stars.

Details of the effects of spatial resolution are discussed in Section 2.7. Since we are interested in spatial variations of stellar ages in M83, we selected 50 regions in the spiral arm and inter-arm areas. Boxes outlined in blue (very young — age ≤ 10 Myr, see Section 2.3), yellow (young — $10 \leq$ age ≤ 20 Myr), and red (intermediate-aged — age ≥ 20 Myr) in Figure 2.1 show the 50 regions selected for detailed study in this chapter.

2.2.2 Photometry and Artificial Star Tests

Photometric analysis of the WFC3 M83 data was performed on the U, B, V, and I images using the DoPHOT package (Schechter et al. 1993) with modifications made by A. Saha. Additional routines to derive parameters for the kurtosis of the analytic PSFs used by DoPHOT, and for post-processing DoPHOT output to obtain calibrated aperture-corrected photometry, were performed using customized IDL code written by Saha. A more detailed description of these procedures can be found in Saha et al. (2010). The kurtosis terms were derived by fitting the functional form of the DoPHOT analytic PSF to 20 relatively bright and isolated stars. The remaining shape parameters (σ_x, σ_y, and σ_{xy}) are dynamically optimized within DoPHOT.

The difference between the shape parameters for an individual object and those for a typical star was calculated and used to classify the object as a star, a galaxy, or a double-star. The shape parameters were determined separately for each image. The numbers of objects classified as stars are approximately 20,000 in U and B, 17,000 in V, and 15,000 in I band images, respectively. The calculated full width at half-maxima (FWHMs) are $U = 0.096''$(2.42 pixel), $B = 0.093''$(2.34 pixel), $V = 0.091''$(2.29 pixel), and $I = 0.113''$(2.85 pixel). All magnitudes are in the WFC3-UVIS VEGAMAG magnitude system, calculated using Equation (4) in Sirianni et al. (2005) and the latest zeropoint magnitudes: $U = 23.46$, $B = 24.98$,

$V = 25.81$, and $I = 24.67$ mag, provided by STScI at the HST/WFC3 Web site-http://www.stsci.edu/hst/wfc3/.

A multi-wavelength $UBVI$ catalog was then constructed by matching the individual objects in each catalog between these filters. Interestingly, we found that the extreme image crowding in these images, combined with the excellent panchromatic sensitivity and unprecedented spatial resolution provided by the newly installed WFC3, introduced a new challenge during this matching step, with large numbers of "pseudo" matches occurring if too-large a match radius was used. We discuss the effects of spatial resolution in Section 2.7.

Figure 2.2 demonstrates this problem by showing the $F555W$ and color composite image cut-outs near Regions 26 and 27. In the middle panel of Figure 2.2, stars circled in red are objects with $(V-I)$ colors that are very red ($(V-I) > 1.2$ mag), but have $(U-B)$ values that are fairly blue ($-0.4 < (U-B) < -1.7$ mag). These can be seen as the spray of points in the upper right parts of the top right panels of Figures 2.3 and 2.4, which will be discussed below. As shown by the postage stamp images in Figure 2.2, about half of these are likely to be blue stars with very high values of reddening (i.e., the bottom panel and the small postage stamps on the right show that they are in dusty regions), while the other half are very close superpositions of at least one red and one blue star, which we will call "pseudo" matches (i.e., the panels on the left show a strong blue and red gradient across many of the objects).

We found that using a very small matching radius of 0.5 pixels was needed to minimize "pseudo" matches in our catalog. Earlier attempts using a matching radius of 3 pixels resulted in $\sim$10% pseudo matches. Accurate matching also requires precise geometric distortion corrections in all filters. However, even when these conditions are met, there is a finite chance that two different stars will fall

within the same aperture. This is most easily seen by blinking the U- and I-band images. While the single stars stay in the same position, the pseudo match stars move slightly, showing they are two different stars with different colors.

The final stellar catalog contains ∼15,000 objects. We found that our procedure results in only a few percent of pseudo matches, as will be discussed in Section 2.4 (i.e., the upper right panel of Figure 2.4).

To measure the photometric completeness, we performed artificial star tests with the same detection and photometry procedure as applied to the actual stars. We inserted 1000 artificial stars with Gaussian PSFs and FWHMs appropriate for these stars at random positions into all four images. The magnitude of the inserted stars varied from 22 to 28 mag in steps of 0.25 mag. The 50% completeness levels at 5 σ detection thresholds for a typical region are reached at recovery magnitudes of approximately 24.3, 25.1, 25.3, and 24.8 mag for the U, B, V, and I images, respectively. These limits can vary by about a magnitude, depending on the brightness of the background in a given region. The exception is Region 48, which includes the nucleus. The completeness thresholds are two or more magnitudes brighter in this region due to the very high background. This region has therefore been excluded from the rest of the discussion, but is included in Table 2.1 for reference.

2.2.3 CMDs and Color–Color Diagrams in M83

The top panels of Figure 2.3 show the I versus $(V-I)$ CMD (left) and the $(U-B)$ versus $(V-I)$ color–color diagram (right) of resolved stars extracted from the cross-matched catalog. The CMD shows the presence of young main-sequence (MS) stars, transition or He-burning "blue loop" stars, red giant stars (hydrogen shell-burning and hydrogen+helium shell-burning stars), and a relatively small

number of low-mass red-giant branch (RGB) stars. This is because the tip of the low-mass RGB stars is at $I = 24.7$ mag (Karachentsev et al. 2007), which is roughly the same as our completeness threshold. The ages of these stars range from $\approx$ 1 to $\approx$ 100 Myr. The Padova isochrones (Marigo et al. 2008) ranging in age from log τ (age/yr) = 6.55 (3.5 Myr) to log τ (age/yr) = 8.0 (100 Myr) are included in Figure 2.3 for reference. Note that the younger isochrones (e.g., 1 Myr) fall nearly on top of the 3.5 Myr isochrone, and hence are not included in the diagram.

The arrows in both panels show $A_V = 1$ reddening vectors for M83 using the $R_V = 3.1$ extinction curve of Cardelli et al. (1989). Corrections have been made for foreground Galactic extinction (Schlegel et al. 1998) using $A_{F336W} = 0.361$, $A_{F438W} = 0.290$, $A_{F555W} = 0.229$, and $A_{F814W} = 0.133$ mag, respectively.[2] In Figure 2.3, we only plot stars with photometric errors less than 0.25 mag in the filters used for each diagram. The numbers of objects plotted in the CMD and the color–color diagram are about 12,000 and 8500 stars, respectively. Since approximately 30% of the stars are not detected in one or more of the U, B, or I filters, due to either reddening or intrinsically red or blue colors, fewer stars are plotted in the color–color diagram.

We adopt a value of 1.5 times solar metallicity (Z=0.03), the highest metallicity isochrones available from the Padova database, for M83 based on Bresolin & Kennicutt (2002). A test using solar metallicity (Z=0.019) isochrones showed that the ages for a typical region would be $\approx$ 2 Myr older if the lower metallicity is adopted. This agrees with the study by Larsen et al. (2011), who found that the simulated CMDs of young massive clusters in M83 with solar and super-solar metallicity isochrones would not look much different. Theoretical isochrones cal-

[2]NASA/IPAC Extragalactic Database (NED): http://ned.ipac.caltech.edu/

culated for the WFC3 filters and Z=0.03 (1.5 $Z_{\odot}$) from the Padova database[3] (Marigo et al. 2008) are overlaid on both panels in Figure 2.3. The dashed line in cyan shows the 50% completeness level in I and $(V-I)$, using the completeness threshold numbers from the artificial star test in Section 2.2.

The bottom panels of Figures 2.3 and 2.4 show the histograms of ages and masses for the same stars plotted in the CMD and color–color diagram. The ages and masses of stars were estimated by finding the closest match between the I and $(V-I)$ values for each star, using a fine mesh of the stellar isochrones plotted in the CMD and color–color diagram in Figures 2.3 and 2.4. More details about the stellar age-dating from the CMDs and the stellar isochrones are given in Section 2.3.1.

2.2.4 Extinction Corrections

Since M83 has an intricate structure of dust lanes associated with active star forming regions in the spiral arms and thin layers of dust in the inter-arm area in Figure 2.1, we cannot use a single value of internal extinction and apply it to correct for the extinction of all stars in a given region. In the color–color diagram in Figure 2.3, we notice that while the bluest stars match the model isochrones quite well after we correct for Galactic foreground extinction, the majority of stars are found redward of the models, implying a typical extinction of $A_V \simeq 0.5$ mag (for the densest part of the data "swarm"). As described below, we can determine the reddening of these stars if we assume that they are intrinsically blue stars that belong on the Padova models (i.e., with $(V-I) \simeq -0.3$ mag). A visual inspection supports this interpretation. Stars with observed values of $(V-I) \approx -0.3$ mag are found in areas with no obvious dust features surrounding them while stars with $(V-I) > 0.5$ mag are near dust filaments.

[3]CMD version 2.3; http://stev.oapd.inaf.it/cgi-bin/cmd

Our basic approach to correct the colors (and luminosities) of individual stars for the effects of extinction is to backtrack the position along the reddening vector for each data point, until we hit the stellar isochrones in the color–color diagram. What makes this method work is the fact that all the isochrones are nearly on top of each other in the range $(U-B) < 0.0$ mag. The way we apply this in practice is to match the observed and predicted values of the reddening free Q parameter defined by:

$$Q_{UBVI} = (U-B) - \frac{E(U-B)}{E(V-I)} \times (V-I) \tag{2.1}$$

(Mihalas & Binney 1981). Using observed values in the U-, B-, V-, and I-band images, we compute the observed $Q_{\rm UBVI}$ values by using the standard slope of $E(U-B)/E(V-I) = 0.58$ (Mihalas & Binney 1981; Whitmore et al. 1999), which corresponds to $R_V = 3.1$. The predicted Q values are calculated using the 1.5 $Z_\odot$ Padova isochrones. A complication is that we cannot simply use the matched Q values to determine corrected values of $(U-B)$ and $(V-I)$, since they would, by definition, fall precisely on the isochrones (i.e., I would be using circular reasoning). Instead, we solve for the extinction in $(U-I)$, which is partly independent and uses the longest wavelength baseline. We then calculate the extinction values in each of U-, B-, V-, I-band image and the color excess values in $(U-B)$ and $(V-I)$.

The averages of the corrected internal extinction and color excess values by our star-by-star correction method are $A_{F336W} = 0.696$, $A_{F438W} = 0.559$, $A_{F555W} = 0.441$, $A_{F814W} = 0.256$ mag, and $E(U-B) = 0.137$ and $E(V-I) = 0.185$ mag. This is similar to the average internal extinction ($A_{F555W} = 0.425$ mag) estimated from the cluster spectral energy distribution (SED) fitting by Bastian et al. (2011). However, our results differ from the average extinction ($A_V = 0.671$ mag) of 45 clusters in the nucleus ($\sim$20″in diameter) of M83, determined

from Hα/Hβ ratios by Harris et al. (2001). This is consistent with the finding of larger extinction in the nuclear region by Chandar et al. (2010).

In the color–color diagram (top right panel) of Figure 2.3, we note that while most of the data points are consistent with the standard reddening vector, the stars located in the green triangle appear to follow a flatter reddening vector. Whether this is actually due to a different reddening law in M83 (e.g., as has been suggested for heavily extincted regions such as 4, 12, and 20) or is some sort of artifact (e.g., due to photometric uncertainties, unresolved star clusters, or the "pseudo" matching problem discussed above) is difficult to determine from our present dataset. However, for our specific needs the precise answer to this question is not critical. Our approach will be to correct the data points in the triangle back to a position near the top of the isochrones, as shown by the intersection of the red dotted line and the isochrones in Figure 2.4. This is equivalent to using a range in R_V between 3.1 and 5.7 (the value represented by the red dotted line).

The upper panels of Figure 2.4 show the CMD and color–color diagram corrected for the internal extinction in M83. The arrows in both panels are the reddening vectors. We do not apply an extinction correction for stars with $(V - I) \geq 1.2$ mag, or above an extrapolation of the flatter extinction vector from the bluest possible isochrones (see the red dotted lines in the upper right panel of Figure 2.4), since we believe that the colors of many of these sources are incorrect (i.e., roughly half are likely to be pseudo matches, as discussed in Section 2.2.2 and shown in Figure 2.2). We note that only about 4 % of the stars fall in this part of the diagram. These stars are removed from the subsequent analysis. If we include these stars, our age estimates typically increase by about 1 Myr.

Also, stars below the blue dotted line in Figure 2.4 are not corrected for extinction, since these are MS turnoff stars (i.e., blue loop or transition stars in

general), and hence, do not have unique $UBVI$ colors for the stars along a given reddening line, unlike the MS stars with $(U-B)<0.0$ mag.

Based on the extinction corrected CMD in Figure 2.4, we note that (1) the corrected data now show a relatively narrow distribution of points along the left side of the CMD in agreement with ages of ∼3 Myr and (2) while the data now align with the model isochrones much better, there is still a fair amount of scatter (especially for $I < 24$), primarily due to observational uncertainties from the fainter stars. The bottom panels of Figure 2.4 show the distribution of ages and masses of stars after we apply our extinction correction technique. Based on the automatic method described in Section 2.3.1, we note that the luminosity weighted mean ages determined from the corrected colors and luminosities are significantly younger (∼14 Myr; Figure 2.4) than the mean ages determined from the uncorrected colors and luminosities (∼27 Myr; Figure 2.3), as we expected.

2.3 Age-dating Populations in M83

In this section we discuss several different methods of age-dating stellar populations in M83, using both individual stars and star clusters, and then intercompare the results. We do not necessarily expect field star and cluster ages to agree, since the dissolution of clusters may bias the observed cluster population toward younger ages than the surrounding field stars.

2.3.1 Age-dating the Resolved Stellar Population Using Color–Magnitude Diagrams

As shown in Figure 2.1, we selected 50 regions that cover spiral arm and inter-arm areas in order to study the recent star formation history of M83. Figures 2.5 and 2.6 show cutouts of Regions 12, 7, 29, and 2. The color–magnitude diagrams and color–color diagrams of all 50 regions (similar to Figures 2.5 and 2.6) are attached

in the Appendix A. These figures include color-color diagrams of the stars in these regions, as well as CMDs that are uncorrected (upper) and corrected (lower) for extinction. The four regions (12, 7, 20, 2) highlight the range in age of the dominant stellar population, from very young to intermediate ages, i.e., Region 12 with very strong Hα emission superposed on the cluster stars; Region 7 with a large bubble of Hα emission surrounding the stars and clusters; Region 29 with no Hα emission, but large numbers of bright red and blue stars; Region 2 with no Hα emission and fainter stars.

A cursory glance at the CMDs of these four regions (Figures 2.5 and 2.6) show clear differences. The primary differences are, as predicted by the isochrones, that younger regions contain: (1) bluer MS stars, (2) larger numbers of upper MS stars, and (3) larger ratios of blue to red stars. Our regions do not, however, contain only stars of a single age. Even these four regions, which were chosen to include a single dominant stellar population, contain a mix of young and old stars. In this chapter, I am primarily interested in the ages of the bright young stars in these regions, which dominate CMDs in luminosity-limited samples.

In practice, this focus on the younger population is carried out by imposing a magnitude cutoff of $M_I = -5.5$ mag (i.e., $I = 22.82$ mag which corresponds to the age cutoff of $\sim$60 Myr in the CMD) for the stars used to estimate ages (i.e., the magenta dashed line in Figure 2.4). This luminosity limit allows us to stay above the completeness limit for all but the very reddest stars (see Figure 2.3), while also focusing on evolved stars and those on the upper MS, which are most sensitive to the age of a stellar population. Our primary goal is to obtain reliable "relative" estimates for the 50 regions (rather than absolute ages), and our magnitude limit is sufficiently deep to accomplish this goal.

We compare the extinction corrected colors and magnitudes of stars with

the Padova stellar isochrones in two ways to estimate the age of the dominant stellar population in each region. First, two of the authors (H.K. and B.C.W.) independently estimated ages based on a visual comparison of the CMDs and isochrones. We focused on features such as the color of the MS stars, the number of stars in the upper MS, and the number ratio of blue to red stars. The left panel of Figure 2.7 shows that the independent, visually determined age estimates are in good agreement with a 7.9σ (slope/uncertainty of the best linear fit) correlation and a slope within 1σ of the unity value. The average ages of these two independent (manual) estimates are listed in column $\mathrm{Age_{CMDman}}$ in Table 2.1.

Next, we estimated the ages automatically, finding the closest match in both age and mass for each star by comparing the extinction corrected I magnitude and $(V-I)$ color with a fine mesh of stellar isochrones generated from the Padova models ($\log \tau$ (age/yr) ranging from 6.05 to 8.35 in steps of 0.05). We then calculate a luminosity-weighted age from the distribution of individual stellar ages in each region. The result of the automatic age estimate is listed in column $\mathrm{Age_{CMDauto}}$ in Table 2.1.

To assess the uncertainties in our age and mass determinations for each star, we ran a test for four different cases by adding and subtracting the photometric errors in the $(V-I)$ color and I-band magnitude. This moves each object on the CMD to the right ($+(V-I)_{\mathrm{error}}$), left ($-(V-I)_{\mathrm{error}}$), down ($+m_{I\mathrm{error}}$), and up ($-m_{I\mathrm{error}}$). We find similar ages of 21.9 Myr (Region 3) and 26.7 Myr (Region 11) for the dominant luminous stellar populations, despite the fact that our photometry includes a significantly larger area around each cluster. Hence we find good agreement between our age estimates and those of Larsen et al. (2011). Each method has its own strengths and weaknesses. Our approach has the advantage of correcting the photometry of individual stars for the effects of extinction

to improve our age estimates, but the disadvantage that this requires imaging in more than three optical bands with a crucial need for the U-band observation. The Larsen et al. (2011) method does not correct for the effects of extinction, but allows for a better determination of the star formation history over a wider age range (i.e., out to $\sim$1 Gyr).

2.3.3 Comparison between $\mathrm{Age_{CMD\,auto}}$ and Compact Cluster Ages

Much of our recent work has involved age-dating star clusters using the integrated light ($UBVI$ and Hαemission) from the cluster and model SED fitting. To compare the age of star clusters in each region to the age determined from individual stars in each region, we adopt the ages and luminosities of compact clusters identified in our previous work (Chandar et al. 2010). Details of the cluster age-dating method can be found in that paper.

We note that the regions sampled in this study are large (i.e., several hundred pc^2) and may include stars and star clusters spanning a wide range of ages. This requires making the comparison between the ages of field stars and star clusters with caution. Only the largest star forming complexes within spiral galaxies have such dimensions (e.g., the giant H II region NGC 604 in M33; Freedman et al. 2001). More typical regions are much smaller, and hence would not dominate the entire field. This will tend to weaken our correlations, especially when comparing resolved stellar ages with cluster ages.

Using the ages of star clusters determined from the SED fitting, we compute the luminosity-weighted mean age of each region, as we did for stars in the same region. The ages of 50 regions are listed in column $\mathrm{Age_{Cl}}$ in Table 2.1. The upper panel of Figure 2.10 shows a comparison between the luminosity-weighted mean age ($\mathrm{Age_{Cl}}$) of the compact clusters in a given region and our stellar age

($\mathrm{Age_{CMDauto}}$) estimates based on the CMDs of all the resolved stars in the region (as discussed in Section 2.3.1). The correlation between these two ages is fair (5.4σ correlation). We note that while the midpoints for the two methods are similar, the slope is steeper, as discussed in more details in the next section.

2.3.4 Comparison between $\mathrm{Age_{CMDauto}}$ and Age Estimates from Integrated Light from the Entire Regions

We obtain an independent estimate of the age of each region by measuring the colors of the entire region, and perform a simple SED fit, in the same way as we did for star clusters (i.e., Chandar et al. 2010). The lower panel of Figure 2.10 shows a comparison between our age estimates for the resolved stellar populations using CMDs ($\mathrm{Age_{CMDauto}}$) and from the integrated light ($\mathrm{Age_{Reg}}$) in each region.

While there is a fair correlation (4.6σ) between the CMD and integrated photometric age estimates, there is also a fair amount of scatter and an apparent gap in the region ages in the range $6.8 < \log\,(\mathrm{age/yr}) < 7.2$. This gap is similar to the well known artifact for cluster age estimates which is due to the looping of predicted cluster colors in this age range (see Chandar et al. 2010). We also note that the slope of the relation is steeper than the unity vector, with integrated light ages ranging to much lower ages than the CMD ages. This is similar to the comparison with $\mathrm{Age_{Cl}}$, as discussed above. This is probably caused by a variety of effects including: (1) the integrated age estimates take into account Hα emission (which is very sensitive to massive young stars) while the CMD estimates do not; (2) the 1 Myr isochrones are essentially on top of the 3 Myr isochrones, making it rare that the minimum age ever gets selected by the software that does the matching with the isochrones; and (3) the adoption of an $\mathrm{M}_V = -5.5$ mag cutoff removes all stars with ages $\geq$100 Myr from the $\mathrm{Age_{CMDauto}}$ estimates, while the light from older stars is still included in the integrated light used for the $\mathrm{Age_{Reg}}$

estimate (hence, the $\mathrm{Age}_{\mathrm{CMDauto}}$ estimate can never be $\geq$50 Myr, while the $\mathrm{Age}_{\mathrm{Reg}}$ can be older).

This difference in slope in Figure 2.10 highlights the fact that each age-dating method has its own idiosyncrasies. By comparing a number of different methods, we begin to understand these artifacts better, and learn how large the true systematic uncertainties can be.

2.4 Comparison between $\mathrm{Age}_{\mathrm{CMDauto}}$ and Other Parameters that Correlate with Age

We are now ready to compare our age estimates for the resolved stellar components in 50 regions to other observables that correlate with age. These include: (1) number ratio of red-to-blue stars (e.g., Larsen et al. 2011), (2) morphological categories (Whitmore et al. 2011a), and (3) stellar surface brightness fluctuations (Whitmore et al. 2011a).

2.4.1 Comparison between $\mathrm{Age}_{\mathrm{CMDauto}}$ and Number Ratio of Red-to-blue Stars

One property that is expected to correlate with age is the number ratio of red-to-blue stars. At very young age, all stars are blue. As the population ages, the number of red giant stars (H-shell burning and H+He-shell burning stars) increases. This effect can be seen by noting that nearly all of the stars in Region 12 (Figure 2.5) are blue, while there are large numbers of red stars in Regions 29 and 2 (Figure 2.6).

The number ratio of red-to-blue stars (column red-to-blue ratio in Table 2.1) is calculated by using a criteria that $(V-I)$ be redder than 0.8 mag for red stars. The top panel of Figure 2.11 shows a fairly good correlation (7.2σ) between $\mathrm{Age}_{\mathrm{CMDauto}}$ and the red-to-blue ratio.

2.4.2 Comparison between $\mathrm{Age_{CMDauto}}$ and Morphological Category

The middle panel of Figure 2.11 shows the correlation between our automatic CMD age estimates and the morphological classification for a given region, as defined in Whitmore (2011b). Briefly, regions with Hα emission superposed on top of the stellar component are type 3 (emerging star clusters), regions with small Hαbubbles are category 4a (very young), regions with large Hαbubbles are category 4b (young) , and regions with no Hαbubbles are category 5 (intermediate age). Based on this criteria, the regions displayed in Figures 2.5 and 2.6 are classified as categories 4a (Region 12), 4b (Region 7), 5a (Region 29), and 5a/5b (Region 2), respectively. Each region was classified independently by two authors (H.K. and B.C.W.). The mean of the two determinations is used in what follows, and is listed in column "Hα Morphology" of Table 2.1.

The middle panel of Figure 2.11 shows that stellar CMD age estimates ($\mathrm{Age_{CMDauto}}$) and morphological categories (Hα morphology) show a fair correlation (5.8σ), but not as good as the strong correlations (9σ for $\log \tau < 7$ and 5σ for $\log \tau > 7$) found with ages for compact clusters in Whitmore et al. (2011a). This is probably due to the fact that most of the regions are not dominated by a single age stellar population, making the morphological classification for an entire region problematic (i.e., there is strong Hα emission in part of the region but none in other parts).

2.4.3 Comparison between $\mathrm{Age_{CMDauto}}$ and Stellar Surface Brightness Fluctuations

In Whitmore et al. (2011a), we developed a method to age-date star clusters based on an observed relation between pixel-to-pixel flux variations (RMS) within star

clusters and their ages. This method relies on the fact that the young clusters with bright stars have higher pixel-to-pixel flux variations, while the old clusters with smoother appearance have small variations. This is because the brightest stars in a 100 Myr population have $M_I \approx -3$ mag, which is below our 50 % photometric completeness limit ($M_I = -3.6$ mag) and well below our magnitude cutoff of $M_I = -5.5$ mag used in our stellar age-dating method described in Section 2.3.1.

The bottom panel of Figure 2.11 shows the correlation between the resolved stellar ages ($\mathrm{Age_{CMDauto}}$) and the surface brightness fluctuations (pixel-to-pixel RMS) measured in the 50 selected regions. We find little or no correlation (1.1σ) with a relatively large amount of scatter, especially for the younger clusters. Part of this scatter may be caused by the two-valued nature of the effect as discussed in Whitmore et al. (2011a), with a maximum value of the surface brightness fluctuations around 10 Myr, and lower values for both smaller and larger ages. Another reason for the scatter is the fact that many of the regions have mixed populations, rather than single age populations.

2.5 Insights into the Star Formation History in M83 Based on Spatial Variations for 50 regions

We first examine how the ages for the 50 regions are distributed in Figure 2.1. The boxes in this figure are color-coded as follows: blue (very young with ages less than about 10 Myr), yellow (young with ages between about 10 and 20 Myr), and red (intermediate aged with ages greater than about 20 Myr). As expected, we find that the very young regions are primarily associated with the spiral arms, the young regions tend to be "downstream" from the spiral structure (i.e., on the clockwise side away from the dust lanes), while the intermediate aged regions are found on both sides of the spiral arms in the inter-arm regions.

A similar, more detailed analysis is being done by Chandar and Chien using the cluster ages in M51 (R. Chandar & L. Chien 2012, in preparation) and M83 (R. Chandar & L. Chien 2012, in preparation). They compare the age gradients they find with models developed by Dobbs & Pringle (2010), assuming a variety of different triggering mechanisms (i.e., spiral arms, bars, stochasticity, and tidal disturbances).

We can perform a similar experiment here, since we have age estimates for each individual star. The three panels in Figure 2.12 show the distribution of stars with ages in the ranges 1–10, 15–35, and 40–100 Myr, respectively. The top panel is the youngest group of stars, clearly showing that the stars in these regions are mostly distributed along the active star-forming region (i.e., associated with strong Hαemission) in the spiral arms. The stars in the middle panel tend to be found slightly downstream of the spiral arms, while the older stars are still farther out in the inter-arm regions, as expected.

These diagrams can also be used to examine whether there is evidence that most of the young stars form in clusters and clustered regions and then dissolve into the field. Pellerin et al. (2007) made a similar set of diagrams for the galaxy NGC 1313, which supported this interpretation. We find that the young star samples show strong clustering, while the older star samples are progressively more uniform. Hence, these distribution maps of stars in the different age group support the idea that the stars form in clusters in spiral arms, and then most of the clusters dissolve, populating the field with stars (Lada & Lada 2003). R. Chandar et al. (2012, in preparation) will examine this subject more quantitatively in the future.

2.6 Using Wolf–Rayet Stars to Check for Consistency with Our Age Estimates

In this section, we compared the ages resulting from a variety of age-dating methods for different star-forming regions in M83. Here, we extend our analysis by considering previously identified Wolf–Rayet (WR) stars in M83, which are ∼1–4 Myr old (Crowther 2007), as another independent age estimate.

Hadfield et al. (2005) identified 283 WR sources in M83 from narrowband imaging centered on the He II λ4686 emission line, plus spectroscopic follow-up. Seventeen of these WR sources fall in our WFC3 field of view. Figure 2.13 shows their locations in the *HST* image, and Table 2 lists the coordinates of these sources, as well as the region in which they are located.

The lower resolution of the ground-based Hadfield et al. (2005) study makes it difficult (in many cases) to uniquely identify the WR sources in the *HST* image, although we can easily determine whether such a source is located within one of our 50 regions. Figure 2.13 shows a color image of M83 (center panel) with five regions, labeled A through E, that contain all 17 WR sources. Here, the Hα and F814W images are shown in red, F555W in green, and F336W in blue. Black and white images are the image cutouts in the F814W and the Hα filters of regions A–E, as outlined in green in the central panel. The original finding chart of the region A taken from Hadfield et al. (2005) is shown in the top right panel in Figure 2.13. In the Hα image, the stellar continuum has been subtracted from the Hα image, leaving just the ionized gas.

We matched the coordinates of the WR sources and the *HST* images, by assuming that the WR source 99 is perfectly centered on a relatively isolated, compact Hα knot. We also compared the locations of the 17 matched WR sources in the M83 *HST* images with the finding charts from Hadfield et al. (2005) to verify

our source matching. The excellent spatial resolution of the *HST* image also makes it possible to check whether any of the WR sources are actually compact star clusters. While the majority do appear to be individual stars, or a dominant star with a little "fuzz" which is likely a faint companion star, there are at least three cases where the counterpart appears to be a bright compact cluster (i.e., 74, 86, 105: circled objects in Figure 2.14). These three objects are brighter than $M_V = -9$ mag with the concentration index (CI) larger than 2.3, consistent with the cluster CI used in Chandar et al. (2010). There are several more cases where the counterpart is in a looser association of stars (e.g., 78, 102, 103).

All the WR sources, except the sources in cutout E and 108 in cutout D, are located in the spiral arms. This is expected, since these are the sites of most recent star formation. Nine of the 17 are in regions of strong Hα emission, seven more are in regions of faint Hα emission, and only one source (107 in cutout D) appears to have no Hα associated with it.

Our primary question is whether the WR sources tend to be found in regions that we estimated to have young ages. In Table 2 we match the WR sources with the region where they are found in and find that their ages range from 1.1 Myr (Region 35) to 50.1 Myr (Region 41). This shows that such a correlation does exist, with 6/8 (75%) of WR sources in regions having $\mathrm{Age_{Reg}}$<4.6 Myr. Similarly, Hadfield et al. (2005) found that five of their WR sources are included in a compact star cluster catalog developed by Larsen (2004), and three of these five clusters (193, 179, 179) have estimated ages in the range 1.5 – 6 Myr, consistent with ages expected for WR stars.

Figure 2.14 shows the CMD and color–color diagram of the measured colors from our *HST* observations of the object that best matches the WR sources from Hadfield et al. (2005). We find that most of these sources are in the top left of the

two-color diagram. We conclude that there is a strong tendency for WR sources to be associated with the youngest regions of star formation. The good correlation provides general support for the accuracy of our CMD age estimates.

2.7 Effect of Spatial Resolution

Spatial resolution affects virtually all studies of individual stars in nearby galaxies. As is typical, in this chapter we have assumed that the point sources identified in Section 2.2 are individual stars, although we also discovered a small fraction of pairs of nearly aligned stars, one red and one blue, that can be identified from their anomalous colors (e.g., "pseudo-match" Figures 2 and 4). Here, we address more generally how spatial resolution affects the measured colors and magnitudes, and hence the derived ages, of stars in our M83 regions.

We begin by answering a simple question: "What would the Orion Nebula look like at the distance of M83? Would we be able to distinguish the four central stars that make up the Trapezium or would they appear as a single star?" The separation between the four stars in the Trapezium ($10''$at $D \approx 0.5\,\mathrm{kpc}$) would be roughly $0.001''$at the distance of M83, approximately a factor of 40 smaller than a single pixel in our image, and hence these would appear as one point-like source. However, we note that the vast majority of the remaining bright stars in the Orion nebula are much more widely separated, and would not suffer from this problem. We also note that our selection criteria are designed to avoid including stars in the crowded central regions of star clusters and associations, which also minimizes the problem.

We perform a more quantitative analysis by degrading *HST*/ACS images of the compact star cluster NGC 2108 in the Large Magellanic Cloud (LMC) (ID:10595; PI: Goudfrooij, see Goudfrooij et al. 2011), which is at a distance of

$\sim$ 50 kpc, by a factor of 100 (i.e., equivalent with the distance of $\approx$ 5 Mpc), as roughly appropriate for M83. The degraded images, created from a combination of rebinning and Gaussian smoothing to approximately mimic the PSF of Advanced Camera for Surveys (ACS), are then run through our normal object-finding software described in Section 2.2. The numbers of objects found in the degraded NGC 2108 images are $\sim$20 in the F555W and F814W ACS images. Figure 2.15 shows the F555W ACS image of NGC 2108, along with the degraded images and a color image (i.e., a color composite of F435W, F555W, and F814W ACS images).

Additionally, we then perform aperture photometry on the detected source positions in the non-degraded ACS images using a radius 300 pixels to collect light from all stars that would fall within our aperture if NGC 2108 was located at a distance of 5 Mpc (i.e., M83). Objects along the edge and within 1000 pixels of the center of the cluster in NGC 2108 are discarded, as would be the case for the corresponding photometry in M83. Figure 2.16 shows the extent of the 300 pixel aperture for several sources in yellow, as well as the nearest dominant star in red. The magnitude of the dominant stars (using a 3 pixel aperture and the appropriate aperture correction) is considered the "truth" measurement while the magnitude in the corresponding 300 pixel aperture is the value that would be determined at the distance of M83. We calculate the magnitude and color offsets, i.e., ΔI and $\Delta(V-I)$ mag of the dominant stars, by taking the difference between the 3 pixel and 300 pixel aperture magnitudes.

One complication is that our default sky subtraction method would remove the vast majority of faint and moderate brightness stars in the background annulus in the NGC 2108 image, but these stars would not be detected individually at the distance of M83 and hence would be included in the sky measurement. We therefore adjusted the "clipping" parameters in the sky subtraction algorithm to

remove only the bright stars in NGC 2108, thereby mimicking the case for M83 to the highest degree possible.

In Figure 2.17 we show the original CMD for Region 3 in M83 (solid points), compared with a version where the magnitudes and colors have been 'perturbed' by an amount ΔI and $\Delta(V-I)$ determined by matching to the closest values of $(V-I)$ from the NGC 2108 data experiment (open points). As expected, corrections for the degraded spatial resolution in M83 tend to make the corrected magnitudes slightly fainter and redder, as can be seen in Figure 2.17. The mean difference in V is -0.24 ± 0.30 mag with a range from $+0.20$ to -0.65 mag. In I, the mean difference is -0.40 ± 0.39 mag with a range from $+0.07$ to -1.18 mag. We note that the largest difference is seen for object 10, as shown in Figure 2.16, where several relatively bright red stars in the 300 pixel aperture cause the largest correction (i.e., -1.18 mag in I and redward by 0.63 mag in $(V-I)$). Object 40, dominated by a single very bright star, shows the opposite extreme, with a change of -0.02 mag in V and -0.01 mag in I. We also note that object 31 does not make it into our sample since the two bright stars are far enough apart that it is clear from the degraded image in Figure 2.15 that this is not a single star. This object gets removed in the DoPHOT photometry as described in Section 2.2, and hence is not used in the experiment described above.

We then rerun our age-dating software on the corrected CMD in Figure 2.17. We find a mean age of 23.8 Myr compared to the original value of 21.9 Myr. Hence, while a specific "star" may be affected by a sizeable amount, the overall effects of degraded spatial resolution are relatively minor for our study.

To summarize, we have performed a numerical experiment using observations of an intermediate-age star cluster in the LMC (NGC 2108) for our "truth" image. Using a factor of 100 in spatial degradation, roughly appropriate for our

measurements in M83, we find that the typical corrections to our photometry are on the order of a few tenths of a magnitude, although much larger values are possible in specific cases. We conclude that while spatial resolution can result in measurable differences in the luminosities and colors of bright stars at the distance of M83, it does not strongly affect the age estimates for the 50 regions studied in this chapter.

2.8 Summary

Color–magnitude diagrams and color–color diagrams of resolved stars from the multi-band *HST*/WFC3 ERS observations of M83 have been used to measure the ages of stellar populations in 50 regions of this well-known face-on spiral galaxy. The diagrams show the presence of multiple stellar features, including recently formed MS, He-burning blue-loop stars, and shell-burning red giant stars. Comparisons between our stellar age estimates and a wide variety of other age estimators allow us to investigate a number of interesting topics. The primary new results from this study are as follows.

(1) An innovative new technique using a combination of CMD and color–color diagrams has been developed in order to correct for the extinction toward each individual star and to age-date the stellar population. The mean extinction values for the 50 regions studied in this galaxy are 0.696 (A_{F336W}), 0.559 (A_{F438W}), 0.441 (A_{F555W}), 0.256 (A_{F814W}) mag, respectively.

(2) The various age estimators (stellar, integrated light, clusters within the region) show fair correlations (i.e., between 4.6σ and 5.4σ). This is expected, since many of the regions have a mixture of different-aged populations within them, and each technique uses light from a different subset of the stars (e.g., the stellar age estimates use only bright stars, while integrated light includes all the

light). A comparison with previous age estimates by Larsen et al. (2011) shows a good agreement (see Section 2.3.2 for details).

(3) Comparisons between the stellar ages and other parameters that are known to correlate with age show a range from very good correlations (e.g., with red-to-blue ratios: i.e., 7.2σ) and fair correlations (e.g., Hα morphology with 5.8σ) to little or no correlation (e.g., pixel-pixel RMS from Whitmore et al. 2011a). This is expected for reasons similar to the ones discussed above.

(4) The regions with ages younger than 10 Myr are generally located along the active star-forming regions in the spiral arm. The intermediate age stars tend to be found "downstream" (i.e., on the opposite side from the dust lane) of the spiral arms, as expected based on density wave models. A more detailed comparison with models with various other triggering mechanisms (e.g., bars, density waves, tidal disturbance, and stochasticity; see Dobbs & Pringle 2010) is in process by Chandar and Chien for M51 and M83 (R. Chandar & L. Chien 2012, in preparation).

(5) The locations of Wolf–Rayet sources from Hadfield et al. (2005) are in broad agreement with the age estimates discussed in the current study. The much better spatial resolution from *HST* shows that many of the Wolf–Rayet "stars" from ground-based observations are actually young star clusters.

(6) Effects of spatial resolution on the measured colors, magnitudes, and the derived ages of stars in our M83 images are described in Section 2.7. Based on a numerical experiment using a star cluster NGC 2108 in the LMC, we found that while individual stars can occasionally show measurable differences in the colors and magnitudes, the age estimates for entire regions are only slightly affected.

Table 2.1: Properties of the 50 Regions in M83

Reg.	R.A.(J200)	Dec.(J2000)	Reg. Size	Age_{man}	Age_{auto}	ΔAge[a]	Age_{Reg}[b]	Age_{Cl}[c]	Pixel-to-Pixel	Red-to-blue	Hα	A_V^d	N_{Star}	N_{Cl}
	(hh:mm:sec)	(°:':")	(pc×pc)	(Myr)	(Myr)	(Myr)	(Myr)	(Myr)	RMS	Ratio	Morphology	(Mag)		
1	13:36:59.78	−29:52:30.19	310×310	18.0	17.8	1.8	47.9	38.8	0.0582	0.493	5.35	0.288	206	3
2	13:37:01.11	−29:52:21.60	350×290	27.5	31.5	2.2	17.4	51.3	0.0539	0.792	5.35	0.214	231	2
3	13:37:02.40	−29:52:10.72	310×310	22.5	21.9	1.7	28.7	28.7	0.0679	0.817	5.00	0.161	311	5
4	13:37:02.48	−29:52:48.35	250×260	8.5	6.9	0.5	—	2.2	0.0442	0.171	4.00	0.858	67	4
5	13:37:03.35	−29:52:42.20	240×290	12.5	12.2	1.0	6.6	24.8	0.0566	0.267	5.00	0.677	174	2
6	13:37:04.18	−29:51:56.32	280×210	17.0	22.6	1.1	24.0	30.9	0.0585	0.400	5.25	0.289	132	1
7	13:37:04.07	−29:52:09.72	250×250	6.5	11.3	1.2	4.2	16.9	0.0891	0.306	4.50	0.305	261	9
8	13:37:04.58	−29:52:22.24	250×260	9.0	9.9	0.5	3.5	20.3	0.0718	0.200	4.35	0.369	198	7
9	13:37:05.22	−29:52:41.88	420×280	27.5	22.3	2.9	114.8	—	0.0349	0.442	5.50	0.542	121	0
10	13:37:05.15	−29:51:43.48	210×170	13.5	10.2	2.6	—	10.7	0.0638	0.156	4.60	0.726	74	3
11	13:37:05.72	−29:51:57.44	240×250	25.0	26.7	1.0	52.5	12.6	0.0639	0.911	5.00	0.186	174	2
12	13:37:05.80	−29:52:18.88	250×200	6.5	6.5	0.3	2.4	4.2	0.0684	0.136	4.10	0.758	133	4
13	13:37:06.42	−29:52:27.48	340×180	19.0	26.5	1.8	81.2	—	0.0383	0.632	5.50	0.378	79	0
14	13:37:07.31	−29:52:15.96	440×310	15.5	17.9	0.9	91.2	31.6	0.0562	0.364	5.25	0.475	323	5
15	13:37:07.53	−29:51:40.04	200×180	20.0	10.8	0.5	52.5	—	0.0686	0.135	5.00	0.322	93	0
16	13:37:08.32	−29:51:42.44	240×300	25.0	15.4	0.6	3.2	2.9	0.0534	0.200	4.10	0.408	108	2
17	13:37:08.31	−29:52:03.56	230×230	20.5	12.9	2.0	32.4	16.9	0.0752	0.377	5.25	0.439	180	4
18	13:37:09.21	−29:51:56.48	230×190	16.5	11.9	0.3	52.5	24.2	0.0928	0.446	4.95	0.204	176	6
19	13:37:08.91	−29:52:17.48	430×180	7.0	8.9	0.5	4.4	4.7	0.0900	0.262	4.65	0.392	288	5
20	13:37:08.62	−29:52:27.07	180×180	10.0	8.3	0.4	0.8	4.3	0.0682	0.188	4.00	0.862	97	2
21	13:37:09.55	−29:52:26.87	320×230	15.5	14.7	0.5	72.4	40.4	0.0939	0.297	5.00	0.303	326	7
22	13:37:10.49	−29:52:24.87	220×320	13.0	9.7	0.6	3.8	21.4	0.0848	0.165	4.60	0.801	248	10

23	13:37:11.07	−29:52:30.76	110×110	12.5	12.0	0.8	4.6	—	0.0979	0.080	4.95	0.510	49	0
24	13:37:09.01	−29:52:37.80	190×250	8.0	5.5	0.5	—	3.4	0.0690	0.079	4.00	0.826	108	3
25	13:37:08.42	−29:52:50.52	180×190	11.5	5.7	1.0	3.2	3.6	0.0497	0.000	3.60	0.627	35	1
26	13:37:11.38	−29:52:48.67	180×260	7.5	14.6	1.1	4.6	23.3	0.0991	0.463	4.50	0.342	224	7
27	13:37:10.73	−29:52:52.56	190×160	8.0	6.6	0.4	4.4	15.3	0.1032	0.157	4.50	0.577	117	6
28	13:37:10.09	−29:52:53.76	160×330	12.0	10.1	0.6	—	5.2	0.0612	0.214	4.25	1.017	126	1
29	13:37:11.31	−29:53:14.47	180×200	27.5	26.0	1.1	102.3	52.5	0.0659	0.625	5.00	0.243	153	1
30	13:37:10.48	−29:53:14.32	240×310	19.0	22.3	0.8	—	55.1	0.0632	0.583	5.35	0.317	253	2
31	13:37:09.57	−29:53:16.20	270×510	17.0	14.8	1.2	4.4	12.7	0.0632	0.404	4.50	0.487	401	4
32	13:37:08.02	−29:53:22.28	240×380	22.5	26.7	3.3	57.5	44.7	0.0432	0.618	5.00	0.306	148	3
33	13:37:11.87	−29:53:41.79	370×270	25.0	18.8	0.9	4.4	72.4	0.0690	0.812	5.10	0.217	375	2
34	13:37:10.65	−29:53:40.31	300×330	21.5	14.4	0.3	4.4	25.2	0.0750	0.418	4.65	0.393	425	6
35	13:37:09.54	−29:53:34.48	260×230	10.5	10.1	0.3	1.1	49.3	0.0576	0.377	4.10	0.782	147	2
36	13:37:07.68	−29:53:43.08	390×490	25.0	30.8	4.4	114.8	51.3	0.0450	0.947	5.10	0.286	309	2
37	13:37:08.93	−29:53:51.84	310×510	25.0	28.5	2.2	26.3	64.1	0.0443	1.865	5.35	0.242	287	4
38	13:37:09.80	−29:53:50.39	180×210	10.5	11.8	1.0	2.1	2.0	0.0727	0.610	4.10	0.520	127	1
39	13:37:10.29	−29:54:04.48	260×410	17.0	20.4	1.0	24.0	14.9	0.0825	0.733	5.00	0.174	440	6
40	13:37:09.39	−29:54:07.59	220×180	10.0	9.9	0.6	3.3	4.4	0.0681	0.429	4.50	0.472	124	1
41	13:37:08.60	−29:54:11.04	200×300	15.5	10.4	0.6	50.1	17.4	0.0752	0.453	4.80	0.449	183	1
42	13:37:04.41	−29:54:14.20	230×370	19.0	20.4	1.5	36.3	—	0.0690	0.825	5.00	0.232	196	0
43	13:37:02.92	−29:54:13.92	250×270	25.0	9.8	0.3	114.8	4.0	0.0516	0.485	5.20	0.300	97	1
44	13:37:02.87	−29:54:00.80	440×260	14.5	16.4	1.0	72.4	5.7	0.0571	0.469	4.95	0.245	224	5
45	13:37:01.77	−29:53:49.24	190×440	6.0	6.7	0.5	5.8	4.6	0.0512	0.179	4.75	0.899	130	6
46	13:37:01.04	−29:53:42.56	220×290	11.5	10.4	0.5	—	4.0	0.0404	0.600	4.10	0.846	82	1
47	13:37:02.99	−29:53:34.17	250×310	11.0	12.4	1.2	72.4	33.1	0.0455	0.333	5.00	0.427	120	2

48[e]	13:37:01.86	−29:53:20.83	270×290	—	6.2	0.5	—	5.0	0.0419	0.242	5.00	0.406	38	83
49	13:37:00.79	−29:53:19.27	330×220	10.0	9.2	0.2	102.3	12.6	0.0333	0.433	5.25	0.507	55	10
50	13:37:01.24	−29:53:09.23	220×220	6.0	8.0	0.5	5.8	27.0	0.0469	0.296	4.35	0.652	72	12

[a] $\Delta\mathrm{Age}_{\mathrm{CMD\,auto}}$ is the mean value of the uncertainties in our age determination. See Section 2.3.1 for details.

[b] $\mathrm{Age}_{\mathrm{Reg}}$ is the region age determined by measuring the colors of the entire regions, and fitting SED. See Section 2.3.4 for details.

[c] The luminosity-weighted mean age of clusters in each region. Age of each cluster is determined by SED fitting. See Section 2.3.3 for details.

[d] Average value of the extinctions (A_V) measured from the resolved stars in each region.

[e] Region 48 is the nucleus of M83. It is not included in the analysis since the bright background results in a completeness limit that is more than 2 mag brighter than other regions.

Table 2.2: Wolf-Rayet Star Candidates in M83

R.A. (hh:mm:sec)	Dec. (°:':")	ID	Reg No.	Age_{Reg} (Myr)	X (Pixel)	Y (Pixel)	Hα Feature
13:37:00.41	−29:52:54.1	72	—	—	3874	606	Faint
13:37:01.18	−29:52:53.9	73	—	—	3618	609	Faint
13:37:01.42	−29:51:25.8	74	4	—	3512	2821	Strong
13:37:03.06	−29:50:49.5	78	7	4.2	2982	3698	Faint
13:37:04.65	−29:52:47.5	82	—	—	2710	772	Strong
13:37:04.65	−29:50:58.4	86	12	2.4	2477	3505	Strong
13:37:07.35	−29:49:39.2	95	20	0.8	1513	3306	Strong
13:37:07.54	−29:52:53.6	96	41	50.1	1552	620	Strong
13:37:07.96	−29:52:07.9	99	—	—	1418	1762	Faint
13:37:08.25	−29:51:13.6	100	24	—	1311	3116	Faint
13:37:08.40	−29:52:54.9	102	—	—	1266	588	Strong
13:37:08.53	−29:52:12.0	103	35	1.1	1224	1659	Strong
13:37:08.70	−29:52:28.9	105	38	2.1	1173	1239	Strong
13:37:08.91	−29:52:05.7	106	31	4.4	1101	1818	Faint
13:37:09.02	−29:52:45.2	107	39	24.0	1067	825	No
13:37:09.80	−29:52:36.2	108	—	—	820	1049	Strong
13:37:10.42	−29:51:28.0	109	26	4.6	610	2756	Faint

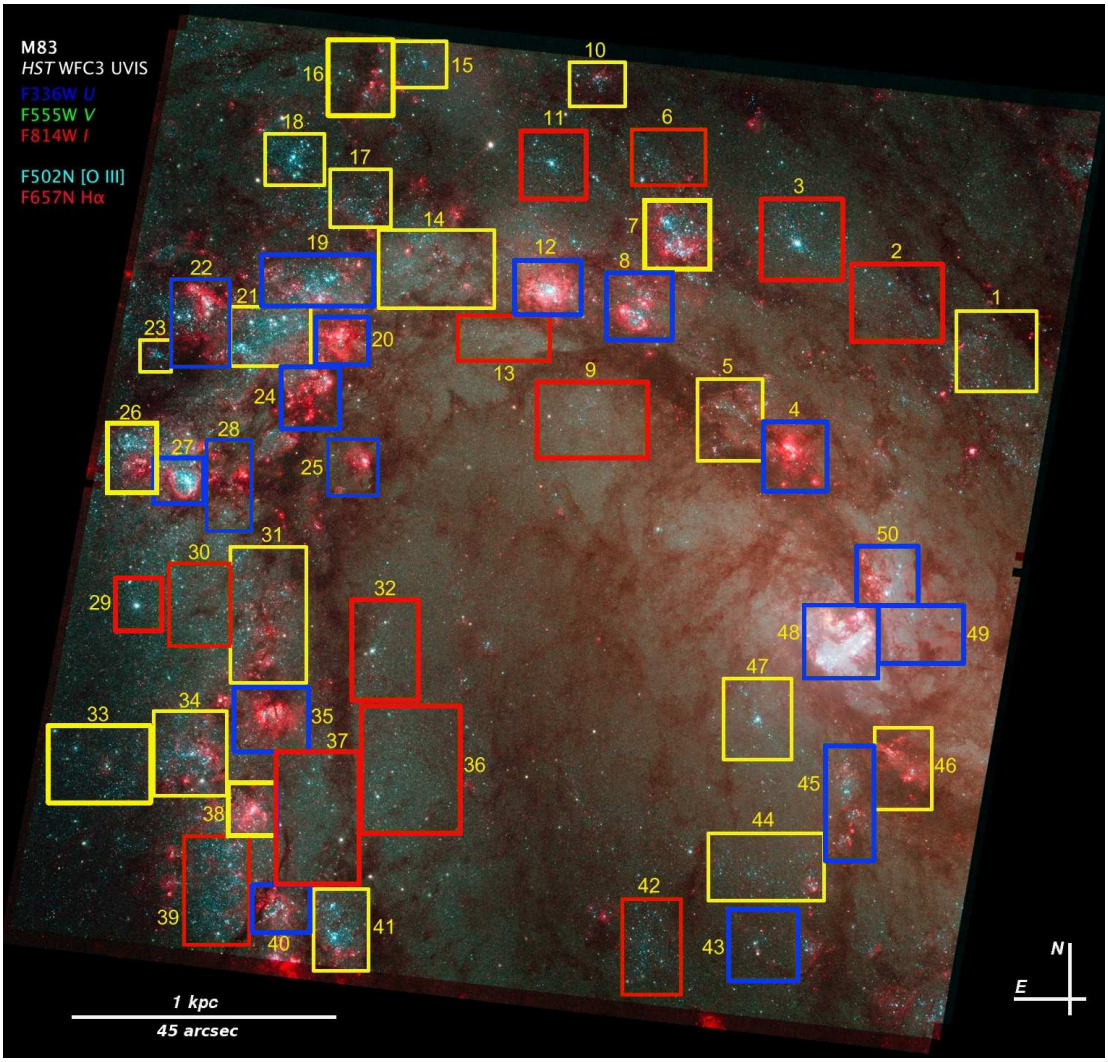

Figure 2.1: Color composite of the M83 WFC3 images [Image Credit: Zolt Levay (STScI)]. The F336W image is shown in blue, the F502N ([O III]) image in cyan, the F555W image in green, and the combined F814W and F657N (Hα) image in red. The 50 selected regions are outlined in boxes of three different colors based on the values of $\mathrm{Age}_{\mathrm{CMD\,auto}}$ determined in this paper (see Section 2.3.1 for details). The regions with ages in the range 1–10 Myr are outlined in blue, ages of 10–20 Myr in yellow, and ages greater than 20 Myr in red.

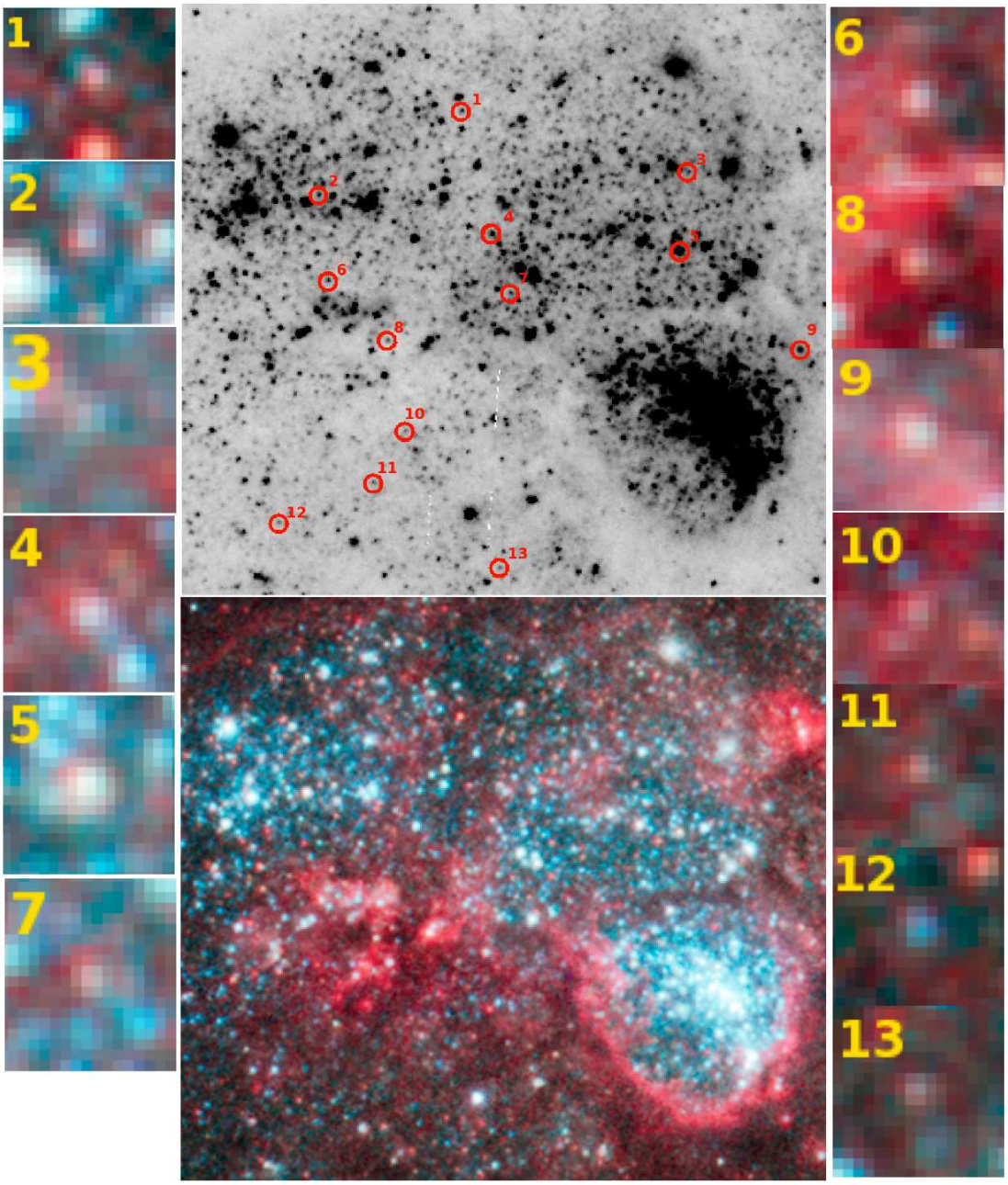

Figure 2.2: Image cutouts (15.2″×13.9″, 340 pc×310 pc) of Regions 26 and 27 in the F555W (top) and the color-composite images (bottom). Stars circled in red have $(V - I)$ >0.8 mag. The "postage stamp" images on the left are"pseudo" matched candidates, while the images on the right appear to be heavily reddened (see Section 2.2.2 for details).

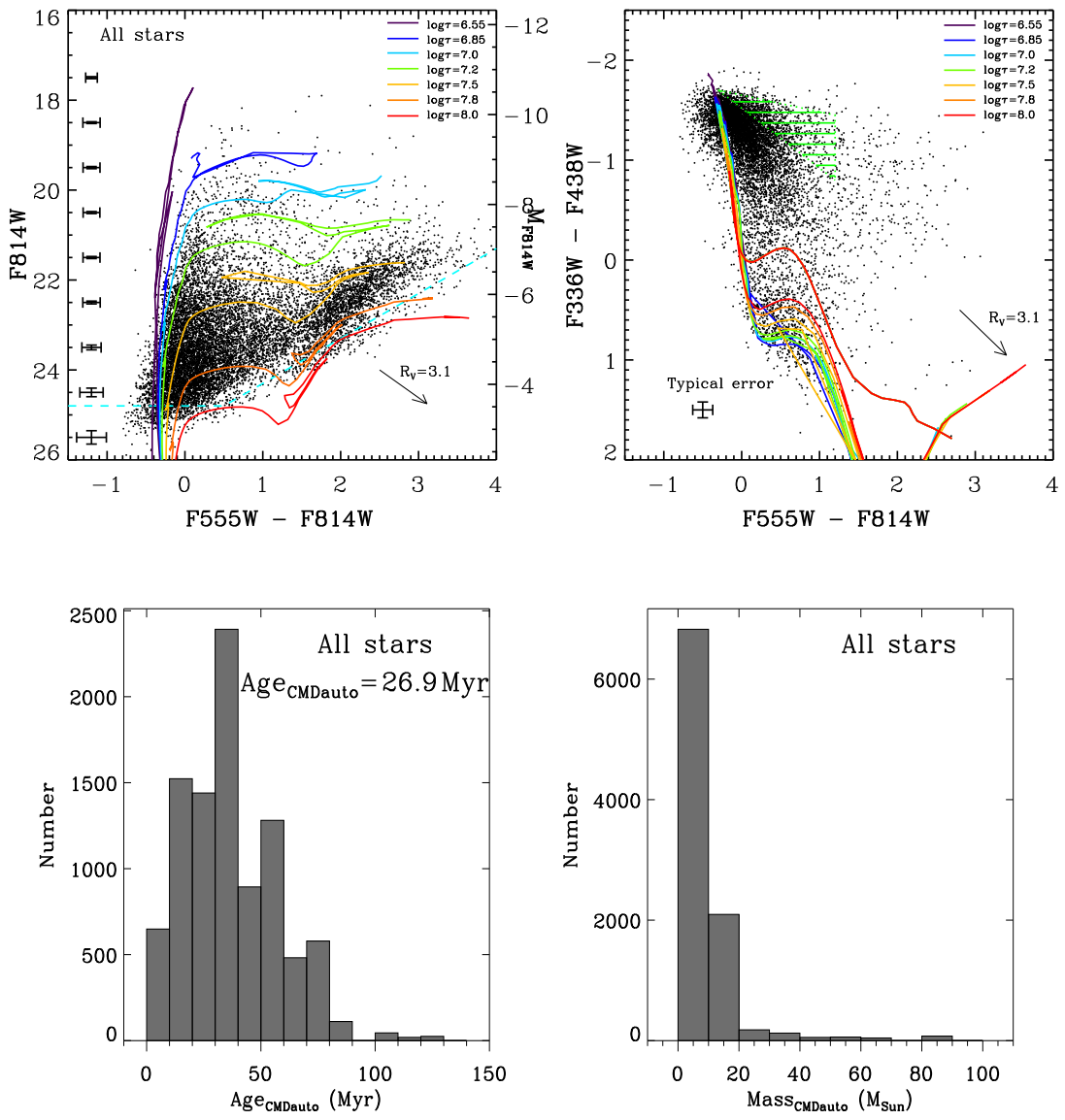

Figure 2.3: Top: the color–magnitude diagram (CMD) and color–color diagram of all stars in our M83 image corrected for Galactic foreground extinction but not for internal extinction. Padova isochrones of logτ (age/yr) = 6.55, 6.85, 7.0, 7.2, 7.5, 7.8, and 8.0 for a metallicity of Z=0.03 (1.5 $Z_{\odot}$) are overlaid in both panels. The dashed line in cyan represents the 50% photometric completeness level. The arrow in each panel indicates the direction of the reddening vector with $R_V = 3.1$. Magnitudes are on the Vega scale. The distance modulus $(m - M)_0 = 28.32$ mag is used to calculate the absolute magnitude M_{F814W}. Bottom: histograms of the distribution of ages and masses, as determined from the CMD (see Section 2.3.1 for details). The age quoted in the bottom left panel is the luminosity-weighted mean age.

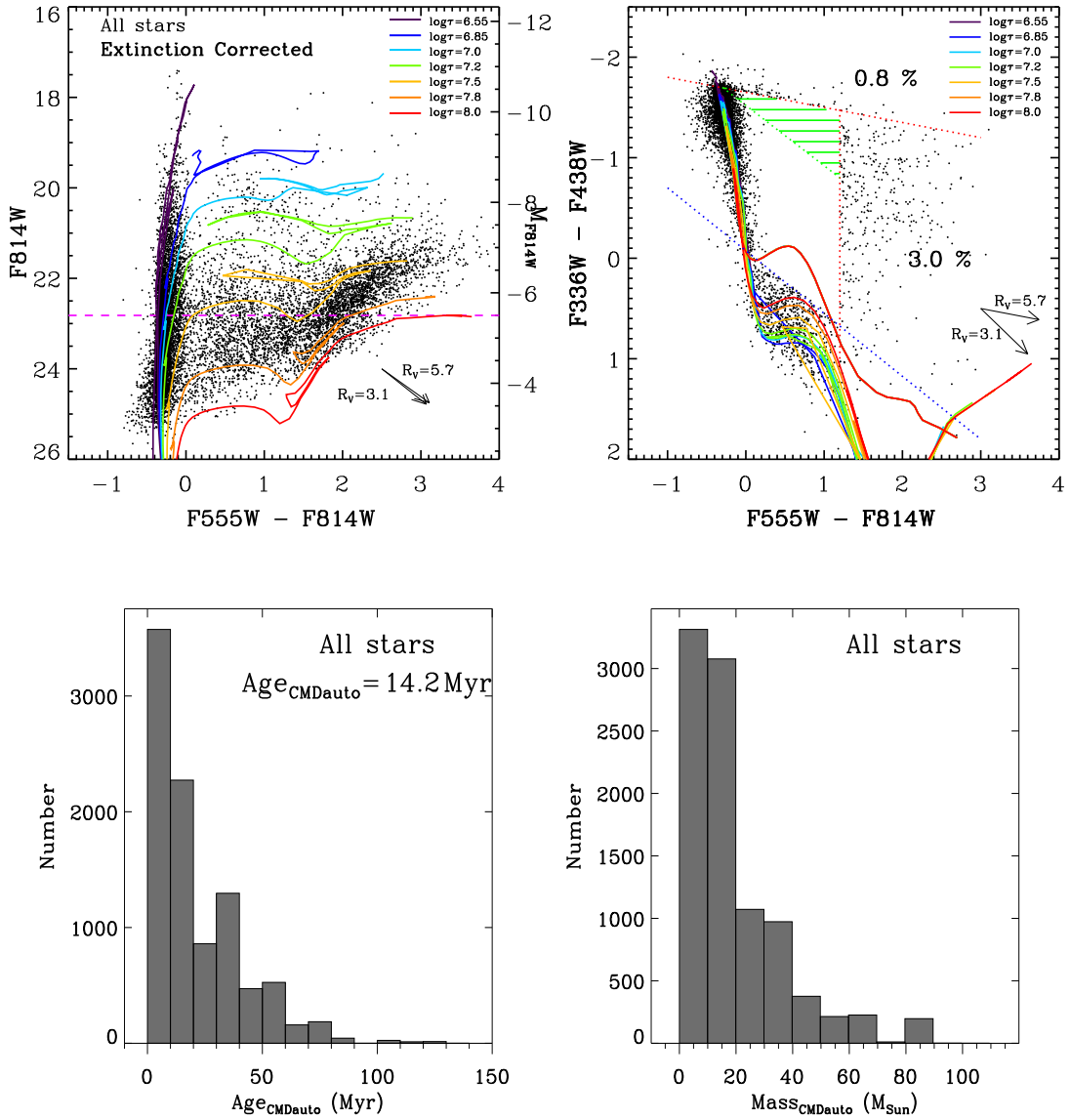

Figure 2.4: Top: the CMD and color–color diagram of all stars corrected for the internal extinction determined for each individual star. The blue and two red dotted lines indicate boundaries for the locations of stars in the color–color diagram uncorrected for internal extinction (see Section 2.2.4 for discussion). Two arrows in the color–color diagram show reddening vectors: one with the standard reddening vector ($R_V = 3.1$) and the other with the flatter reddening vector ($R_V = 5.7$) which appears to be more appropriate for some of the data in the green triangle (see Section 2.2.4 for discussion). The dashed line in magenta shows the M_I<−5.5 mag cutoff used for the $\mathrm{Age_{CMDauto}}$. Bottom: same as described in Figure 2.3.

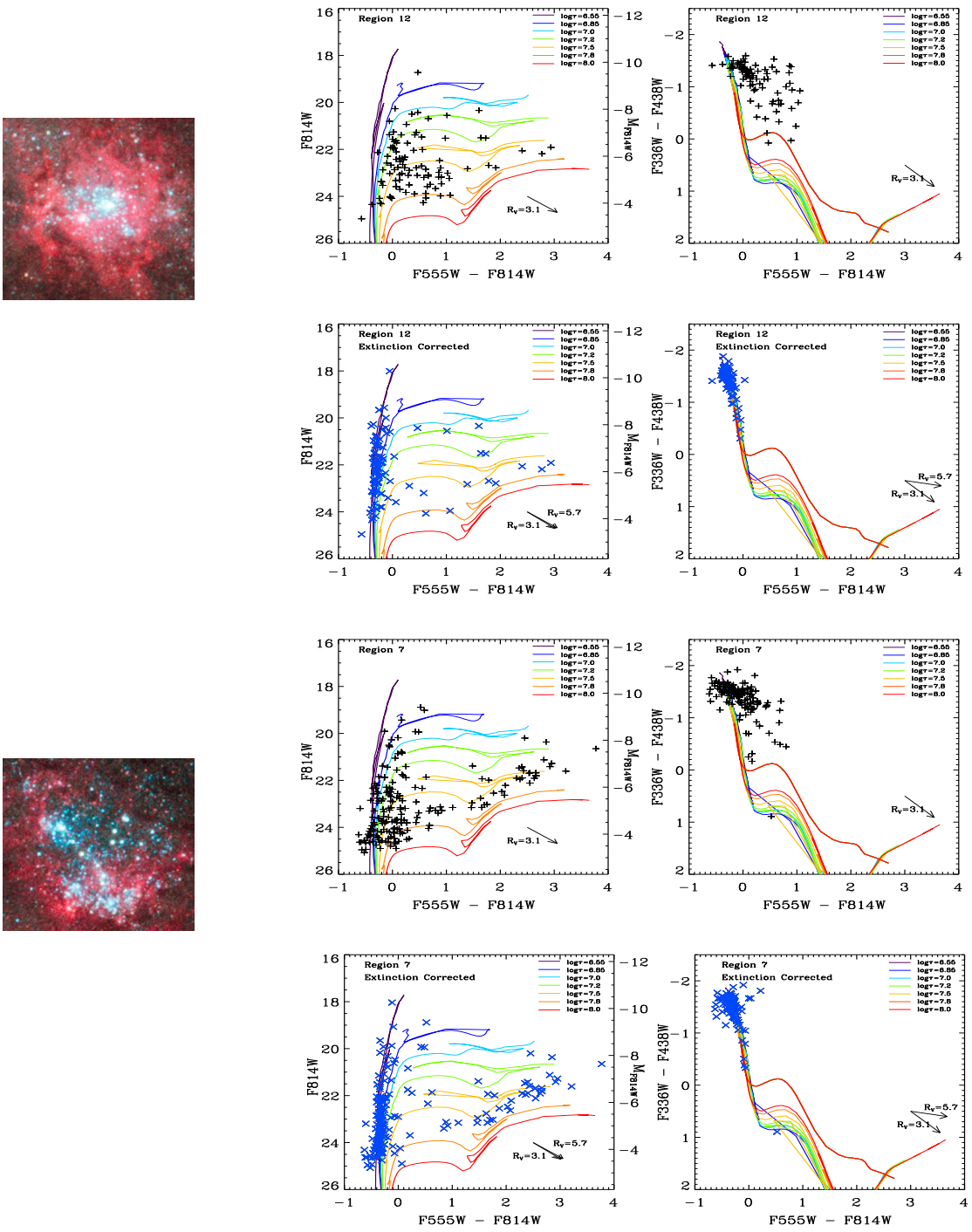

Figure 2.5: CMDs, color–color diagrams, and the image cut-outs of Regions 12 and 7. Data points before and after the individual extinction correction are plotted as black crosses (upper: uncorrected) and blue Xs (lower: corrected). The Padova isochrones in these diagrams are the same as the ones plotted in Figure 2.3. See Section 2.2.4 for details.

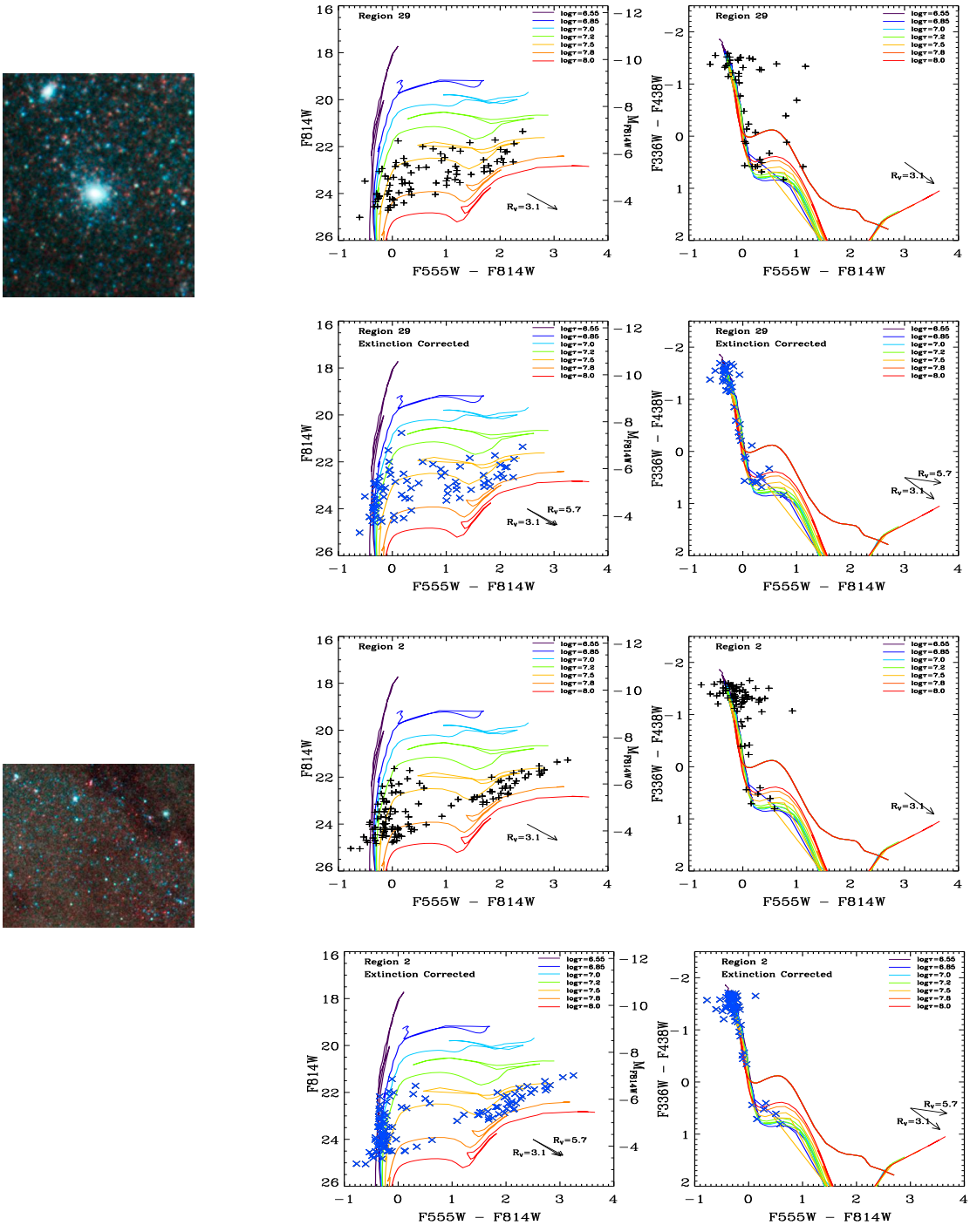

Figure 2.6: Same as Figure 2.5 for Regions 29 and 2.

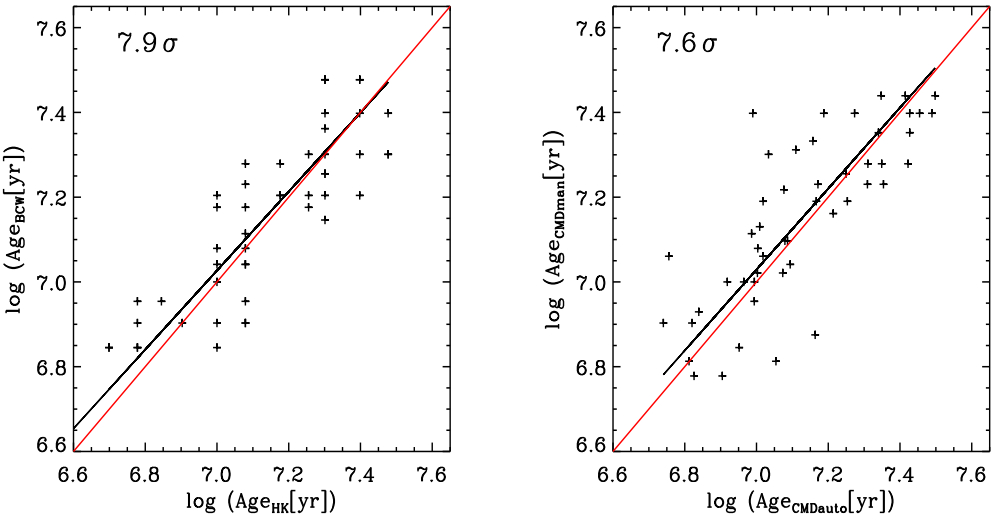

Figure 2.7: Correlation plots between the ages of the stellar populations in the 50 regions from CMD isochrone fitting. Left: correlation between the manual ages determined by HK and BCW. Right: correlation between the average of manual ages and automatic ages (see Section 2.3.1 for details). The best linear fits are shown in black with the significance of the correlation in unit of σ (i.e., slope/uncertainty) in the top left of each panel. The solid red line is the unity line.

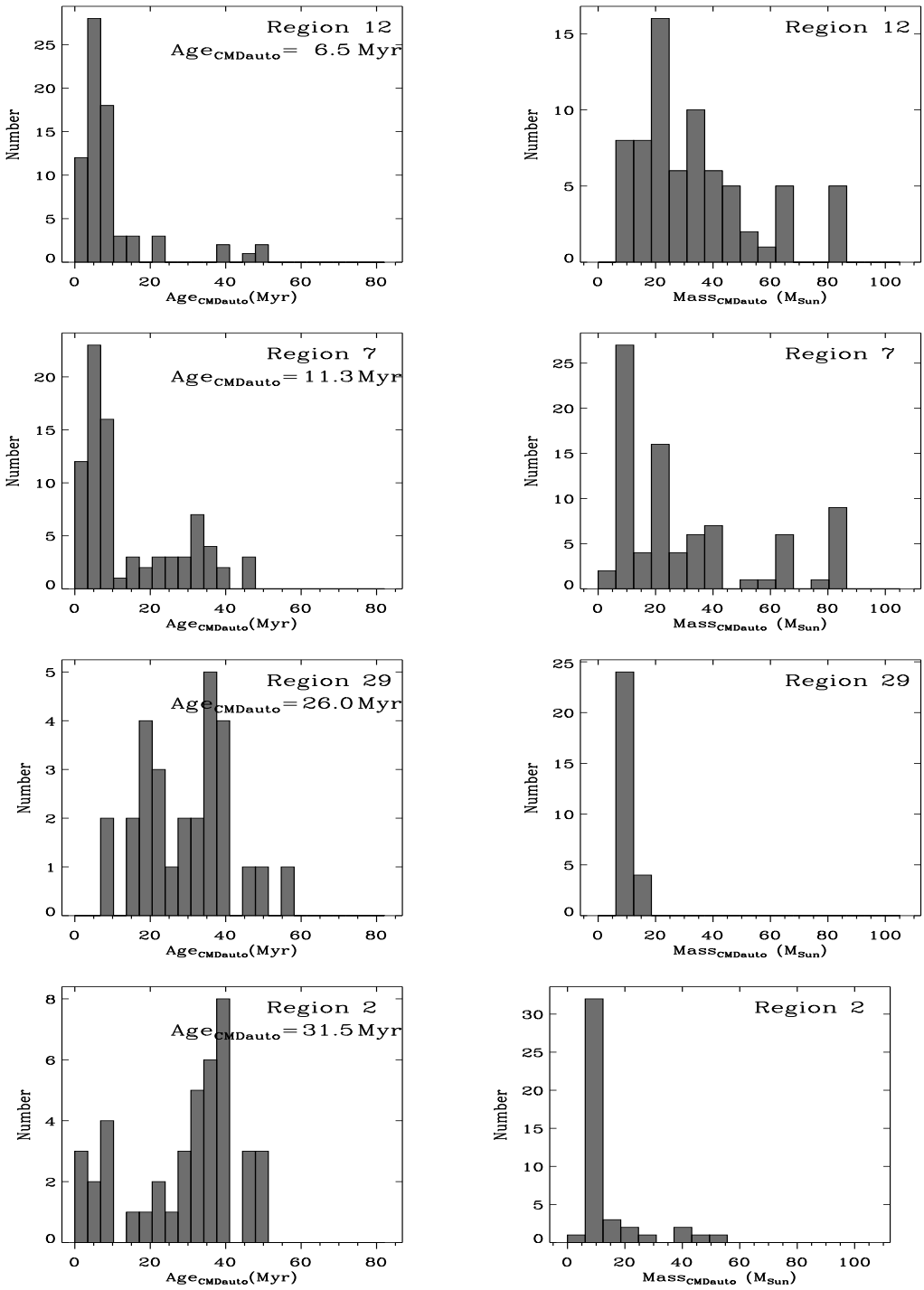

Figure 2.8: Histograms of the distribution of ages and masses of the individual stars in Regions 12, 7, 29, and 2, as determined by the automated isochrone fitting technique (see Section 2.3.1). The age indicated at the top right in each age histogram is the luminosity-weighted mean age of all stars with $M_I<-5.5$ in each region.

Figure 2.9: Image cutout ($18.3'' \times 16.9''$, $410\,\mathrm{pc} \times 380\,\mathrm{pc}$) of the area near Region 9 as an example of a "field" region with old red giant stars, and a small population of isolated young blue stars. See Section 2.3.1 for detail.

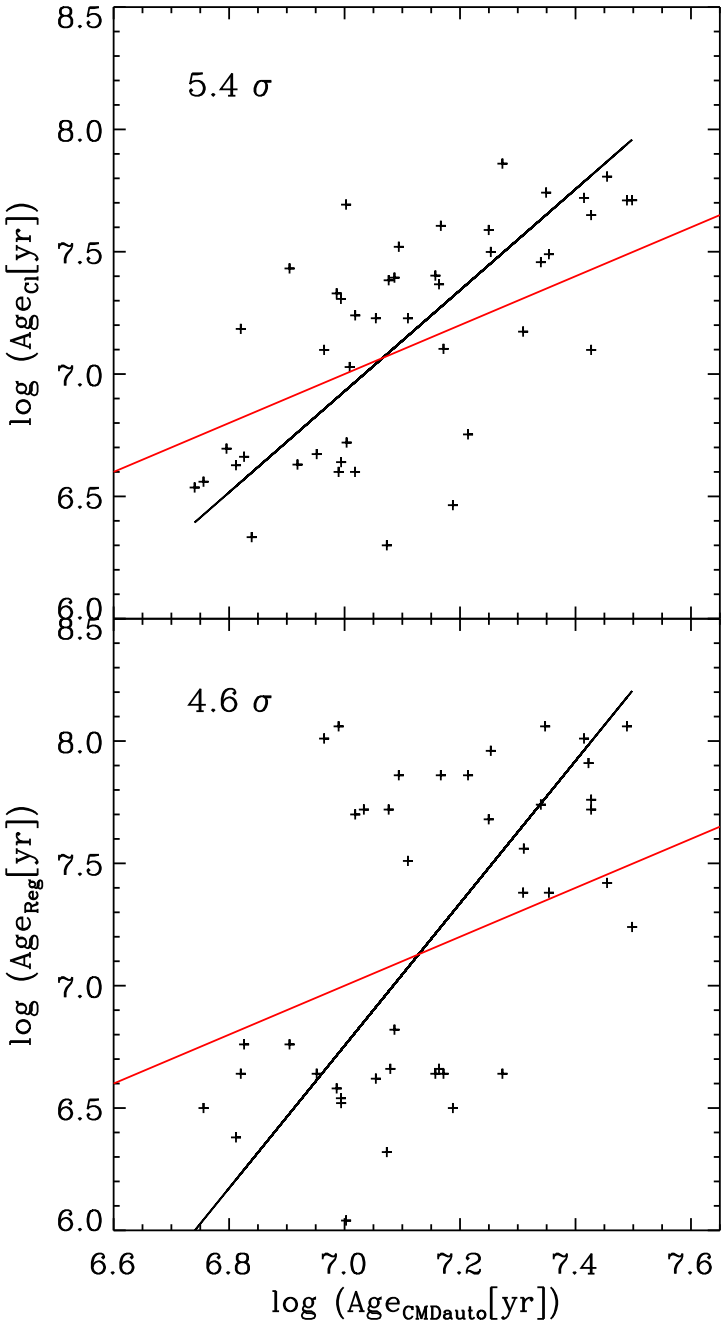

Figure 2.10: Top: correlations between the ages of stars ($\mathrm{Age_{CMDauto}}$) and clusters ($\mathrm{Age_{Cl}}$). Bottom: correlation between the ages of stars determined by $\mathrm{Age_{CMDauto}}$ and the integrated light within the region ($\mathrm{Age_{Reg}}$). See Section 2.3.4 for details. The best linear fits are shown in black solid line with 5.4σ (top) and 4.6σ (bottom) correlations. The red line is the unity line.

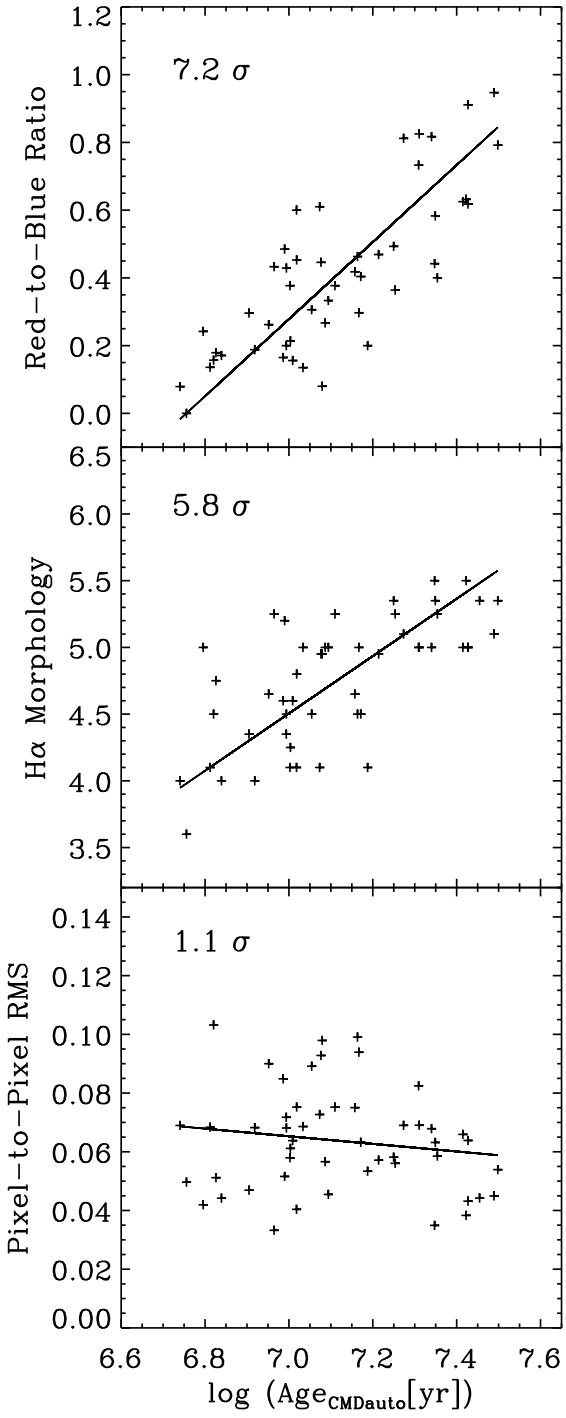

Figure 2.11: Correlations between the stellar ages ($\mathrm{Age_{CMDauto}}$) and the number ratio of red-to-blue stars (top), Hα morphology (middle), and pixel-to-pixel fluctuations (bottom) for the 50 selected regions. See Section 2.2.4 for details. The best linear fits are indicated in solid black line with 7.2σ (top), 5.8σ (middle), and 1.1σ (bottom) correlations.

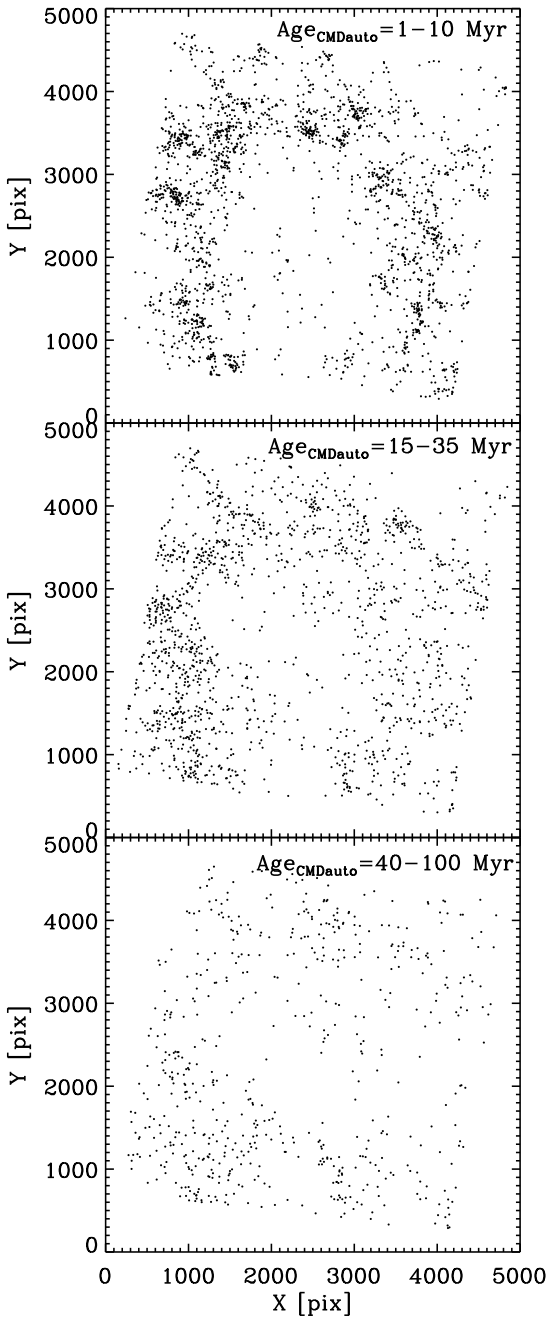

Figure 2.12: Spatial distribution of stars with ages of 1–10, 15–35, and 40–100 Myr determined in this study. Each panel has the same orientation and scale as Figure 1. The top panel is the youngest group of stars, clearly showing that the stars in these regions are mostly distributed along the active star-forming region (i.e., associated with the strong Hαemission) in the spiral arms. The stars in the middle panel tend to be found slightly downstream of the spiral arms while the older stars are still farther out in the inter-arm regions, as expected. See Section 2.2.5 for details.

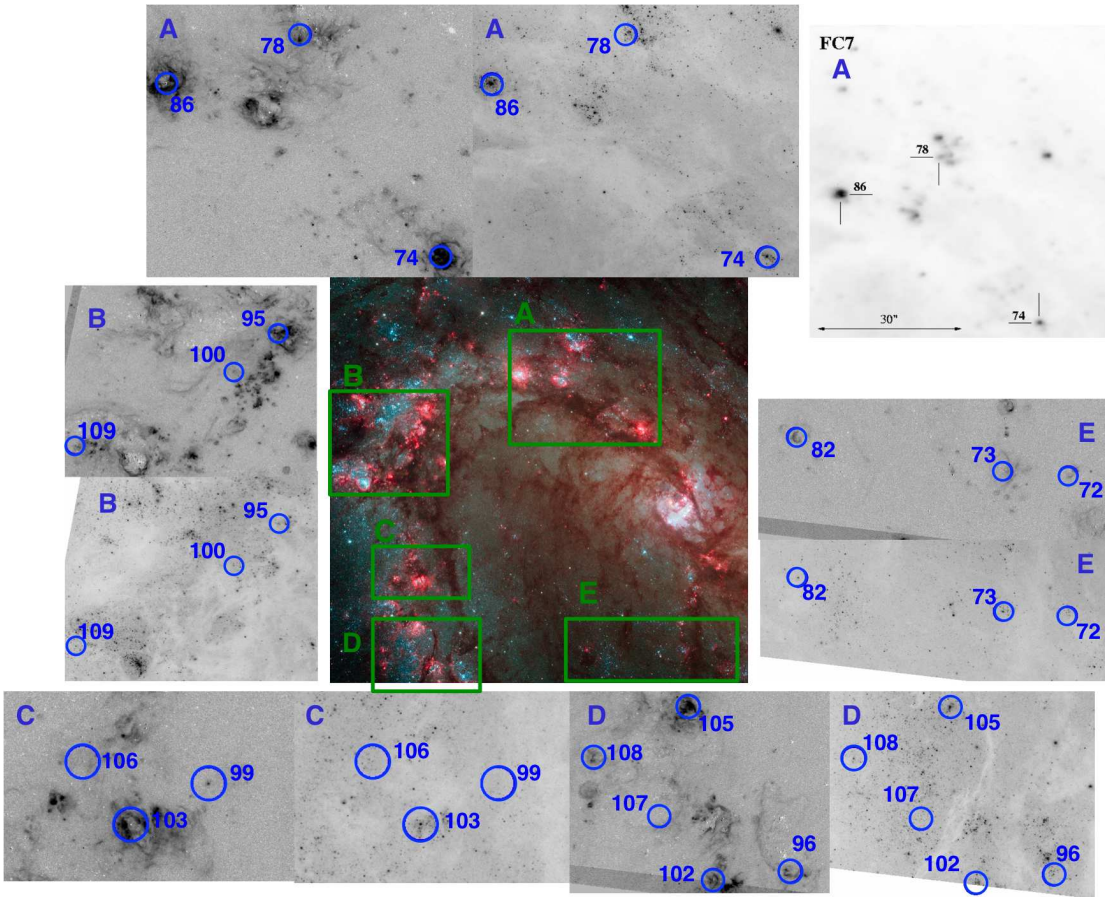

Figure 2.13: Distribution of Wolf–Rayet sources in our *HST* WFC3 M83 images. The color image at the center is the $UBVI$Hα composite and the image cutouts are the Hα(left or *top*) and F814W (right or bottom) images for regions A–E. The top right panel is an original finding chart (Hadfield et al. 2005, λ4684 narrowband FORS2 image) for the region A. Numbers in blue are the IDs of Wolf–Rayet sources identified by Hadfield et al. (2005).

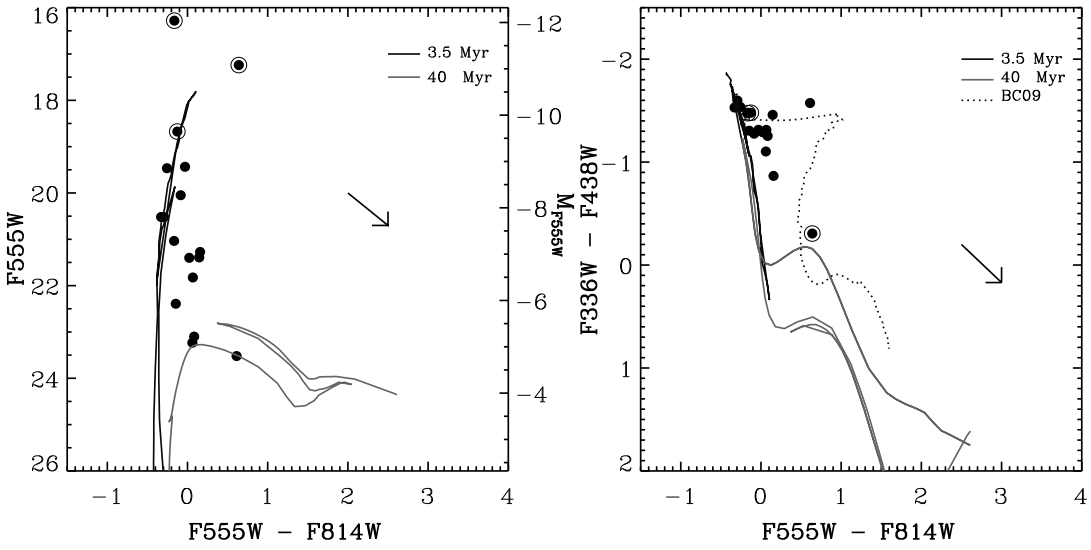

Figure 2.14: CMD and color–color diagram of Wolf–Rayet sources in M83 marked in Figure 2.13. Three sources (78, 86, 105) circled in both diagrams are identified as clusters in our M83 WFC3 images. A twice solar metallicity BC09 cluster model (Bruzual & Charlot 2009, private communication; see also Bruzual & Charlot 2003) is shown in the right panel (dots), and Padova stellar models (Marigo et al. 2008) are shown in both panels. No correction has been made for internal reddening, which appears to be minimal for all but one object. The arrow indicates the Galactic reddening vector.

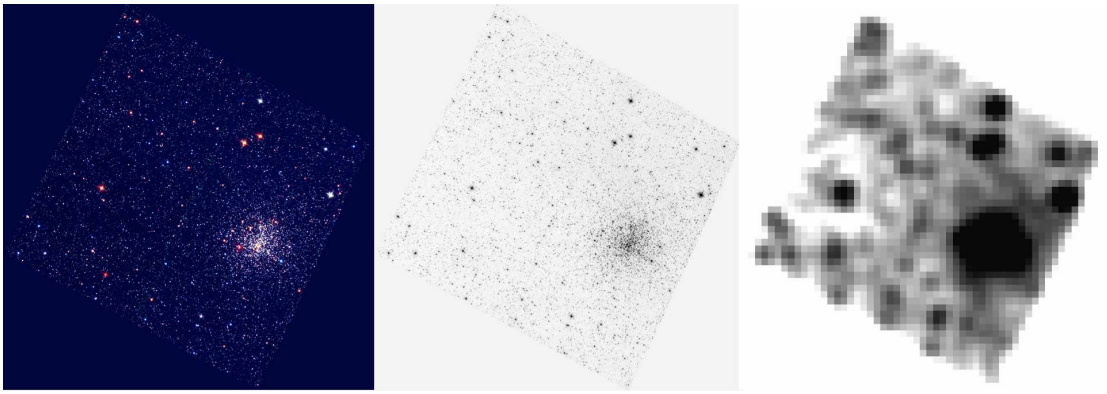

Figure 2.15: *HST*/ACS images (290″×290″, 68 pc×68 pc) of the compact star cluster NGC 2108 in the LMC: a color composite of the F435W, F555W, and F814W ACS images (left), the F555W ACS image (middle), and the degraded F555W ACS image (right) by a factor of 100 (from a distance of ∼50 kpc to a distance of ∼5 Mpc). See Section 2.2.7 for details.

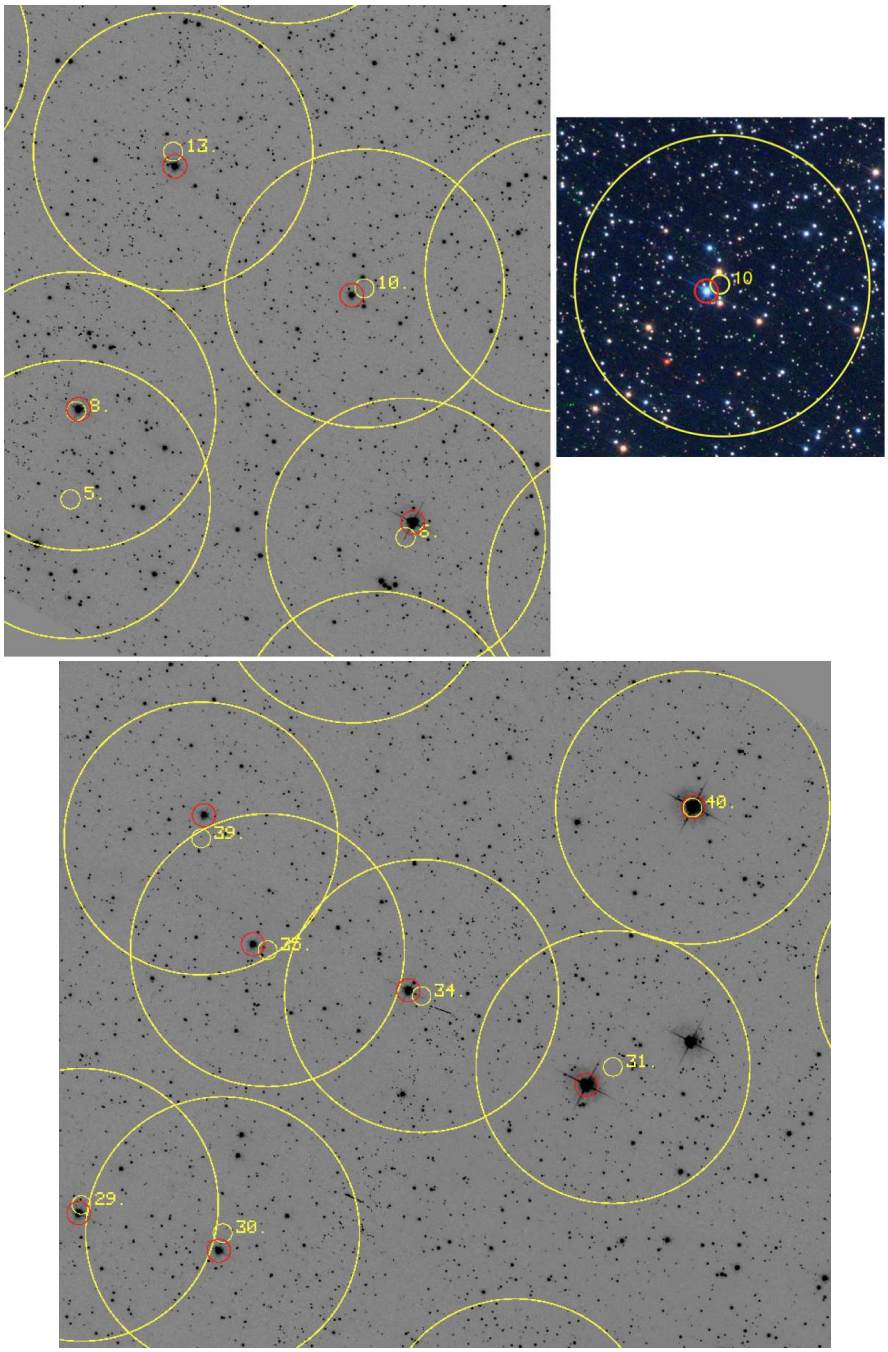

Figure 2.16: Image cutouts of *HST*/ACS F555W image of NGC 2108. The large circles in yellow show the 300 pixel aperture (corresponding to a ∼3 pixel aperture at the distance of M83) centered at the location determined from the degraded image in Figure 15. The location of the dominant star (used to determine the "truth" value) is shown in red. See Section 2.2.7 for details.

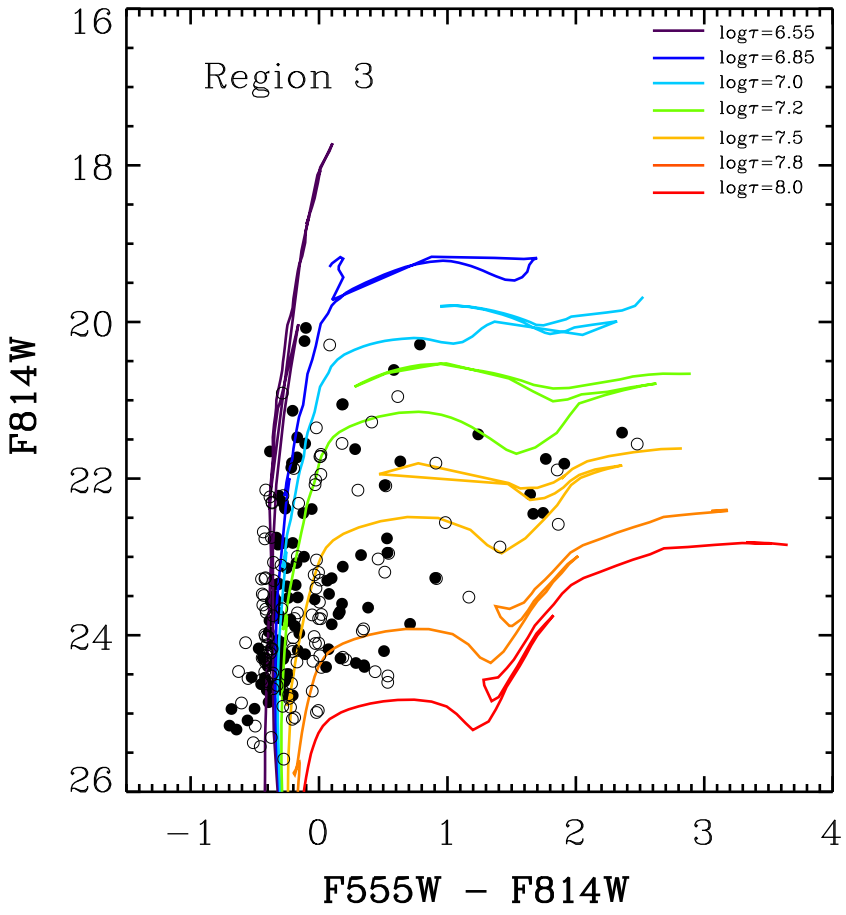

Figure 2.17: Original CMD of Region 3 in M83 (solid points) with the effect of simulation representing a factor of 100 degradation in spatial resolution (open points). The $\mathrm{Age}_{\mathrm{CMDauto}}$ of this region changes from 21.9 Myr (determined from the solid points) to 23.8 Myr (from the open points). The difference in the age estimates is within $\sim 1\,\sigma$ error listed in Table 1. See Section 2.2.7 for detail.

Chapter 3

MAPPING THE RESOLVED STELLAR POPULATIONS IN METAL-POOR IRREGULAR NGC 4214

3.1 Overview

A starburst is one of the intense star-forming phenomena lasted over a short period of time. Dwarf galaxies have limited supplies of gas to sustain this vigorous activities over their lifetime. Therefore, most dwarf galaxies and dwarf irregulars are dominant populations among the starbursting galaxies. Understanding this type of star formation history (SFH) is more complex than the SFH of the galaxies with a continuous star-forming activity. NGC 4214 is the best example in the category of nearby starbursting dwarf galaxies. It is well-studied and classified as type IAB(s)m (de Vaucouleurs et al. 1991) and SBmIII (Sandage & Bedke 1985) with a mass of $\sim 1.5 \times 10^9 M_\odot$ (Karachentsev et al. 2004). NGC 4214 is known to be moderately metal-deficient with a hint of an abundance gradient measured as 12+log(O/H)= 8.15−8.28 by Kobulnicky & Skillman (1996). Notably, this galaxy has several highly photoionized complexes near its center with intense star-forming activity.

There have been multiple *HST* observations on NGC 4214 with the Wide Field Planetary Camera 2 (WFPC2) and the Advanced Camera for Survey (ACS) covering the near-UV to near-IR to probe these recently formed young populations along with the old stellar populations (MacKenty et al. 2000; Maíz-Apellániz et al. 2002; Drozdovsky et al. 2002; Úbeda et al. 2007a,b; Williams et al. 2011). Despite being at a relatively close distance (Dopita et al. 2010, D=2.98 Mpc), stellar crowding caused by the underlying sheet of old populations in this galaxy makes the photometric analysis challenging. The recent installation of the Wide Field Camera 3 (WFC3) provides a high sensitivity with a panchromatic imaging

capability and a superb angular resolution, which are critical for studying the resolved stellar populations in nearby galaxies.

Here we present the *HST*/WFC3 observations of NGC 4214 performed as part of the WFC3 Early Release Science (ERS) program (ID:11360). The multi-wavelength photometry of resolved stars in F225W, F336W, F438W, F547M, and F814W are used to study the spatial distribution of stars with different ages. All magnitudes are measured in the Vega magnitude system. In our previous work on nearby spiral galaxy M83 (Kim et al. 2012), we demonstrate the variation of dust extinction in the central field of the galaxy and correct the internal dust extinction for the individual stars. By using a combined information from the extinction-corrected color–magnitude and color–color diagrams, we determine ages and masses of the individual stars. We estimate their ages and masses by the stellar spectral energy distribution (SED) fitting method newly developed in this study. The ages from these two different measurements are used to understand the recent star formation history of NGC 4214. The scientific questions addressed in this study are listed as follows: (1) Is each of active star-forming regions correlated with the bar at the center or any other structure of NGC 4214? (2) How can we relate the evolution of the galaxy and the history of recent star formation with the spatial variation map of stellar ages? (3) Do age estimates from the CMD and SED fitting correlate with number ratios of re-to-blue stars, as they do in the results of M83 study by Kim et al. (2012)?

This chapter is organized as follows. In Section 3.2, we describe the *HST*/WFC3 observation, photometric analysis, and the corrections made for the foreground and internal extinctions. Section 3.3 describes the CMD and SED fitting methods to estimate the ages and masses of individual stars. In Section 3.4, we discuss what we learn from the spatial distribution maps of stellar ages

and how to interpret them to tell the star formation history of NGC 4214. The main results are summarized in Section 3.5.

3.2 WFC3 Observations

3.2.1 Data

The *HST*/WFC3 data observations of NGC 4214 were performed in 2009 December as part of the WFC3 Science Oversight Committee (SOC) Early Release Science (ERS) program (ID:11360, PI: Robert O'Connell). The data were obtained in seven broadband and seven narrowband filters in the WFC3 UVIS and IR channels. Details of the observations are described in Dopita et al. (2010) and J. Andrews et al. (2012, in preparation). In this paper we use five broadband observations including F225W (1665s), F336W (1683s), F438W (1530s), F547M (1050s), and F814W (1339s). Although we do not make transformations to the standard UBVI system, we will refer to these filters as NUV, U, B, V, and I, respectively. The raw data were processed through the `MULTIDRIZZLE` software (Fruchter et al. 2009; Fruchter & Hook 2002) with a final pixel scale of $0.0396''$, which corresponds to 0.568 pc pixel^{-1} at a distance of 2.98 Mpc (Dopita et al. 2010). Each multidrizzled image is combined, cosmic-ray removed, and distortion-corrected. At this resolution stars in the compact star clusters are not resolved but stars in the field and the outskirts of the star clusters are generally resolved into individual stars in this image.

Figure 3.1 is a color composite of the F225W, F336W, F547M, F814W (broadband), and F657N (narrowband; Hα+[NII]) images. It shows the central region (2.9 kpc$\times$2.9 kpc) of NGC 4214 observed for this program. The bright star cluster in Region 18 is considered as the center of the galaxy in the literature (Hunter & Gallagher 1986; MacKenty et al. 2000). Our WFC3 images show detailed feature of resolved stellar populations in NGC 4214. Most of luminous

blue and red stars are concentrated in the two main star formation complexes (Drozdovsky et al. 2002); one near the center of the Hα cavity (super star cluster NGC 4214-I-a (MacKenty et al. 2000)), and the other one looking like a letter "J" (the southeast complex). Due to high crowding, the photometry in these two regions was challenging (described in Section 2.2). The yellow boxes overlaid in Figure 3.1 are an adaptive grid used for detailed study of resolved stellar population in this chapter. We divided the image into individual regions, using an adaptive grid. The sizes and shapes of each box grid are determined based on different feature, such as the strong Hα emission (Regions 6, 13, 14, 20), the OB association (2,3, 29, 35), and other feature.

3.2.2 Photometry and Artificial Star Tests

We performed Point Spread Function (PSF) photometry on the WFC3 NUV, U, B, V, and I images using the `DoPHOT` photometry package (Schechter et al. 1993) with modifications made by A. Saha. Details of our photometric analysis are described in Kim et al. (2012) for the case study of nearby spiral galaxy M83. We use the same procedure to measure the photometry of stars in NGC 4214. All magnitudes are calculated using the photometric conversion from counts per second to the VEGAMAG system with the WFC3 UVIS zero-point magnitudes: NUV=22.40, U=23.46, B=24.98, V=25.81, and I=24.67 mag, provided by STScI. The measured FWHMs of stars in our WFC3 UVIS images are 0.080″(2.02 pixel) in NUV, 0.081″(2.05 pixel) in U-, 0.083″(2.11 pixel) in B-, 0.085″(2.14 pixel) in V-,and 0.088″(2.23 pixel) in I-bands.

To measure the photometric completeness, we inserted artificial stars and measured our ability to detect them as a function of magnitude. We applied the same detection and photometry procedure as applied to the actual stars. For each run of the test 1000 artificial stars were inserted with Gaussian PSFs and

FWHMs appropriate for these stars at random positions into all five images. The magnitude of the inserted stars varied from 22 to 30 mag in steps of 0.25 mag. Figure 3.2 show the 50% completeness levels at 5 σ detection thresholds for the five broadband images of NGC 4214. The limiting magnitudes are 25.2, 26.2, 27.4, 26.7, and 25.8 mag for the NUV, U, B, V, and I images, respectively.

In order to make a multiwavelength master catalog of all objects, we matched the individual objects in each of the NUV-, U-, B-, and V-band catalogs with the I-band catalog, which contains the largest number of objects. We used a matching radius of 0.5 pixel to avoid false matches of two or more close stars due to crowding of the field. This is also because our WFC3 images have the excellent panchromatic sensitivity and spatial resolution on top of the extreme image crowding. Details of the effect of the image crowding are described in Kim et al. (2012). The final NUV+$UBVI$ stellar catalog contains ∼46,000 objects. Note that the stars in the compact star clusters are not included in our photometric catalog but the field stars and the stars located outskirts of those clusters are.

In Figure 3.3, the top panels are the I versus $(V-I)$ CMD (left) and the $(U-B)$ versus $(V-I)$ color-color diagram (right) of stars in the master catalog covering all regions. We use these diagrams to determine the ages and masses of stars using the stellar model isochrones. In this paper we use Padova isochrones (Marigo et al. 2008; Girardi et al. 2010, 2008; Bertelli et al. 1994) generated from the Padova database[1]. Since NGC 4214 is known as a moderately metal-deficient galaxy, with a metallicity of 12+log(O/H)=8.15–8.28 (Kobulnicky & Skillman 1996), which is about $Z = 0.34Z_{\odot} = 0.006$, the Padova isochrones used in this work are with the metallicity of $Z = 0.006$, ranging in age from 1 Myr to 12.6 Gyr. The isochrones plotted in Figure 3.3 are in the age range of 5 Myr to 5 Gyr. We

[1]CMD version 2.3; http://stev.oapd.inaf.it/cgi-bin/cmd

adopt the distance of 2.98±0.13 Mpc (Dopita et al. 2010) estimated from the Planetary Nebulae Luminosity Function (PNLF) technique and the tip of the RGB method (Maíz-Apellániz et al. 2002; Dalcanton et al. 2009), in order to calculate the absolute magnitude plotted on the right axis of the CMD. It shows the typical characteristics of the CMDs of other dwarf galaxies, with a presence of both old and young populations including the high concentration of stars in 0.8 $< (V-I) <$ 2.5 mag, called "red tangle" (Drozdovsky et al. 2002). The diagram is populated with RGB, AGB, and He-burning blue-loop stars. The CMD also shows the young blue population with $(V-I) <$ 0.3 mag.

3.2.3 Extinction Corrections

In the previous study on the nearby spiral galaxy M83, we found that in active star-forming regions in the galaxy, stars are partially obscured by dust and correcting only for a uniform foreground extinction does often result in overestimates or underestimates of ages and masses of individual stars. Although Galactic foreground extinction for NGC 4214 is negligibly small $A_V = 0.06$ mag (Schlegel et al. 1998), internal extinction for the central part of NGC 4214 is very uncertain with large discrepancies in the values from $E(B-V) = 0.09$ mag (Sargent & Filippenko 1991) up to $E(B-V) = 0.28$ mag (Mass-Hesse & Kunth 1999). In the color-color diagram in the top right panel of Figure 3.3, we notice that the majority of stars in the range of -0.5$<(V-I)<$0.3 and -1.8$<(U-B)<$1.0 match the model isochrones quite well, while the rest of stars are found redward of the models. In our previous work (Kim et al. 2012), we have used the reddening-free Q parameter and developed the star-by-star correction technique for the internal extinction in M83. We apply the same correction method to calculate and correct the internal extinction of individual stars in NGC 4214 to get better estimates of stellar ages and masses.

In the bottom two panels of Figure 3.3, each data point of the CMD and color-color diagram is corrected for the internal extinction in NGC 4214. The arrows in both panels are the reddening vectors of $R_V = 3.1$. We do not apply our correction method for stars redder than 1.2 in $(V-I)$ color, or above the red dotted line shown in the bottom right panel of Figure 3.3, since some of these red stars could have been mismatched due to the crowding, and for the stars above the dotted line we do not have a valid Q value to match with (see the detailed discussion in Kim et al. (2012)). Note that the majority of AGB and RGB stars in the "red tangle" in the CMD are not included in the color–color diagrams, since they are intrinsically faint in U and we would not be able to correct for the internal reddening for these stars. Fortunately, the younger regions that have the most dust generally have few of these red giant stars. By the time the stars are evolved to the AGB stage, those regions have had time to clear out most of the dust. The extinction corrected color–color diagram shows a relatively narrow distribution of data points along the blue side of the isochrones in the $(U-B)$ range of -0.8 to 0.2 mag. The internal extinctions and color excesses averaged over all stars are $A_{F225W} = 0.698$, $A_{F336W} = 0.660$, $A_{F438W} = 0.530$, $A_{F547M} = 0.402$, $A_{F814W} = 0.243$, and 0.130 and 0.160 mag in $(U-B)$ and $(V-I)$ colors, respectively.

3.3 Age-Dating Populations in NGC 4214

In this section we describe two different methods of age-dating stellar populations in NGC 4214. For both of these methods, we use the same photometric catalog (see Section 2) of individual stars in the field and the outskirts of the star clusters, where stars are resolved. In Figure 3.1, we divide our WFC3 NGC 4214 into a 38 box-grid, since we are interested in spatial variations of stellar population along with the ages and masses of individual stars.

3.1 CMD Fitting

We estimated the ages and masses of individual stars in our catalog by the CMD fitting age-dating method described in Kim et al. (2012). The basic idea of this method is finding the closest match in both age and mass for each star by comparing the extinction corrected I magnitude and $(V-I)$ color with the stellar isochrones. Figure 3.4 show the distribution of ages and masses of all stars. We estimate the age averaged over all stars with the I-band magnitude bright than -5.5 mag to calculate a luminosity-weight mean age, shown at the top right of the left panel in this figure. Once we get the matched age and mass for each star, we also calculate the luminosity-weighted average of stars in each grid box shown in Figure 3.1. Again, we only used the stars brighter than M_I=-5.5 mag to our calculation to avoid stars older than $\sim$500 Myr and get the age estimate weighted more on the younger populations in each region. This is the same magnitude cut used in the M83 study (Kim et al. 2012). The result of the average ages of the 38 grid boxes is described in Table 3.1. These luminosity-weighted ages are more appropriate for comparing with other ages or age-correlated parameters such as ages of star clusters or stellar groupings, and Hα morphology, which will be discussed in the future paper by C. Kaleida et al. (2012 in preparation).

Figure 3.5 shows the CMDs and color–color diagrams of Regions 6, 14, 35, and 23. The data points in each plot are all extinction corrected. The isochrones and the reddening vectors are the same as in Figure 3.3. A cursory glance at these plots show the several differences. The younger regions (Regions 6 and 14) contain more of blue main sequence stars and also larger numbers of upper MS stars. In comparison the CMDs of Regions 35 and 23 show stronger enhancement in the old populations ("red tangle" in (Drozdovsky et al. 2002)). Each region appears to

contain multiple populations, strongly contaminated by the underlying sheet of old populations. This makes our luminosity-weighted ages skew to the older ages than we expected from a comparison to the ages we determined for the 50 selected regions in M83 (Kim et al. 2012). As shown in the left panels of age histograms in Figure 3.6, the age sequence of these four regions is not as expected. Region 6 with the "J" feature shows strong Hα emmision in Figure 3.1 and it is expected to be the youngest region among the four regions. The average age determined for Region 6 is 19.2 Myr, while the age of Region 14 (central super star cluster complex) is 17.4 Myr. We think this reverse age sequence between Region 6 and 14 is caused by the underlying old populations included in the calculation. Region 6 contains more field stars, while Region 14 is mostly made up of the young blue giant stars located in the big Hα cavity.

In the column 6 of Table 3.1 we also listed the number ratio of red-to-blue giants using the stars above the magnitude cut of $M_I = -5.5$ mag. Regions 28 and 38 have no blue stars above the magnitude cut. The luminosity-weighted ages and the red-to-blue star fraction show a positive correlation, as we find the same result from the M83 study.

3.2 Stellar SED Fitting

Here we present a new method of age determination by the stellar Spectral Energy Distribution (SED) fitting to a set of stellar SED models. The model SEDs that are used for the Padova isochrones are distributed along with the isochrones used in our CMD age-dating in the previous section. The broad-band photometry is fit to the model SED where the only free parameter is the normalization. The best fit SED is chosen by the one that minimized the χ^2 statistic for each star. The

χ^2 is defined by:

$$\chi^2 = \sum_i \left(\frac{D_i - M_i}{\sigma_i} \right)^2 \tag{3.1}$$

where D_i is data flux in ith band, M_i is model flux, and σ_i is photometric error. Note that we do not fit the integrated flux of multiple stars or star cluster made of a single stellar population, but fit the individual stellar flux to the model SED. The first step of the stellar SED fitting method is to convert the magnitude to the flux for stars with the five-band (NUV and $UBVI$) photometry. About 3500 stars with NUV+$UBVI$ photometry are used to our calculation. The Padova model isochrones in NUV and $UBVI$ filters with the age range from 1 Myr to 10 Gyr are also converted to the flux unit. We then perform a χ^2 fit between the observations and the model SEDs and select the model with the minimum χ^2 as the best-fit age, mass, and other properties (e.g., temperature, gravitation). The SED fit of each star will be included in the electronic version of this paper. In Section 4, we show the age and mass distributions from our SED fitting method.

3.4 Discussion

We investigate the age distribution of individual stars determined by the CMD and SED fitting methods in order to get insights into the star formation history of NGC 4214. As described in Section 1, NGC 4214 is classified as type SBmIII by Sandage & Bedke (1985), and also widely known as a nearby dwarf irregular IAB(s)m (de Vaucouleurs et al. 1991). The H I distribution obtained from the Owens Valley Radio Observatory's millimeter array (OVRO) observations shows a large scale of different structure including H I holes and shells, and a hint of a bar and multiple spiral structures in NGC 4214 (Walter et al. 2001). Although our WFC3 images only covering the central 3 kpc by 3 kpc area of the galaxy make the direct comparison hard, we can still find the associated structures in our WFC3 field. The "J" region and two super star clusters at the center of Figure 3.1

are located in the two clumpy zones with high density of H I gas, which may be the major source producing sporadic generations of young stars in these regions. These stars are younger than the stellar background.

In Dobbs & Pringle (2010) they developed the models of spatial distributions of star clusters with different ages in spiral and barred galaxies. According to their study, younger stars are primarily associated with the spiral arms or barred structure, with the older stars (>100 Myr) downstream in the interarm regions. As expected we find that the young stars in our WFC3 field of NGC 4214 show the similar distributions. Figures 3.7 and 3.8 are the distributions of resolved stars with ages determined by the CMD and stellar SED fitting methods in the Section 3. Note that the age ranges in the four panels in these two figures are slightly different due to the fact that the SED fitting is more sensitive to the NUV and U-band fluxes from the youngest populations. Both figures clearly show that the youngest group ($<$10 Myr) of stars are mostly distributed along the central bar structure and also associated with the regions (two super star clusters and the "J" region) with the strong Hα emission. The stars in the intermediate ages tend to be more spread out to the field, while the oldest group of stars (underlying sheet of old populations) are found across the entire field. These diagrams also support for the scenario that the stars form in clusters in spiral arms or barred structures, and then they dissolved to the field.

3.5 Summary

We analyze the multi-band HST/WFC3 ERS observations of NGC 4214 to determine the ages of resolved stellar populations. We have used the CMD and color–color diagram along with the stellar model isochrones and developed the new age-dating method by the individual stellar SED fitting. NGC 4214 is a dwarf irregular galaxy clearly showing the presence of multiple stellar population

features, including recently formed main-sequence stars, two distinct branches of He-burning blue-loop giants, and a large population of shell-burning red-giant stars. The results of this study is summarized as follows:

(1) The star-by-star extinction correction methods developed in the previous study (Kim et al. 2012) are applied to NGC 4214, showing the significant amount of internal extinctions in $UBVI$ photometric system. The mean extinction values of this galaxy are $A_{F336W} = 0.660$, $A_{F438W} = 0.530$, $A_{F547M} = 0.402$, $A_{F814W} = 0.243$ mag, respectively.

(2) We develop a new age-dating technique using the individual stellar SED fitting in order to estimate the ages and masses of stars with the five-band photometry. This method is relatively more sensitive to the luminous stars in NUV, and uses all five bands at once.

(3) The WFC3 field of NGC 4214 is divided into the 38 adaptive grid boxes in order to compare our stellar ages from the CMD and SED fitting to other age indicators. In this paper we show the positive correlation between stellar ages and the number ratio of red-to-blue stars.

(4) The age distributions determined from both CMD and SED age-dating methods show that the youngest group of stars is generally located along the active star-forming regions in the central bar area, This supports for the model distributions of star clusters in spiral and barred galaxies by Dobbs & Pringle (2010).

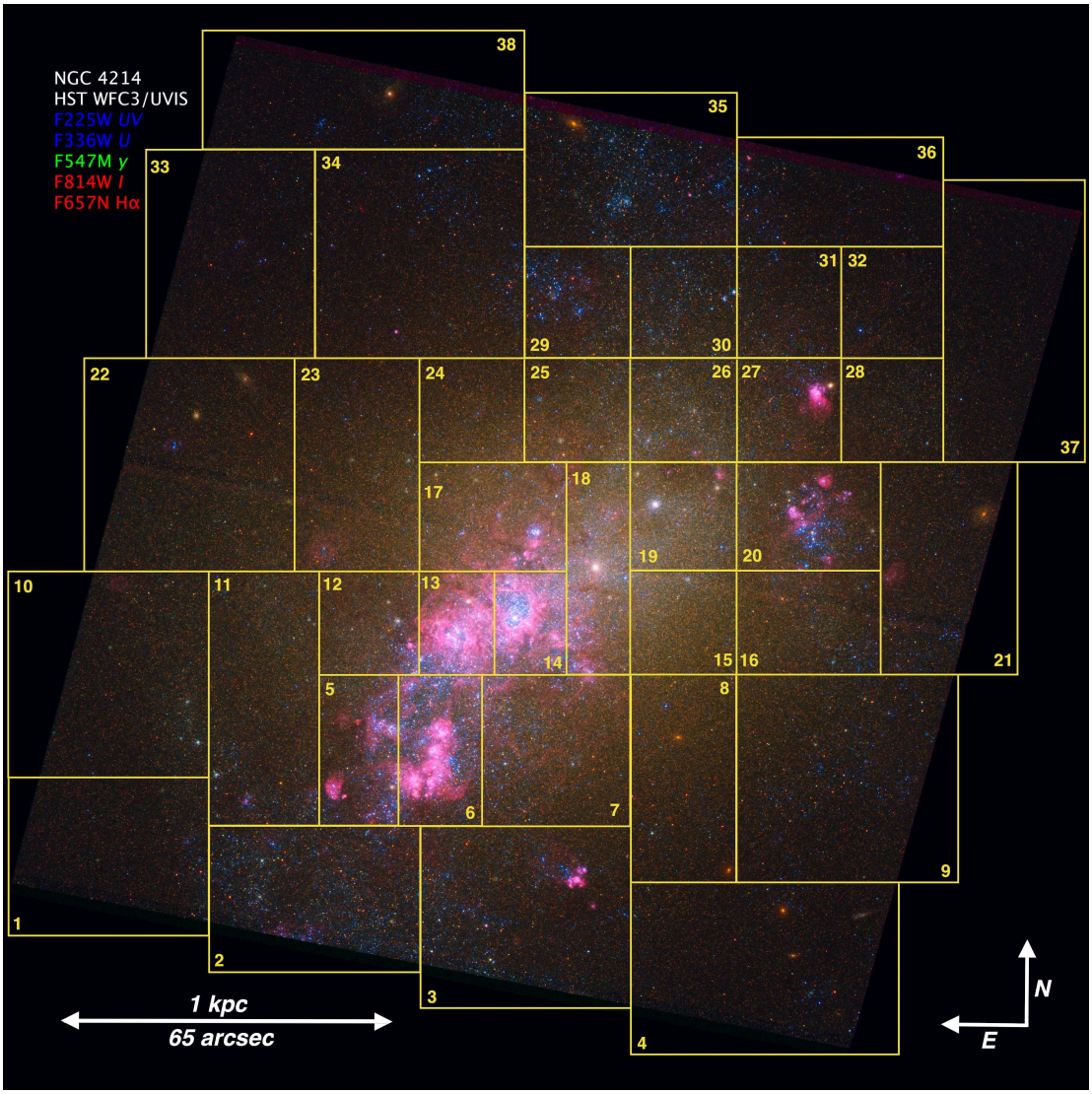

Figure 3.1: Color composite of the central 2.9 kpc×2.9 kpc of the NGC 4214 WFC3 images [Image Credit: Zolt Levay (STScI)]. The combined F225W and F336W images are in blue, the F547M in green, and the combined F814W and F657N (Hα) image in red. The 38 adaptive box-grid is outlined in yellow.

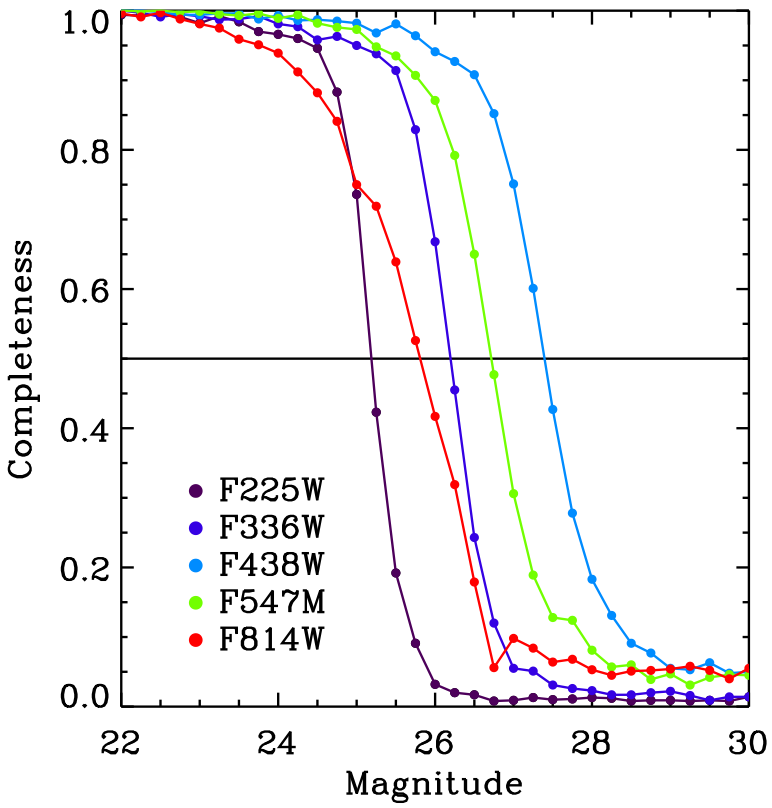

Figure 3.2: Completeness of stellar photometry for WFC3/UVIS images used in this study. Completeness was determined by inserting artificial stars with the magnitude range from 22 to 30 mag in Vega magnitude system. See Section 3.2.2 for more details.

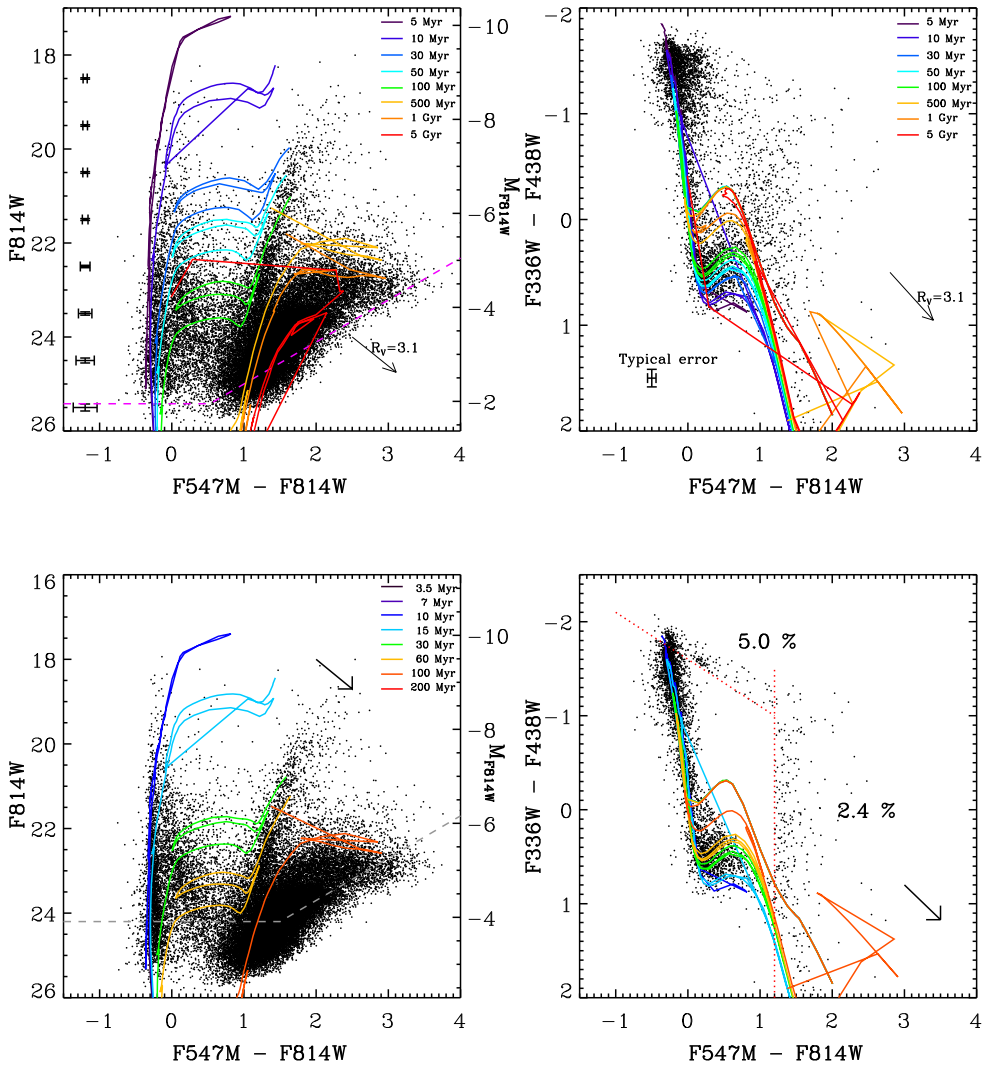

Figure 3.3: Top: the color–magnitude diagram (CMD) and color–color diagram of all stars in our NGC 4214 image corrected for Galactic foreground extinction. Padova isochrones of age = 5, 10, 30, 50, 100, 500 Myr, and 1, and 5 Gyr for a metallicity of Z=0.006 (0.3 $Z_{\odot}$) are overlaid in both panels. The dashed line in magenta represents the 50% photometric completeness level. The arrow in each panel indicates the direction of the reddening vector with $R_V = 3.1$. All magnitudes are in Vega magnitude system. We use the distance modulus $(m - M)_0 = 27.37$ mag (Dopita et al. 2010) to calculate the absolute magnitude M_{F814W}. Bottom: the CMD and color–color diagram of all stars corrected for the internal extinction determined for each individual star. The blue and two red dotted lines indicate boundaries for the locations of stars in the color–color diagram uncorrected for internal extinction (see Section 2.2.3 for discussion).

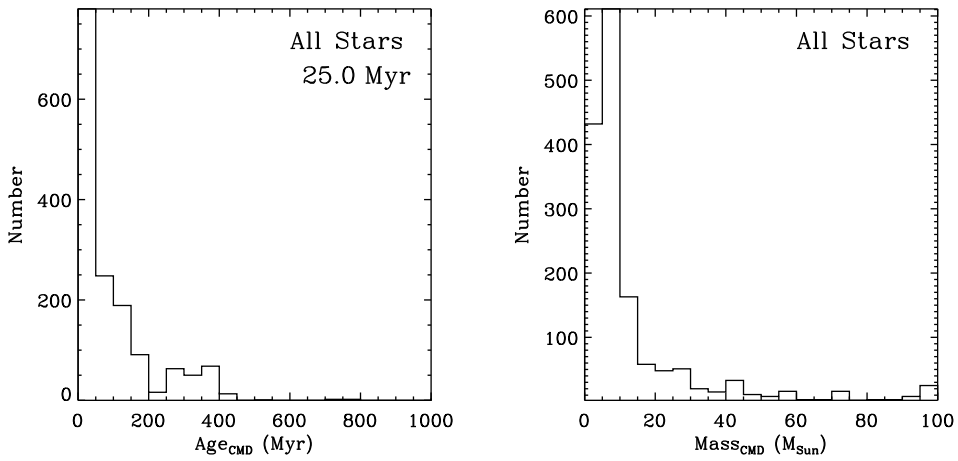

Figure 3.4: Histograms of stellar ages and masses determined from the CMD age-dating method (see Section 3.1 for details). The luminosity-weighted age averaged over all stars is at the top right in the left panel of this figure.

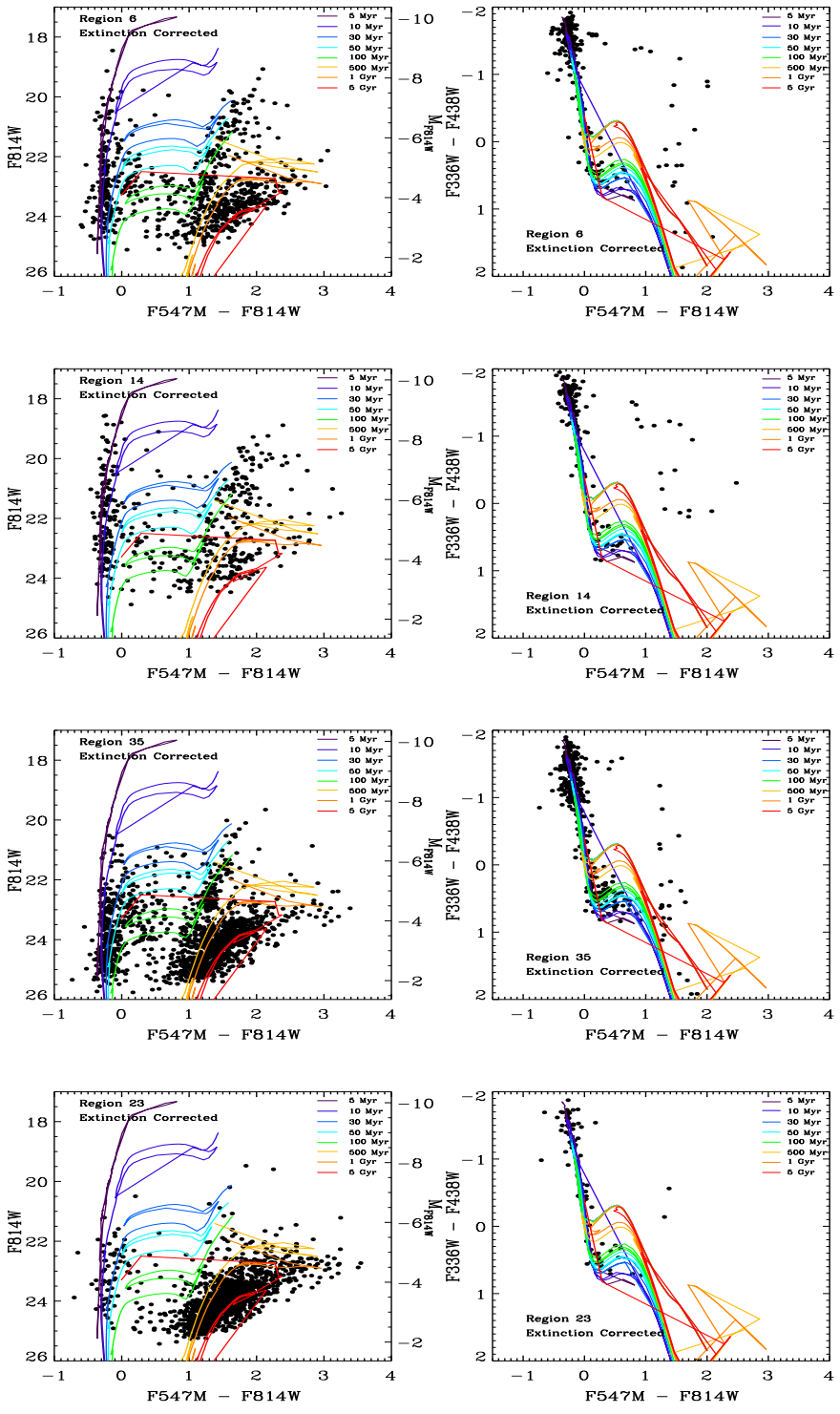

Figure 3.5: CMDs, color-color diagrams of Regions 6, 14, 35, and 23. Each data point is extinction corrected by the method described in Section 3.2.3. The Padova isochrones in these diagrams are the same as the ones plotted in Figure 3.3.

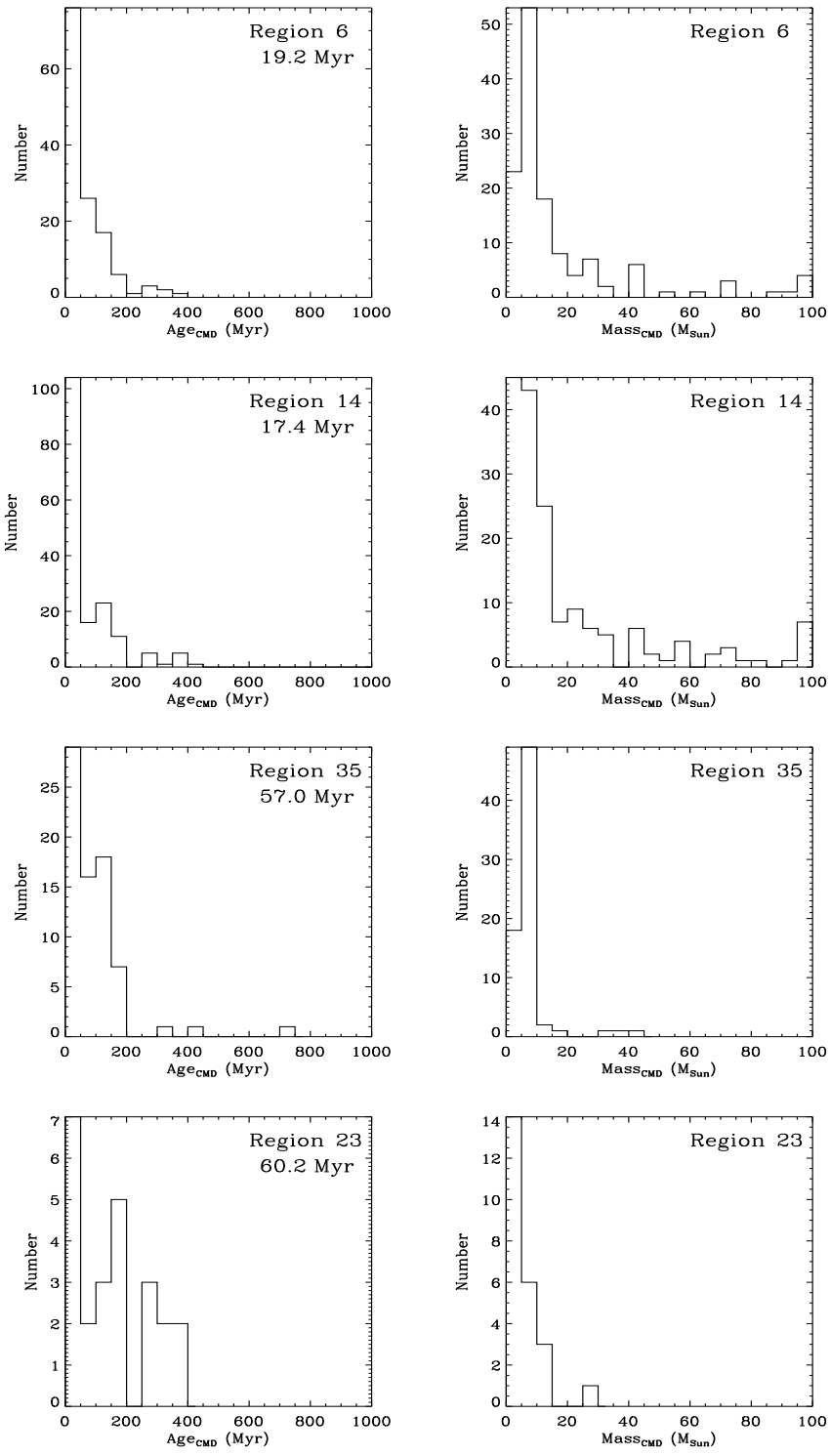

Figure 3.6: Histograms of the distribution of ages and masses of the individual stars in Regions 6, 14, 35, and 23, as determined by the automated CMD age-dating method (see Section 3.3.1). The age at the top right in each age histogram is the luminosity-weighted mean age of all stars in each region.

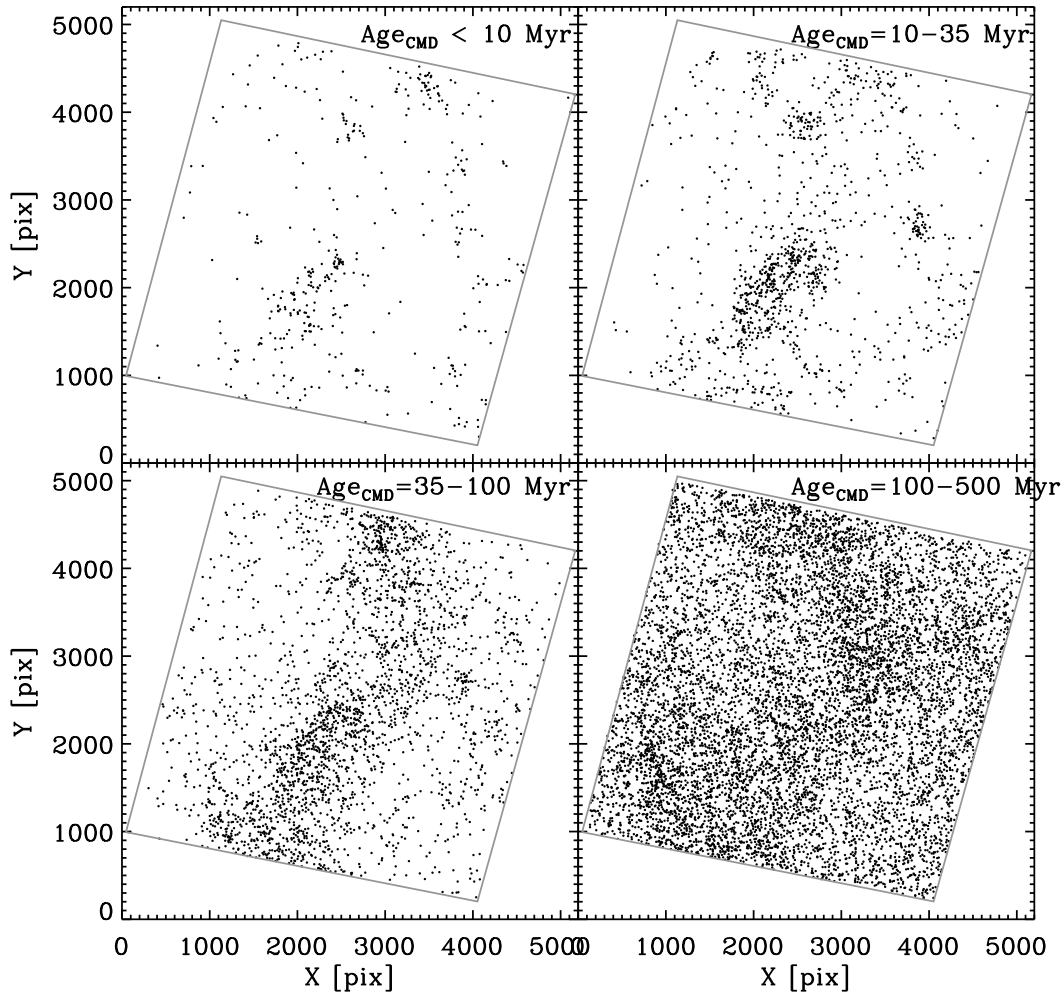

Figure 3.7: Age$_{CMD}$ distribution of stars in our WFC3 field outlined in grey. Ages are determined using the extinction-corrected CMD and the model isochrones in Figure 3.3. Each panel has the same orientation and scale as Figure 3.1. The top panels are the youngest (age $<$ 10 Myr) and the second youngest (10 $\leq$ age $<$ 35 Myr) groups of stars, clearly showing that the stars in these regions are mostly distributed along the active star-forming region (i.e., associated with the strong Hα emission) in the central bar of the galaxy. The stars in the bottom left panel (35 $\leq$ age $<$ 100 Myr) tend to show less clustered feature and more evenly distributed, except the loosely bound OB associations in the north part of the image. See Sections 3.1 for details.

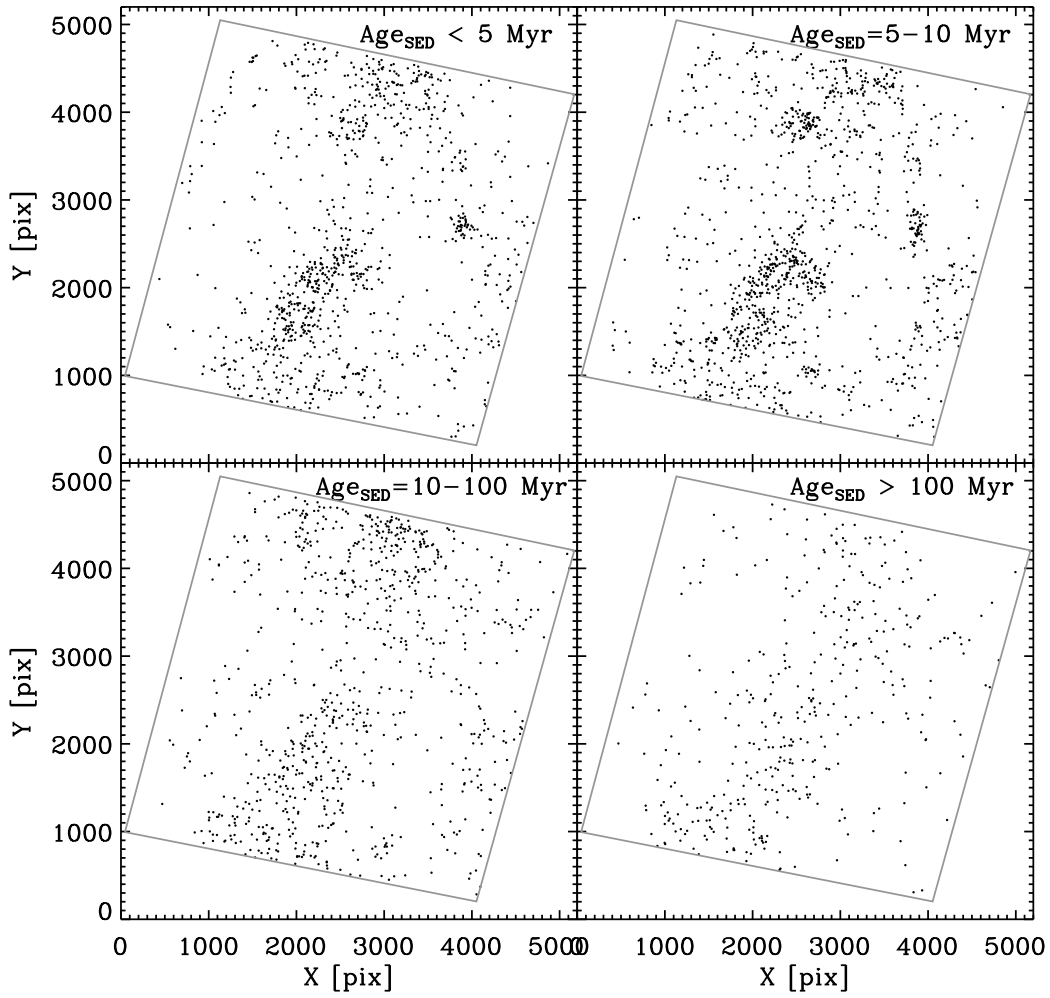

Figure 3.8: Spatial distribution of stars with ages determined from the SED fitting method. Due to the smaller number of stars with all five-band photometry used in the SED fitting, fewer objects (∼3500 total) are shown in each panel. Note that we use age ranges different from the ones used in Figure 3.7. The top left panel is the youngest (age < 5 Myr) group of stars, showing the enhancement of stars distributed in the southern part of the central bar and the stars in the star-forming region in the west side of the image. The top right panel is the stars with ages of 5 to 10 Myr, clearly showing that stars in the super star cluster of the center and in the OB association are not far from their birthplace associated with the strong Hα emission.

Table 3.1: Properties of the 38 Regions in NGC 4214

Region	R.A.(J200) (hh:mm:sec)	Decl.(J2000) (°:':")	Region Size (pc×pc)	Age_{CMD} (Myr)	Red-to-blue	N^a_{Star}	A_V (Mag)
1	12:15:45.832	+36:18:48.95	568×454	65.1	6.00	14	0.000
2	12:15:42.556	+36:18:40.05	568×426	44.7	3.00	84	0.084
3	12:15:39.280	+36:18:37.08	568×511	23.0	1.43	56	0.082
4	12:15:35.512	+36:18:29.16	738×454	37.5	1.56	23	0.036
5	12:15:41.901	+36:19:09.75	227×426	25.1	1.36	78	0.157
6	12:15:40.590	+36:19:09.75	227×426	19.2	1.75	132	0.129
7	12:15:38.788	+36:19:09.75	398×426	28.6	1.79	67	0.072
8	12:15:36.822	+36:19:04.80	284×568	32.3	2.60	18	0.035
9	12:15:34.201	+36:19:04.80	625×568	56.0	3.18	46	0.021
10	12:15:45.833	+36:19:24.59	568×568	61.4	3.00	16	0.014
11	12:15:43.375	+36:19:19.64	284×710	50.7	4.00	25	0.052
12	12:15:41.737	+36:19:34.50	284×284	19.8	2.86	27	0.157
13	12:15:40.345	+36:19:34.50	199×284	12.5	1.26	113	0.203
14	12:15:39.198	+36:19:34.50	199×284	17.4	1.51	168	0.186
15	12:15:36.822	+36:19:34.50	284×284	100.0	5.00	18	0.000
16	12:15:34.856	+36:19:34.50	398×284	31.8	1.20	22	0.092
17	12:15:39.771	+36:19:54.30	398×284	23.2	1.74	63	0.157
18	12:15:38.133	+36:19:44.40	170×568	21.7	2.42	89	0.158
19	12:15:36.822	+36:19:54.30	284×284	57.3	4.67	34	0.028
20	12:15:34.856	+36:19:54.30	398×284	10.8	0.64	36	0.224
21	12:15:32.562	+36:19:44.39	398×568	59.2	2.75	15	0.166
22	12:15:44.523	+36:20:04.19	568×568	50.1	9.00	20	0.031
23	12:15:41.901	+36:20:04.19	341×568	60.2	7.00	24	0.016
24	12:15:40.099	+36:20:14.10	284×284	52.7	7.00	8	0.000
25	12:15:38.460	+36:20:14.10	284×284	33.9	2.38	27	0.069
26	12:15:36.822	+36:20:14.10	284×284	38.3	3.00	32	0.117
27	12:15:35.183	+36:20:14.10	284×284	33.4	2.25	26	0.043
28	12:15:33.544	+36:20:14.10	284×284	171.7	—	6	0.000
29	12:15:38.460	+36:20:33.90	284×284	17.5	1.18	37	0.139
30	12:15:36.822	+36:20:33.90	284×284	40.4	2.44	31	0.216
31	12:15:35.183	+36:20:33.90	284×284	59.2	2.00	15	0.148
32	12:15:33.544	+36:20:33.90	284×284	10.3	0.33	4	0.133
33	12:15:43.868	+36:20:43.80	454×568	50.8	1.40	12	0.000
34	12:15:40.919	+36:20:43.80	568×568	23.0	1.86	40	0.130
35	12:15:37.641	+36:20:59.64	568×454	57.0	3.56	73	0.026
36	12:15:34.363	+36:20:55.67	568×341	61.6	2.00	15	0.087
37	12:15:31.578	+36:20:33.89	398×852	43.9	5.00	6	0.051

38	12:15:41.902	+36:21:15.48	909×341	77.1	—	9	0.000

[a] Total number of stars used in the luminosity-weighted average age calculation.

Chapter 4

EXTREMELY METAL-POOR DWARF GALAXY CGCG 269-049

4.1 Overview

A small fraction of starforming dwarf galaxies in the local universe had oxygen to hydrogen abundance ratios of $12 + \log(\mathrm{O/H}) < 7.65$ in their emission-line gas, with an implied metallicity below $\sim$10% of the solar value (e.g., Kniazev et al. 2003; Izotov et al. 2006; Pustilnik & Martin 2007; Izotov & Thuan 2007). It is reasonable to hypothesize that such extremely metal-poor galaxies (XMPGs) are young objects, forming their first generation of stars, and considerable effort has recently been devoted to testing this hypothesis by studying the stellar populations of XMPGs including the prototype object, I Zw 18.

While most XMPGs have been found to contain evolved stars (e.g., Aloisi et al. 2005; Corbin et al. 2006; see also the reviews by Kunth & Östlin 2000 and Kunth & Östlin 2007), the results for I Zw 18 itself have been controversial, with some studies based on deep Hubble Space Telescope imaging reporting no stars older than $\sim$1 Gyr (Izotov & Thuan 2004; Östlin & Mouhcine 2005), while subsequent analyses of the Izotov & Thuan (2004) data and more recent *HST* observations indicate the presence of red giant stars in the galaxy (Momany et al. 2005; Aloisi et al. 2007). Both possibilities for the nature of XMPGs (evolved or non-evolved) have important implications for models of galaxy formation, which motivates the detailed study of more members of this class. In particular, the resolution of individual stars by *HST* imaging is the best way to establish the presence or absence of an evolved population.

At shorter infrared wavelengths (< 10 μm), Spitzer Space Telescope photometry also helps constrain the age of their stellar populations, and at longer

infrared wavelengths Spitzer photometry is important for assessing the dust content of the galaxies, which both affects their optical photometry and carries implications for their star formation histories.

With these motivations we have obtained deep *HST* and Spitzer images of the galaxy CGCG 269-049, identified as an XMPG by Kniazev et al. (2003), who measure a value of 12 + log(O/H) = 7.43 ± 0.06 from its Sloan Digital Sky Survey spectrum. CGCG 269-049 is an isolated low-surface brightness dwarf galaxy with g = 15.75 and z = 0.00052 (Kniazev et al. 2003), placing it at a distance of only 4.7 ± 0.4 Mpc after correction to the frame of the Cosmic Microwave Background (assuming H_0 = 73 km s^{-1} Mpc^{-1}, $\Omega_M = 0.27$, $\Omega_\Lambda = 0.73$; Spergel et al. 2007). This distance presents an excellent opportunity to study CGCG 269-049 in detail. Most importantly, it allows the resolution of its stars with the *HST* Advanced Camera for Surveys High Resolution Channel. The galaxy also has a major axis diameter of approximately 30″, allowing it to be resolved by the Spitzer Infrared Array Camera (IRAC) and Multiband Imaging Photometer (MIPS). A color composite image of CGCG 269-049 from the Sloan Digital Sky Survey is shown in Figure 4.1; a population of evolved stars is not obviously present. H I observations of CGCG 269-049 reveal a semi-ordered velocity field and a symmetric H I envelope extending ≈ 2.3 Holmberg radii beyond the galaxy's optical disk (Begum et al. 2005). These authors also measure a dynamical mass for the galaxy of only 1.2 × 10^8 $M_\odot$. The symmetry of the H I envelope argues against the possibility that the galaxy's current star formation has been triggered by interaction with a neighbor, although it is only approximately 14.5 kpc from the dwarf galaxy UGC 7298, and is a member of the Canes Venatici I galaxy cloud (see Begum et al. 2005). Most of the star formation in the galaxy is also concentrated in a star cluster near the galaxy's nominal center (Figure 4.1), hereafter referred to as the Central Cluster.

In the following sections we present our Spitzer and *HST* observations of CGCG 269-049, including a stellar color-magnitude diagram from the *HST* photometry that clearly shows the presence of asymptotic giant branch and red giant branch stars in the galaxy, with ages up to ∼10 Gyr. We conclude with a discussion of these results in the context of recent models of the origin of the global galaxy mass / metallicity relation and dwarf galaxy formation. In the following calculations we assume a distance of 4.9 ± 0.2 Mpc to the galaxy, measured from the magnitude of the tip of the RGB we detect in its color-magnitude diagram (Section 4.2.4).

4.2 Observations

4.2.1 Spitzer Images and Photometry

CGCG 269-049 was observed by the Spitzer IRAC and MIPS instruments on UT 12/24/2005 and 12/6/2005, respectively. The total integration times were 3701s (IRAC) and 6322s (MIPS). The galaxy was detected in all four IRAC bands (3.6 μm, 4.5 μm, 5.8 μm, and 8.0 μm) and in the MIPS 24 μm and 70 μm bands, but not the 160 μm band. Figure 4.1 shows the images of these galaxies in four of these bands. The images reveal a progressive decrease in the stellar flux of the galaxy in the regions away from the Central Cluster with increasing wavelength, and a gradual increase in the emission from the Central Cluster, which becomes strongest at 24 μm and 70 μm (compare to Figure 4.1). This likely represents the decline of the stellar continuum emission beyond ∼10 μm and the increase of thermal dust emission and possibly Polyaromatic Hydrocarbon (PAH) emission from the Central Cluster. Similar spatial correlation between emission above ∼10 μm and star-forming regions detected at optical wavelengths is seen in Spitzer images of other nearby galaxies (e.g., Jackson et al. 2006; Barmby et al. 2006; Cannon et al. 2006; Hinz et al. 2006). No significant emission beyond the Central

Cluster is detected in the MIPS bands, which is likely due to the lack of hot stars in the region (Section 4.2.3).

Photometry was performed on these images with the IRAF "polyphot" task, using comparable polygonal apertures for all images to include the flux from the entire galaxy. The measured fluxes are given in Table 4.1. Figure 4.3 presents the resulting spectral energy distribution (SED). The SED is well-fitted by the combination of a Bruzual & Charlot (2003) stellar population synthesis model at the shorter wavelengths, and a Draine & Li (2007) thermal dust emission spectrum at longer wavelengths, including a significant contribution to the flux at 8.0 μm from PAH emission. The Bruzual & Charlot (2003) model that best fits the IRAC fluxes is an instantaneous burst with a Chabrier initial mass function, a metallicity of 0.02 $Z_{\odot}$, no internal extinction, and an age of 10 Gyr. We note, however, that the same model with an age of 1 Gyr also fits the data to within the estimated errors, so ages in the range of $\sim$1 – 10 Gyr are also possible, in addition to the newly-formed stars. This nonetheless provides the first evidence of evolved stars within the galaxy. The Draine & Li (2007) model that best fits the data has a dust composition based on that of the Large Magellanic Cloud, and a range of the parameter $U = 5 - 10^4$, where U represents the intensity of the radiation field incident on the dust in units of the ambient radiation field in the solar neighborhood. The implied dust temperature from the fitted curve is 72 $\pm$ 10 K.

4.2.2 Estimate of Dust Mass

We estimate the total mass of dust from the fitted dust emission spectrum using equation (31) of Draine & Li (2007) and assuming a value of the ratio of the total dust mass to the total mass in H I. We specifically use the mean value of this ratio, 2×10^{-4}, from the sample of 16 Blue Compact Dwarf Galaxies studied

by Hirashita, Tajiri, & Kamaya (2002), which gives $M_{dust} \approx 3 \times 10^3 M_\odot$. Such a value is roughly consistent with the amount of dust expected to be produced by the Central Cluster over its lifetime. Specifically, models of the dust production of primordial galaxies by Morgan & Edmunds (2003) predict the formation of such dust masses within $\sim 10^7$yr of the onset of star formation (see their Figure 8), which is comparable to the age of the central cluster implied by the presence of its OB stars. Morgan & Edmunds (2003) assume a star formation rate of 1 $M_\odot$ yr^{-1}, which we can compare with an estimate of the current SFR of CGCG 269-049 from its 8.0 μm luminosity using the calibration of Wu et al. (2005). We find from this calibration a SFR of ≈ 0.2 $M_\odot$ yr^{-1}, suggesting a higher SFR for the cluster in the recent past, but note also the large uncertainty in this calibration (see Wu et al. 2005 and Calzetti et al. 2007). The galaxy's SDSS spectrum was obtained from a 3″diameter fiber centered on the Central Cluster, and so a value of the SFR estimated from the H line of this spectrum would be an underestimate.

As another check of the dust content of CGCG 269049, we measure the Balmer decrement in its Sloan Digital Sky Survey spectrum. This spectrum was taken through a 3″aperture centered on the Central Cluster. We measure $f_\lambda(H\alpha)/f_\lambda(H\beta) = 2.93 \pm 0.05$, with an associated $E(B-V)$ value of 0.056 mag, corresponding to $A_V \approx 0.2$ mag under the assumption of a Large Magellanic Cloud extinction curve (Gordon et al. 2003). We use this value and associated A_I and $E(V-I)$ values to correct our *HST* photometry for internal reddening, noting that the extinction in the areas away from the Central Cluster may differ.

4.2.3 *HST*/ACS Data

CGCG 269-049 was imaged by the *HST* Advanced Camera for Surveys / High Resolution Channel (ACS/HRC) on UT 11/2/2006 under GO program 10843. The filters and exposure times were F330W (2000s), F550M (6320s), F814W

(2120s), and F658N (2192s). The broadband filters were selected to cover a wide wavelength range and also to avoid strong emission lines including [O III] $\lambda\lambda$ 4959, 5007, while the F658N filter includes Hα and the underlying stellar continuum. The exposure times were chosen to detect individual red giants stars at the distance to the galaxy estimated from its redshift (Section 4.1). The raw data were processed with the standard ACS On-The-Fly-Recalibration Pipeline using the multidrizzling process. A correction for Galactic foreground extinction was applied to the image flux levels using the values of Schlegel et al. (1998).

A color composite of the F330W, F550M, and F814W images is shown in Figure 4.4. Individual stars of varying colors are clearly resolved. The Central Cluster is revealed to be more of a loose association dominated by the emission from $\sim$20 OB stars. A faint background galaxy appears to be present approximately 6$''$SE of the Central Cluster. This region was excluded from the stellar photometry, as was the area around the "coronagraphic finger" of the camera seen near the bottom of the figure, and the edges of the images.

A portion of the F658N image is shown in Figure 4.5. The Hα emission is concentrated around the Central Cluster, with what may be a single O9 star at the cluster center appearing to dominate the ionization. With the exception of its southwestern portion (possibly because of dust extinction), the emission is remarkably circular, indicative of a classical Strömgren sphere. This contrasts with the more filamentary appearance of ionized gas in "superwinds" from starburst galaxies (see the review by Veilleux, Cecil, & Bland-Hawthorn 2005). Although we lack data on the gas kinematics, the morphology and small size of the ionized volume do not indicate that a significant amount of gas is being driven from the Central Cluster. We additionally find no clear evidence of supernova remnants beyond the Central Cluster in this image.

4.2.4 Photometry from *HST* Images

Point-Spread Function (PSF) photometry was performed using the DAOPHOT package (IRAF version 2.12.2). A master catalog of the point sources in each image was created through a three-step process with progressively fainter detecting thresholds of 15, 10, and 5 sigma, where sigma is the standard deviation measured from the histogram of the sky background pixels. Detection thresholds below 5 sigma were not used in this study because the stars in CGCG 269-049 are crowded and fainter thresholds did not reliably detect additional stars. In the second and the third steps, we used the residual images produced from the previous step after subtraction of the previously found brighter stars.

The PSFs used are a combination of an analytical base-function and an empirical image that describes the difference between a composite stellar image and the best-fit base-function. Since the sampling of the PSF differs in F330W, F550M, and F814W, to minimize the residuals, we used different base-functions: Gaussian for F330W and F550M and Moffat15 for F814W. The residual images show that most of the point sources had been cleanly subtracted out from the original images. After the third and final step, only a few stars that were affected by bad pixels or residuals from cosmic ray hits remain. This process also revealed a component of unresolved stars underlying the resolved sources. All magnitudes were placed on a Vega scale, using equation (4) of Sirianni et al. (2005) and updated zero-points from the ACS website[1]; they are 22.907, 24.392 and 24.861 for the F330W, F550M, and F814W images, respectively. These zero points assume an aperture of 5.5″, and our magnitudes were corrected accordingly, using the results of Sirianni et al. (2005).

[1] http://www.stsci.edu/hst/acs/analysis/zeropoints

Figure 4.6a presents a color-magnitude diagram (CMD) from the cross-matched lists of magnitudes in the F550M and F814W filters. We only plot magnitudes with formal 1σ errors less than 0.2 mag. The CMD indicates the presence of a red giant branch, along with asymptotic giant branch stars and carbon stars. The stars near the 50% completeness limit shown on the plot are most likely to be dust-reddened post-AGB or carbon stars. These stars were visually verified to be genuine detections, and are distributed roughly uniformly over the portion of the galaxy imaged.

We estimate a distance to the galaxy from the apparent F814W magnitude of the tip of the red giant branch (TRGB), 24.5 ± 0.1, and the assumption of M(I) $= -4.05$ for the TRGB of metal-poor systems (Da Costa & Armandroff 1990). Transforming the F814W magnitude to I (equation 12 and Table 23 of Sirianni et al. 2005) yields a distance of 4.9 ± 0.2 Mpc, in agreement with the value estimated from CGCG 269-049's redshift (Section 4.1). We overplot the theoretical isochrones calculated for ACS/HRC and these filters from the Padova database (http://pleiadi.pd.astro.it/isoc_photsy.02/isoc_acs_hrc/index.html; see also Girardi et al. 2002), assuming a distance of 4.9 ± 0.2 Mpc and a metallicity of Z = 0.0004 . Good agreement is seen between the individual isochrones and the various branches of the CMD. Notably, the reddest RGB stars in the galaxy appear to be $\sim$10 Gyr old. This CMD is similar to that obtained by Aloisi et al. (2005) for the XMPG SBS 1415+437 using ACS/WFC and the F606W and F814W filters.

Figure 4.6b plots the F330W – F550M and F550M – F814W colors for the relatively small number of stars detected in the F330W filter. This comparison provides a check on the accuracy of the isochrone fitting to the CMD by including the F330W magnitudes. Specifically, the blue horizontal branch loops in the isochrones seen in Figure 4.6a produce a nearly linear feature in this color space

that fits the data very well. If systematic errors were present in our photometry or in the isochrone fitting they would likely be evident on one or both of Figures 4.6a and 4.6b, but the correspondence of the data and isochrones indicates otherwise.

To assess the completeness of the PSF-fitting, we inserted 100 artificial stars at random positions into the actual images for all three filters. For each filter, we repeated this task 32 times, using different PSF functions such as Gaussian, Moffat15, Moffat25, and the "Auto" function defined in the IRAF task 'daopars'. The magnitude of the inserted stars was varied from 21 to 29 in steps of 0.25 mag. Therefore, total number of trials was 544 times for each filter. The recovery of artificial stars was performed with the same three-step process with which we measured the actual stars. The results are shown in Figure 4.7, where it can be seen that the 50% (90%) completeness levels are reached at magnitudes of approximately 25.3, 27.2, 26.7 (24.8, 26.6, 26.0) for the F330W, F550M, and F814W filters, respectively. The F330W image was not deep enough to recover stars to the faint limits reached in the F550M and F814W images. Of the three filters, F550M effectively is the deepest image with a completeness limit approaching 27 mag. The F814W photometry reaches 0.5 mag brighter. Before applying cuts on the formal photometric errors, we detect 1550 stars in F330W, 5993 in F550M, and 4164 in F814W. After requiring the error less than 0.2 mag, 309, 3128, and 4339 stars remain in F330W, F550M, and F814W, respectively.

4.3 Results

4.3.1 Mass Fraction of Old Stars

It is of interest to estimate the fraction of stellar mass represented by the stars in CGCG 269-049 older than $\sim$1 Gyr as an indicator of its star formation history. Corbin et al. (2006) find that the $\sim$10 Gyr old populations in nearby "ultra-compact" blue dwarf galaxies, including two that qualify as XMPGs, comprise

$\sim$90% of their stellar mass, with their light being dominated by the early-type stars formed in their starbursts. These estimates were however based on a decomposition of the objects' optical spectra into its constituent stellar populations, obtained through apertures containing nearly all of their emission. Such a spectrum is not available for CGCG 269-049, so we must rely on the *HST* stellar photometry to make this estimate, with corrections for completeness in depth and spatial coverage, and the assumption of a stellar initial mass function.

We begin by noting that stars at the main-sequence turnoff in a $\sim$10 Gyr population will have a mass $\sim$1 $M_{\odot}$. Their combined post main-sequence stages last $\sim$500 Myr, most of which is spent on the RGB. Hence the masses of the $\sim$10 Gyr stars we detect should be in the range $\sim$1 – 1.02 $M_{\odot}$. Stars on the main-sequence turnoff in a $\sim$1 Gyr population, by contrast, have masses $\sim$2.5 $M_{\odot}$ and linger less than $\sim$50 Myr on the RGB, making it probable that the RGB stars we detect have ages closer to 10 Gyr. We count 1432 stars on the red branch of our CMD (having F550M – F814W $>$ 0.4 mag and F814W $<$ 27.0 mag). Correcting for incompleteness at 26 $<$ F814W $<$ 27 mag and for RGB stars with 27 $<$ F814W $<$ 31.3 mag (the magnitude of the main-sequence turn-off), and also for the RGB stars outside the area covered by our images, we estimate the total number of RGB stars to be approximately 12,890. Direct integration of the Miller & Scalo (1979) and Scalo (1986) initial mass functions implies that the total zero age main-sequence mass of the $\sim$10 Gyr old population is 200 – 300 times larger than the total mass of stars in the $\sim$1 – 1.02 $M_{\odot}$ range. With our estimated number of RGB stars, this yields a total mass of 2.6 – 3.9 $\times$ 10^6 $M_{\odot}$, where the range represents the difference between the Scalo (1986) and Miller & Scalo (1979) initial mass functions, both with lower and upper mass limits of 0.1 and 125 $M_{\odot}$. More details on mass fraction calculation are described in Appendix B.5.

We similarly estimate the masses of stars younger than ∼1 Gyr by counting the number of stars on the blue branch of the CMD (having F550M – F814W < 0.4 mag and F814W < 27); we find 1104. Their distribution in the CMD and color-color diagram suggests that they belong to populations with ages of 250 Myr and younger. For corresponding main-sequence turnoff masses between 4.0 and 20 $M_{\odot}$ we estimate a total zero-age main sequence mass of $0.34 - 2.6 \times 10^6$ $M_{\odot}$. Changing the upper mass limit to 100 $M_{\odot}$ decreases this mass by less than 10%. The total mass in stars of CGCG 269-049 is thus $\sim 3 - 6.5 \times 10^6$ $M_{\odot}$, of which ∼60% – 90% is contained in stars older than 1 Gyr. This is consistent with the findings of Corbin et al. (2006) and with Aloisi et al. (2005) for SBS 1415+437.

4.3.2 Evidence of Past Outflows?

One likely contribution to galaxy metal deficiency is the escape of supernova ejecta into the intergalactic medium (see e.g., Davé, Finlator, & Oppenheimer 2006; Calura et al. 2007 and references therein). This in part motivated obtaining an Hα image of CGCG 269-049 in addition to broad-band images. While the Hα image (Figure 4.4) does not indicate a current outflow, such outflows may have occurred in the past, during more vigorous episodes of star formation. Evidence of such an outflow from the blue compact dwarf galaxy IC 691 has been reported by Keeney et al. (2006), who find a metal-line absorption system in the spectrum of a background QSO with a projected distance of 33 kpc from this galaxy. Motivated by this result, we searched the NASA Extragalactic Database for QSOs near CGCG 269-049 that could be used as probes of past outflows. We find one object, SDSS J121507.48+522055.7 (z = 1.21) located approximately 6′from CGCG 269-049 (a projected separation of 8.6 kpc) and at a position angle of approximately 230°, which is roughly aligned with its minor axis. However, we find no evidence for absorption lines (e.g., Ca II H & K) in the Sloan Digital Sky Survey optical

spectrum of this QSO that could arise from a past outflow from CGCG 269-049. Thus, either such an outflow did not occur, or occurred in a direction other than along the sight-line to the QSO, or else its column density is presently too low to produce measurable absorption in the QSO's spectrum.

4.4 Discussion

The clear presence of asymptotic giant branch and red giant branch stars in CGCG 269-049 revealed by these data rules out the possibility that it is a newly-formed galaxy. In addition to the studies discussed in Section 4.1, these results argue strongly against this possibility for XMPGs in general. While the mean stellar ages among star-forming dwarf galaxies will be skewed to lower values than their quiescent counterparts, studies of extremely metal-poor dwarf galaxies in the Local Group without active star formation have shown them to consist mainly of evolved stars (see, e.g., Schulte-Ladbeck et al. 2002; Momany et al. 2005; Walsh, Jerjen, & Willman 2007). Among star-forming XMPGs such as CGCG 269-049, it appears that their current starbursts dominate their light and create a "blue façade" over stellar populations that are predominantly $\sim$10 Gyr old (e.g., compare Figure 4.1 and Figure 4.4; see also Corbin et al. 2006).

For more distant XMPGs whose stars cannot be resolved by *HST*, e.g., SBS 0335-052W (see Izotov, Thuan, & Guseva 2005), the best way to test for the presence of evolved stars is by the decomposition of their spectra into constituent stellar populations, using codes such as STARLIGHT (see Asari et al. 2007 and references therein). We note that in contrast to SBS 0335-052 (see Houck et al. 2004), the mid-infrared SED of CGCG 269-049 (Figure 4.3) shows evidence for significant PAH emission. This agrees with evidence that the strength of PAH features among star-forming dwarf galaxies depends more strongly on star-formation rate than metallicity (Rosenberg et al. 2004; Jackson et al. 2006), noting that SBS

0335-052 has six "super" star clusters and an inferred star formation rate twice that of what we estimate for CGCG 269-049 (see Thuan, Izotov, & Lipovetsky 1997; Section 4.2.2).

Brooks et al. (2007) have recently modeled the galaxy mass / metallicity relation (see Tremonti et al. 2004; Lee et al. 2006) using smoothed particle hydrodynamics and N-body simulations of galaxy formation including supernova feedback and associated metal enrichment. Their simulations extend down to metallicities as low as that measured for CGCG 269-049. They find that inefficient star formation among low-mass galaxies, rather than galaxy age or metal loss from supernova ejecta, is the main cause of the relation (but see Davé et al. 2006 and Calura et al. 2007 for arguments regarding the importance of supernova ejecta). The results for CGCG 269-049 support this model, because in addition to an old population of stars we find no strong evidence for current or past outflows, and the galaxy also has a high ratio of H I mass to stellar mass ($\sim$1; Begum et al. 2005), indicative of an inefficient conversion of gas to stars. The Brooks et al. (2007) model of inefficient star formation is also supported by the finding of Kannappan (2004) that galaxy stellar mass and the ratio of H I mass to stellar mass are inversely correlated over several decades in both quantities. Specifically, this correlation would lead to low O/H gas abundance ratios in dwarf galaxies because of their higher relative H I content. Using the mass values from Begum et al. (2005), CGCG 269-049 falls roughly on the Kannappan (2004) correlation, as well as the galaxy mass / metallicity correlation of Tremonti et al. (2004) as calibrated by Brooks et al. (2007).

While the present data do not offer a simple picture of CGCG 269-049's star-formation history, the dominance of old stars in it supports models of the formation of isolated dwarf galaxies in which the photo-evaporation of baryons

from their dark matter halos at the epoch of reionization strongly lowers their star formation rates, leading to galaxies at the present epoch comprised mainly of $\sim$10 Gyr old stars with some residual star formation (Hoeft et al. 2006; Wyithe & Loeb 2006).

Table 4.1: CGCG 269-049 Spitzer Space Telescope and MIPS Fluxes

Wavelength(μm)	Detector	f_ν(mJy)
3.6	IRAC	1.14 $\pm$ 0.05
4.5	IRAC	0.76 $\pm$ 0.05
5.8	IRAC	0.50 $\pm$ 0.05
8.0	IRAC	0.41 $\pm$ 0.05
24	MIPS	0.33 $\pm$ 0.03
70	MIPS	2.03 $\pm$ 0.03

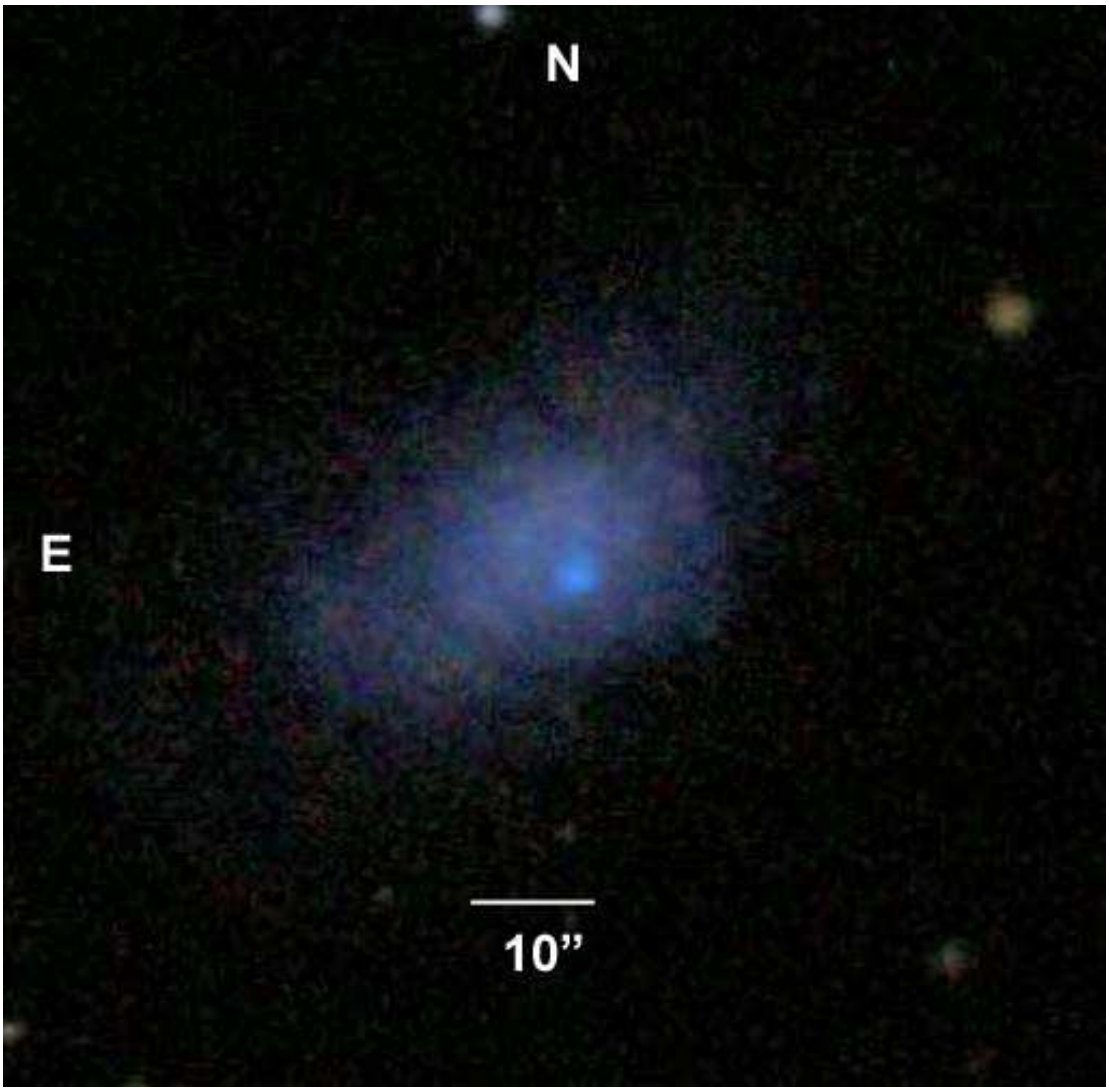

Figure 4.1: Optical image of CGCG 269-049 from the Sloan Digital Sky Survey, representing a composite of images in the SDSS g, r, and i bands. The integrated Petrosian g magnitude of the galaxy is 15.75 (Kniazev et al. 2003).

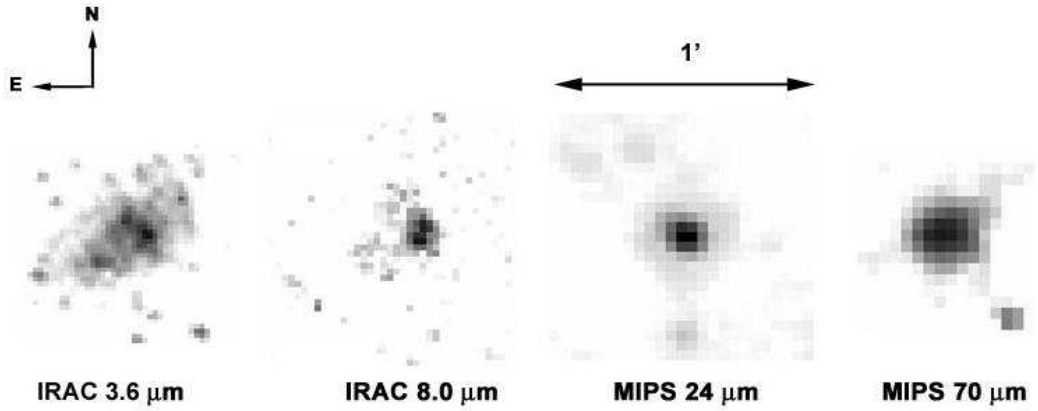

Figure 4.2: Spitzer Space Telescope IRAC and MIPS images of CGCG 269-049. The galaxy is also detected in the IRAC 4.5 μm and 5.8 μm bands, with an appearance intermediate between that in the 3.6 μm and 8.0 μm bands.

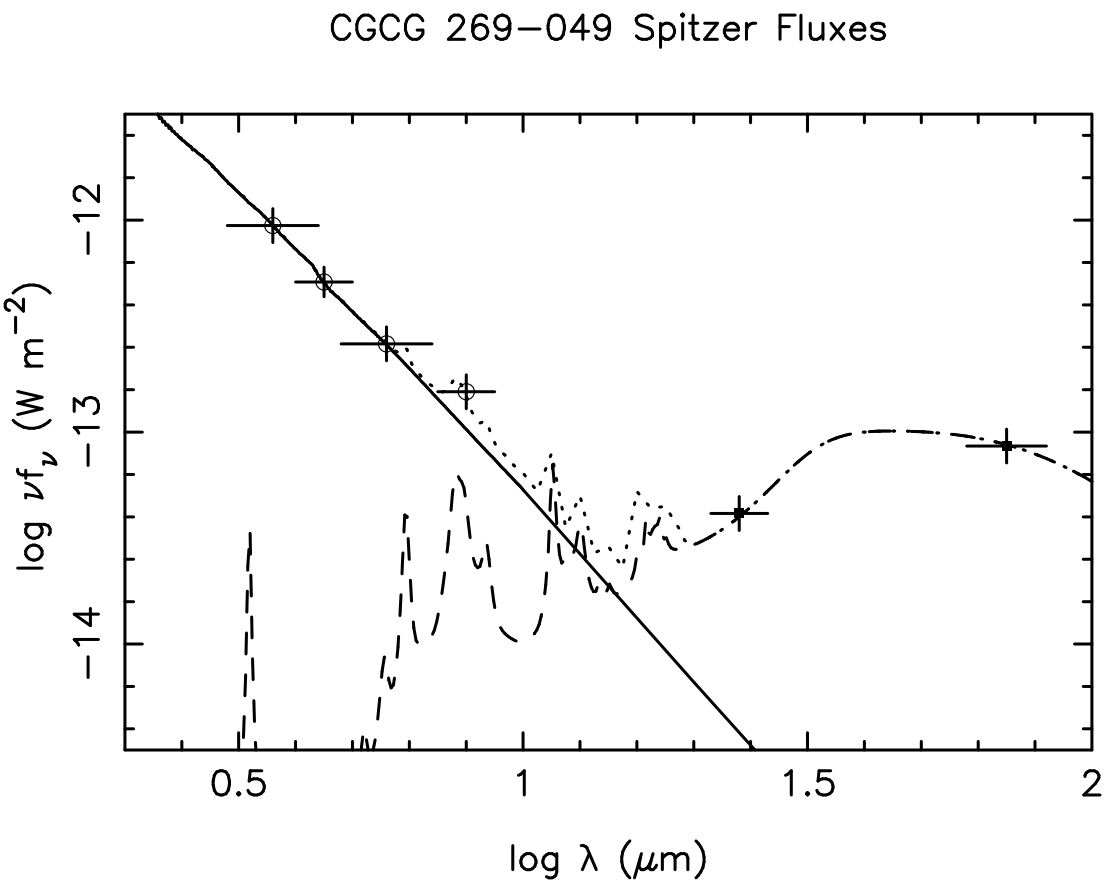

Figure 4.3: Infrared spectral energy distribution of CGCG 269-049 from the Spitzer IRAC and MIPS fluxes, shown with open circles and solid squares, respectively. The solid line is a Bruzual & Charlot (2003) population synthesis model for an instantaneous burst evolved to an age of 10 Gyr, a Chabrier initial mass function, and a metallicity of 0.02 $Z_{\odot}$. The dashed line is a Draine & Li (2007) thermal dust model for a Large Magellanic Cloud dust composition and a range in the parameter U = 5 – 10^4, where U represents the intensity of the radiation field incident on the dust in units of the ambient radiation field in the solar neighborhood. The dotted line is the sum of the two models.

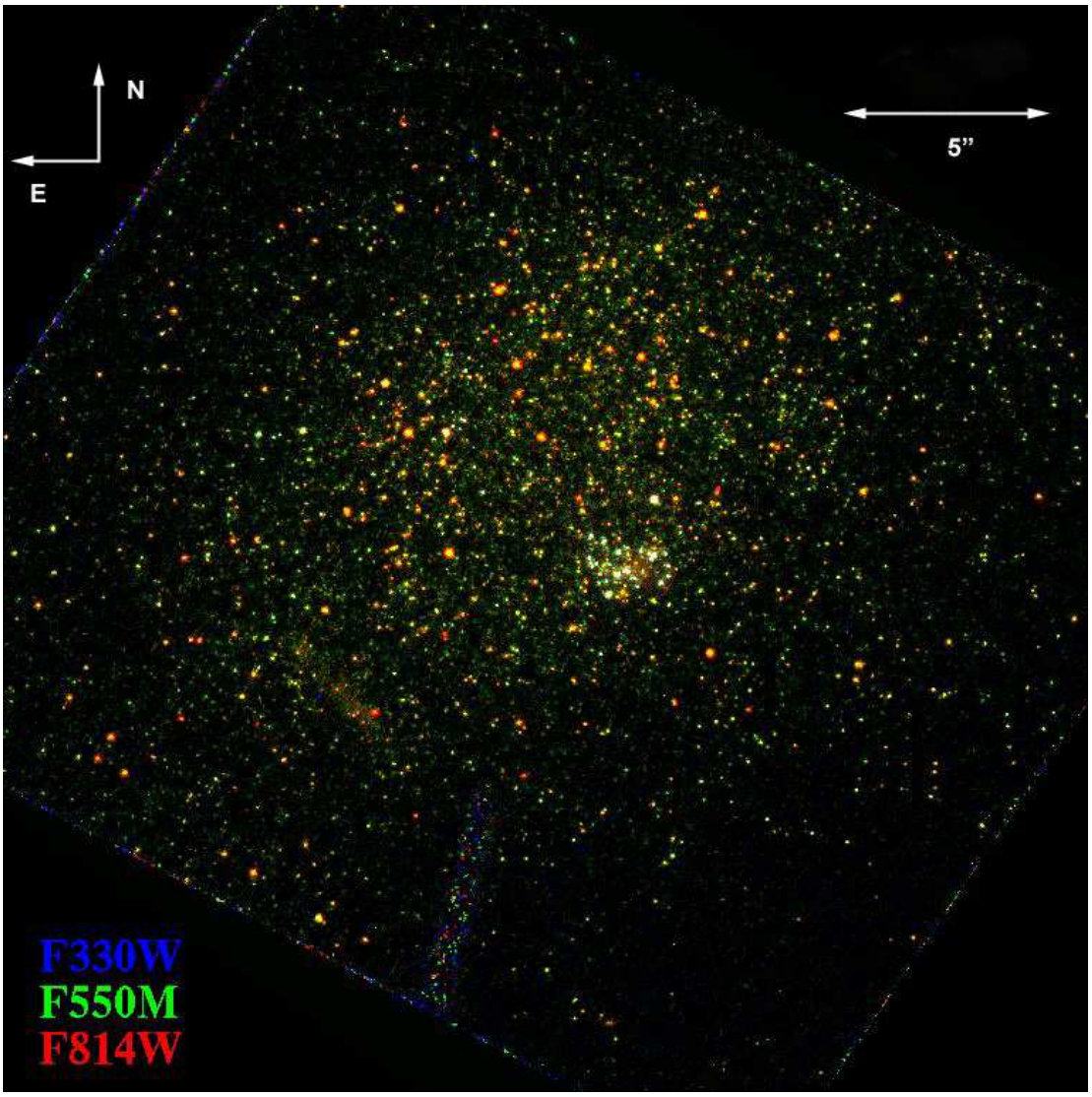

Figure 4.4: Color composite of the HST Advanced Camera for Surveys / High Resolution Channel F330W, F550M, and F814W images of CGCG 269-049. The feature at the bottom of the image is the “coronagraphic finger” of the ACS/HRC.

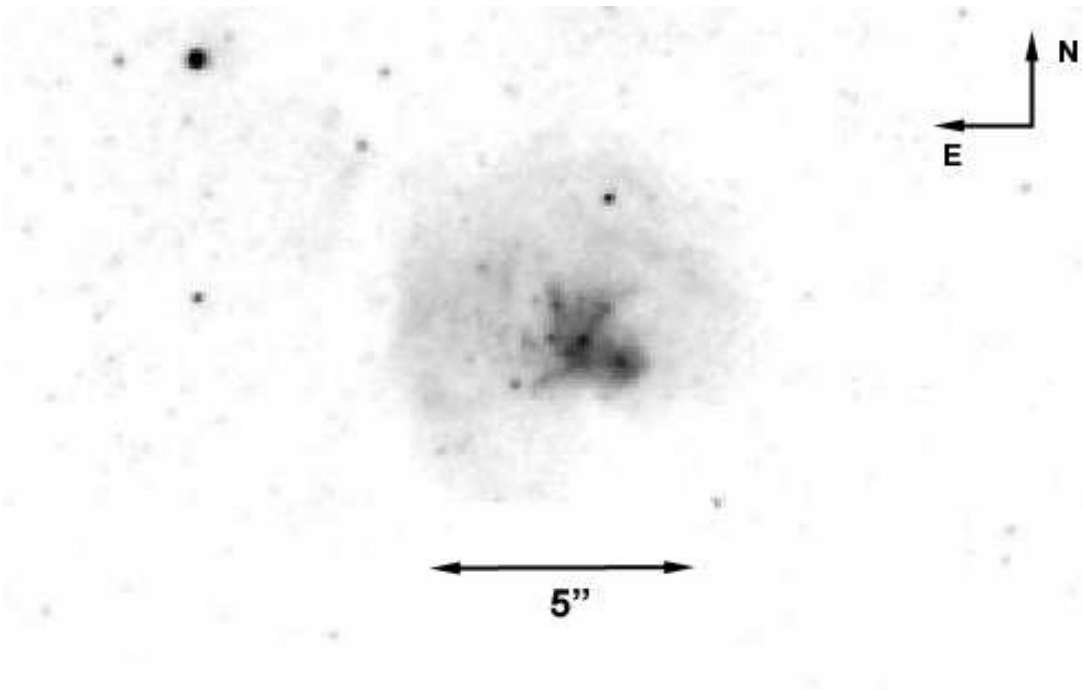

Figure 4.5: Hα image of CGCG 269-049 obtained in the F658N filter of the Advanced Camera for Surveys / High Resolution Channel. The image is centered on the Central Cluster (see Figures 1 and 4).

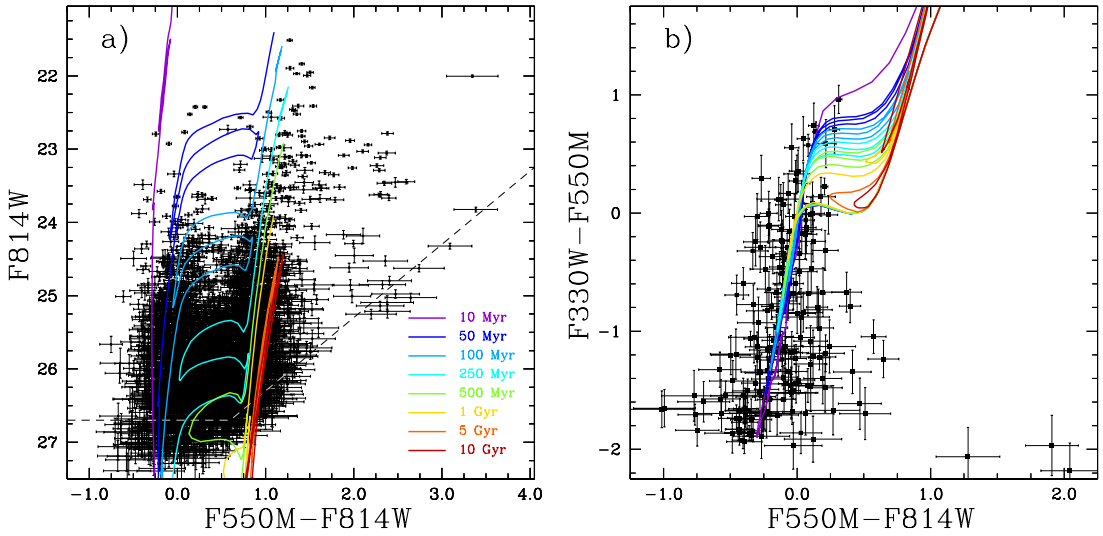

Figure 4.6: (a) Color-magnitude diagram of CGCG 269-049 from the photometry of the F550M and F814W images. Magnitudes are on a Vega scale. Padua isochrones for these filters and for a metallicity of Z = 0.0004 are plotted (see text for details). The dashed line represents the 50% completeness level. (b) Color-color diagram for the stars detected in the F330W, F550M, and F814W filters, with the same isochrones as in 6(a). The roughly linear portions of the isochrones on this plot correspond to the blue horizonal branch loops on 6(a).

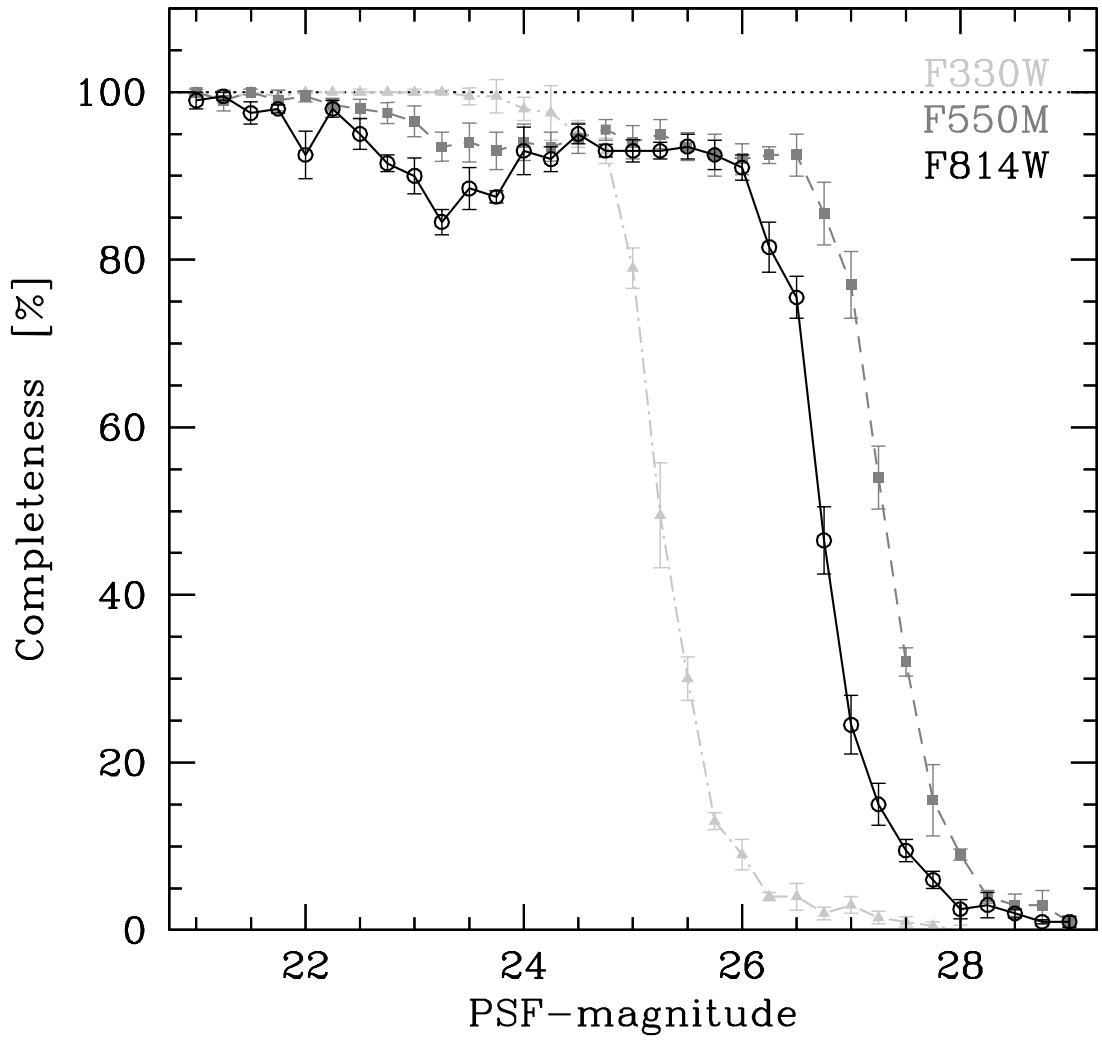

Figure 4.7: Completeness of stellar photometry as a function of magnitude for each of the three filters used, as determined by inserting artificial stars into the images (see text for details). The error bars represent the variance between different simulations, where stars were inserted at different positions in the images.

Chapter 5

CONCLUSION

5.1 Summary of Current Work

I have analyzed CMDs and color-color diagrams of resolved stars in three nearby star-forming galaxies: M83, NGC 4214, and CGCG 269-049. The data used in this project are all based on multi-band *HST* ACS and WFC3 observations ranging from ∼2100Å (F225W) to 8800Å (F814W) in wavelength. The CMDs of these three galaxies show the presence of multiple stellar features, including main-sequence stars, He-burning blue-loop stars, and shell-burning red and blue giant stars. These multi-population features make the study of stellar populations in nearby galaxies more challenging but interesting. By comparing our observations to stellar model isochrones we are able to estimate ages, masses, and other physical properties of stars. I have listed the primary new results from this study in the following.

From the study of nearby star-bursting galaxy M83,

(1) we have developed an innovative new technique to correct the internal extinction for the individual stars and estimate their ages and masses, using a combination of CMD and color–color diagrams.

(2) The various age indicators (stellar, integrated light, clusters within the region) are compared and shown fair correlations between them. A comparison with previous age estimates by Larsen et al. (2011) also shows a good agreement.

(3) We have compared the stellar ages to other parameters that are known to correlate with the age. Those correlations show a range from very good (e.g., with red-to-blue star ratios) and fair (e.g., Hα morphology) to little or no correlation (e.g., pixel-to-pixel surface brightness fluctuation).

(4) The distribution map of stars with ages younger than 10 Myr shows that young stars are generally located along the active star-forming regions in the spiral arm and also more clustered. The intermediate age stars tend to be found "downstream" (i.e., on the opposite side from the dust lane) of the spiral arms.

(5) We also used the locations of Wolf–Rayet sources to test the correlation with the stellar ages and found a broad agreement between them.

(6) The unprecedented spatial resolution of the *HST* observations allows us to carry out this project and hence it is important to test the effects of spatial resolution on the measure colors, magnitudes, and the derived ages of individual stars in M83. Based on a numerical experiment using a star cluster image of NGC 2108 in the LMC, we found that while individual stars can show measurable differences in the colors and magnitudes, the age estimate for each region is only slightly affected.

From the study of nearby irregular galaxy NGC 4214,

(1) The star-by-star extinction correction methods developed in the previous study (Kim et al. 2012) are applied to NGC 4214, showing the significant amount of internal extinctions in $UBVI$ photometric system. The mean extinction values of this galaxy are $A_{F336W} = 0.660$, $A_{F438W} = 0.530$, $A_{F547M} = 0.402$, $A_{F814W} = 0.243$ mag, respectively.

(2) We develop a new age-dating technique using the individual stellar SED fitting in order to estimate the ages and masses of stars with the five-band photometry. This method is relatively more sensitive to the luminous stars in NUV.

(3) The WFC3 field of NGC 4214 is divided into the 38 adaptive grid boxes in order to compare our stellar ages from the CMD and SED fitting to other age

indicators. In this paper we show the positive correlation between stellar ages and the number ratio of red-to-blue stars.

(4) The age distributions determined from both CMD and SED age-dating methods show that the youngest group of stars is generally located along the active star-forming regions in the central bar area. This supports the model distributions of star clusters in spiral and barred galaxies by Dobbs & Pringle (2010).

From the study of the extremely metal-poor dwarf galaxy CGCG 269-049,

(1) the presence of AGB and RGB stars in CGCG 269-049 revealed by our *HST* ACS data rules out the possibility that this galaxy is a newly-formed galaxy and other XMPGs are in general.

(2) While the mean stellar ages of star-forming dwarf galaxies are possibly skewed to lower values than the quiescent dwarfs, recent studies of XMPGs in the Local Group have shown to consist mainly of evolved stars.

(3) The mid-infrared SED of CGCG 269-049 shows strong evidence of significant PAH emission. This agrees with that the strength of PAH features in the star-forming dwarf galaxies depends more on star-formation rate than their metallicity.

(4) The results for CGCG 269-049 support the model of inefficient star formation among low-mass galaxies by its high ratio of HI mass to stellar mass.

To conclude, deep *HST* observations of the resolved stellar populations in three nearby galaxies M83, NGC 4214, and CGCG 269-049 allow us to construct the CMD and color-color diagram and determine ages, masses, and other properties of individual stars. We are able to reconstruct the history of star formation, and evolution and disruption of star clusters in these galaxies from various independent age-dating methods.

5.2 Future Work

The cycle 19 *HST* program (ID:12513, PI: Blair) with the WFC3 will add five more fields in M83 to the existing ERS data with observations in five broadband (F336W, F438W, F547M, F814W, F160W) and four narrowband (F502N, F657N, F673N, F164N) filters. These additional data will allow us to expand our analysis on the resolved stellar populations to the entire field in M83 and provide the most detailed multiwavelength study of individual stars in the starforming spiral galaxy. I will apply the age-dating method developed in this study to the future observations and compare the stellar populations in the active star-forming regions in the central field to those in the outer disk of the galaxy. Bastian et al. (2011) searched for the evidence of environmentally dependent cluster disruption scenario using two fields (inner and outer regions) of M83 and claimed that a large fraction of stars clusters in the outer field are older by tens of Myr than in the inner field. I will directly compare the properties of resolved field populations to their results from the study of stars clusters. The comparison between these two studies with the additional observations will provide a more complete picture of how clusters form and then dissolve into the field in M83.

In addition to the future study with the new WFC3 datasets, I will investigate the variation of the initial mass functions (IMFs) in the 50 selected regions of M83. I have measured the mass of individual stars in M83 in this study and showed the mass distribution of each region in the right column of Figure 2.8 and the bottom right figures in the Appendix. The mass histogram of each region shows different distribution from the mass histogram of all stars in the bottom right panel of Figure 2.4. These results can be useful to study the stellar IMF in the different environment and compare to the universal IMF.

Aloisi, A., van der Marel, R.P., Mack, J., Leitherer, C., Sirianni, M., & Tosi, M. 2005, ApJ, 631, L45

Aloisi, A. et al. 2007, ApJ, 667, 151

Asari, N.V., Cid Fernandes, R., Stasínska, G., Torres-Papaqui, J.P., Mateus, A., Sodré Jr., L., Schoenell, W., & Gomes, J.M. 2007, MNRAS, 381, 263

Barmby, P. et al. 2006, ApJ, 650, L45

Bastian, N., Adamo, A., Gieles, M., et al. 2011, MNRAS, 417, L6

Begum, A., Chengalur, J.N., Karachentsev, I.D., Kaisin, S.S., & Sharina, M.E. 2005, MNRAS, 365, 1220

Bertelli, G., Mateo, M., Chiosi, C., & Bressan, A. 1992 ApJ, 388, 400

Bertelli, G., Bressan, A., Chiosi, C., Fagotto, F., & Nasi, E. 1994 A&AS, 106, 275

Bresolin, F., & Kennicutt, R. C. 2002, ApJ, 572, 838

Brooks, A.M., Governato, F., Booth, C.M., Willman, B., Gardner, J.P., Wadsley, J., Stinson, G., & Quinn, T. 2007, ApJ, 655, L17

Bruzual, G., & Charlot, S. 2003, MNRAS, 344, 1000

Calura, F., Jimenez, R., Panter, B., Matteucci, F., & Heavens, A.F. 2008, ApJ, 682, 252

Calzetti, D. et al 2007, ApJ, 666, 870

Cananzi, K. 1992, A&A, 259, 17

Cannon, J.M. et al. 2006, ApJ, 652, 1170

Cardelli, J. A., Clayton, G. C., & Mathis, J. S. 1989, AJ, 345, 245

Chandar, R., Whitmore, B. C., Kim, H., Kaleida, C., Mutchler, M., Calzetti, D., Saha, A., O'Connell, R., Balick, B., Bond, H., Carollo, M., Disney, M., Dopita, M. A., Frogel, J. A., Hall, D., Holtzman, J. A., Kimble, R. A., McCarthy, P., Paresce, F., Silk, J., Trauger, J., Walker, A. R., Windhorst, R. A., Young, E. 2010, ApJ, 719, 966

Corbin, M.R., Vacca, W.D., Cid Fernandes, R., Hibbard, J.E., Somerville, R.S., & Windhorst, R.A. 2006, ApJ, 651, 861

Corbin, M. R., Kim, H., Jansen, R. A., Windhorst, R. A., & Fernandes, R. C. 2008a, ApJ 675, 194

Corbin, M. R., Kim, H., Jansen, R. A., Windhorst, R. A., & Fernandes, R. C. 2008b, ApJ 678, 567

Crowther, P. A. 2007, ARA&A, 45, 177

Da Costa, G.S. & Armandroff, T.E. 1990, AJ, 100, 162

Da Costa, G.S. 1991, in *TheMagellanicClouds*, R. Haynes & D. Milnes, Dordrecht: Kluwer, 183

Dalcanton, J. J., Williams, B. F., Seth, A. C., et al. 2009, ApJS, 183, 67

Dalcanton, J. J., Williams, B. F., Lang, D., et al. 2012, ApJS, 200, 18

Davé, R., Finlator, K., & Oppenheimer, B.D. 2006, in EAS Pub. Ser. 24, Chemodynamics: From First Stars to Local Galaxies, ed. E. Emsellem et al.(Les Ulis: EDP Sciences), 183

De Marchi, G., Paresce, F., Panagia, N., et al. 2011, ApJ, 739, 27

de Vaucouleurs, G., de Vaucouleurs, A., Corwin, H. G., Buta, R. J., Paturel, G., & Fouque, P. 1991, Third Reference Catalogue of Bright Galaxies, Vols. 1–3 (Berlin: Springer)

Dobbs, C. L., & Pringle, J. E. 2010, MNRAS, 409, 396

Dolphin, A. E. 1997, New Astron., 2, 397

Dolphin, A. E. 2002, MNRAS, 332, 91

Dopita, M. A., Blair, W. P., Ling, K. S., et al. 2010, ApJ, 710, 964

Dopita, M. A., Calzetti, D., Apellaniz, J. M., et al. 2010, Ap&SS, 330, 123

Draine, B.T., & Li, A. 2007, ApJ, 657, 810

Drozdovsky, I. O., Schulte-Ladbeck, R. E., Hopp, U., Greggio, L., & Crone, M. M. 2002, AJ, 124, 811

Elson, R. A. W., Gilmore, G. F., & Santiago, B. X. 1997, MNRAS, 289, 157

Freedman, W. L., Madore, B. F., Gibson, D. K., et al. 2001, ApJ, 553, 47

Fruchter, A. S., Sosey, M., et al. 2009, The MultiDrizzole Handbook, STScI, Baltimore, Version 3.0

Fruchter, A. S., & Hook, R. N. 2002, Publ. Astron. Soc. Pac. 114, 144

Gallagher, J. S., Mould, J. R., de Feijter, E., et al. 1996, ApJ, 466, 732

Geha, M. C., Holtzman, J. A., Mould, J. R., et al. 1998, AJ, 115, 1045

Girardi, L., Bertelli, G., Bressan, A., Chiosi, C., Groenewegan, M.A.T., Marigo, P., Salasnich, B., & Weiss, A. 2002, A&A, 391, 195

Girardi, L., Dalcanton, J., Williams, B. F., et al. 2008, PASP, 120, 583

Girardi, L., Williams, B. F., Gilbert, K. M., et al. 2010, ApJ, 724, 1030

Gordon, K.D., Clayton, G.C., Misselt, K.A., Landolt, A.U., & Wolff, M.J. 2003, ApJ, 594, 279

Goudfrooij, P., Puzia, T. H., Kozhuria-Platais, V., & Chandar, R. 2011, ApJ, 737, 3

Hadfield, L. J., Crowther, P. A., Schild, H., & Schmutz, W. 2005, A&A, 439, 265

Harris, J., Calzetti, D., Galagher, J. S., Conselice, C. J., & Smith, D. A. 2001, AJ, 122, 3046

Hinz, J.L., Misselt, K., Rieke, M.J., Rieke, G.H., Smith, P.S., Blaylock, M. & Gordon, K.D. 2006, AJ, 651, 874

Hirashita, H., Tajiri, Y.Y., & Kamaya, H. 2002, A&A, 388, 439

Hoeft, M., Yepes, G., Gottlöber, S., & Springel, V. 2006, MNRAS, 371, 29

Hodge, P. W. 1979, AJ, 84, 744

Houck, J.R. et al. 2004, ApJS, 154, 211

Hubble, E. P. 1929, ApJ, 69, 103

Hunter, D. A., & Gallagher, J. S. 1986, PASP, 98, 5

Izotov, Y.I., Thuan, T.X., & Guseva, N.G. 2005, ApJ, 632, 210

Izotov, Y.I. & Thuan, T.X. 2004, ApJ, 616, 768

Izotov, Y.I., StasM-mska, G., Meynet, G., Guseva, N.G., Thuan, T.X. 2006, ApJ, 448, 955

Izotov, Y.I. & Thuan, T.X. 2007, 665, 1115

Jackson, D.C., Cannon, J.M., Skillman, E.D., Lee, H., Gehrz, R.D., Woodward, C.E., & Polomski, E. 2006, ApJ, 646, 192

Kannappan, S.J. 2004, ApJ, 611, L89

Karachentsev, I. D., Karachentseva, V. E., Huchtmeier, W. K., & Makarov, D. I. 2004, AJ, 127, 2031

Karachentsev, I. D., Tully, R. B., Dolphin, A., et al. 2007, AJ, 133, 504

Keeney, B.A., Stocke, J.T., Rosenberg, J.L., Tumlinson, J., & York, D.G. 2006, AJ, 132, 2496

Kim, H., Whitmore, B. C., Chandar, R., Saha, A., Kaleida, C. C., Mutchler, M., Cohen, S. H., Calzetti, D., O'Connell, R., Windhorst, R. A., Balick, B., Bond, H. E., Carollo, M., Disney, M. J., Dopita, M. A., Frogel, J. A., Hall, D. N. B., Holtzman, J. A., Kimble, R. A., McCarthy, P. J., Paresce, F., Silk, J. I., Trauger, J. T., Walker, A. R., Young, E. T. 2012, ApJ, 753, 26

Koekemoer, A. M., Fruchter, A. S., Hook, R. N., & Hack, W. 2002, in The 2002 *HST* Calibration Workshop: Hubble after the Installation of the ACS and the NICMOS Cooling System, ed. S. Arribas, A. Koekemoer, & B. Whitmore (Baltimore, MD: STScI), 337

Kniazev, A.Y., Grebel, E.K., Hao, L., Strauss, M.A., Brinkmann, J., & Fukugita, M. 2003, ApJ, 593, L73

Kobulnicky, H. A., & Skillman, E. D. 1996, ApJ, 471, 211

Kunth, D. & Östlin, G. 2000, A&A Rev., 10, 1

——————— 2007, in IAU Symp. 235, Galaxy Evolution Across the Hubble Time, ed F. Combes & J. Palous (Cambridge: Cambridge Univ. Press), 61

Lada, C. J., & Lada, E. A. 2003, ARA&A, 41, 57

Larsen, S. S. 2004, A&A, 416, 537

Larsen, S. S., de Mink, S. E., Eldridge, J. J., et al. 2011, A&A, 532, A147

Lee, H., Skillman, E.D., Cannon, J.M., Jackson, D.C., Gehrz, R.D., Polomski, E.F., & Woodward, C.E. 2006, ApJ, 647, 970

MacKenty, J. W., Maíz-Apellániz, J., Pickens, C. E., Norman, C. A., & Walborn, N. R. 2000, AJ, 120, 3007

Maíz-Apellániz, J., Cieza, L., & MacKenty, J. W. 2002, AJ, 123, 1307

Marigo, P., Girardi, L., Bressan, A., et al. 2008, A&A, 482, 883

Massey, P., Armandroff, T. E., & Conti, P. S. 1986. AJ, 92, 1303

Mass-Hesse, J. M., & Kunth, D. 1999, A&A, 349, 765

Mighell, K. J. 1995, AJ, 110, 1649

Mighell, K. J., Rich, R. M., Shara, M., & Fall, S. M. 1996, AJ, 111, 2314

Mihalas, D., & Binney, J. 1981, Galactic Astronomy (San Francisco, CA: Freeman), 187

Miller, G.E., & Scalo, J.M. 1979, ApJS, 41, 513

Momany, Y. et al. 2005, A&A, 439, 111

Morgan, H.L. & Edmunds, M.G. 2003, MNRAS, 343, 427

Östlin, G. & Mouhcine, M. 2005, A&A, 433, 797

Pellerin, A., Meyer, M., Harris, J., & Calzetti, D. 2007, ApJ, 658, L87

Pustilnik, S.A., & Martin, J.M. 2007, A&A, 464, 859

Rich, R. M., Mighell, K., Freedman, W. L., & Neill, J. D. 1996, AJ, 111, 768

Rosenberg, J., Ashby, M. L. N., Salzer, J.J., & Huang, J.S. 2006, ApJ, 636, 742

Saha, A., Thim, F., Tammann, G. A., Reindl, B., & Sandage, A. 2006, ApJS, 165, 108

Saha, A., Olszewski, E. W., Brondel, B., et al. 2010, AJ, 140, 1719

Sandage, A., & Bedke, J. 1985, AJ, 90, 1992

Sargent, W. L. M., & Filippenko, A. V. 1991, AJ., 102, 107

Scalo, J.M. 1986, FCPh, 11, 1

Schechter, P. L., Mateo, M., & Saha, A. 1993, PASP, 105, 1342

Schlegel, D. J., Finkbeiner, D. P., & Davis, M. 1998, ApJ, 500, 525

Schulte-Ladbeck, R.E., Hopp, U., Drozdovsky, I.O., Greggio, L., & Crone, M.M. 2002, AJ, 124, 896

Sirianni, M., Jee, M. J., Benítez, N., et al. 2005, PASP, 117, 1049

Spergel, D.N. et al. 2007, ApJS, 170, 377

Stetson, P. 1987, PASP, 99, 191

Thuan, T.X., Izotov, Y.I., & Lipovetsky, V.A. 1997, ApJ, 477, 661

Tremonti, C. et al. 2004, ApJ, 613, 898

Úbeda, L., Maíz-Apellániz, J., & MacKenty, J. W. 2007a, AJ, 133, 917

Úbeda, L., Maíz-Apellániz, J., & MacKenty, J. W. 2007b, AJ, 133, 932

van den Bergh, S. 1964, ApJS, 9, 65

van den Bergh, S. 1966, AJ, 71, 219

Veilleux, S., Cecil, G., & Bland-Hawthorn, J. 2005, ARA&A, 43, 769

Walsh, S. M., Jerjen, H., & Willman, B. 2007, ApJ, 662, 83

Walter, F., Taylor, C. L., Hüttemeister, S., Scoville, N., & McIntyre, V. 2001, AJ, 121, 727

Weisz, D. R., Skillmas, E. D., Cannon, J. M., Dolphin, A. E., Kennicutt, R. C., Jr., Lee, J., & Walter, F. 2008, ApJ, 689, 160

Whitmore, B. C., Zhang, W., Leitherer, C., et al. 1999, AJ, 118, 1551

Whitmore, B. C., Chandar, R., Kim, H., Kaleida, C., Mutchler, M., Stankiewicz, M., Calzetti, D., Saha, A., O'Connell, R., Balick, B., Bond, H. E., Carollo, M., Disney, M. J., Dopita, M. A., Frogel, J. A., Hall, D. N. B., Holtzman, J. A., Kimble, R. A., McCarthy, P. J., Paresce, F., Silk, J. I., Trauger, J. T., Walker, A. R., Windhorst, R. A., Young, E. T. 2011, ApJ, 729, 78

Whitmore, B. C. & The WFC3 SOC Team 2011b, in ASP Conf. Ser. 440, UP2010: Have Observations Revealed a Variable Upper End of the Initial Mass Function?, ed. M. Treyer, T. K. Wyder, J. D. Neill, M. Seibert, & J. C. Lee (San Francisco, CA: ASP), 161

Williams, B. F., et al. 2009, AJ, 137,419

Williams, B. F., Dalcanton, J. J., Gilbert, K. M., et al. 2011, ApJ, 735, 22

Windhorst, R. A., Cohen, S. H., Hathi, N. P., et al. 2011, ApJS, 193, 27

Wu, H. et al. 2005, ApJ, 632, L79

Wyithe, S.B.J. & Loeb, A. 2006, Nature, 441, 322

Appendix A

ADDITIONAL FIGURES FOR CHAPTER TWO

Here we present the CMDs, color-color diagrams, and the histograms of the age and mass distribution of the rest of 50 selected Regions not included in Chapter 2. Data points before and after the individual extinction correction are plotted as black crosses (top: uncorrected) and blue Xs (middle: corrected). The Padova model isochrones in each diagram are the same as the ones plotted in Figure 2.3.

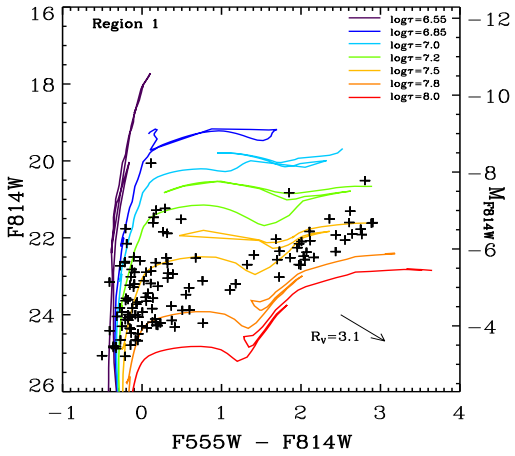
Region 1
logτ=6.55
logτ=6.85
logτ=7.0
logτ=7.2
logτ=7.5
logτ=7.8
logτ=8.0
R_V=3.1
F814W
M_F814W
F555W − F814W

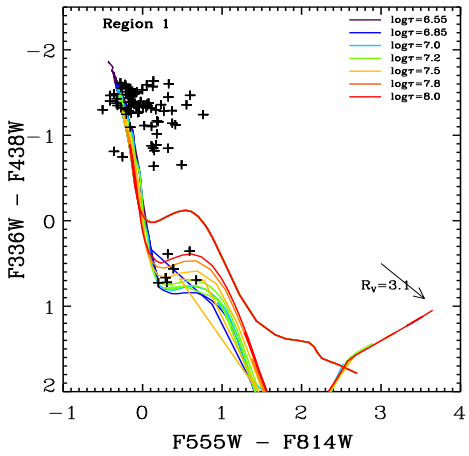
Region 1
logτ=6.55
logτ=6.85
logτ=7.0
logτ=7.2
logτ=7.5
logτ=7.8
logτ=8.0
R_V=3.1
F336W − F438W
F555W − F814W

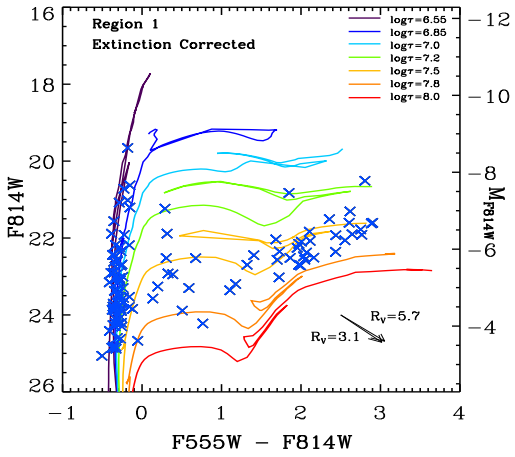
Region 1
Extinction Corrected
logτ=6.55
logτ=6.85
logτ=7.0
logτ=7.2
logτ=7.5
logτ=7.8
logτ=8.0
R_V=5.7
R_V=3.1
F814W
M_F814W
F555W − F814W

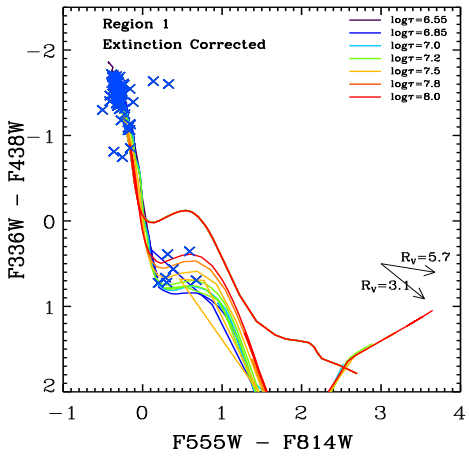
Region 1
Extinction Corrected
logτ=6.55
logτ=6.85
logτ=7.0
logτ=7.2
logτ=7.5
logτ=7.8
logτ=8.0
R_V=5.7
R_V=3.1
F336W − F438W
F555W − F814W

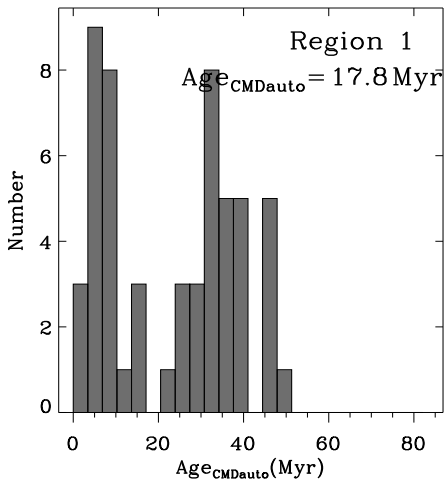
Region 1
Age_CMDauto = 17.8 Myr
Number
Age_CMDauto (Myr)

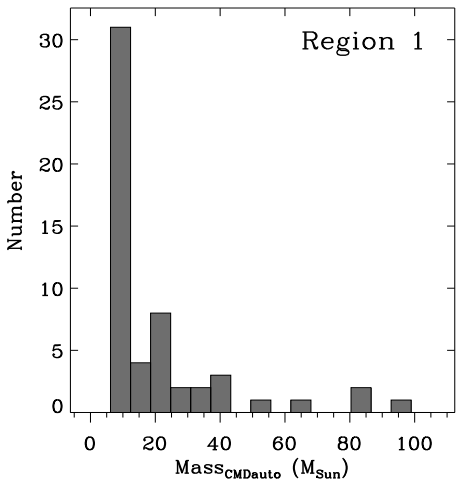
Region 1
Number
Mass_CMDauto (M_Sun)

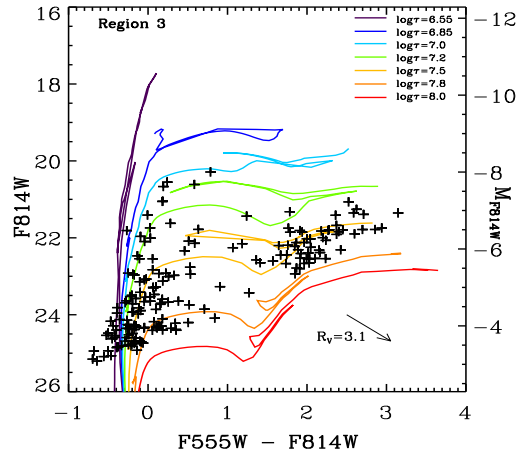
Region 3
logτ=6.55
logτ=6.85
logτ=7.0
logτ=7.2
logτ=7.5
logτ=7.8
logτ=8.0
R_V=3.1
F814W
M_F814W
F555W − F814W

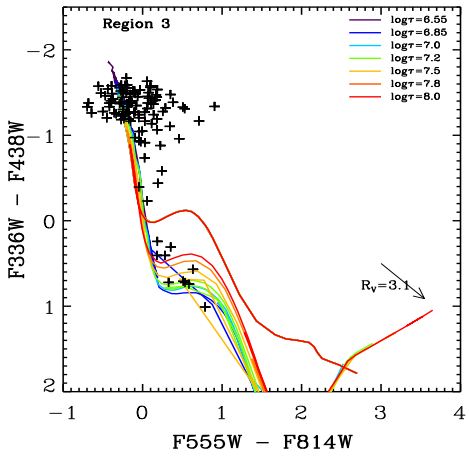
Region 3
logτ=6.55
logτ=6.85
logτ=7.0
logτ=7.2
logτ=7.5
logτ=7.8
logτ=8.0
R_V=3.1
F336W − F438W
F555W − F814W

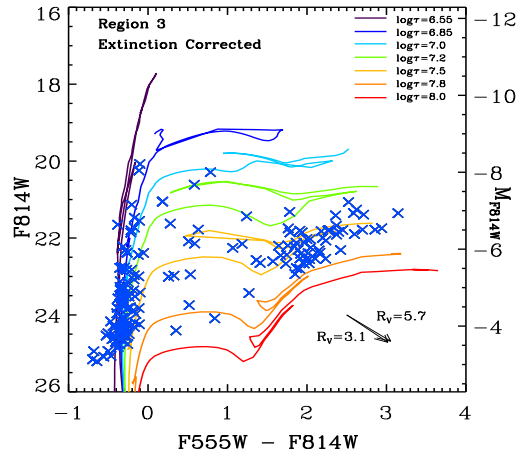
Region 3
Extinction Corrected
logτ=6.55
logτ=6.85
logτ=7.0
logτ=7.2
logτ=7.5
logτ=7.8
logτ=8.0
R_V=5.7
R_V=3.1
F814W
M_F814W
F555W − F814W

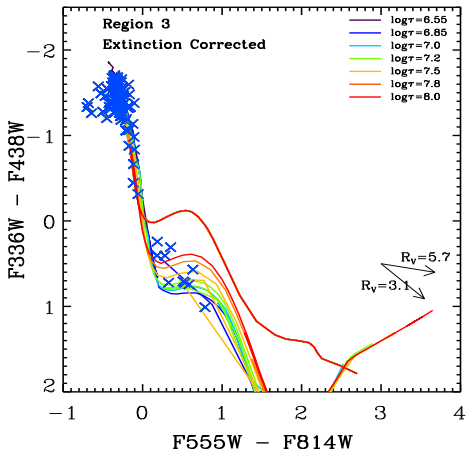
Region 3
Extinction Corrected
logτ=6.55
logτ=6.85
logτ=7.0
logτ=7.2
logτ=7.5
logτ=7.8
logτ=8.0
R_V=5.7
R_V=3.1
F336W − F438W
F555W − F814W

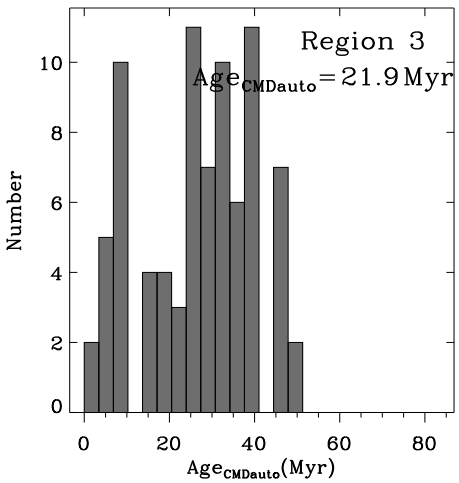
Region 3
Age_CMDauto=21.9Myr
Number
Age_CMDauto(Myr)

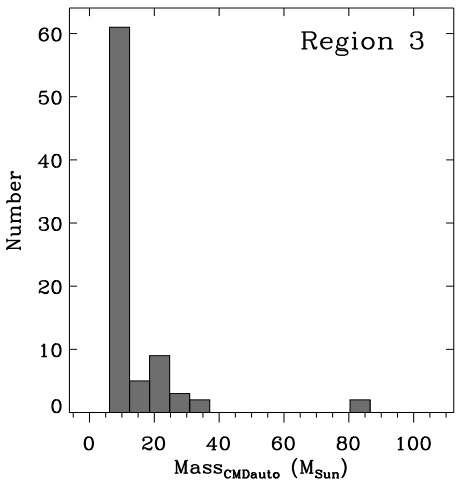
Region 3
Number
Mass_CMDauto (M_Sun)

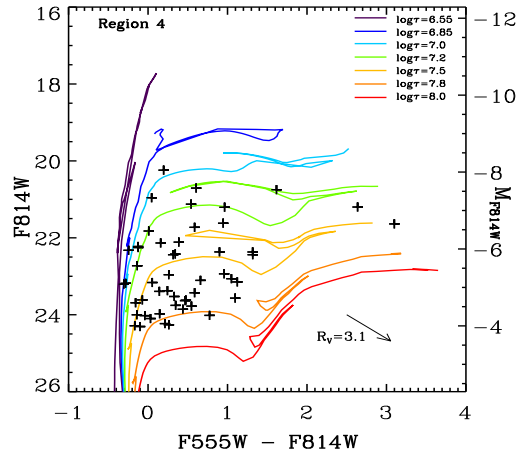
Region 4
logτ=6.55
logτ=6.85
logτ=7.0
logτ=7.2
logτ=7.5
logτ=7.8
logτ=8.0
R_V=3.1
F814W
M_F814W
F555W − F814W

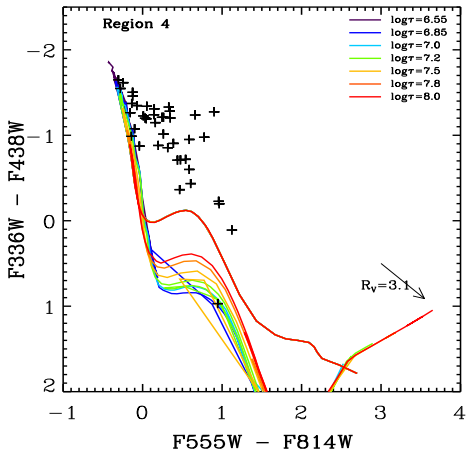
Region 4
logτ=6.55
logτ=6.85
logτ=7.0
logτ=7.2
logτ=7.5
logτ=7.8
logτ=8.0
R_V=3.1
F336W − F438W
F555W − F814W

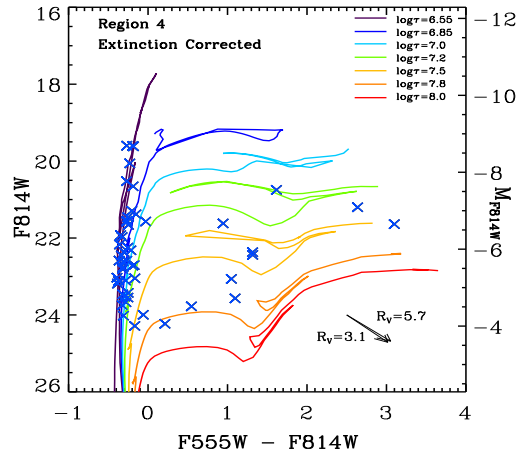
Region 4
Extinction Corrected
logτ=6.55
logτ=6.85
logτ=7.0
logτ=7.2
logτ=7.5
logτ=7.8
logτ=8.0
R_V=5.7
R_V=3.1
F814W
M_F814W
F555W − F814W

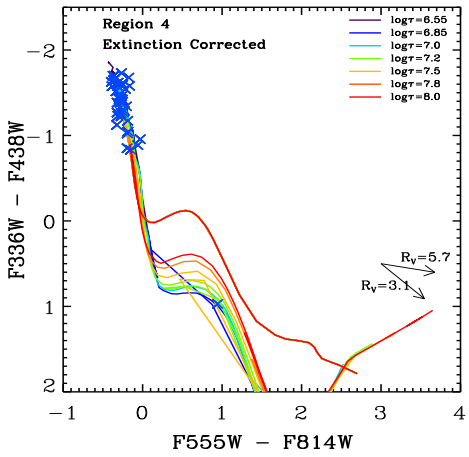
Region 4
Extinction Corrected
logτ=6.55
logτ=6.85
logτ=7.0
logτ=7.2
logτ=7.5
logτ=7.8
logτ=8.0
R_V=5.7
R_V=3.1
F336W − F438W
F555W − F814W

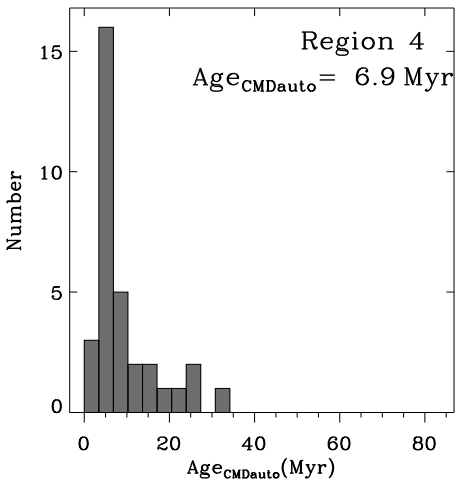
Region 4
Age_CMDauto= 6.9 Myr
Number
Age_CMDauto(Myr)

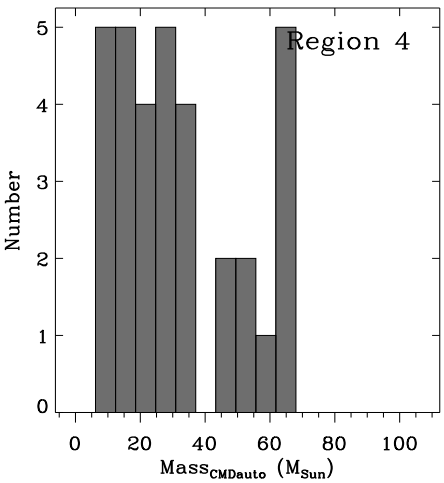
Region 4
Number
Mass_CMDauto (M_Sun)

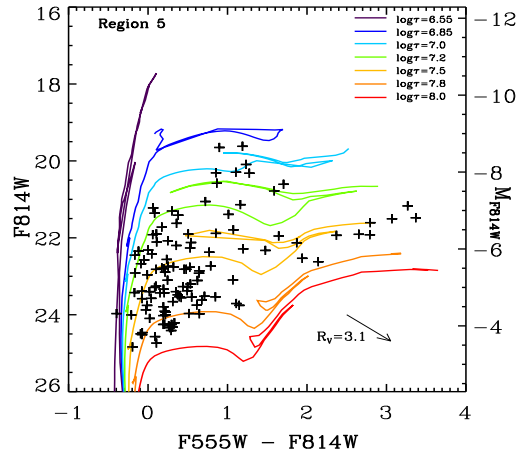
Region 5
logτ=6.55
logτ=6.85
logτ=7.0
logτ=7.2
logτ=7.5
logτ=7.8
logτ=8.0
Rv=3.1
F814W
M F814W
F555W − F814W

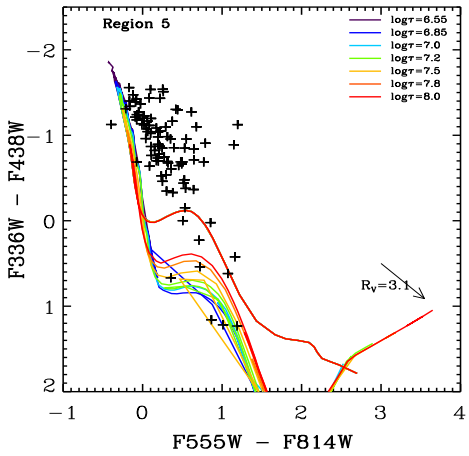
Region 5
logτ=6.55
logτ=6.85
logτ=7.0
logτ=7.2
logτ=7.5
logτ=7.8
logτ=8.0
Rv=3.1
F336W − F438W
F555W − F814W

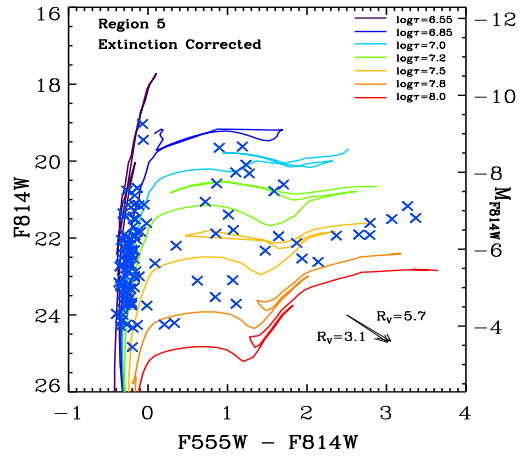
Region 5
Extinction Corrected
logτ=6.55
logτ=6.85
logτ=7.0
logτ=7.2
logτ=7.5
logτ=7.8
logτ=8.0
Rv=5.7
Rv=3.1
F814W
M F814W
F555W − F814W

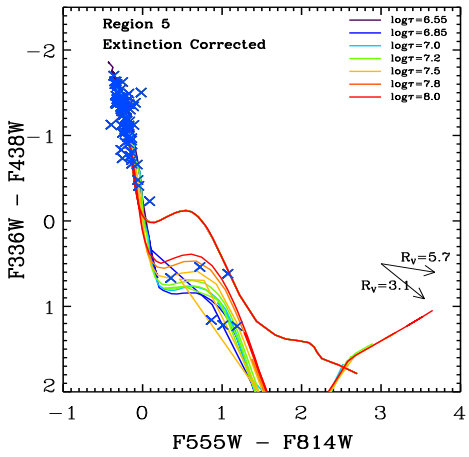
Region 5
Extinction Corrected
logτ=6.55
logτ=6.85
logτ=7.0
logτ=7.2
logτ=7.5
logτ=7.8
logτ=8.0
Rv=5.7
Rv=3.1
F336W − F438W
F555W − F814W

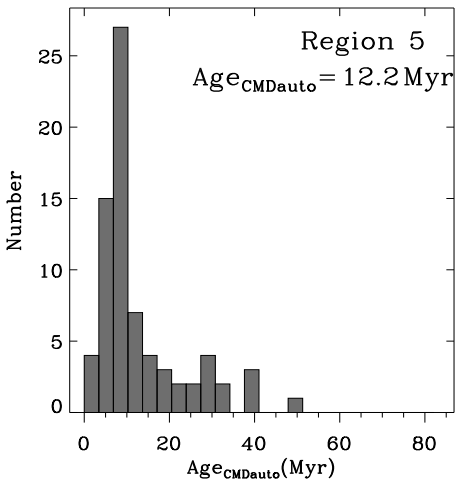
Region 5
Age CMDauto = 12.2 Myr
Number
Age CMDauto (Myr)

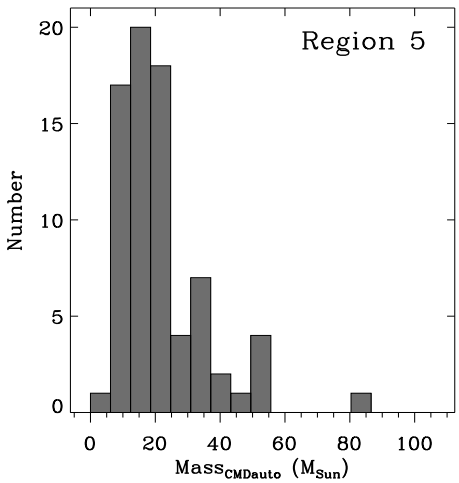
Region 5
Number
Mass CMDauto (M Sun)

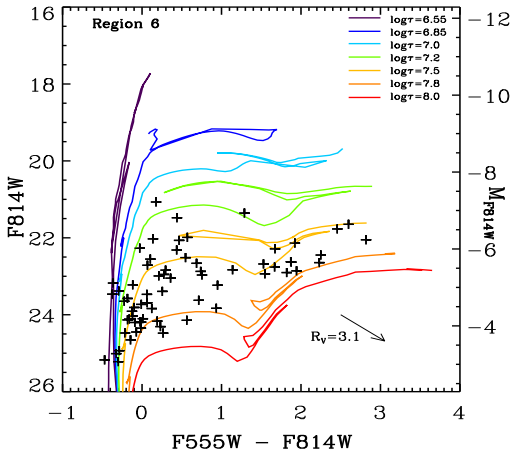
Region 6
logτ=6.55
logτ=6.85
logτ=7.0
logτ=7.2
logτ=7.5
logτ=7.8
logτ=8.0
R_V=3.1
F814W
M_F814W
F555W − F814W

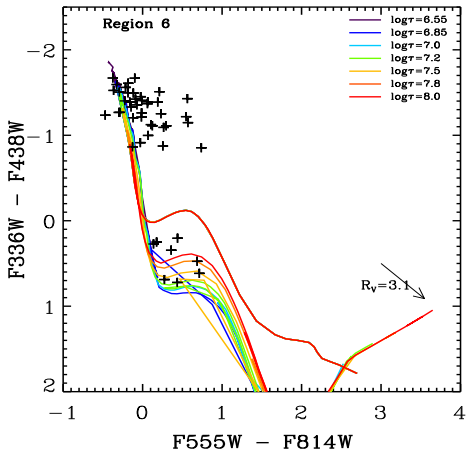
Region 6
logτ=6.55
logτ=6.85
logτ=7.0
logτ=7.2
logτ=7.5
logτ=7.8
logτ=8.0
R_V=3.1
F336W − F438W
F555W − F814W

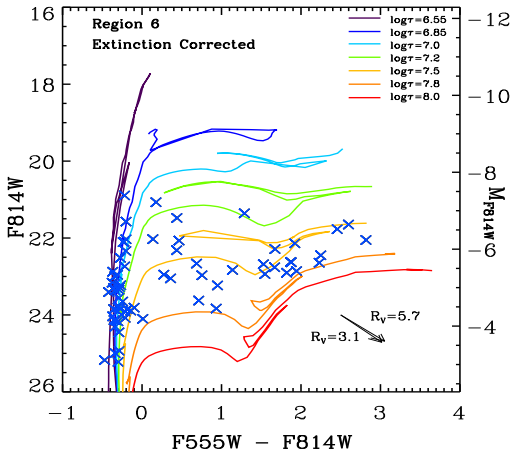
Region 6
Extinction Corrected
logτ=6.55
logτ=6.85
logτ=7.0
logτ=7.2
logτ=7.5
logτ=7.8
logτ=8.0
R_V=5.7
R_V=3.1
F814W
M_F814W
F555W − F814W

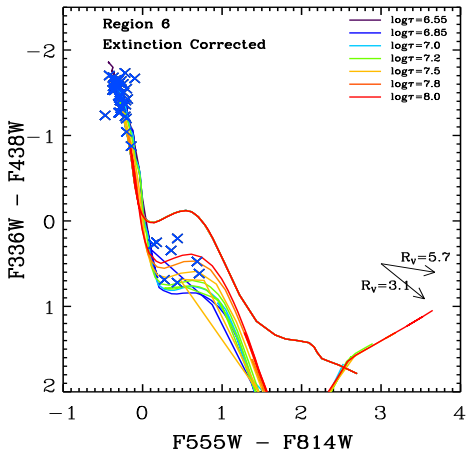
Region 6
Extinction Corrected
logτ=6.55
logτ=6.85
logτ=7.0
logτ=7.2
logτ=7.5
logτ=7.8
logτ=8.0
R_V=5.7
R_V=3.1
F336W − F438W
F555W − F814W

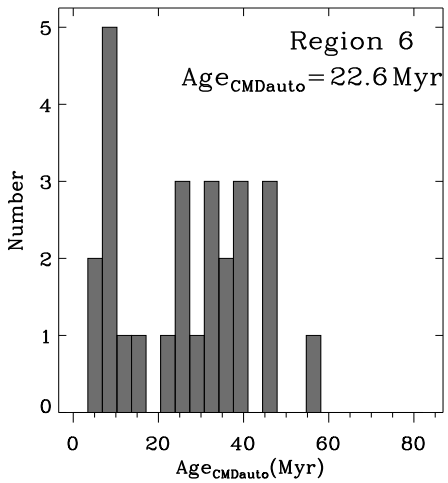
Region 6
Age_CMDauto=22.6 Myr
Number
Age_CMDauto(Myr)

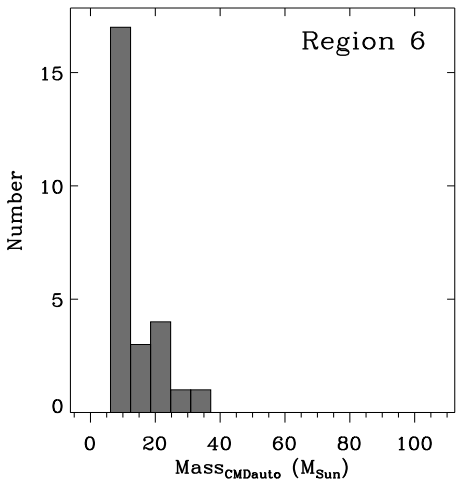
Region 6
Number
Mass_CMDauto (M_Sun)

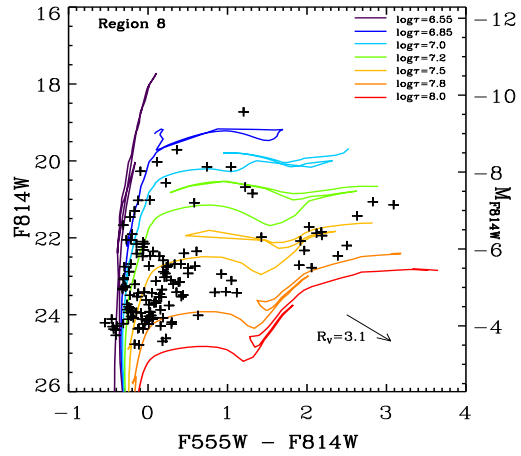
Region 8
logτ=6.55
logτ=6.85
logτ=7.0
logτ=7.2
logτ=7.5
logτ=7.8
logτ=8.0
R_V=3.1
F814W
M_F814W
F555W − F814W

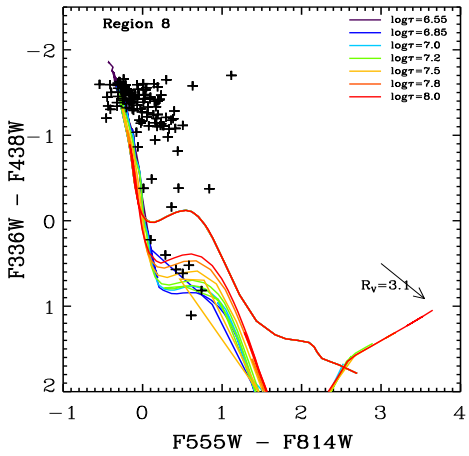
Region 8
logτ=6.55
logτ=6.85
logτ=7.0
logτ=7.2
logτ=7.5
logτ=7.8
logτ=8.0
R_V=3.1
F336W − F438W
F555W − F814W

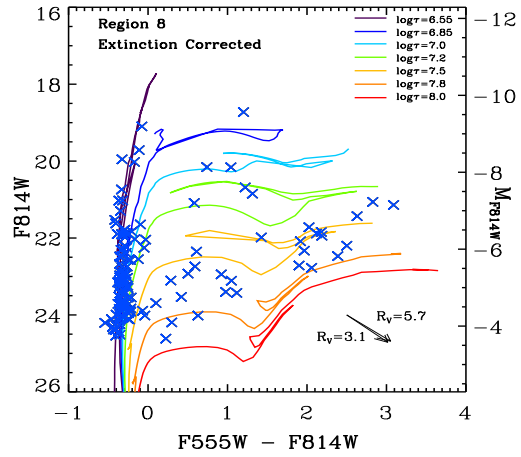
Region 8
Extinction Corrected
logτ=6.55
logτ=6.85
logτ=7.0
logτ=7.2
logτ=7.5
logτ=7.8
logτ=8.0
R_V=5.7
R_V=3.1
F814W
M_F814W
F555W − F814W

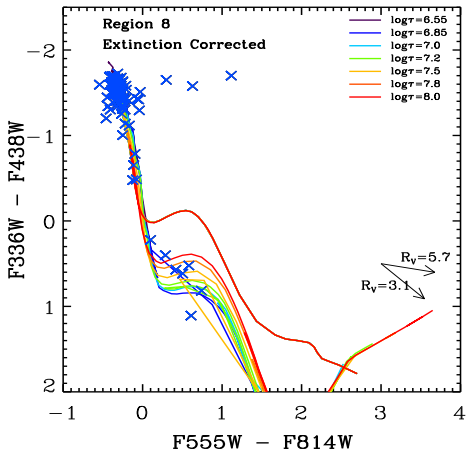
Region 8
Extinction Corrected
logτ=6.55
logτ=6.85
logτ=7.0
logτ=7.2
logτ=7.5
logτ=7.8
logτ=8.0
R_V=5.7
R_V=3.1
F336W − F438W
F555W − F814W

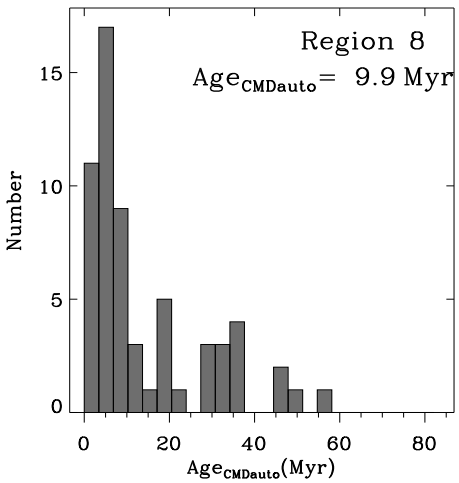
Region 8
Age_CMDauto= 9.9 Myr
Number
Age_CMDauto(Myr)

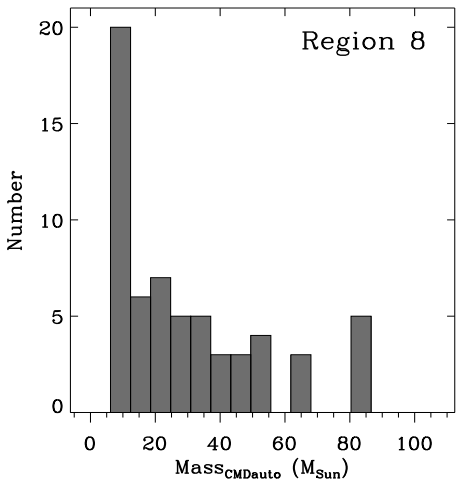
Region 8
Number
Mass_CMDauto (M_Sun)

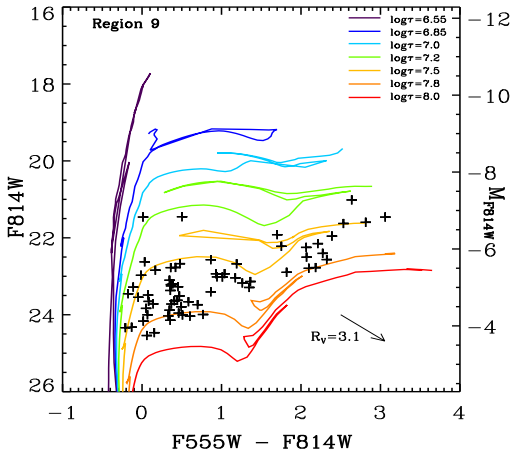
Region 9
logτ=6.55
logτ=6.85
logτ=7.0
logτ=7.2
logτ=7.5
logτ=7.8
logτ=8.0
R_V=3.1
F814W
M_F814W
F555W − F814W

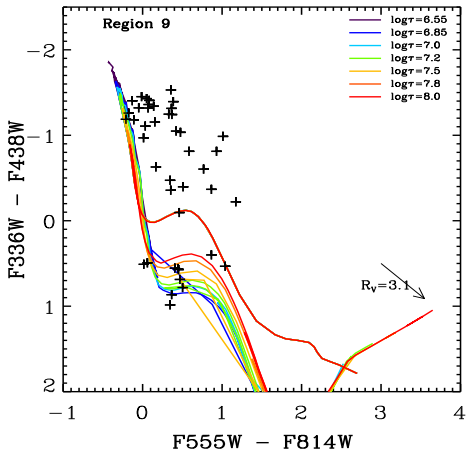
Region 9
logτ=6.55
logτ=6.85
logτ=7.0
logτ=7.2
logτ=7.5
logτ=7.8
logτ=8.0
R_V=3.1
F336W − F438W
F555W − F814W

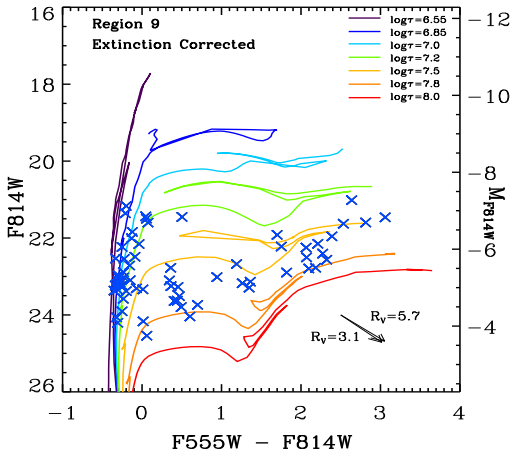
Region 9
Extinction Corrected
logτ=6.55
logτ=6.85
logτ=7.0
logτ=7.2
logτ=7.5
logτ=7.8
logτ=8.0
R_V=5.7
R_V=3.1
F814W
M_F814W
F555W − F814W

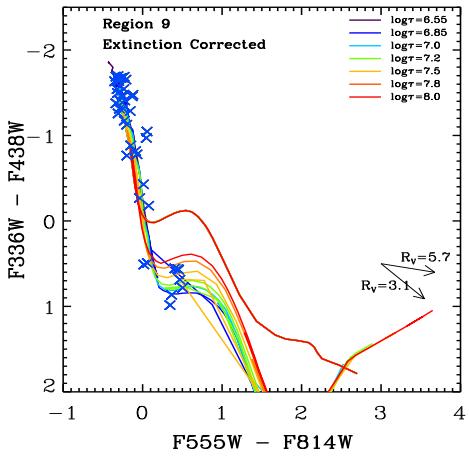
Region 9
Extinction Corrected
logτ=6.55
logτ=6.85
logτ=7.0
logτ=7.2
logτ=7.5
logτ=7.8
logτ=8.0
R_V=5.7
R_V=3.1
F336W − F438W
F555W − F814W

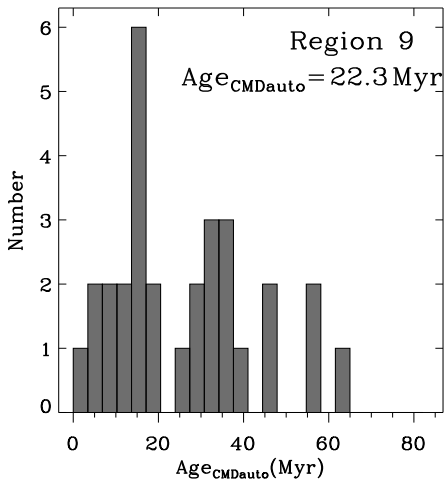
Region 9
Age_CMDauto = 22.3 Myr
Number
Age_CMDauto (Myr)

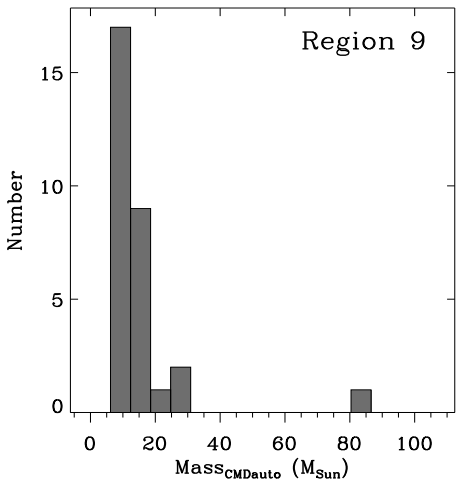
Region 9
Number
Mass_CMDauto (M_Sun)

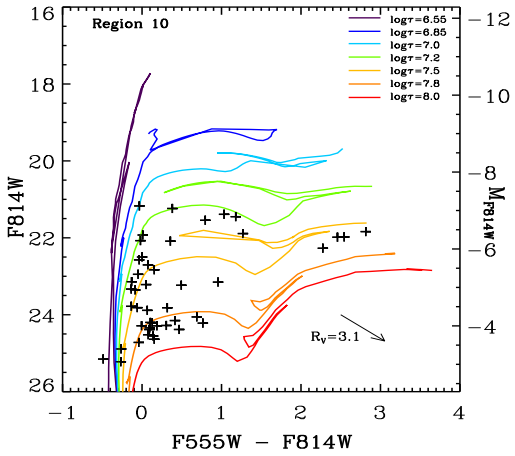
Region 10
logτ=6.55
logτ=6.85
logτ=7.0
logτ=7.2
logτ=7.5
logτ=7.8
logτ=8.0
R_V=3.1
F814W
M_F814W
F555W − F814W

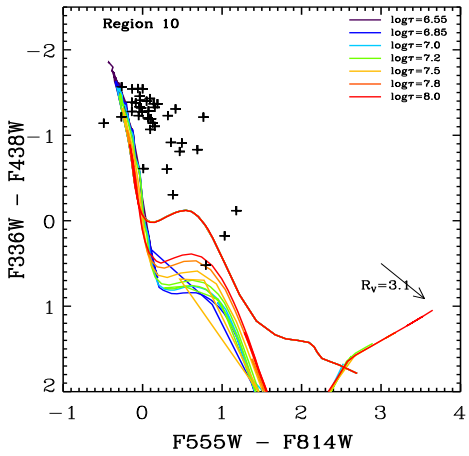
Region 10
logτ=6.55
logτ=6.85
logτ=7.0
logτ=7.2
logτ=7.5
logτ=7.8
logτ=8.0
R_V=3.1
F336W − F438W
F555W − F814W

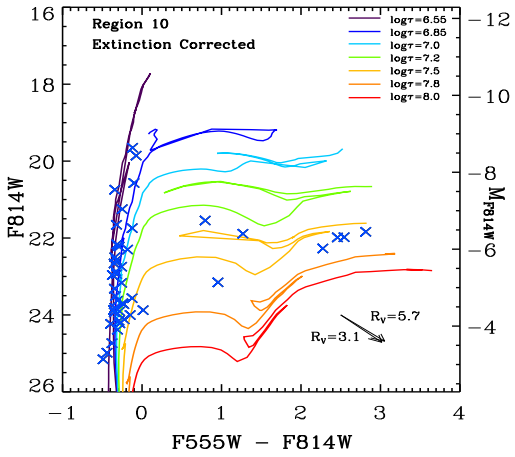
Region 10
Extinction Corrected
logτ=6.55
logτ=6.85
logτ=7.0
logτ=7.2
logτ=7.5
logτ=7.8
logτ=8.0
R_V=5.7
R_V=3.1
F814W
M_F814W
F555W − F814W

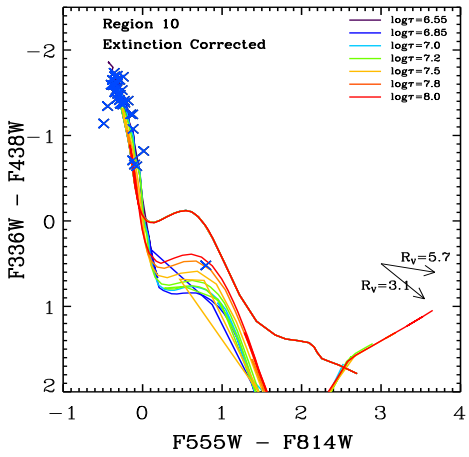
Region 10
Extinction Corrected
logτ=6.55
logτ=6.85
logτ=7.0
logτ=7.2
logτ=7.5
logτ=7.8
logτ=8.0
R_V=5.7
R_V=3.1
F336W − F438W
F555W − F814W

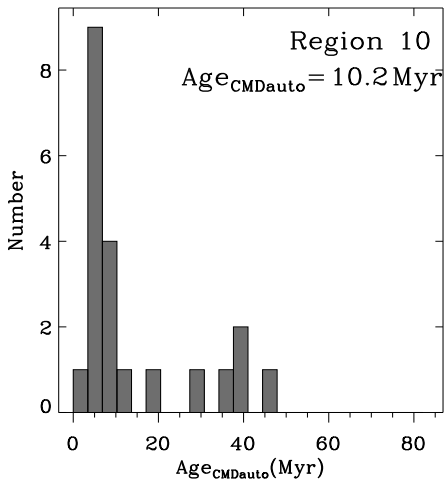
Region 10
Age_CMDauto = 10.2 Myr
Number
Age_CMDauto (Myr)

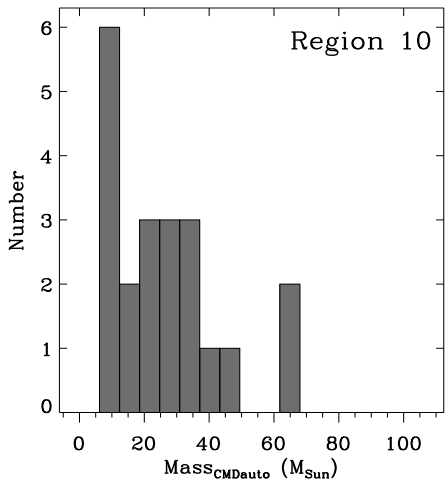
Region 10
Number
Mass_CMDauto (M_Sun)

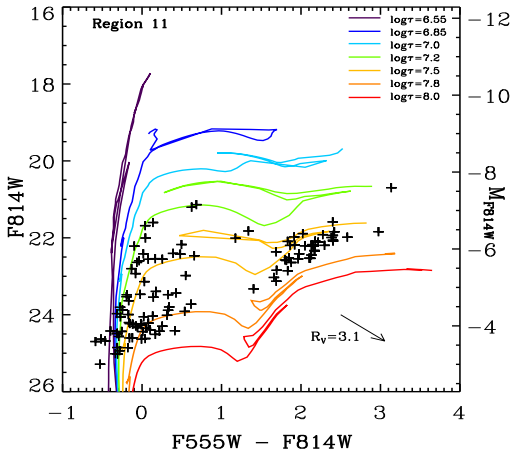
Region 11
logτ=6.55
logτ=6.85
logτ=7.0
logτ=7.2
logτ=7.5
logτ=7.8
logτ=8.0
R_V=3.1
F814W
M_F814W
F555W − F814W

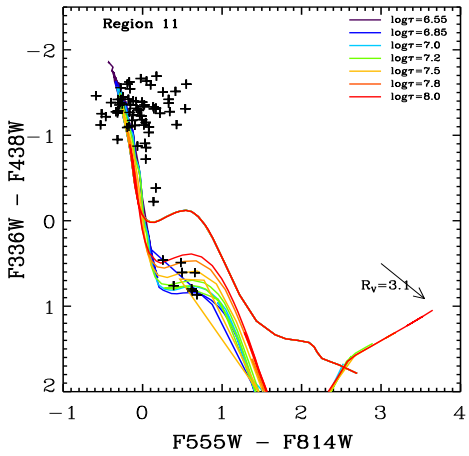
Region 11
logτ=6.55
logτ=6.85
logτ=7.0
logτ=7.2
logτ=7.5
logτ=7.8
logτ=8.0
R_V=3.1
F336W − F438W
F555W − F814W

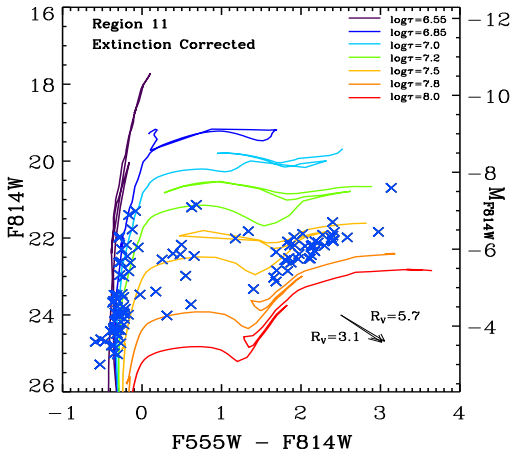
Region 11
Extinction Corrected
logτ=6.55
logτ=6.85
logτ=7.0
logτ=7.2
logτ=7.5
logτ=7.8
logτ=8.0
R_V=5.7
R_V=3.1
F814W
M_F814W
F555W − F814W

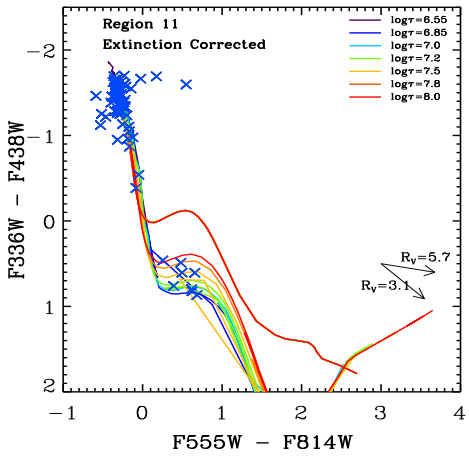
Region 11
Extinction Corrected
logτ=6.55
logτ=6.85
logτ=7.0
logτ=7.2
logτ=7.5
logτ=7.8
logτ=8.0
R_V=5.7
R_V=3.1
F336W − F438W
F555W − F814W

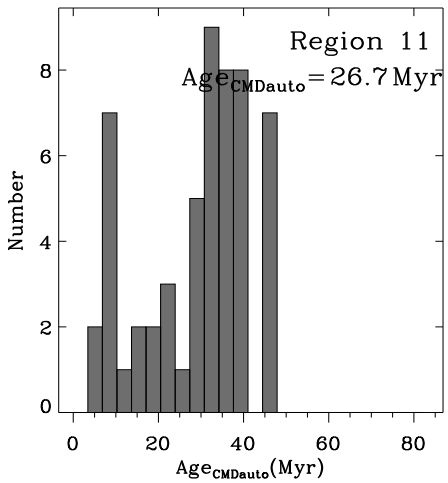
Region 11
Age_CMDauto = 26.7 Myr
Number
Age_CMDauto (Myr)

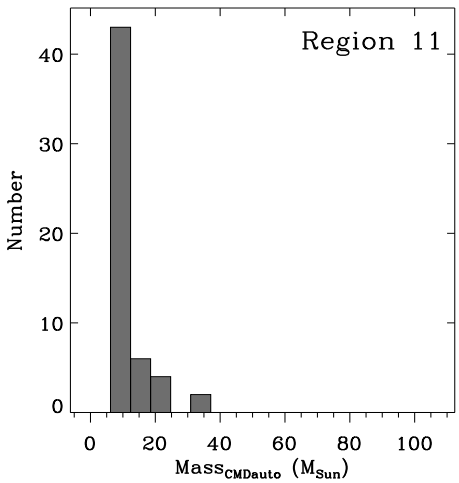
Region 11
Number
Mass_CMDauto (M_Sun)

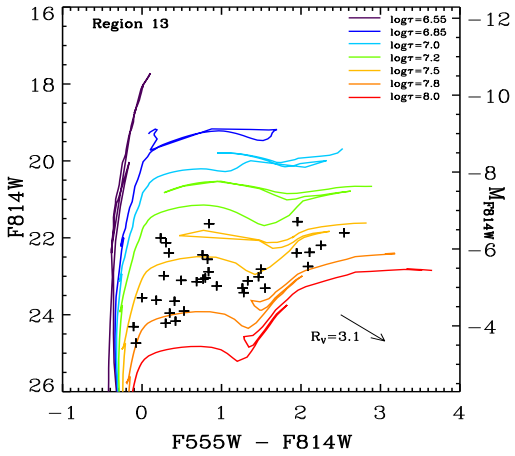
Region 13
logτ=6.55
logτ=6.85
logτ=7.0
logτ=7.2
logτ=7.5
logτ=7.8
logτ=8.0
R_V=3.1
F814W
M_F814W
F555W − F814W

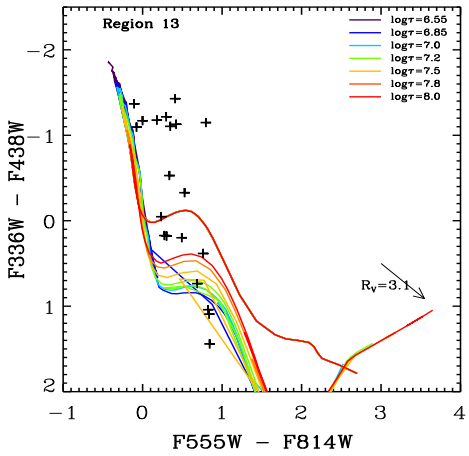
Region 13
logτ=6.55
logτ=6.85
logτ=7.0
logτ=7.2
logτ=7.5
logτ=7.8
logτ=8.0
R_V=3.1
F336W − F438W
F555W − F814W

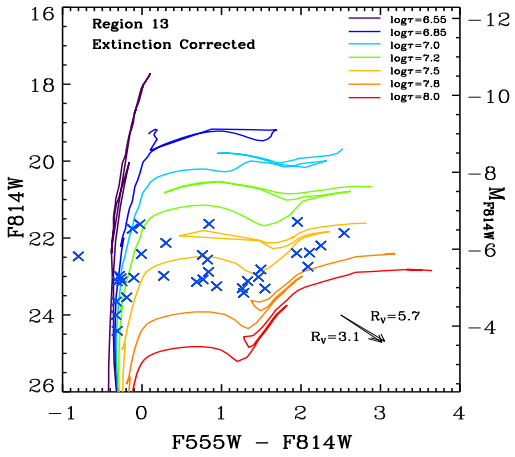
Region 13
Extinction Corrected
logτ=6.55
logτ=6.85
logτ=7.0
logτ=7.2
logτ=7.5
logτ=7.8
logτ=8.0
R_V=5.7
R_V=3.1
F814W
M_F814W
F555W − F814W

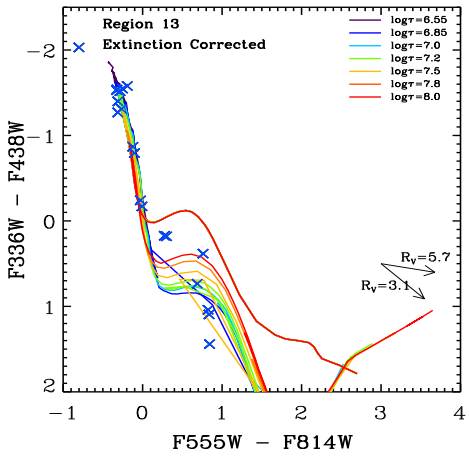
Region 13
Extinction Corrected
logτ=6.55
logτ=6.85
logτ=7.0
logτ=7.2
logτ=7.5
logτ=7.8
logτ=8.0
R_V=5.7
R_V=3.1
F336W − F438W
F555W − F814W

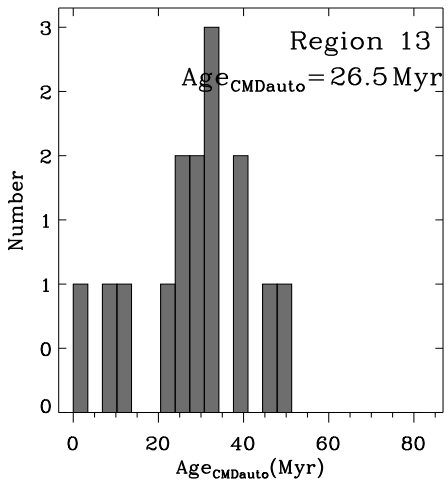
Region 13
Age_CMDauto = 26.5 Myr
Number
Age_CMDauto (Myr)

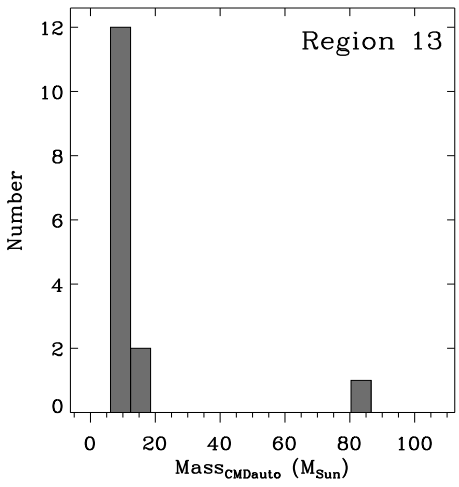
Region 13
Number
Mass_CMDauto (M_Sun)

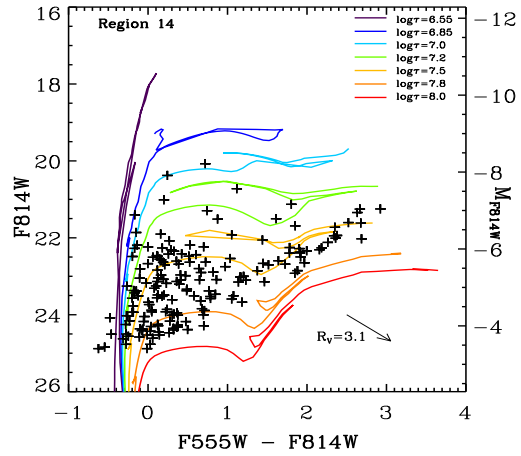
Region 14
logτ=6.55
logτ=6.85
logτ=7.0
logτ=7.2
logτ=7.5
logτ=7.8
logτ=8.0
R_V=3.1
F814W
M_F814W
F555W − F814W

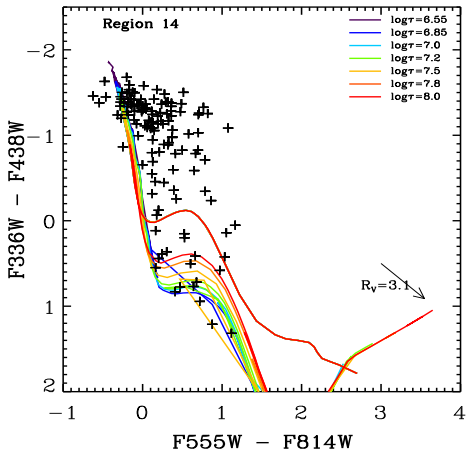
Region 14
logτ=6.55
logτ=6.85
logτ=7.0
logτ=7.2
logτ=7.5
logτ=7.8
logτ=8.0
R_V=3.1
F336W − F438W
F555W − F814W

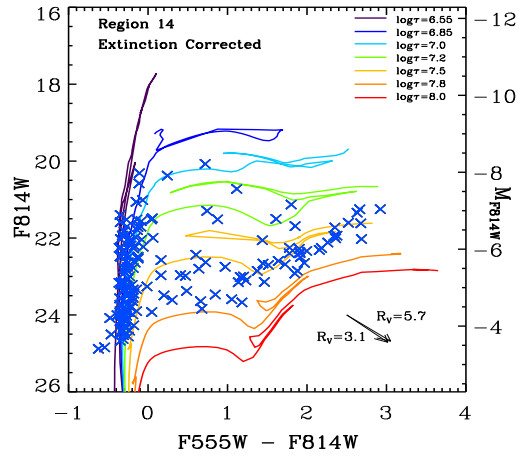
Region 14
Extinction Corrected
logτ=6.55
logτ=6.85
logτ=7.0
logτ=7.2
logτ=7.5
logτ=7.8
logτ=8.0
R_V=5.7
R_V=3.1
F814W
M_F814W
F555W − F814W

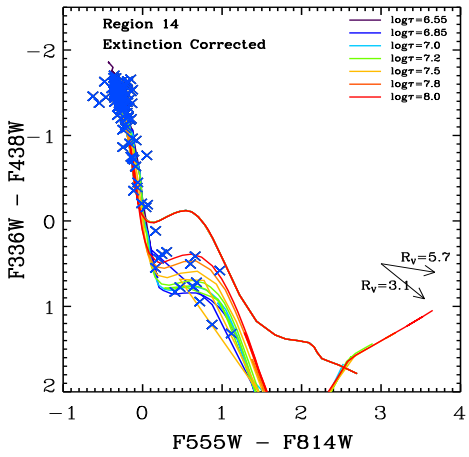
Region 14
Extinction Corrected
logτ=6.55
logτ=6.85
logτ=7.0
logτ=7.2
logτ=7.5
logτ=7.8
logτ=8.0
R_V=5.7
R_V=3.1
F336W − F438W
F555W − F814W

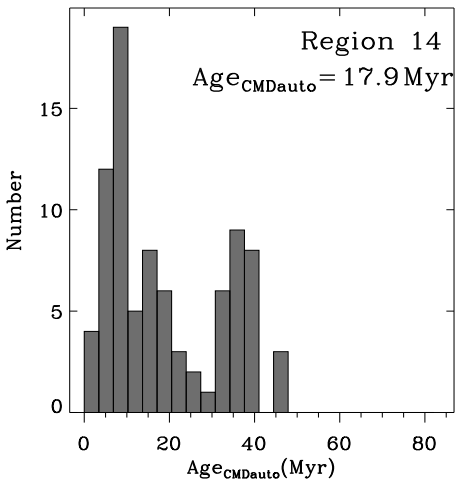
Region 14
Age_CMDauto = 17.9 Myr
Number
Age_CMDauto (Myr)

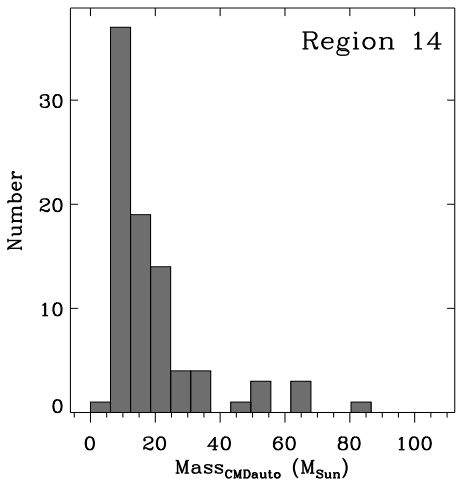
Region 14
Number
Mass_CMDauto (M_Sun)

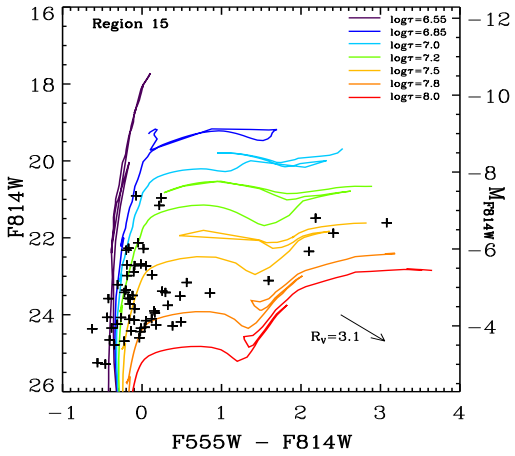
Region 15
logτ=6.55
logτ=6.85
logτ=7.0
logτ=7.2
logτ=7.5
logτ=7.8
logτ=8.0
R_V=3.1
F814W
M_F814W
F555W − F814W

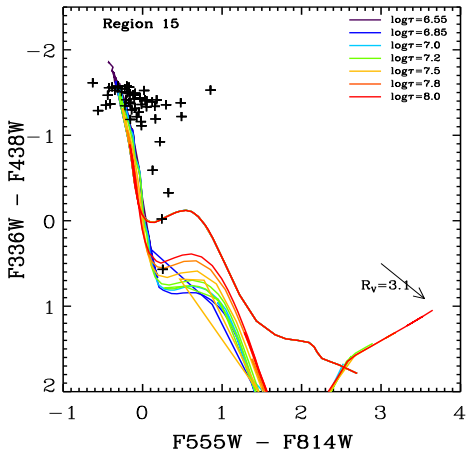
Region 15
logτ=6.55
logτ=6.85
logτ=7.0
logτ=7.2
logτ=7.5
logτ=7.8
logτ=8.0
R_V=3.1
F336W − F438W
F555W − F814W

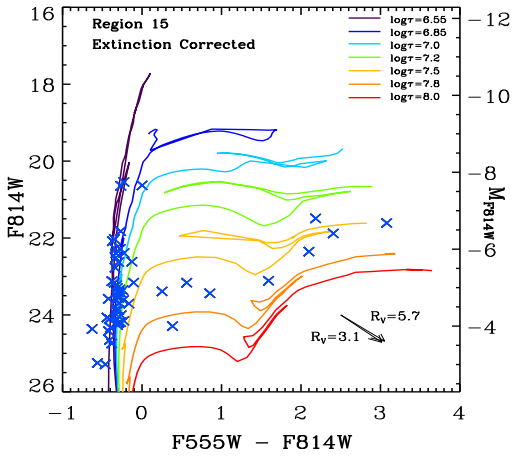
Region 15
Extinction Corrected
logτ=6.55
logτ=6.85
logτ=7.0
logτ=7.2
logτ=7.5
logτ=7.8
logτ=8.0
R_V=5.7
R_V=3.1
F814W
M_F814W
F555W − F814W

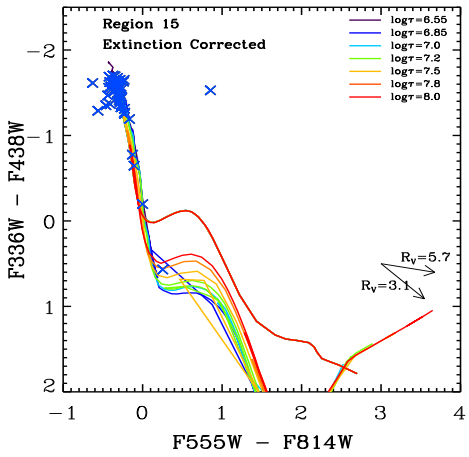
Region 15
Extinction Corrected
logτ=6.55
logτ=6.85
logτ=7.0
logτ=7.2
logτ=7.5
logτ=7.8
logτ=8.0
R_V=5.7
R_V=3.1
F336W − F438W
F555W − F814W

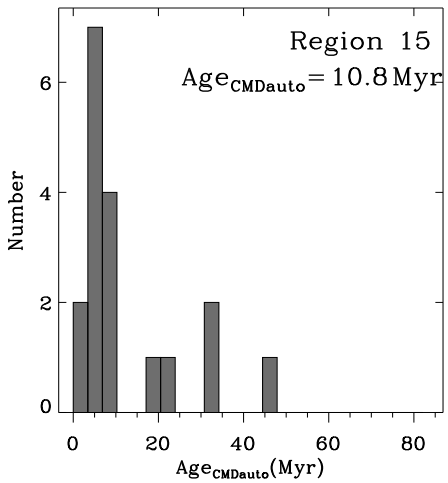
Region 15
Age_CMDauto = 10.8 Myr
Number
Age_CMDauto (Myr)

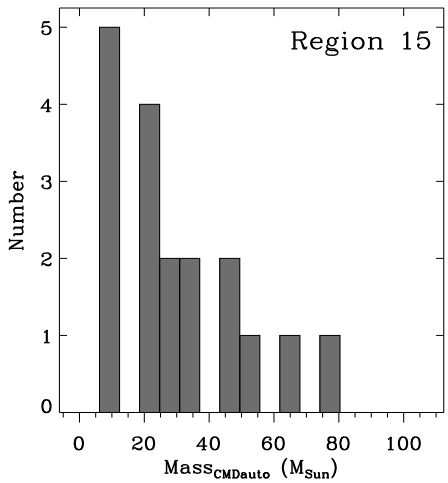
Region 15
Number
Mass_CMDauto (M_Sun)

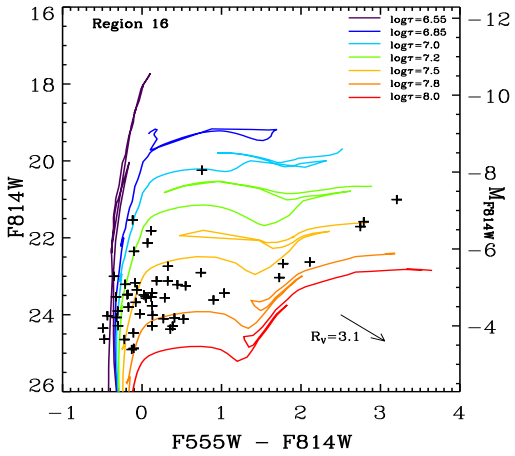
Region 16
logτ=6.55
logτ=6.85
logτ=7.0
logτ=7.2
logτ=7.5
logτ=7.8
logτ=8.0
R_V=3.1
F814W
M_F814W
F555W − F814W

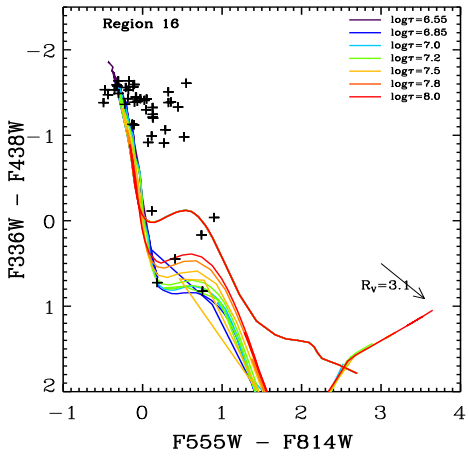
Region 16
logτ=6.55
logτ=6.85
logτ=7.0
logτ=7.2
logτ=7.5
logτ=7.8
logτ=8.0
R_V=3.1
F336W − F438W
F555W − F814W

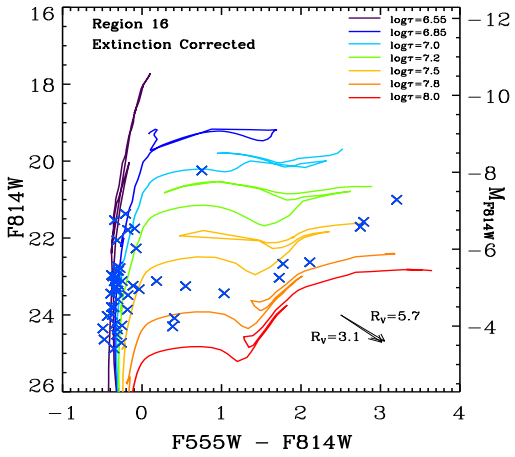
Region 16
Extinction Corrected
logτ=6.55
logτ=6.85
logτ=7.0
logτ=7.2
logτ=7.5
logτ=7.8
logτ=8.0
R_V=5.7
R_V=3.1
F814W
M_F814W
F555W − F814W

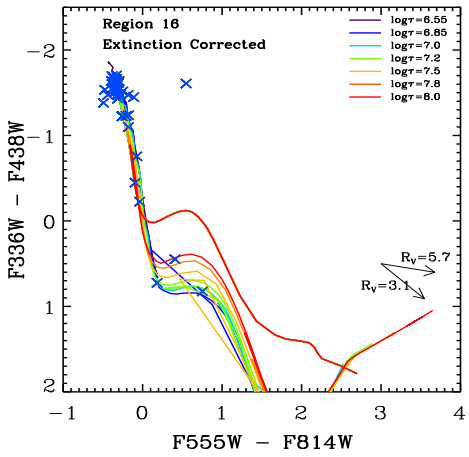
Region 16
Extinction Corrected
logτ=6.55
logτ=6.85
logτ=7.0
logτ=7.2
logτ=7.5
logτ=7.8
logτ=8.0
R_V=5.7
R_V=3.1
F336W − F438W
F555W − F814W

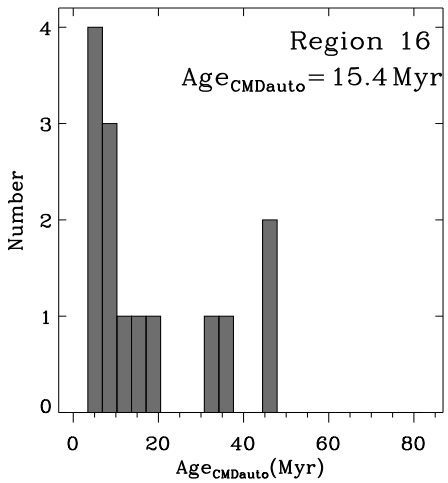
Region 16
Age_CMDauto = 15.4 Myr
Number
Age_CMDauto (Myr)

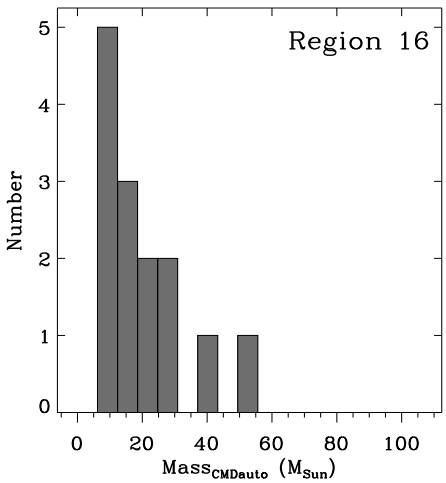
Region 16
Number
Mass_CMDauto (M_Sun)

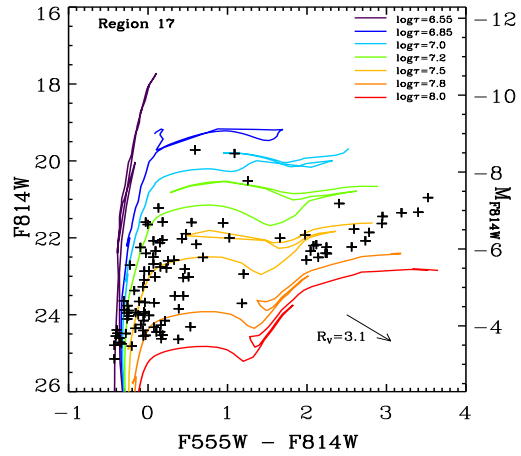
Region 17
logτ=6.55
logτ=6.85
logτ=7.0
logτ=7.2
logτ=7.5
logτ=7.8
logτ=8.0
R_V=3.1
F814W
M_F814W
F555W − F814W

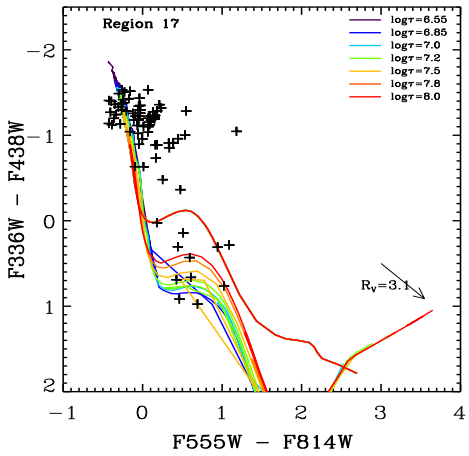
Region 17
logτ=6.55
logτ=6.85
logτ=7.0
logτ=7.2
logτ=7.5
logτ=7.8
logτ=8.0
R_V=3.1
F336W − F438W
F555W − F814W

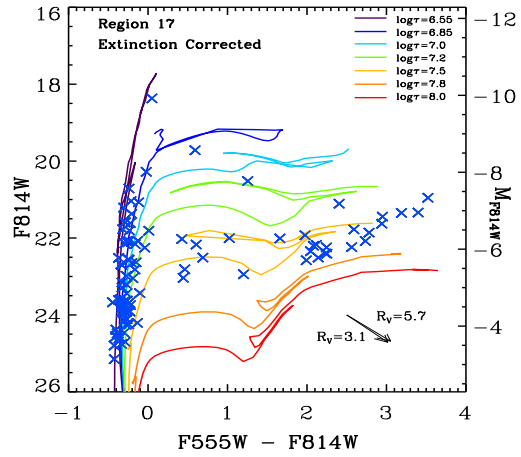
Region 17
Extinction Corrected
logτ=6.55
logτ=6.85
logτ=7.0
logτ=7.2
logτ=7.5
logτ=7.8
logτ=8.0
R_V=5.7
R_V=3.1
F814W
M_F814W
F555W − F814W

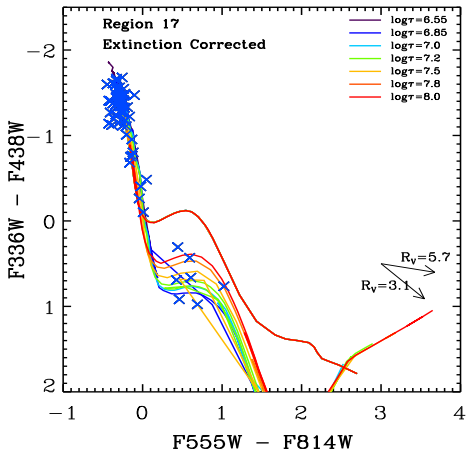
Region 17
Extinction Corrected
logτ=6.55
logτ=6.85
logτ=7.0
logτ=7.2
logτ=7.5
logτ=7.8
logτ=8.0
R_V=5.7
R_V=3.1
F336W − F438W
F555W − F814W

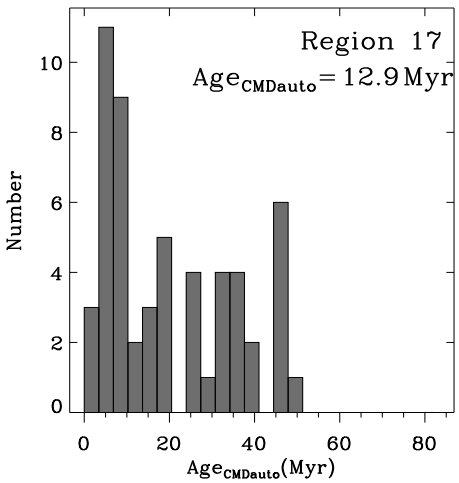
Region 17
Age_CMDauto = 12.9 Myr
Number
Age_CMDauto (Myr)

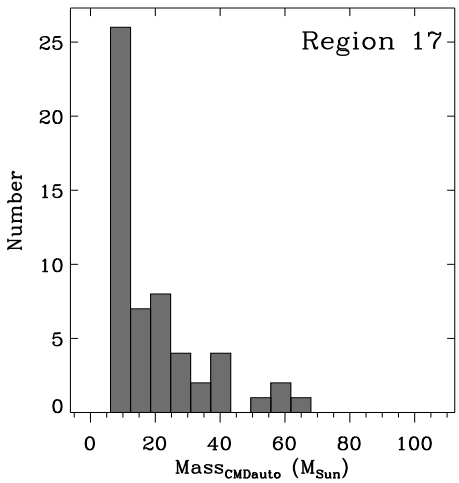
Region 17
Number
Mass_CMDauto (M_Sun)

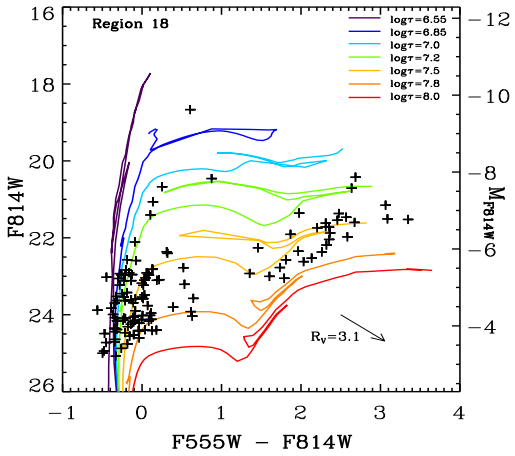
Region 18
logτ=6.55
logτ=6.85
logτ=7.0
logτ=7.2
logτ=7.5
logτ=7.8
logτ=8.0
R_V=3.1
F814W
M_F814W
F555W − F814W

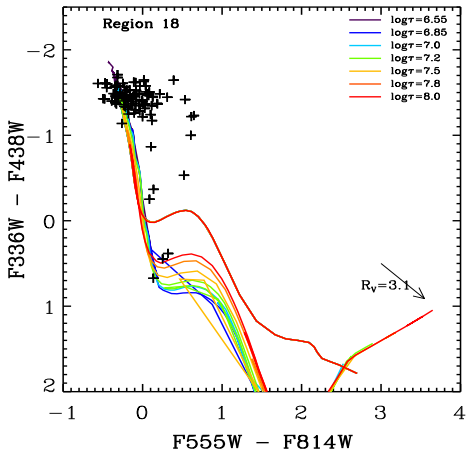
Region 18
logτ=6.55
logτ=6.85
logτ=7.0
logτ=7.2
logτ=7.5
logτ=7.8
logτ=8.0
R_V=3.1
F336W − F438W
F555W − F814W

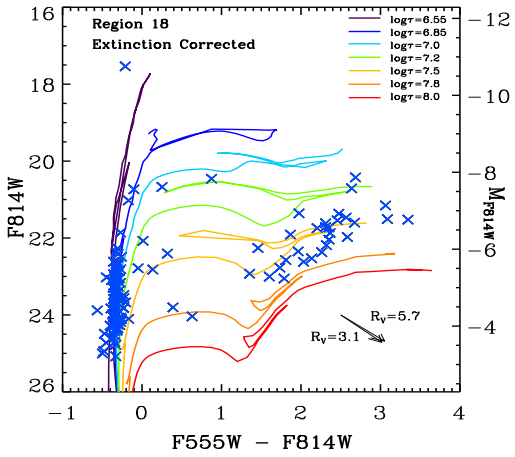
Region 18
Extinction Corrected
logτ=6.55
logτ=6.85
logτ=7.0
logτ=7.2
logτ=7.5
logτ=7.8
logτ=8.0
R_V=5.7
R_V=3.1
F814W
M_F814W
F555W − F814W

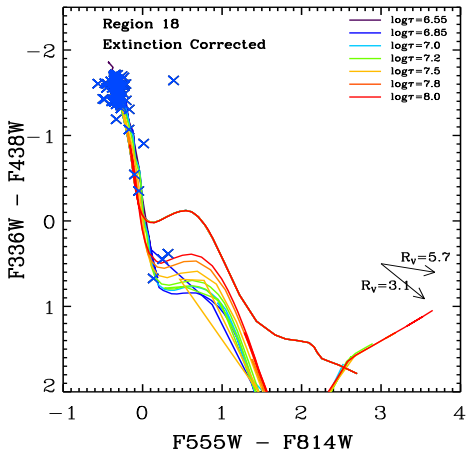
Region 18
Extinction Corrected
logτ=6.55
logτ=6.85
logτ=7.0
logτ=7.2
logτ=7.5
logτ=7.8
logτ=8.0
R_V=5.7
R_V=3.1
F336W − F438W
F555W − F814W

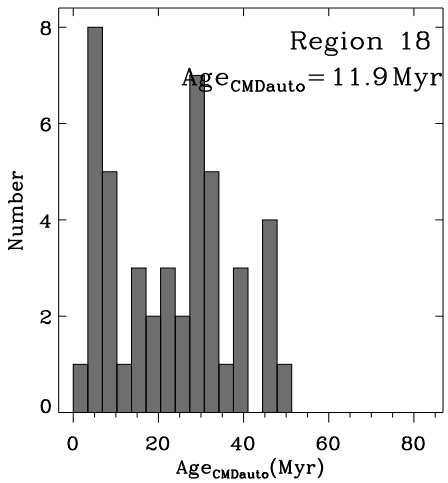
Region 18
Age_CMDauto = 11.9 Myr
Number
Age_CMDauto (Myr)

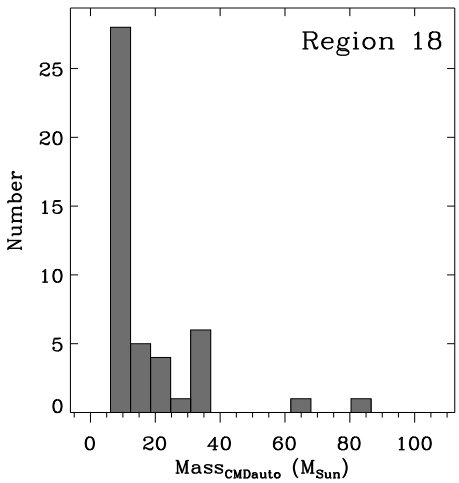
Region 18
Number
Mass_CMDauto (M_Sun)

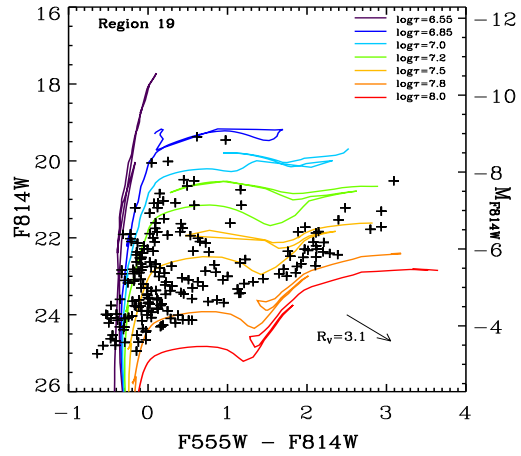
Region 19
logτ=6.55
logτ=6.85
logτ=7.0
logτ=7.2
logτ=7.5
logτ=7.8
logτ=8.0
R_V=3.1
F814W
M_F814W
F555W − F814W

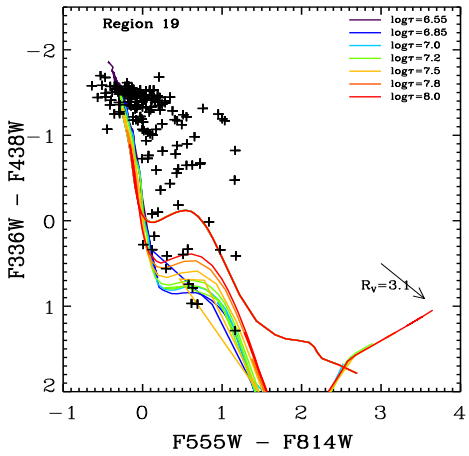
Region 19
logτ=6.55
logτ=6.85
logτ=7.0
logτ=7.2
logτ=7.5
logτ=7.8
logτ=8.0
R_V=3.1
F336W − F438W
F555W − F814W

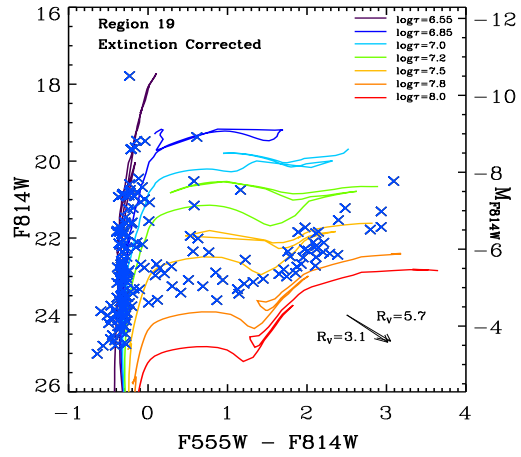
Region 19
Extinction Corrected
logτ=6.55
logτ=6.85
logτ=7.0
logτ=7.2
logτ=7.5
logτ=7.8
logτ=8.0
R_V=5.7
R_V=3.1
F814W
M_F814W
F555W − F814W

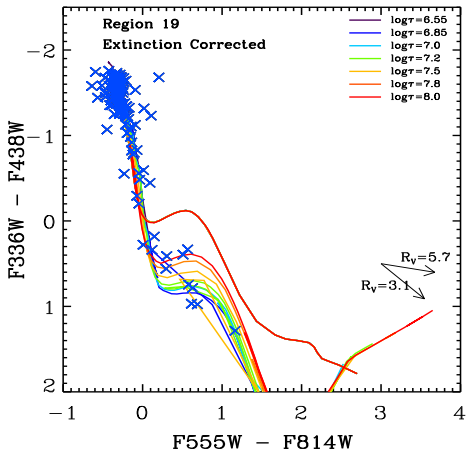
Region 19
Extinction Corrected
logτ=6.55
logτ=6.85
logτ=7.0
logτ=7.2
logτ=7.5
logτ=7.8
logτ=8.0
R_V=5.7
R_V=3.1
F336W − F438W
F555W − F814W

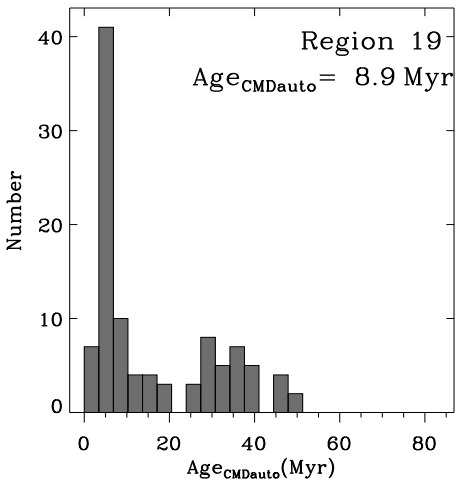
Region 19
Age_CMDauto= 8.9 Myr
Number
Age_CMDauto(Myr)

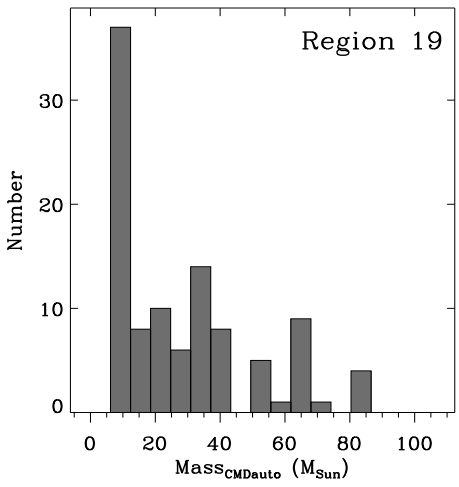
Region 19
Number
Mass_CMDauto (M_Sun)

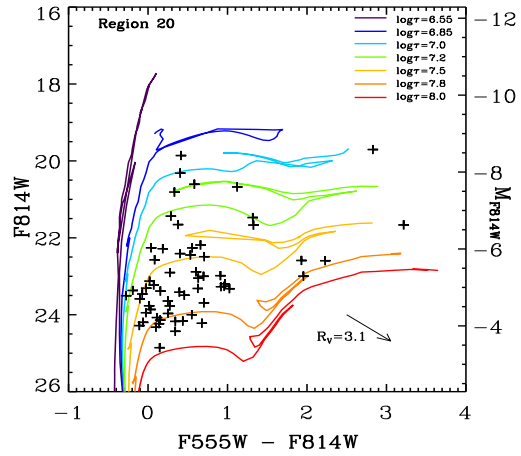
Region 20
logτ=6.55
logτ=6.85
logτ=7.0
logτ=7.2
logτ=7.5
logτ=7.8
logτ=8.0
Rv=3.1
F814W
M F814W
F555W − F814W

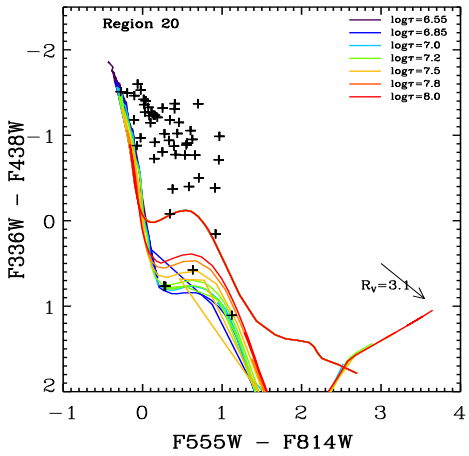
Region 20
logτ=6.55
logτ=6.85
logτ=7.0
logτ=7.2
logτ=7.5
logτ=7.8
logτ=8.0
Rv=3.1
F336W − F438W
F555W − F814W

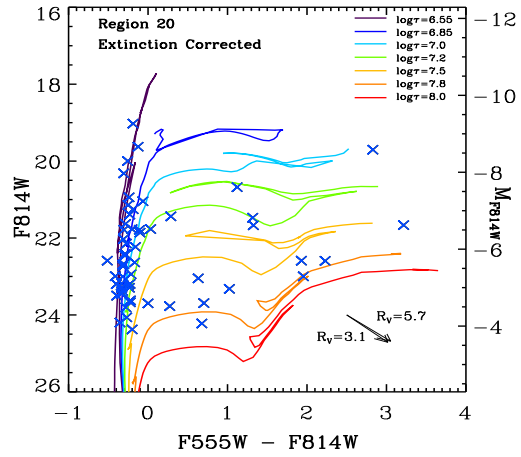
Region 20
Extinction Corrected
logτ=6.55
logτ=6.85
logτ=7.0
logτ=7.2
logτ=7.5
logτ=7.8
logτ=8.0
Rv=5.7
Rv=3.1
F814W
M F814W
F555W − F814W

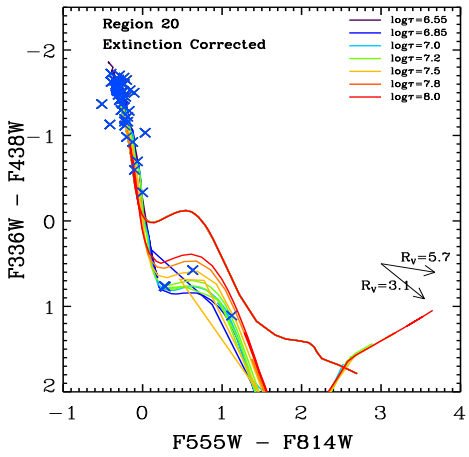
Region 20
Extinction Corrected
logτ=6.55
logτ=6.85
logτ=7.0
logτ=7.2
logτ=7.5
logτ=7.8
logτ=8.0
Rv=5.7
Rv=3.1
F336W − F438W
F555W − F814W

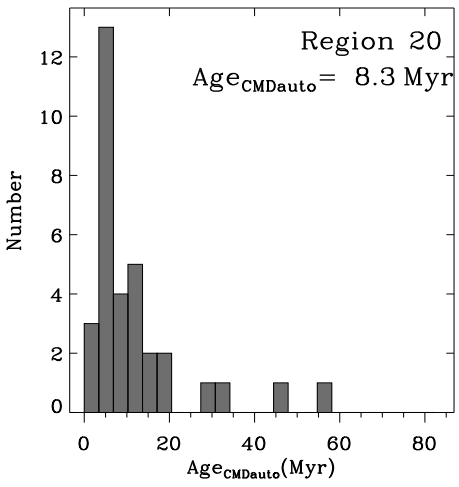
Region 20
Age CMDauto = 8.3 Myr
Number
Age CMDauto (Myr)

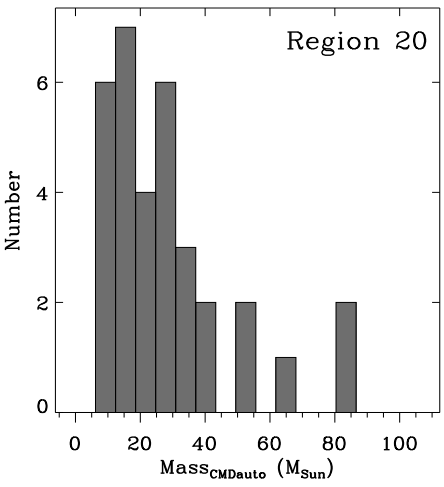
Region 20
Number
Mass CMDauto (M Sun)

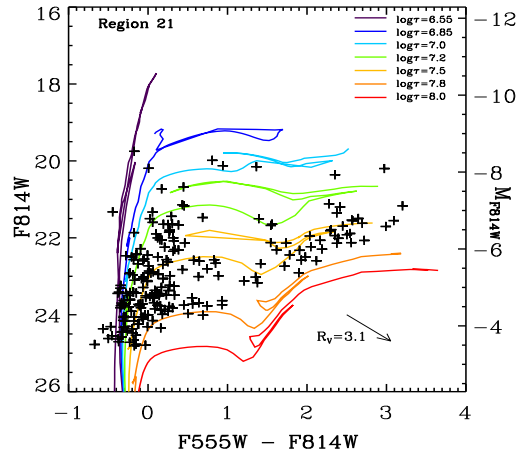
Region 21
logτ=6.55
logτ=6.85
logτ=7.0
logτ=7.2
logτ=7.5
logτ=7.8
logτ=8.0
R_V=3.1
F814W
M_F814W
F555W − F814W

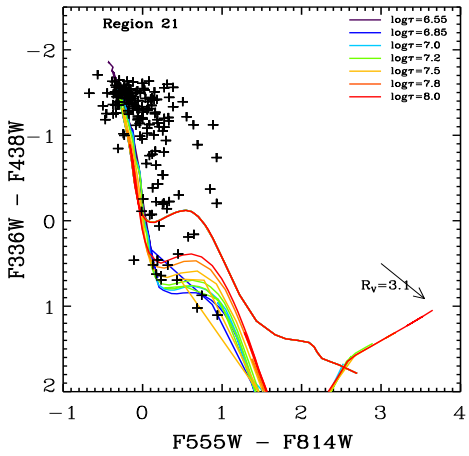
Region 21
logτ=6.55
logτ=6.85
logτ=7.0
logτ=7.2
logτ=7.5
logτ=7.8
logτ=8.0
R_V=3.1
F336W − F438W
F555W − F814W

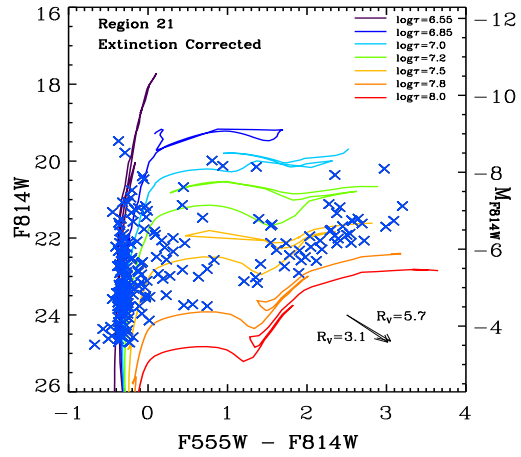
Region 21
Extinction Corrected
logτ=6.55
logτ=6.85
logτ=7.0
logτ=7.2
logτ=7.5
logτ=7.8
logτ=8.0
R_V=5.7
R_V=3.1
F814W
M_F814W
F555W − F814W

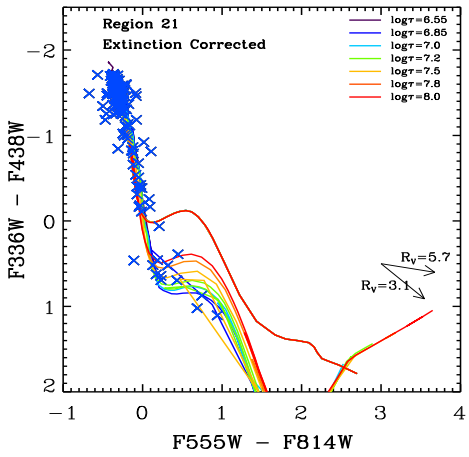
Region 21
Extinction Corrected
logτ=6.55
logτ=6.85
logτ=7.0
logτ=7.2
logτ=7.5
logτ=7.8
logτ=8.0
R_V=5.7
R_V=3.1
F336W − F438W
F555W − F814W

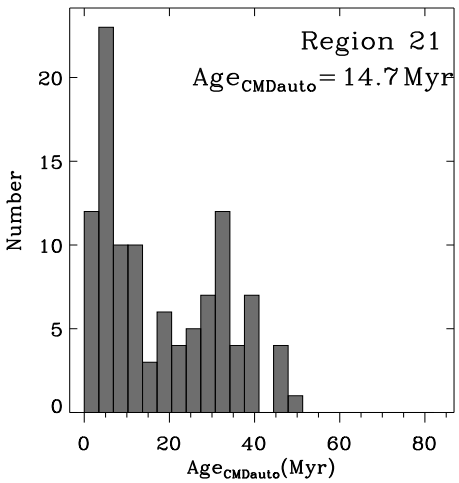
Region 21
Age_CMDauto = 14.7 Myr
Number
Age_CMDauto (Myr)

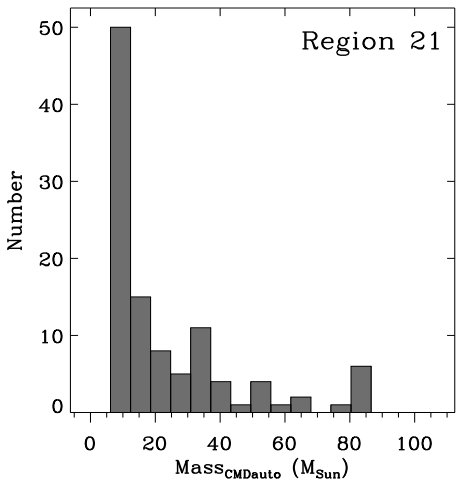
Region 21
Number
Mass_CMDauto (M_Sun)

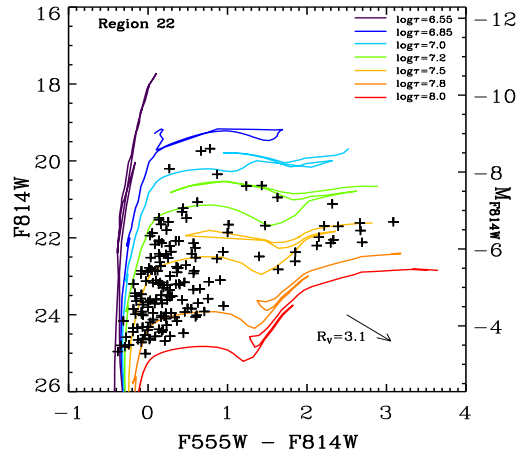
Region 22
logτ=6.55
logτ=6.85
logτ=7.0
logτ=7.2
logτ=7.5
logτ=7.8
logτ=8.0
R_V=3.1
F814W
M_F814W
F555W − F814W

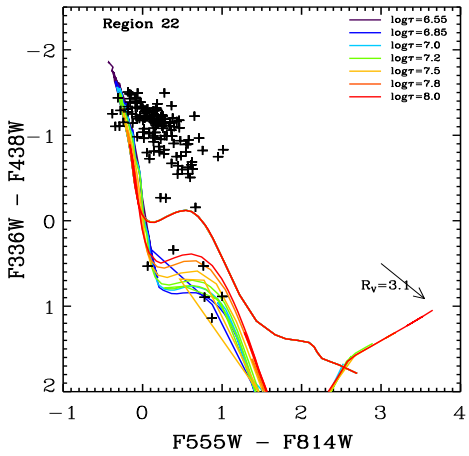
Region 22
logτ=6.55
logτ=6.85
logτ=7.0
logτ=7.2
logτ=7.5
logτ=7.8
logτ=8.0
R_V=3.1
F336W − F438W
F555W − F814W

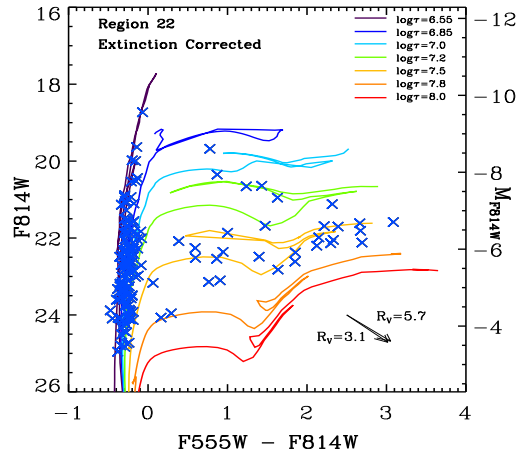
Region 22
Extinction Corrected
logτ=6.55
logτ=6.85
logτ=7.0
logτ=7.2
logτ=7.5
logτ=7.8
logτ=8.0
R_V=5.7
R_V=3.1
F814W
M_F814W
F555W − F814W

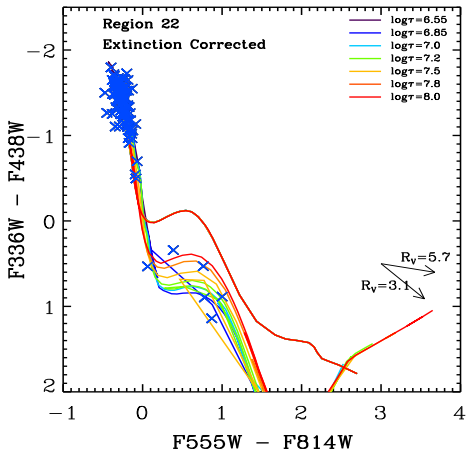
Region 22
Extinction Corrected
logτ=6.55
logτ=6.85
logτ=7.0
logτ=7.2
logτ=7.5
logτ=7.8
logτ=8.0
R_V=5.7
R_V=3.1
F336W − F438W
F555W − F814W

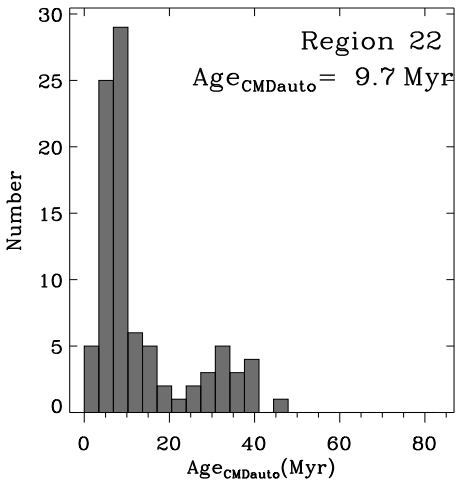
Region 22
Age_CMDauto= 9.7 Myr
Number
Age_CMDauto(Myr)

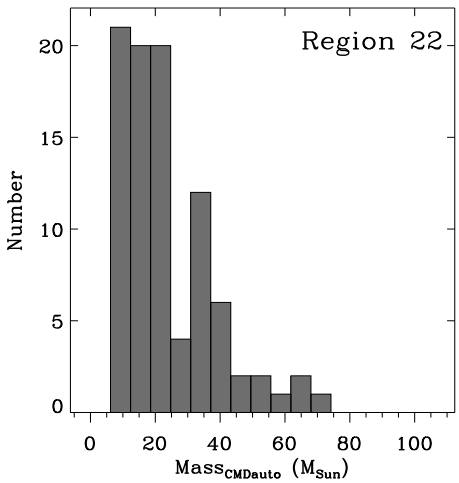
Region 22
Number
Mass_CMDauto (M_Sun)

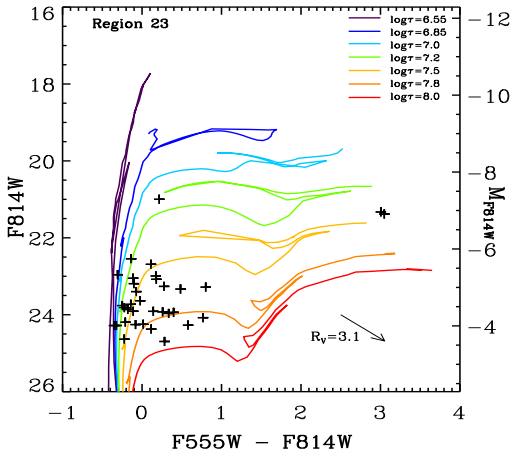
Region 23
logτ=6.55
logτ=6.85
logτ=7.0
logτ=7.2
logτ=7.5
logτ=7.8
logτ=8.0
R_V=3.1
F814W
M_F814W
F555W − F814W

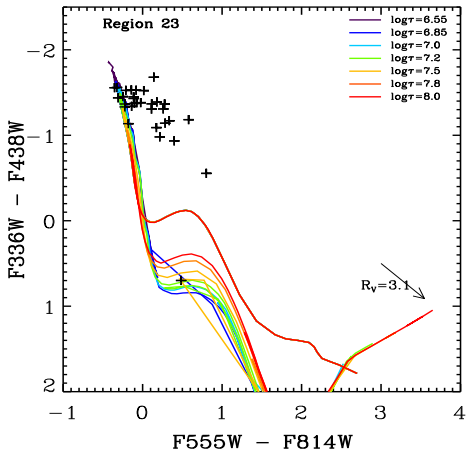
Region 23
logτ=6.55
logτ=6.85
logτ=7.0
logτ=7.2
logτ=7.5
logτ=7.8
logτ=8.0
R_V=3.1
F336W − F438W
F555W − F814W

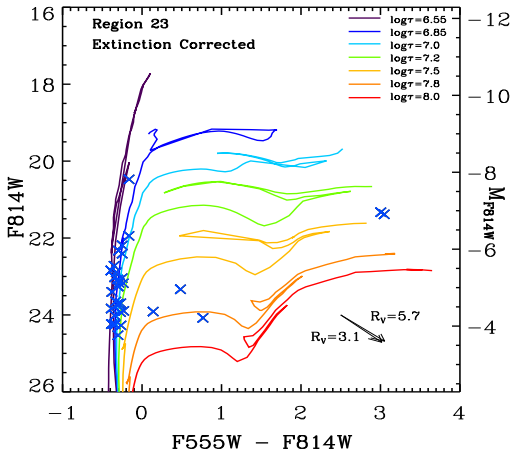
Region 23
Extinction Corrected
logτ=6.55
logτ=6.85
logτ=7.0
logτ=7.2
logτ=7.5
logτ=7.8
logτ=8.0
R_V=5.7
R_V=3.1
F814W
M_F814W
F555W − F814W

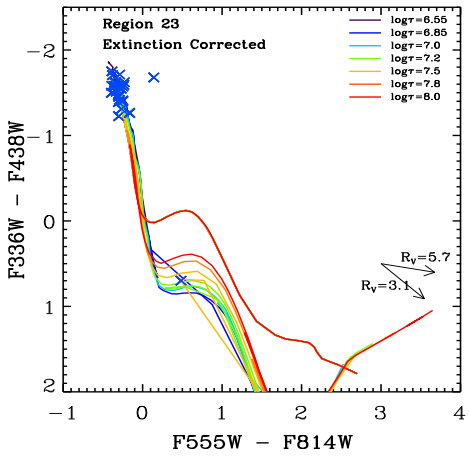
Region 23
Extinction Corrected
logτ=6.55
logτ=6.85
logτ=7.0
logτ=7.2
logτ=7.5
logτ=7.8
logτ=8.0
R_V=5.7
R_V=3.1
F336W − F438W
F555W − F814W

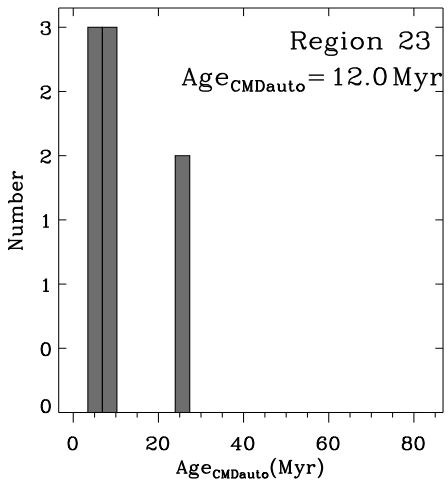
Region 23
Age_CMDauto = 12.0 Myr
Number
Age_CMDauto (Myr)

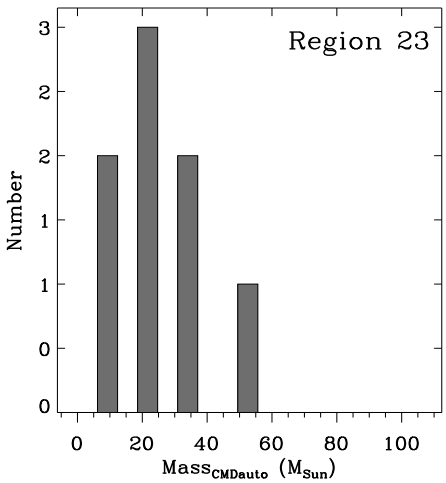
Region 23
Number
Mass_CMDauto (M_Sun)

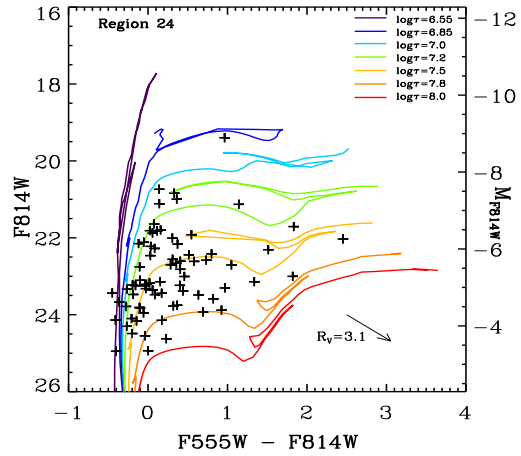
Region 24
logτ=6.55
logτ=6.85
logτ=7.0
logτ=7.2
logτ=7.5
logτ=7.8
logτ=8.0
R_V=3.1
F814W
M_F814W
F555W − F814W

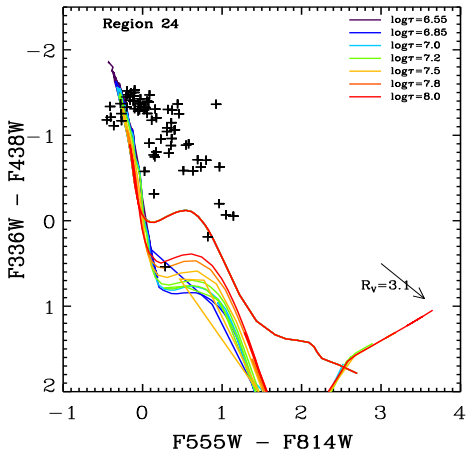
Region 24
logτ=6.55
logτ=6.85
logτ=7.0
logτ=7.2
logτ=7.5
logτ=7.8
logτ=8.0
R_V=3.1
F336W − F438W
F555W − F814W

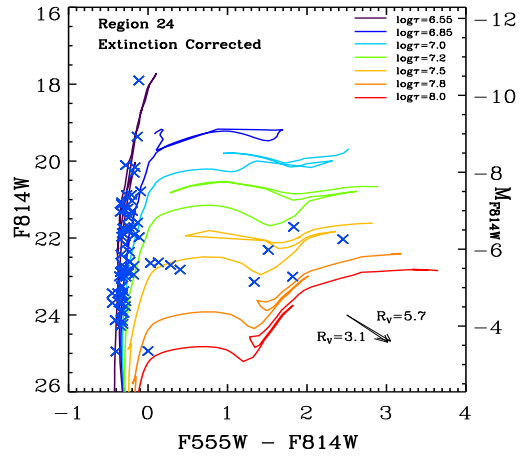
Region 24
Extinction Corrected
logτ=6.55
logτ=6.85
logτ=7.0
logτ=7.2
logτ=7.5
logτ=7.8
logτ=8.0
R_V=5.7
R_V=3.1
F814W
M_F814W
F555W − F814W

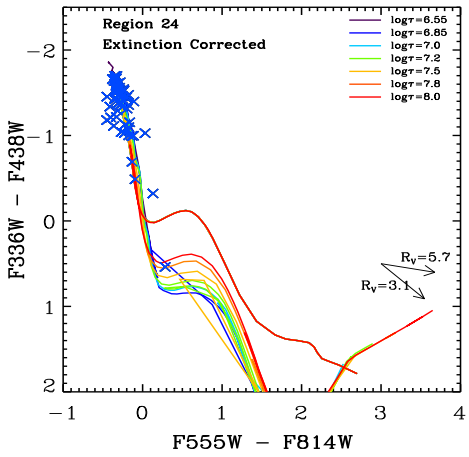
Region 24
Extinction Corrected
logτ=6.55
logτ=6.85
logτ=7.0
logτ=7.2
logτ=7.5
logτ=7.8
logτ=8.0
R_V=5.7
R_V=3.1
F336W − F438W
F555W − F814W

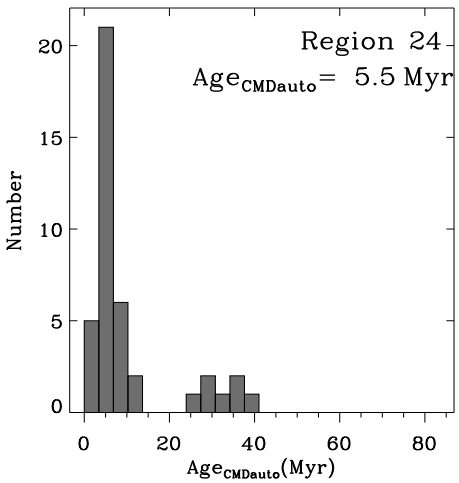
Region 24
Age_CMDauto= 5.5 Myr
Number
Age_CMDauto(Myr)

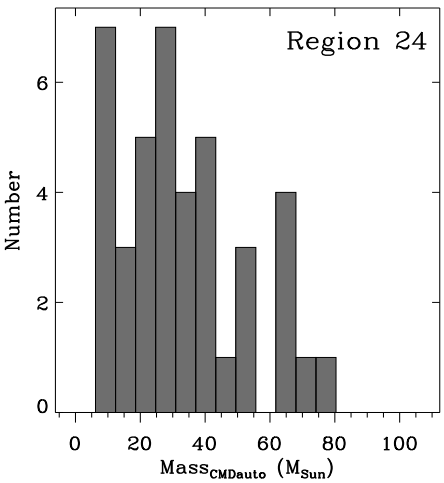
Region 24
Number
Mass_CMDauto (M_Sun)

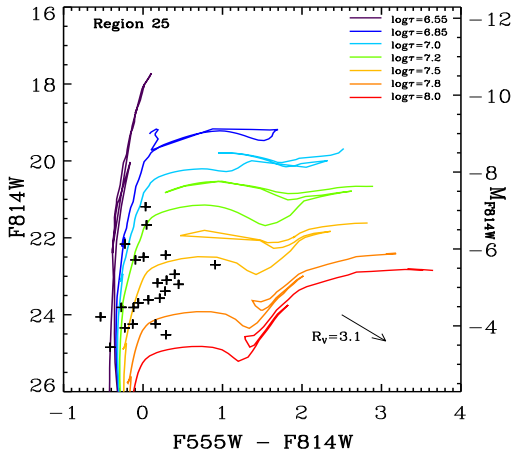
Region 25
logτ=6.55
logτ=6.85
logτ=7.0
logτ=7.2
logτ=7.5
logτ=7.8
logτ=8.0
R_V=3.1
F814W
M_F814W
F555W − F814W

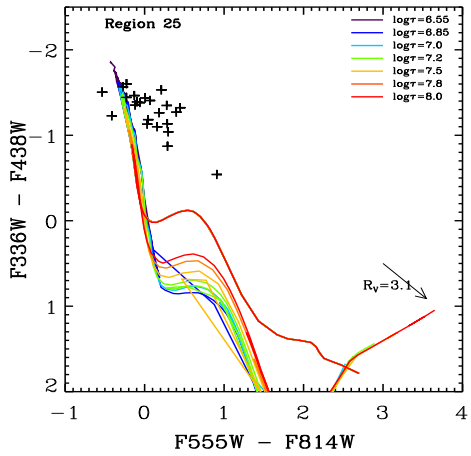
Region 25
logτ=6.55
logτ=6.85
logτ=7.0
logτ=7.2
logτ=7.5
logτ=7.8
logτ=8.0
R_V=3.1
F336W − F438W
F555W − F814W

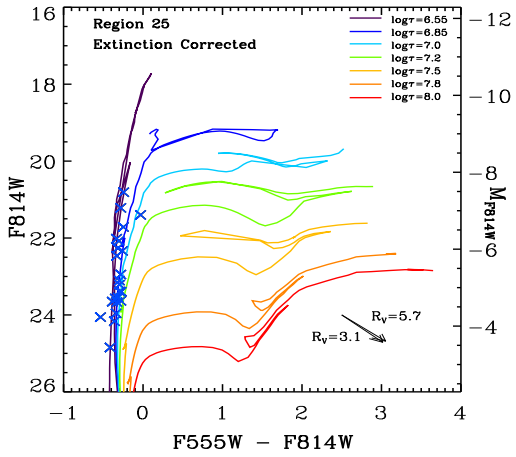
Region 25
Extinction Corrected
logτ=6.55
logτ=6.85
logτ=7.0
logτ=7.2
logτ=7.5
logτ=7.8
logτ=8.0
R_V=5.7
R_V=3.1
F814W
M_F814W
F555W − F814W

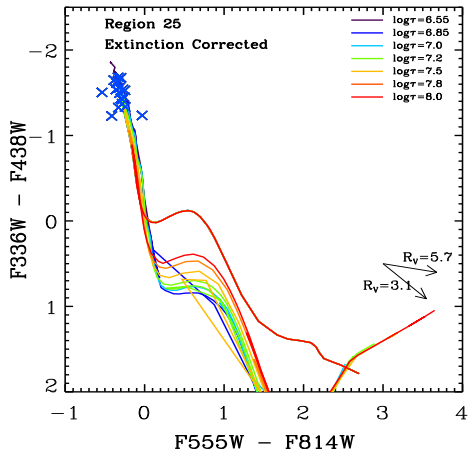
Region 25
Extinction Corrected
logτ=6.55
logτ=6.85
logτ=7.0
logτ=7.2
logτ=7.5
logτ=7.8
logτ=8.0
R_V=5.7
R_V=3.1
F336W − F438W
F555W − F814W

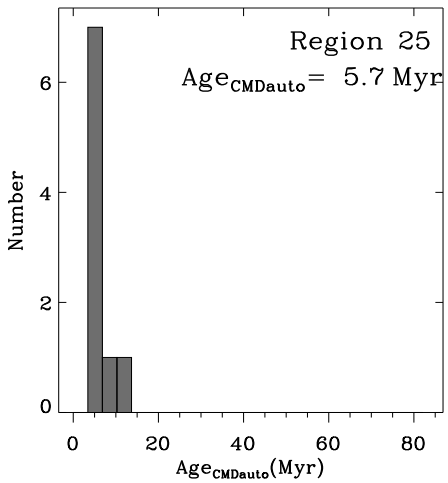
Region 25
Age_CMDauto= 5.7 Myr
Number
Age_CMDauto(Myr)

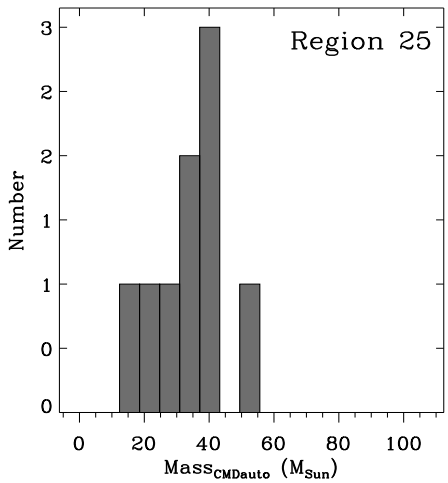
Region 25
Number
Mass_CMDauto (M_Sun)

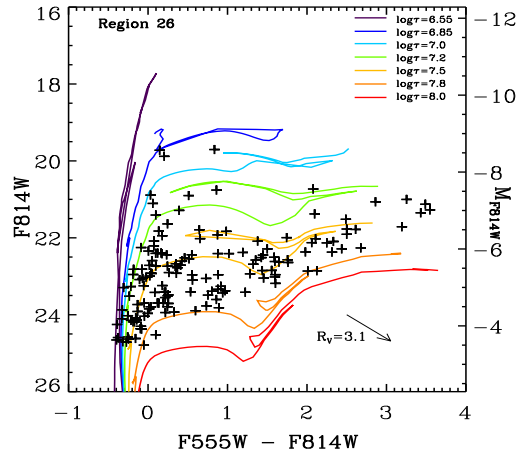
Region 26
logτ=6.55
logτ=6.85
logτ=7.0
logτ=7.2
logτ=7.5
logτ=7.8
logτ=8.0
R_V=3.1
F814W
M_F814W
F555W − F814W

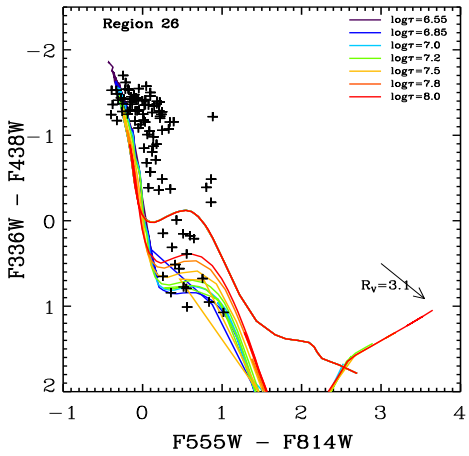
Region 26
logτ=6.55
logτ=6.85
logτ=7.0
logτ=7.2
logτ=7.5
logτ=7.8
logτ=8.0
R_V=3.1
F336W − F438W
F555W − F814W

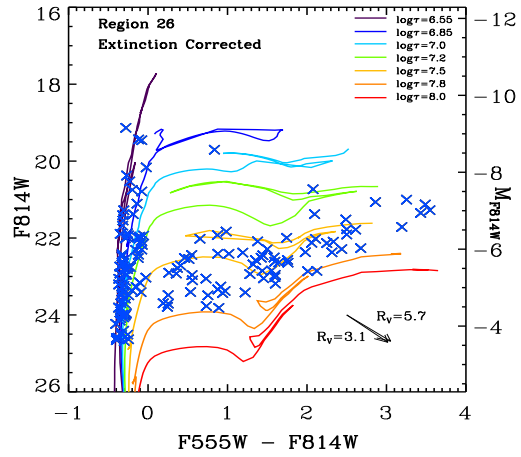
Region 26
Extinction Corrected
logτ=6.55
logτ=6.85
logτ=7.0
logτ=7.2
logτ=7.5
logτ=7.8
logτ=8.0
R_V=5.7
R_V=3.1
F814W
M_F814W
F555W − F814W

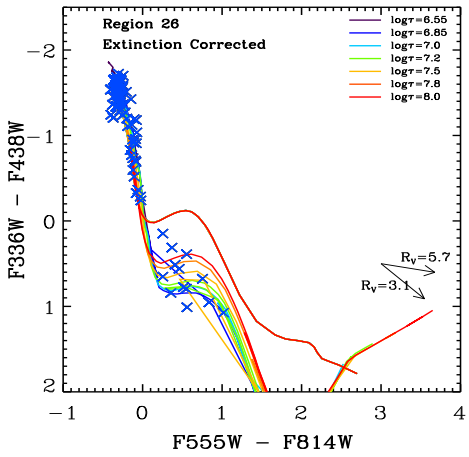
Region 26
Extinction Corrected
logτ=6.55
logτ=6.85
logτ=7.0
logτ=7.2
logτ=7.5
logτ=7.8
logτ=8.0
R_V=5.7
R_V=3.1
F336W − F438W
F555W − F814W

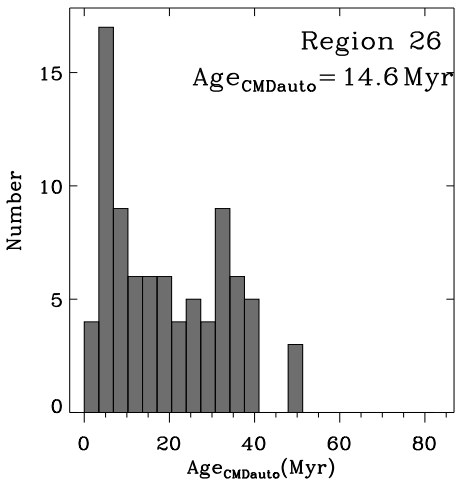
Region 26
Age_CMDauto = 14.6 Myr
Number
Age_CMDauto (Myr)

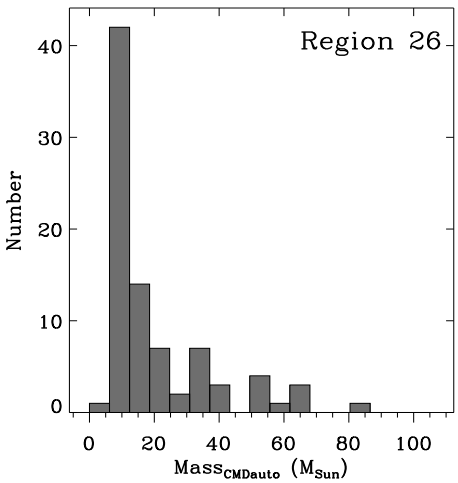
Region 26
Number
Mass_CMDauto (M_Sun)

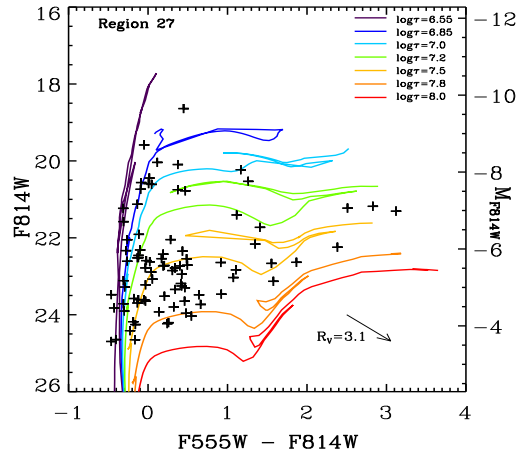
Region 27
logτ=6.55
logτ=6.85
logτ=7.0
logτ=7.2
logτ=7.5
logτ=7.8
logτ=8.0
R_V=3.1
F814W
M_F814W
F555W − F814W

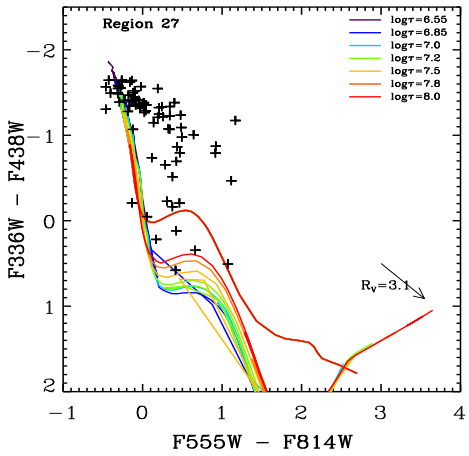
Region 27
logτ=6.55
logτ=6.85
logτ=7.0
logτ=7.2
logτ=7.5
logτ=7.8
logτ=8.0
R_V=3.1
F336W − F438W
F555W − F814W

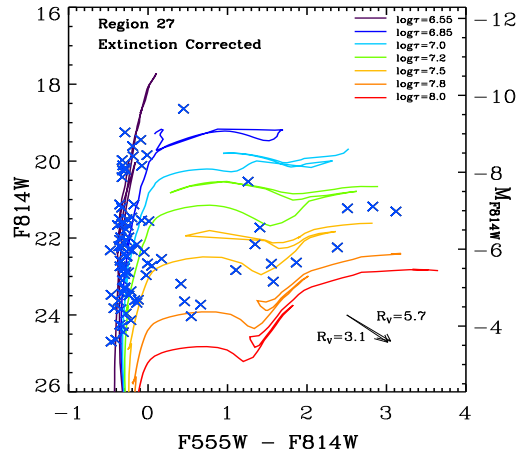
Region 27
Extinction Corrected
logτ=6.55
logτ=6.85
logτ=7.0
logτ=7.2
logτ=7.5
logτ=7.8
logτ=8.0
R_V=5.7
R_V=3.1
F814W
M_F814W
F555W − F814W

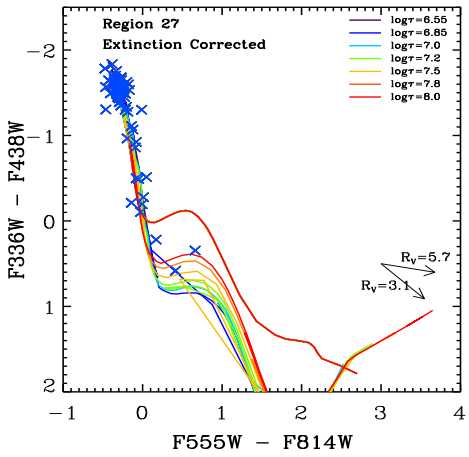
Region 27
Extinction Corrected
logτ=6.55
logτ=6.85
logτ=7.0
logτ=7.2
logτ=7.5
logτ=7.8
logτ=8.0
R_V=5.7
R_V=3.1
F336W − F438W
F555W − F814W

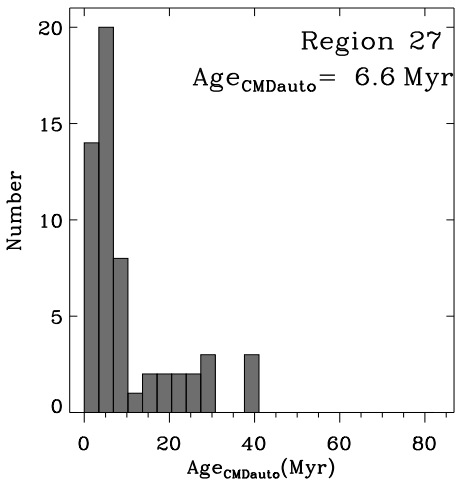
Region 27
Age_CMDauto= 6.6 Myr
Number
Age_CMDauto(Myr)

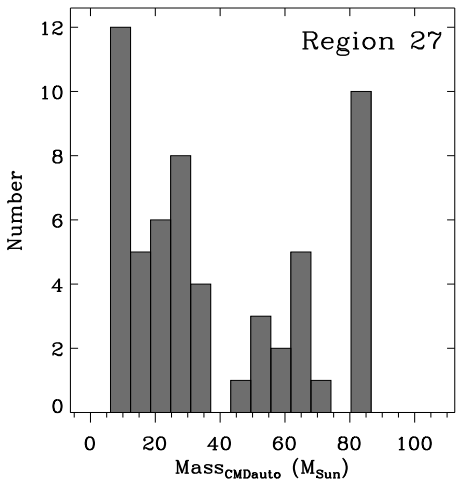
Region 27
Number
Mass_CMDauto (M_Sun)

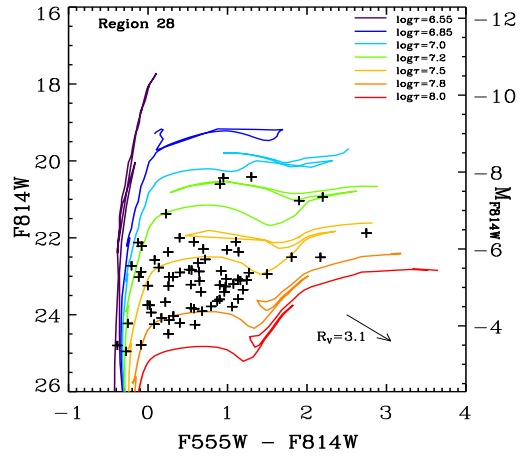
Region 28
logτ=6.55
logτ=6.85
logτ=7.0
logτ=7.2
logτ=7.5
logτ=7.8
logτ=8.0
R_V=3.1
F814W
M_F814W
F555W − F814W

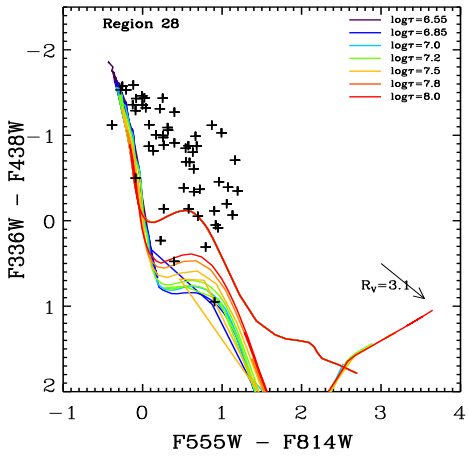
Region 28
logτ=6.55
logτ=6.85
logτ=7.0
logτ=7.2
logτ=7.5
logτ=7.8
logτ=8.0
R_V=3.1
F336W − F438W
F555W − F814W

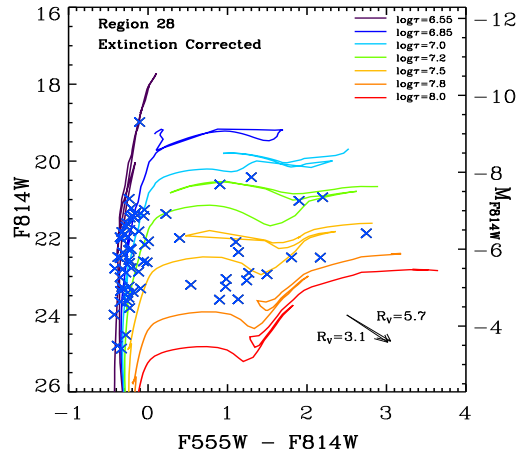
Region 28
Extinction Corrected
logτ=6.55
logτ=6.85
logτ=7.0
logτ=7.2
logτ=7.5
logτ=7.8
logτ=8.0
R_V=5.7
R_V=3.1
F814W
M_F814W
F555W − F814W

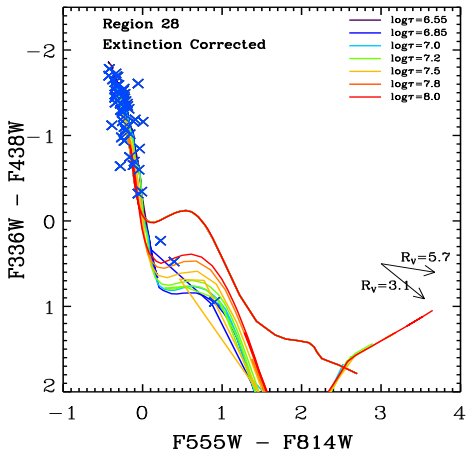
Region 28
Extinction Corrected
logτ=6.55
logτ=6.85
logτ=7.0
logτ=7.2
logτ=7.5
logτ=7.8
logτ=8.0
R_V=5.7
R_V=3.1
F336W − F438W
F555W − F814W

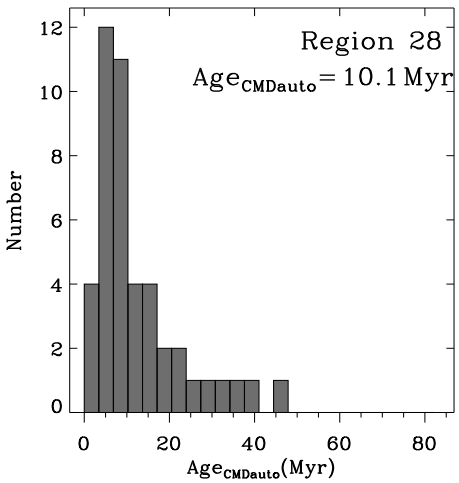
Region 28
Age_CMDauto = 10.1 Myr
Number
Age_CMDauto (Myr)

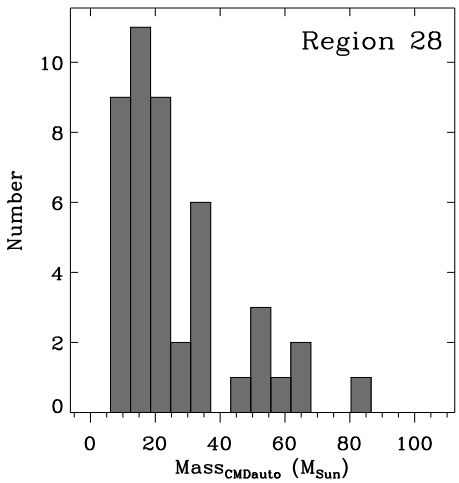
Region 28
Number
Mass_CMDauto (M_Sun)

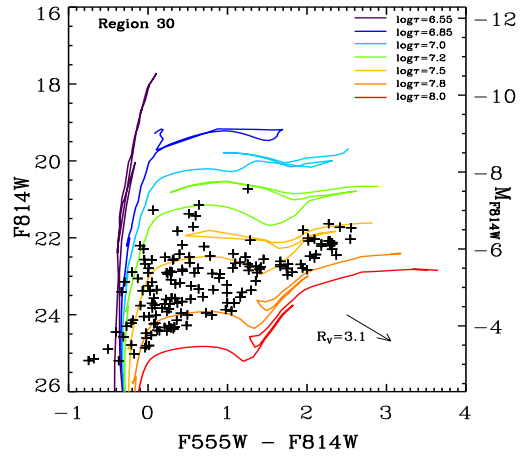
Region 30
logτ=6.55
logτ=6.85
logτ=7.0
logτ=7.2
logτ=7.5
logτ=7.8
logτ=8.0
R_V=3.1
F814W
M_F814W
F555W − F814W

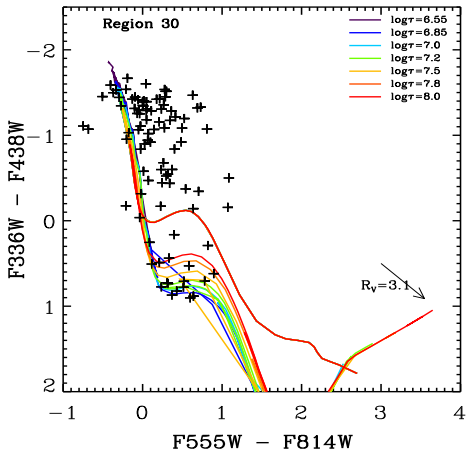
Region 30
logτ=6.55
logτ=6.85
logτ=7.0
logτ=7.2
logτ=7.5
logτ=7.8
logτ=8.0
R_V=3.1
F336W − F438W
F555W − F814W

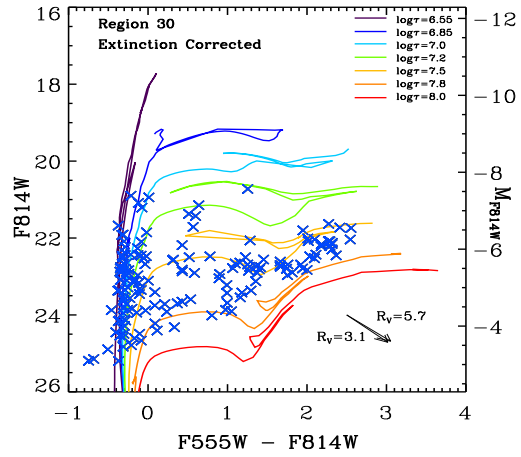
Region 30
Extinction Corrected
logτ=6.55
logτ=6.85
logτ=7.0
logτ=7.2
logτ=7.5
logτ=7.8
logτ=8.0
R_V=5.7
R_V=3.1
F814W
M_F814W
F555W − F814W

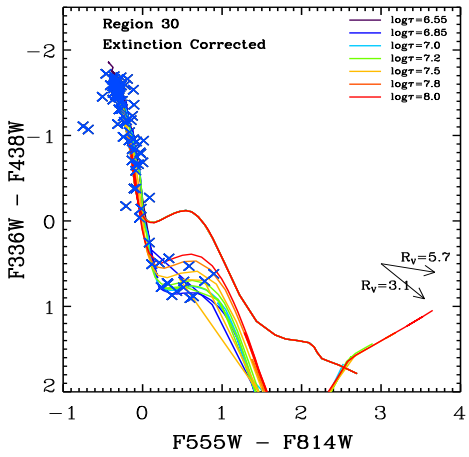
Region 30
Extinction Corrected
logτ=6.55
logτ=6.85
logτ=7.0
logτ=7.2
logτ=7.5
logτ=7.8
logτ=8.0
R_V=5.7
R_V=3.1
F336W − F438W
F555W − F814W

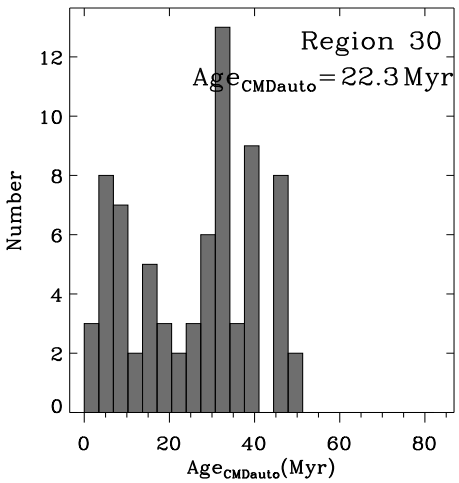
Region 30
Age_CMDauto = 22.3 Myr
Number
Age_CMDauto (Myr)

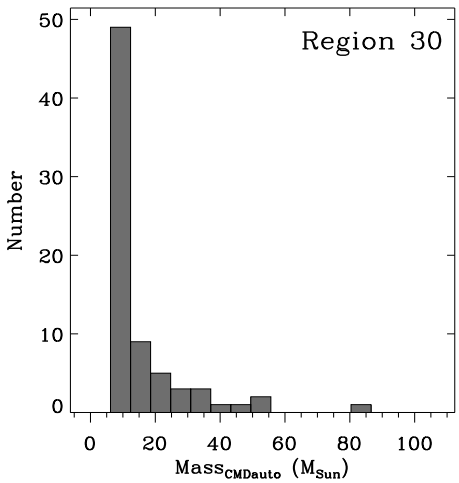
Region 30
Number
Mass_CMDauto (M_Sun)

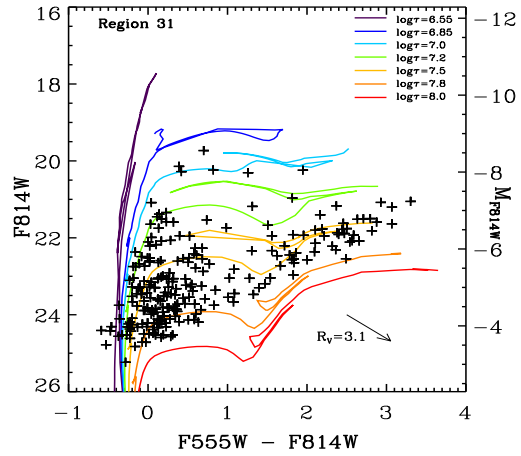
Region 31
logτ=6.55
logτ=6.85
logτ=7.0
logτ=7.2
logτ=7.5
logτ=7.8
logτ=8.0
R_V=3.1
F814W
M_F814W
F555W − F814W

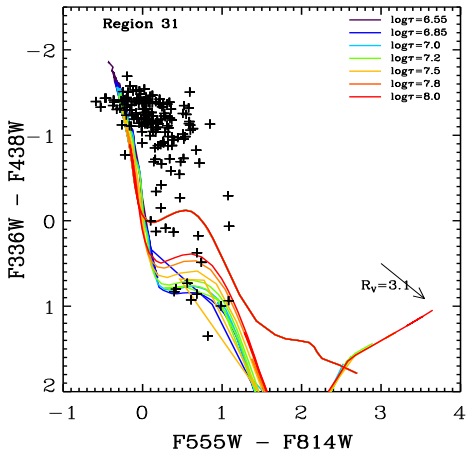
Region 31
logτ=6.55
logτ=6.85
logτ=7.0
logτ=7.2
logτ=7.5
logτ=7.8
logτ=8.0
R_V=3.1
F336W − F438W
F555W − F814W

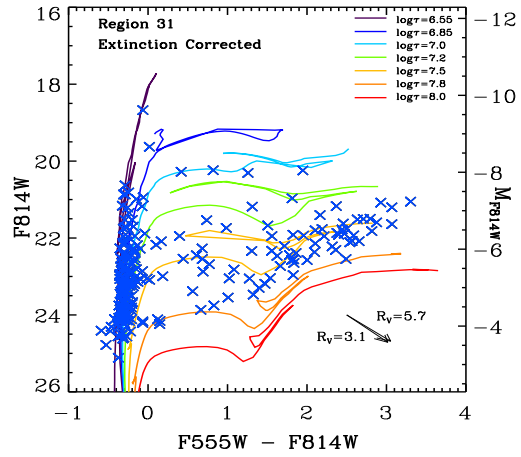
Region 31
Extinction Corrected
logτ=6.55
logτ=6.85
logτ=7.0
logτ=7.2
logτ=7.5
logτ=7.8
logτ=8.0
R_V=5.7
R_V=3.1
F814W
M_F814W
F555W − F814W

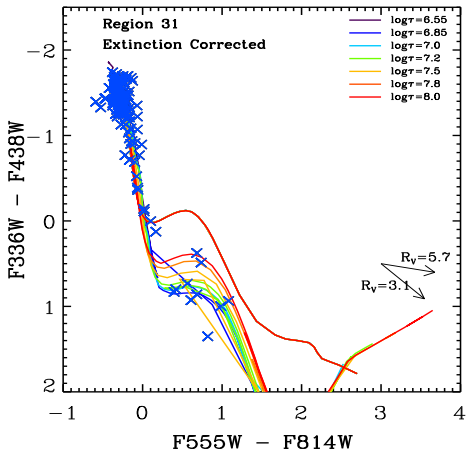
Region 31
Extinction Corrected
logτ=6.55
logτ=6.85
logτ=7.0
logτ=7.2
logτ=7.5
logτ=7.8
logτ=8.0
R_V=5.7
R_V=3.1
F336W − F438W
F555W − F814W

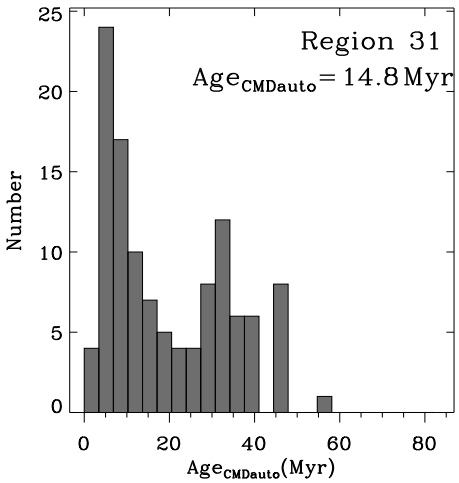
Region 31
Age_CMDauto = 14.8 Myr
Number
Age_CMDauto (Myr)

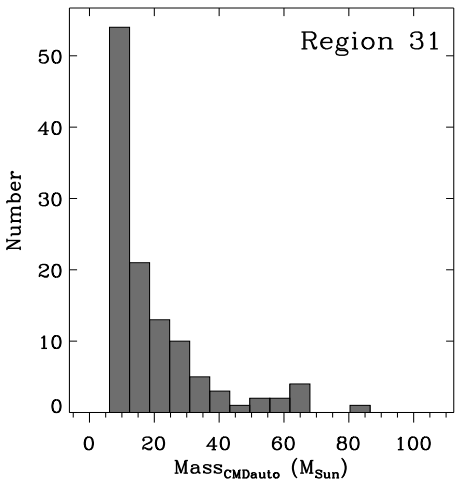
Region 31
Number
Mass_CMDauto (M_Sun)

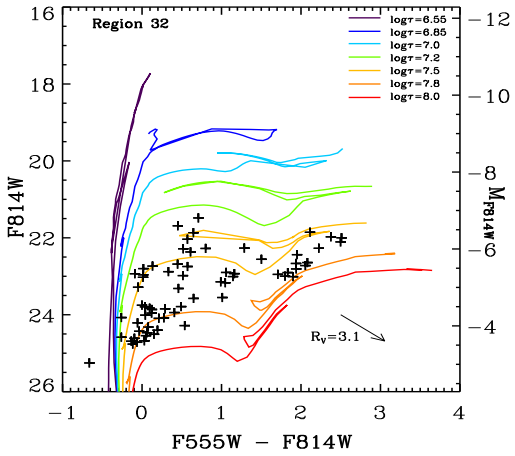
Region 32
logτ=6.55
logτ=6.85
logτ=7.0
logτ=7.2
logτ=7.5
logτ=7.8
logτ=8.0
R_V=3.1
F814W
M_F814W
F555W − F814W

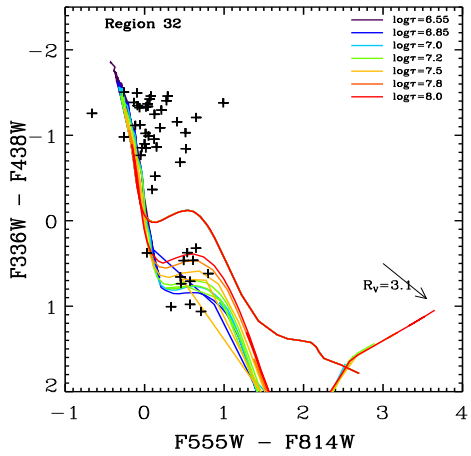
Region 32
logτ=6.55
logτ=6.85
logτ=7.0
logτ=7.2
logτ=7.5
logτ=7.8
logτ=8.0
R_V=3.1
F336W − F438W
F555W − F814W

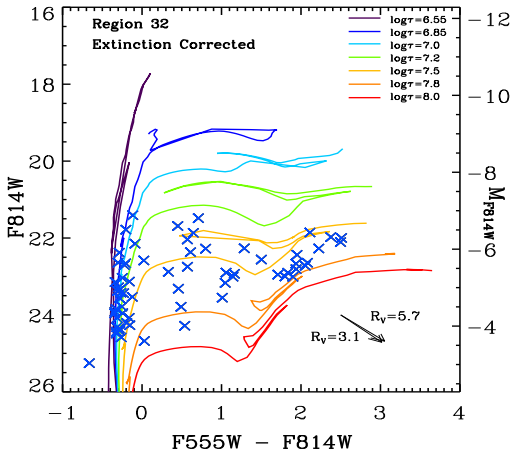
Region 32
Extinction Corrected
logτ=6.55
logτ=6.85
logτ=7.0
logτ=7.2
logτ=7.5
logτ=7.8
logτ=8.0
R_V=5.7
R_V=3.1
F814W
M_F814W
F555W − F814W

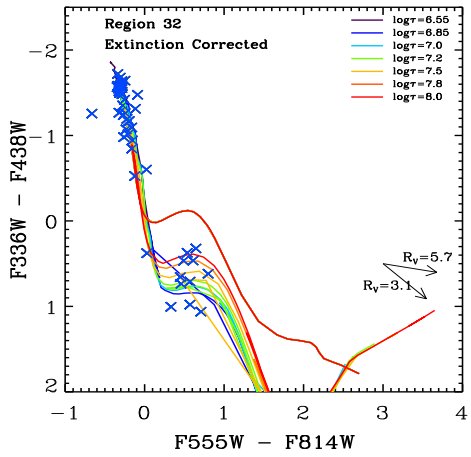
Region 32
Extinction Corrected
logτ=6.55
logτ=6.85
logτ=7.0
logτ=7.2
logτ=7.5
logτ=7.8
logτ=8.0
R_V=5.7
R_V=3.1
F336W − F438W
F555W − F814W

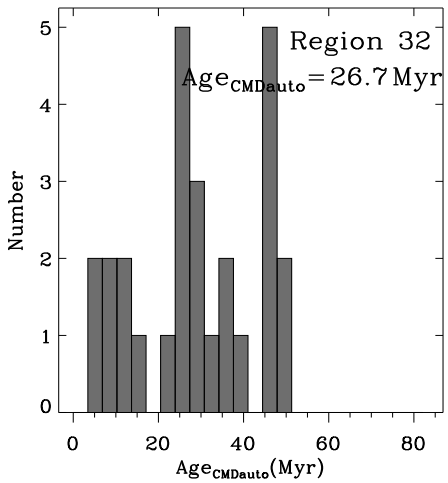
Region 32
Age_CMDauto=26.7 Myr
Number
Age_CMDauto(Myr)

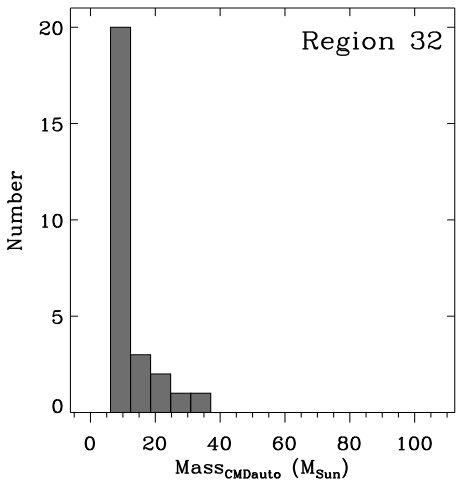
Region 32
Number
Mass_CMDauto (M_Sun)

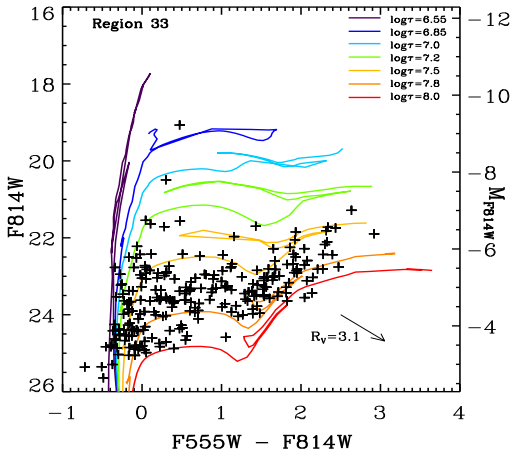
Region 33
logτ=6.55
logτ=6.85
logτ=7.0
logτ=7.2
logτ=7.5
logτ=7.8
logτ=8.0
R_V=3.1
F814W
M_F814W
F555W − F814W

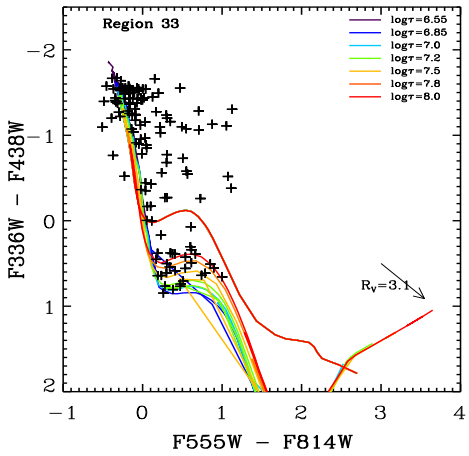
Region 33
logτ=6.55
logτ=6.85
logτ=7.0
logτ=7.2
logτ=7.5
logτ=7.8
logτ=8.0
R_V=3.1
F336W − F438W
F555W − F814W

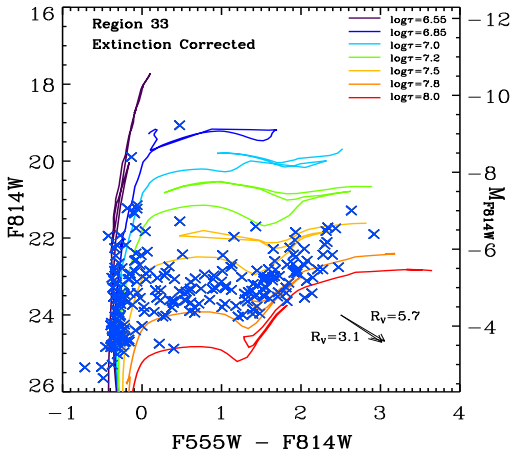
Region 33
Extinction Corrected
logτ=6.55
logτ=6.85
logτ=7.0
logτ=7.2
logτ=7.5
logτ=7.8
logτ=8.0
R_V=5.7
R_V=3.1
F814W
M_F814W
F555W − F814W

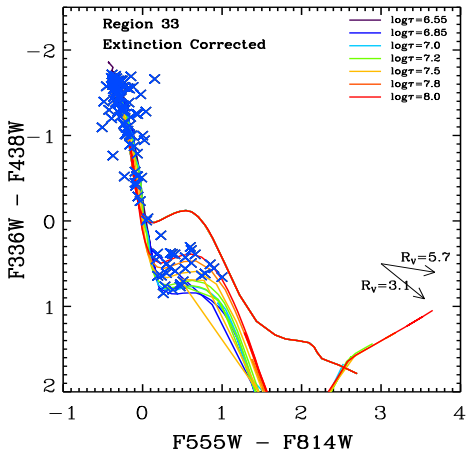
Region 33
Extinction Corrected
logτ=6.55
logτ=6.85
logτ=7.0
logτ=7.2
logτ=7.5
logτ=7.8
logτ=8.0
R_V=5.7
R_V=3.1
F336W − F438W
F555W − F814W

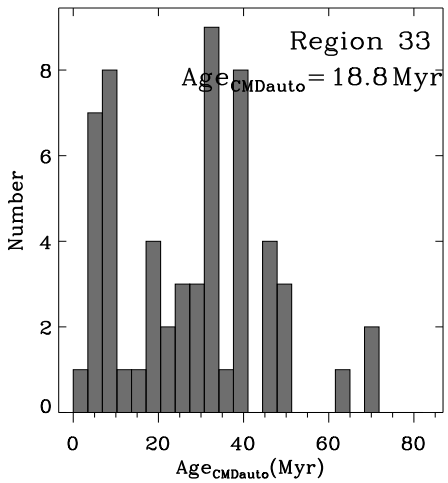
Region 33
Age_CMDauto = 18.8 Myr
Number
Age_CMDauto (Myr)

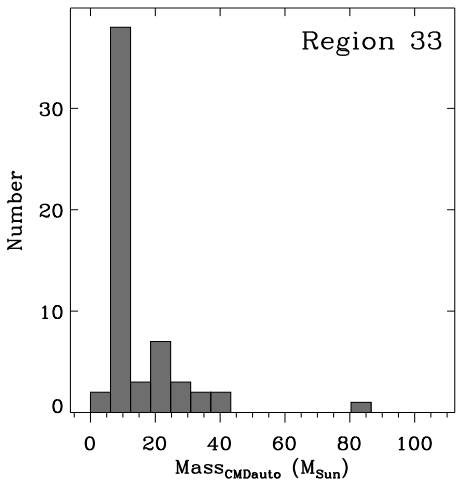
Region 33
Number
Mass_CMDauto (M_Sun)

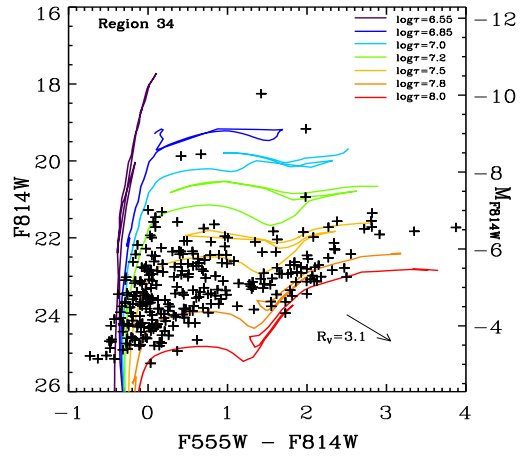
Region 34
logτ=6.55
logτ=6.85
logτ=7.0
logτ=7.2
logτ=7.5
logτ=7.8
logτ=8.0
R_V=3.1
F814W
M_F814W
F555W − F814W

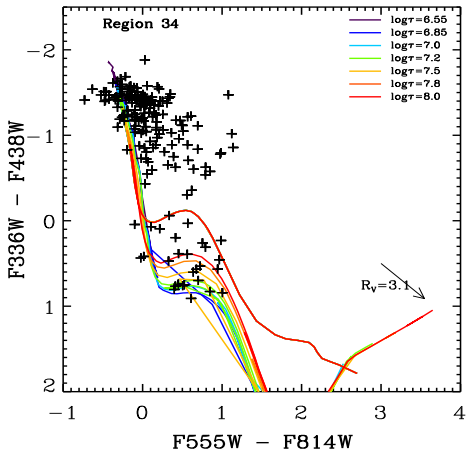
Region 34
logτ=6.55
logτ=6.85
logτ=7.0
logτ=7.2
logτ=7.5
logτ=7.8
logτ=8.0
R_V=3.1
F336W − F438W
F555W − F814W

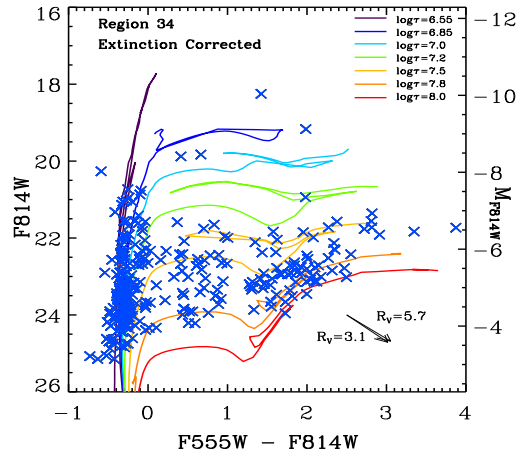
Region 34
Extinction Corrected
logτ=6.55
logτ=6.85
logτ=7.0
logτ=7.2
logτ=7.5
logτ=7.8
logτ=8.0
R_V=5.7
R_V=3.1
F814W
M_F814W
F555W − F814W

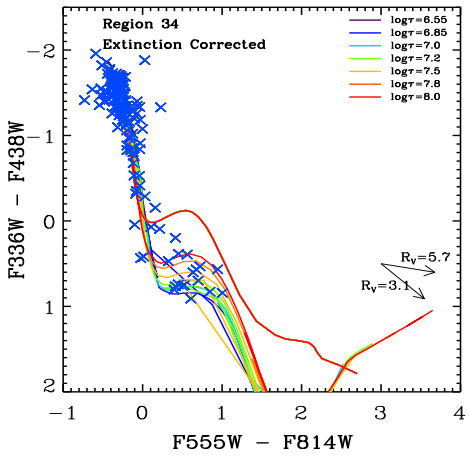
Region 34
Extinction Corrected
logτ=6.55
logτ=6.85
logτ=7.0
logτ=7.2
logτ=7.5
logτ=7.8
logτ=8.0
R_V=5.7
R_V=3.1
F336W − F438W
F555W − F814W

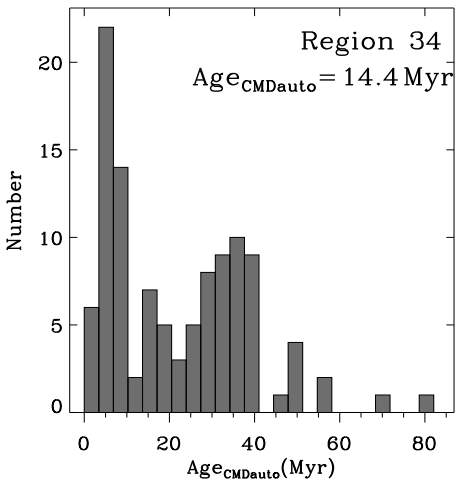
Region 34
Age_CMDauto = 14.4 Myr
Number
Age_CMDauto (Myr)

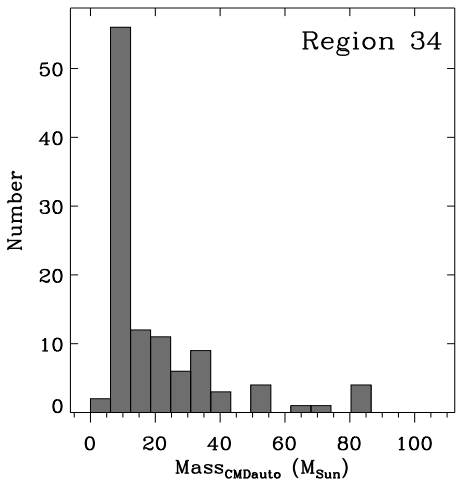
Region 34
Number
Mass_CMDauto (M_Sun)

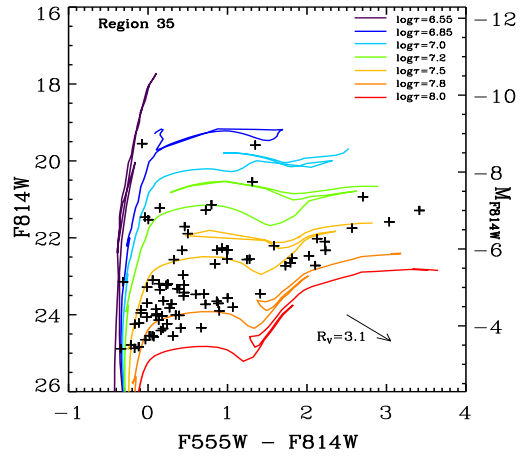
Region 35
logτ=6.55
logτ=6.85
logτ=7.0
logτ=7.2
logτ=7.5
logτ=7.8
logτ=8.0
R_V=3.1
F814W
M_F814W
F555W − F814W

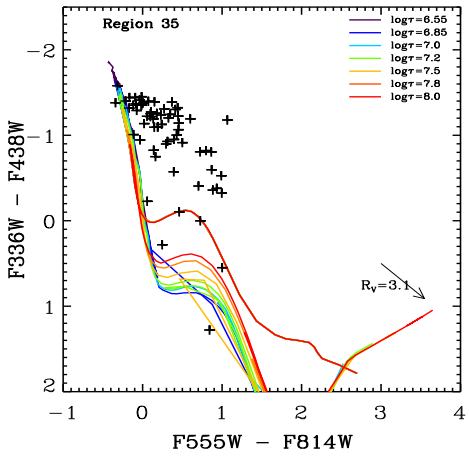
Region 35
logτ=6.55
logτ=6.85
logτ=7.0
logτ=7.2
logτ=7.5
logτ=7.8
logτ=8.0
R_V=3.1
F336W − F438W
F555W − F814W

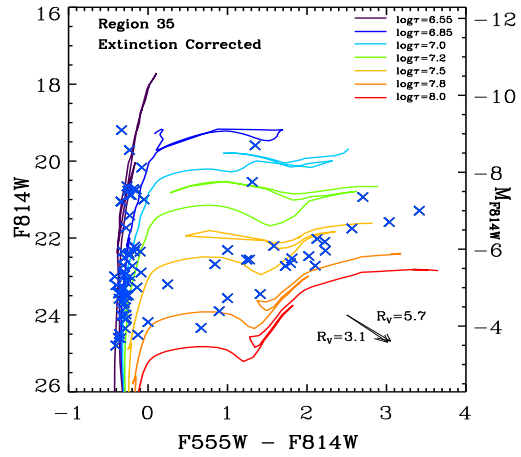
Region 35
Extinction Corrected
logτ=6.55
logτ=6.85
logτ=7.0
logτ=7.2
logτ=7.5
logτ=7.8
logτ=8.0
R_V=5.7
R_V=3.1
F814W
M_F814W
F555W − F814W

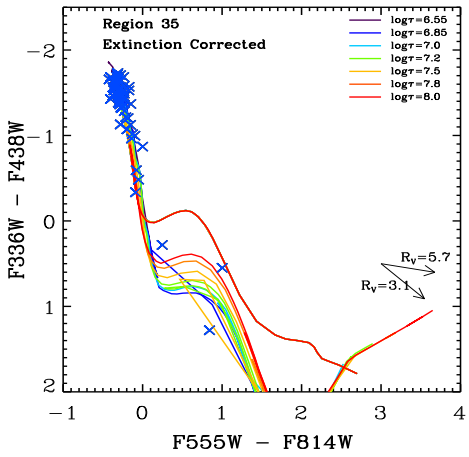
Region 35
Extinction Corrected
logτ=6.55
logτ=6.85
logτ=7.0
logτ=7.2
logτ=7.5
logτ=7.8
logτ=8.0
R_V=5.7
R_V=3.1
F336W − F438W
F555W − F814W

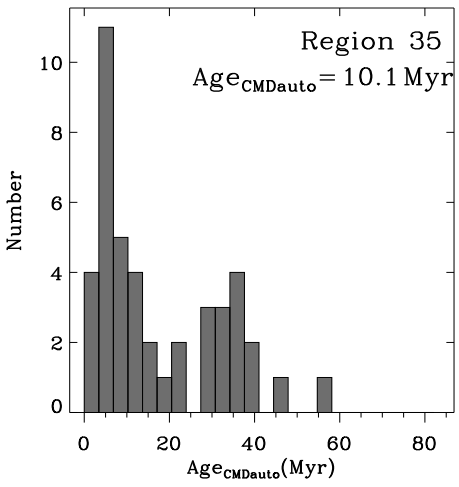
Region 35
Age_CMDauto = 10.1 Myr
Number
Age_CMDauto (Myr)

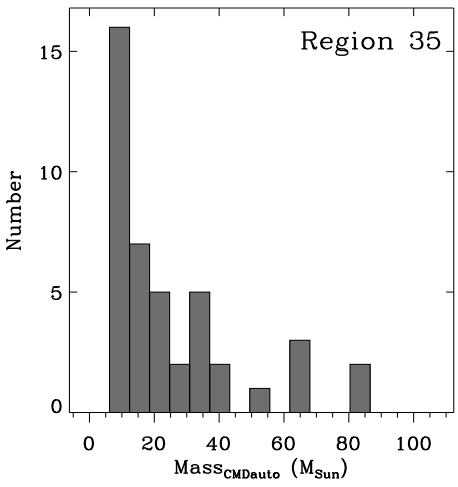
Region 35
Number
Mass_CMDauto (M_Sun)

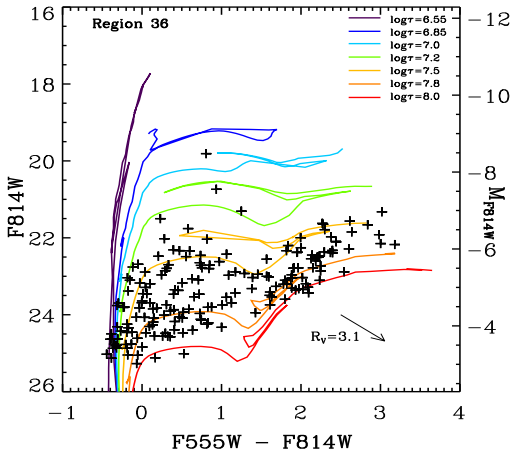
Region 36
logτ=6.55
logτ=6.85
logτ=7.0
logτ=7.2
logτ=7.5
logτ=7.8
logτ=8.0
R_V=3.1
F814W
M_F814W
F555W − F814W

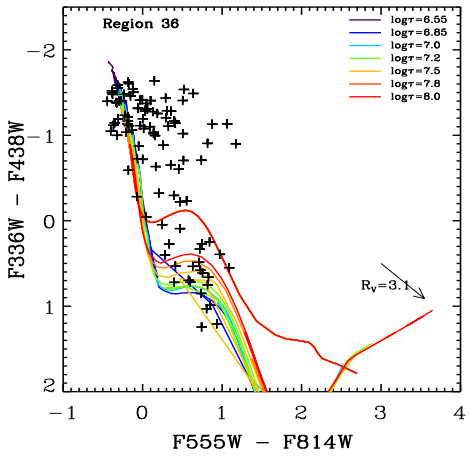
Region 36
logτ=6.55
logτ=6.85
logτ=7.0
logτ=7.2
logτ=7.5
logτ=7.8
logτ=8.0
R_V=3.1
F336W − F438W
F555W − F814W

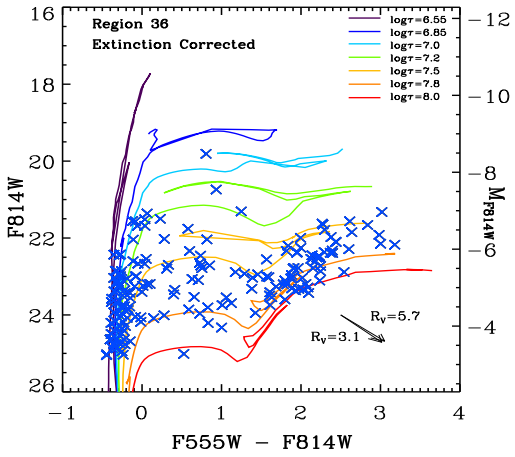
Region 36
Extinction Corrected
logτ=6.55
logτ=6.85
logτ=7.0
logτ=7.2
logτ=7.5
logτ=7.8
logτ=8.0
R_V=5.7
R_V=3.1
F814W
M_F814W
F555W − F814W

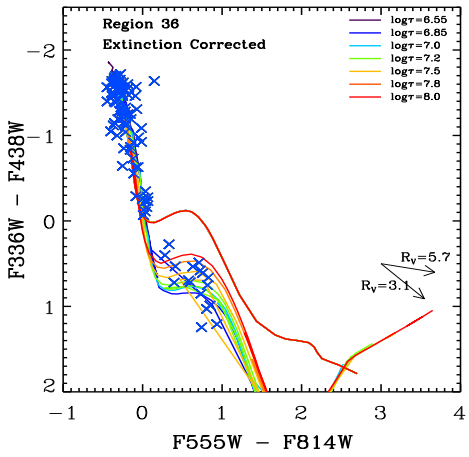
Region 36
Extinction Corrected
logτ=6.55
logτ=6.85
logτ=7.0
logτ=7.2
logτ=7.5
logτ=7.8
logτ=8.0
R_V=5.7
R_V=3.1
F336W − F438W
F555W − F814W

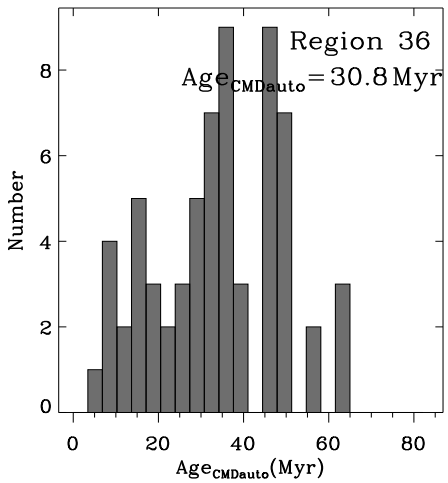
Region 36
Age_CMDauto = 30.8 Myr
Number
Age_CMDauto (Myr)

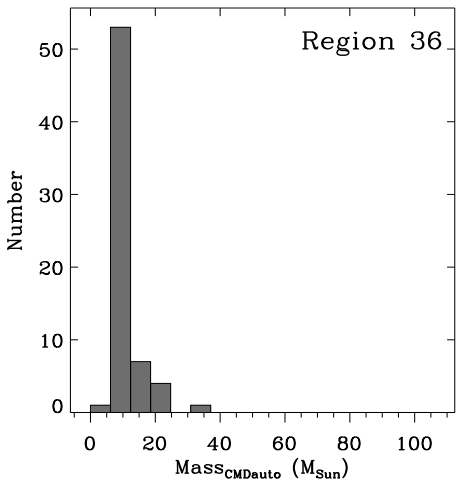
Region 36
Number
Mass_CMDauto (M_Sun)

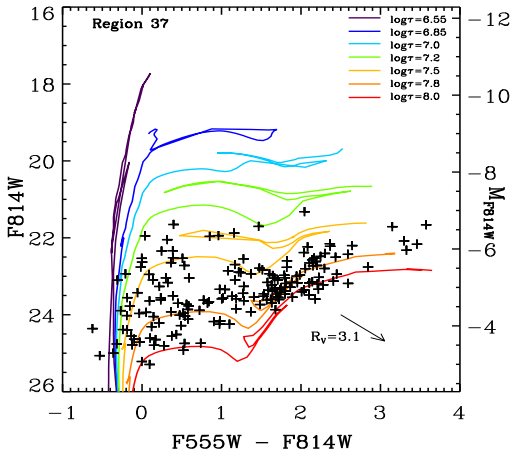
Region 37
logτ=6.55
logτ=6.85
logτ=7.0
logτ=7.2
logτ=7.5
logτ=7.8
logτ=8.0
R_V=3.1
F814W
M_F814W
F555W − F814W

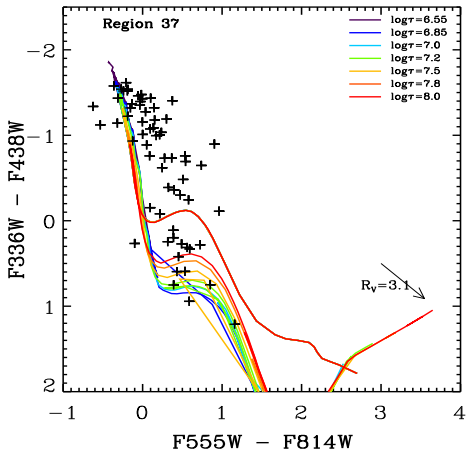
Region 37
logτ=6.55
logτ=6.85
logτ=7.0
logτ=7.2
logτ=7.5
logτ=7.8
logτ=8.0
R_V=3.1
F336W − F438W
F555W − F814W

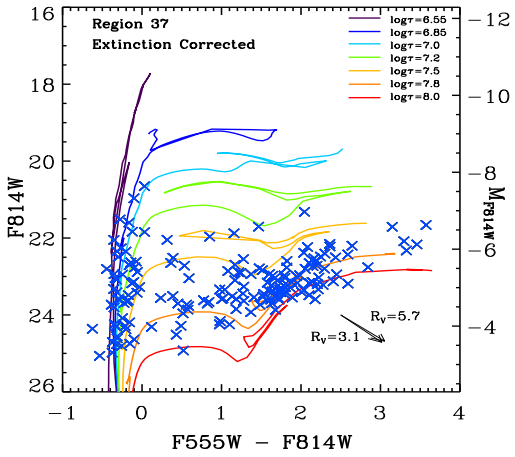
Region 37
Extinction Corrected
logτ=6.55
logτ=6.85
logτ=7.0
logτ=7.2
logτ=7.5
logτ=7.8
logτ=8.0
R_V=5.7
R_V=3.1
F814W
M_F814W
F555W − F814W

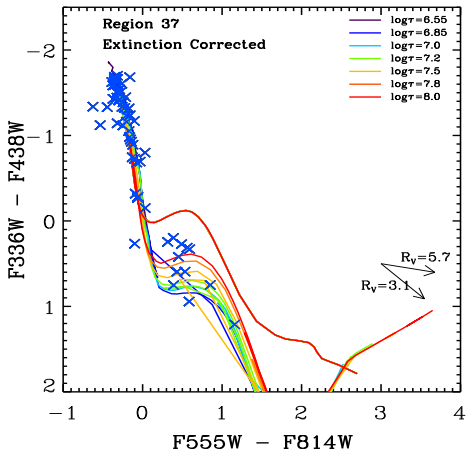
Region 37
Extinction Corrected
logτ=6.55
logτ=6.85
logτ=7.0
logτ=7.2
logτ=7.5
logτ=7.8
logτ=8.0
R_V=5.7
R_V=3.1
F336W − F438W
F555W − F814W

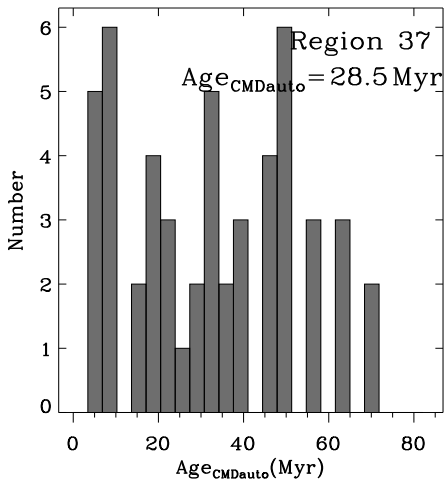
Region 37
Age_CMDauto = 28.5 Myr
Number
Age_CMDauto (Myr)

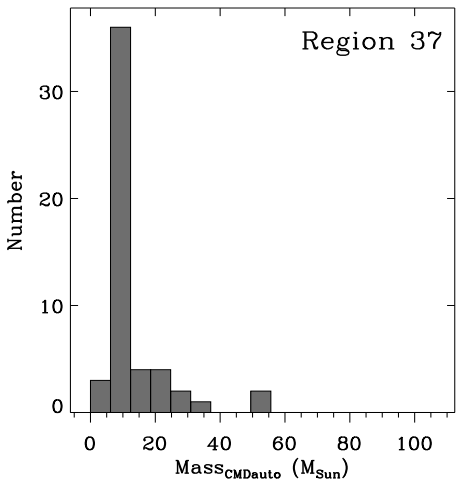
Region 37
Number
Mass_CMDauto (M_Sun)

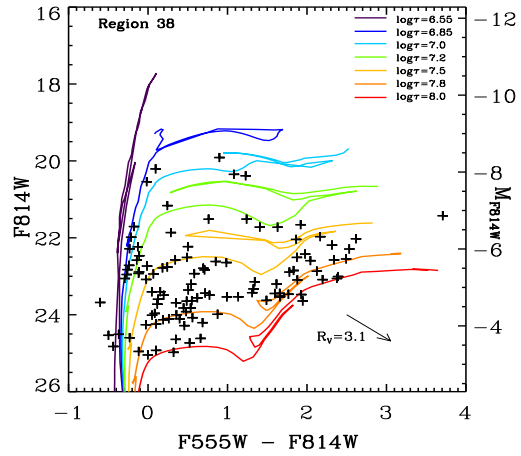
Region 38
logτ=6.55
logτ=6.85
logτ=7.0
logτ=7.2
logτ=7.5
logτ=7.8
logτ=8.0
R_V=3.1
F814W
M_F814W
F555W − F814W

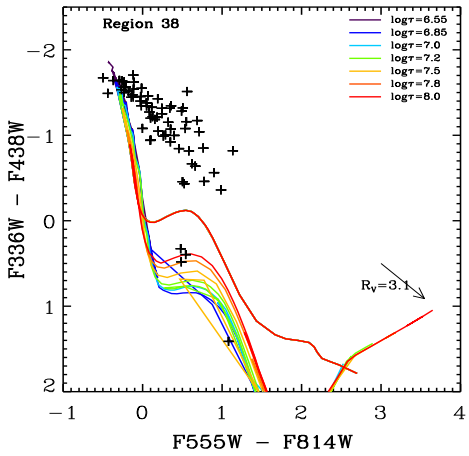
Region 38
logτ=6.55
logτ=6.85
logτ=7.0
logτ=7.2
logτ=7.5
logτ=7.8
logτ=8.0
R_V=3.1
F336W − F438W
F555W − F814W

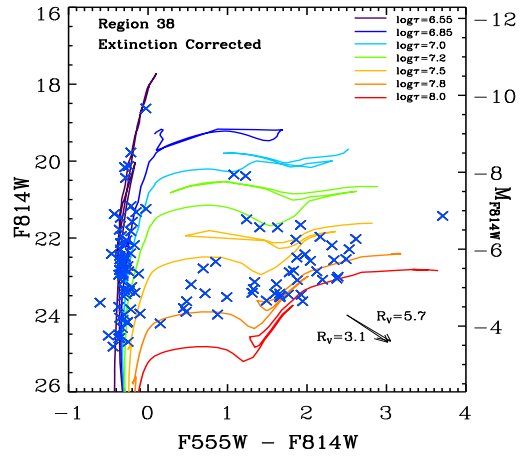
Region 38
Extinction Corrected
logτ=6.55
logτ=6.85
logτ=7.0
logτ=7.2
logτ=7.5
logτ=7.8
logτ=8.0
R_V=5.7
R_V=3.1
F814W
M_F814W
F555W − F814W

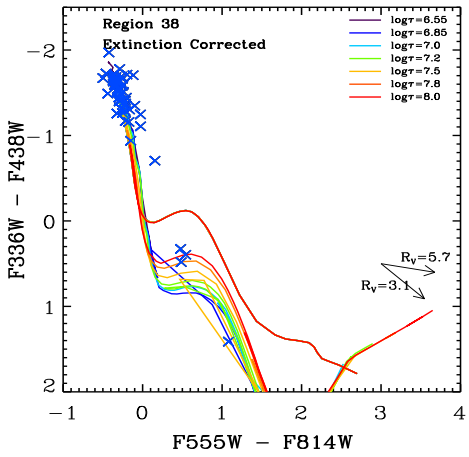
Region 38
Extinction Corrected
logτ=6.55
logτ=6.85
logτ=7.0
logτ=7.2
logτ=7.5
logτ=7.8
logτ=8.0
R_V=5.7
R_V=3.1
F336W − F438W
F555W − F814W

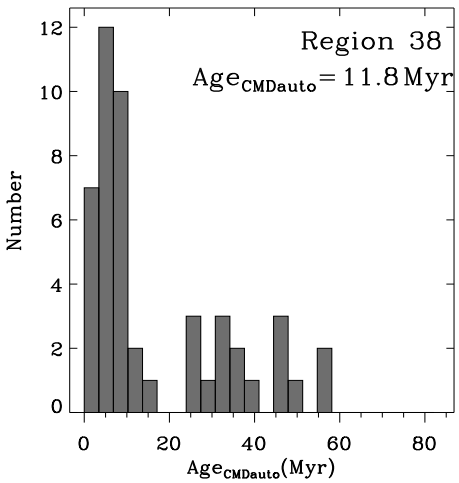
Region 38
Age_CMDauto = 11.8 Myr
Number
Age_CMDauto (Myr)

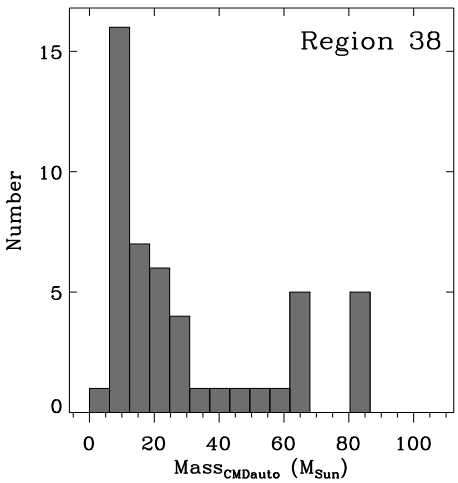
Region 38
Number
Mass_CMDauto (M_Sun)

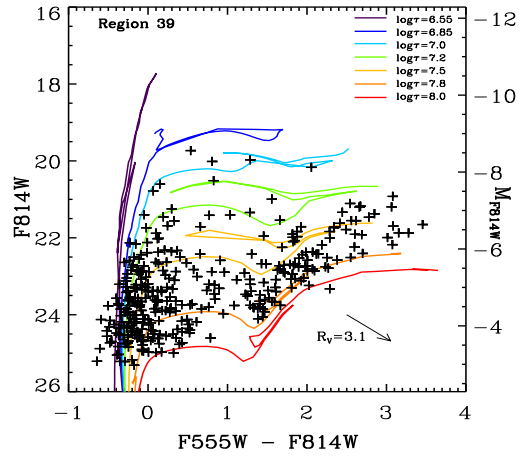
Region 39
logτ=6.55
logτ=6.85
logτ=7.0
logτ=7.2
logτ=7.5
logτ=7.8
logτ=8.0
R_V=3.1
F814W
M_F814W
F555W − F814W

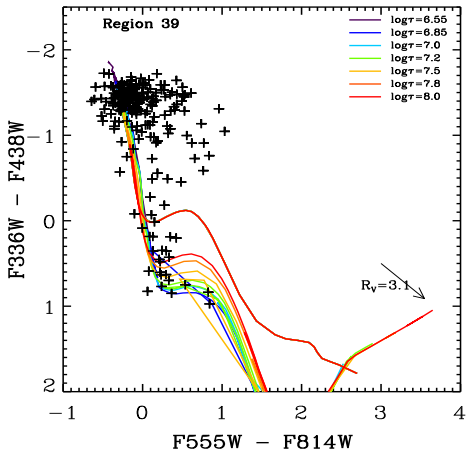
Region 39
logτ=6.55
logτ=6.85
logτ=7.0
logτ=7.2
logτ=7.5
logτ=7.8
logτ=8.0
R_V=3.1
F336W − F438W
F555W − F814W

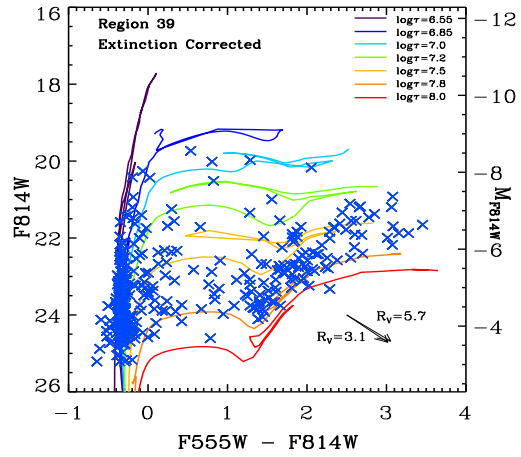
Region 39
Extinction Corrected
logτ=6.55
logτ=6.85
logτ=7.0
logτ=7.2
logτ=7.5
logτ=7.8
logτ=8.0
R_V=5.7
R_V=3.1
F814W
M_F814W
F555W − F814W

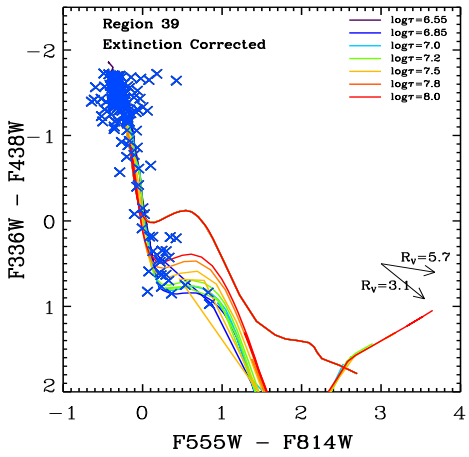
Region 39
Extinction Corrected
logτ=6.55
logτ=6.85
logτ=7.0
logτ=7.2
logτ=7.5
logτ=7.8
logτ=8.0
R_V=5.7
R_V=3.1
F336W − F438W
F555W − F814W

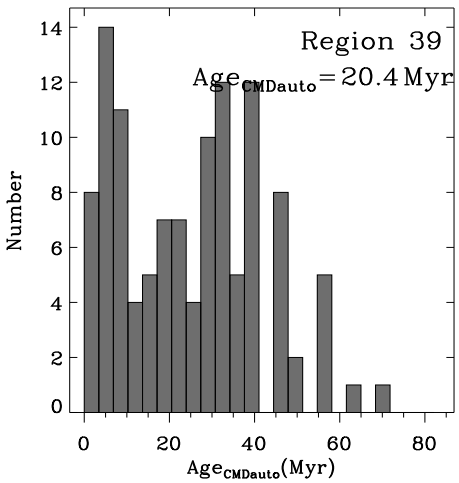
Region 39
Age_CMDauto = 20.4 Myr
Number
Age_CMDauto (Myr)

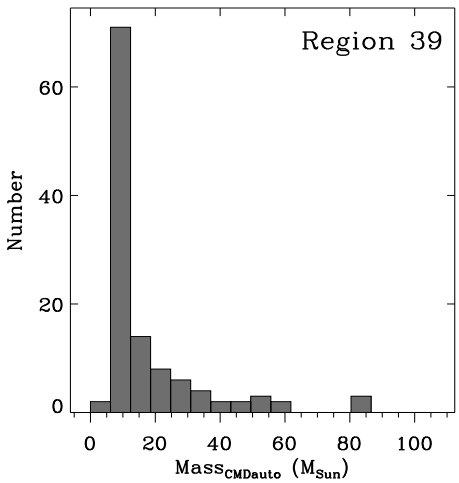
Region 39
Number
Mass_CMDauto (M_Sun)

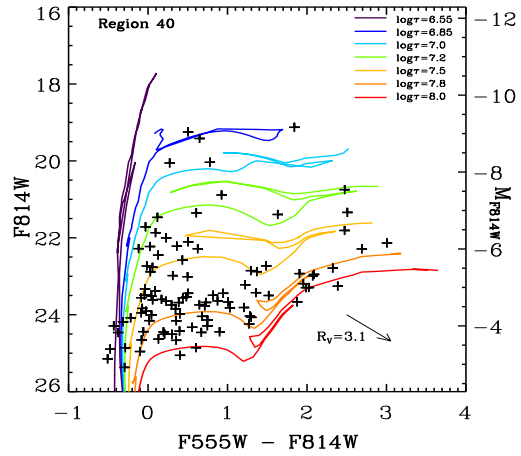
Region 40
logτ=6.55
logτ=6.85
logτ=7.0
logτ=7.2
logτ=7.5
logτ=7.8
logτ=8.0
R_V=3.1
F814W
M_F814W
F555W − F814W

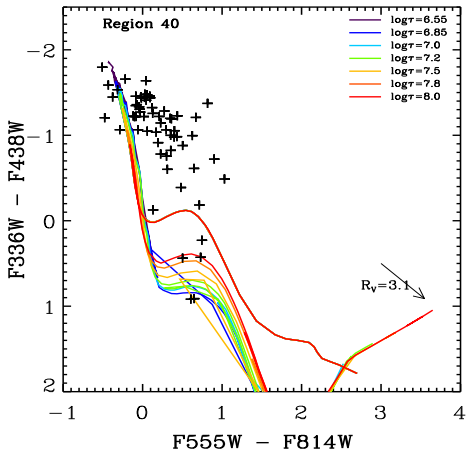
Region 40
logτ=6.55
logτ=6.85
logτ=7.0
logτ=7.2
logτ=7.5
logτ=7.8
logτ=8.0
R_V=3.1
F336W − F438W
F555W − F814W

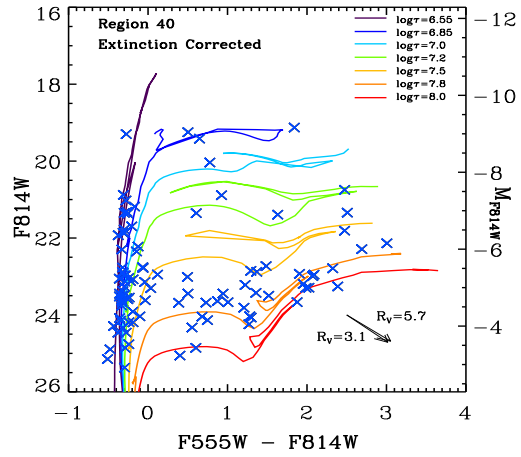
Region 40
Extinction Corrected
logτ=6.55
logτ=6.85
logτ=7.0
logτ=7.2
logτ=7.5
logτ=7.8
logτ=8.0
R_V=5.7
R_V=3.1
F814W
M_F814W
F555W − F814W

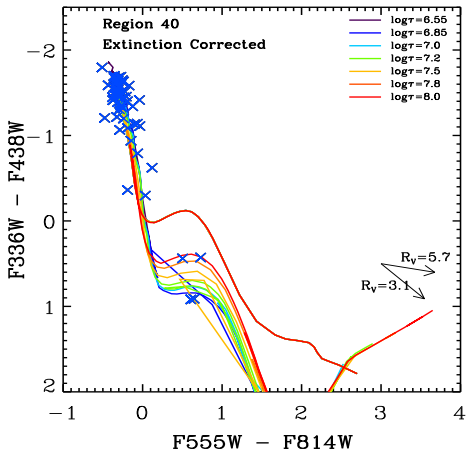
Region 40
Extinction Corrected
logτ=6.55
logτ=6.85
logτ=7.0
logτ=7.2
logτ=7.5
logτ=7.8
logτ=8.0
R_V=5.7
R_V=3.1
F336W − F438W
F555W − F814W

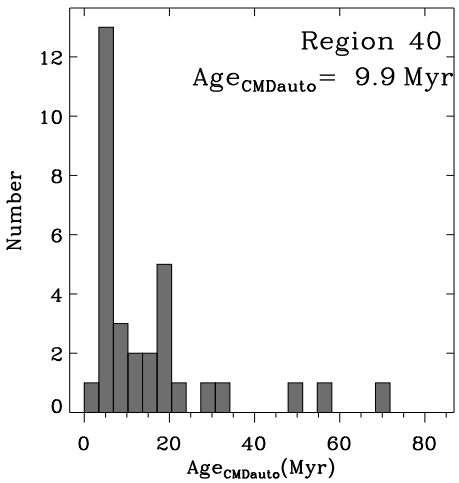
Region 40
Age_CMDauto= 9.9 Myr
Number
Age_CMDauto(Myr)

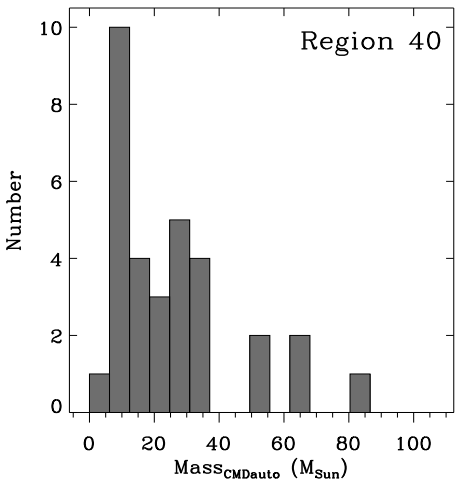
Region 40
Number
Mass_CMDauto (M_Sun)

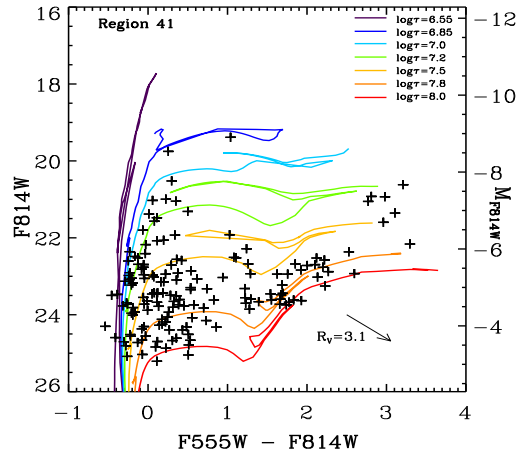
Region 41
logτ=6.55
logτ=6.85
logτ=7.0
logτ=7.2
logτ=7.5
logτ=7.8
logτ=8.0
R_V=3.1
F814W
M_F814W
F555W − F814W

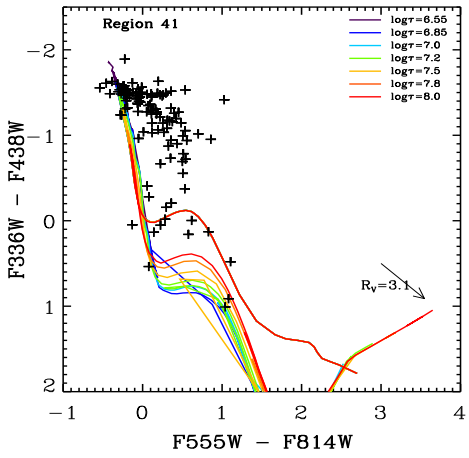
Region 41
logτ=6.55
logτ=6.85
logτ=7.0
logτ=7.2
logτ=7.5
logτ=7.8
logτ=8.0
R_V=3.1
F336W − F438W
F555W − F814W

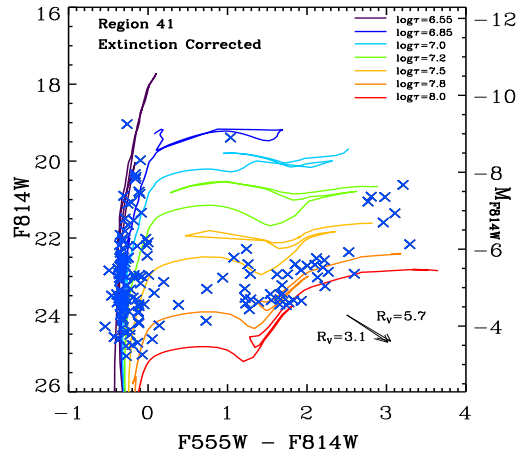
Region 41
Extinction Corrected
logτ=6.55
logτ=6.85
logτ=7.0
logτ=7.2
logτ=7.5
logτ=7.8
logτ=8.0
R_V=5.7
R_V=3.1
F814W
M_F814W
F555W − F814W

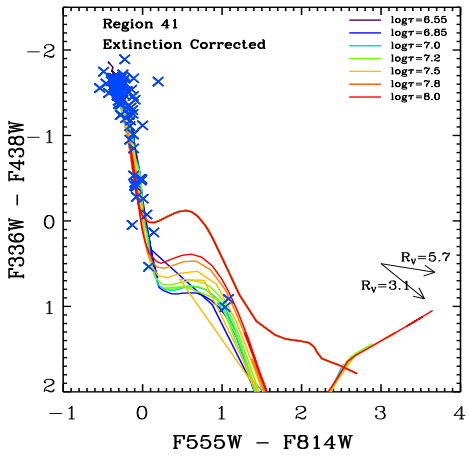
Region 41
Extinction Corrected
logτ=6.55
logτ=6.85
logτ=7.0
logτ=7.2
logτ=7.5
logτ=7.8
logτ=8.0
R_V=5.7
R_V=3.1
F336W − F438W
F555W − F814W

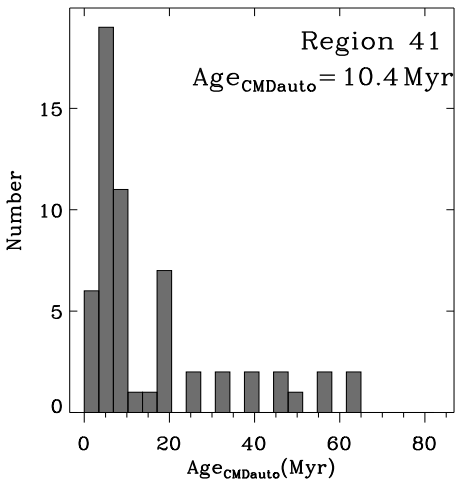
Region 41
Age_CMDauto = 10.4 Myr
Number
Age_CMDauto (Myr)

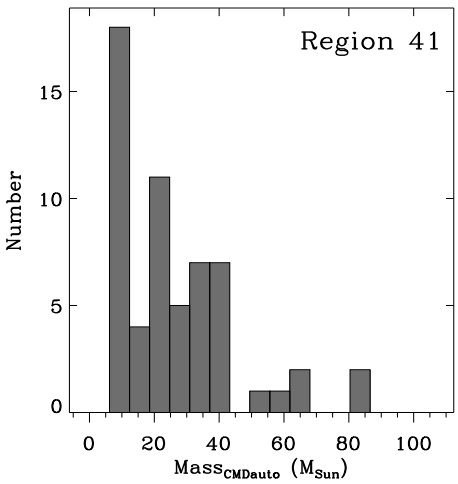
Region 41
Number
Mass_CMDauto (M_Sun)

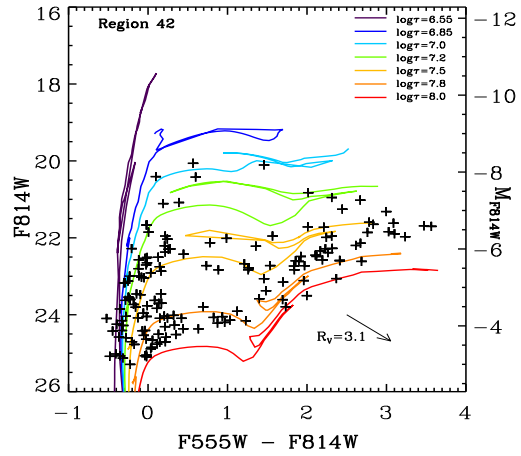
Region 42
logτ=6.55
logτ=6.85
logτ=7.0
logτ=7.2
logτ=7.5
logτ=7.8
logτ=8.0
R_V=3.1
F814W
M_F814W
F555W − F814W

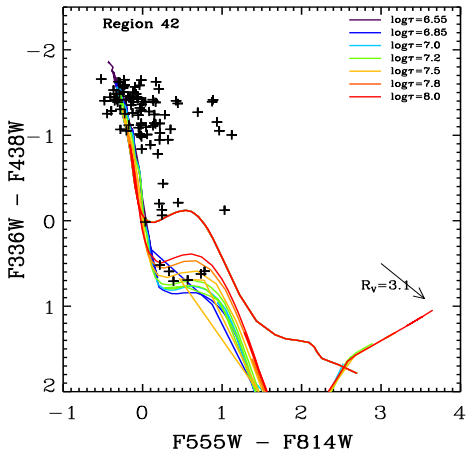
Region 42
logτ=6.55
logτ=6.85
logτ=7.0
logτ=7.2
logτ=7.5
logτ=7.8
logτ=8.0
R_V=3.1
F336W − F438W
F555W − F814W

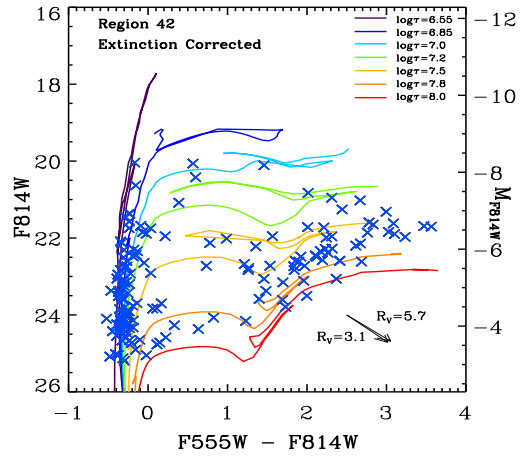
Region 42
Extinction Corrected
logτ=6.55
logτ=6.85
logτ=7.0
logτ=7.2
logτ=7.5
logτ=7.8
logτ=8.0
R_V=5.7
R_V=3.1
F814W
M_F814W
F555W − F814W

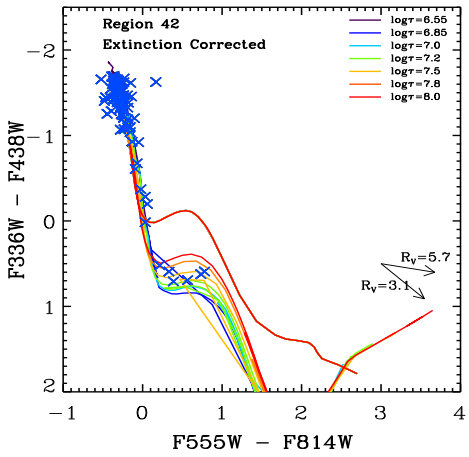
Region 42
Extinction Corrected
logτ=6.55
logτ=6.85
logτ=7.0
logτ=7.2
logτ=7.5
logτ=7.8
logτ=8.0
R_V=5.7
R_V=3.1
F336W − F438W
F555W − F814W

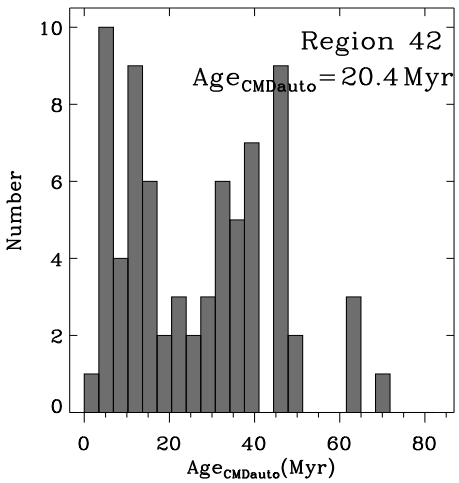
Region 42
Age_CMDauto=20.4 Myr
Number
Age_CMDauto(Myr)

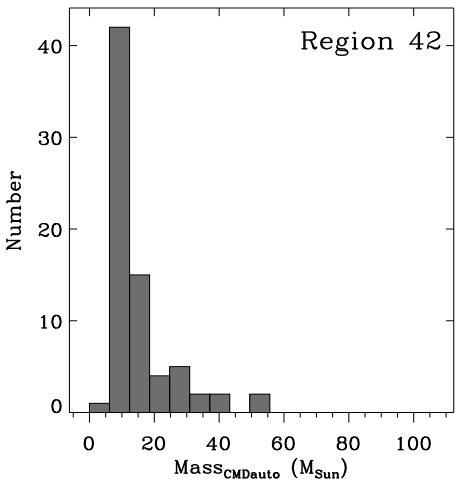
Region 42
Number
Mass_CMDauto (M_Sun)

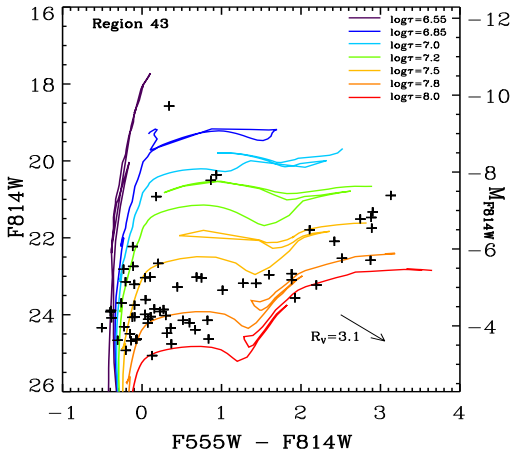
Region 43
logτ=6.55
logτ=6.85
logτ=7.0
logτ=7.2
logτ=7.5
logτ=7.8
logτ=8.0
R_V=3.1
F814W
M_F814W
F555W − F814W

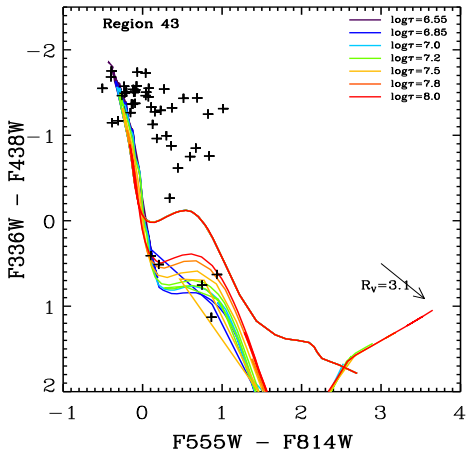
Region 43
logτ=6.55
logτ=6.85
logτ=7.0
logτ=7.2
logτ=7.5
logτ=7.8
logτ=8.0
R_V=3.1
F336W − F438W
F555W − F814W

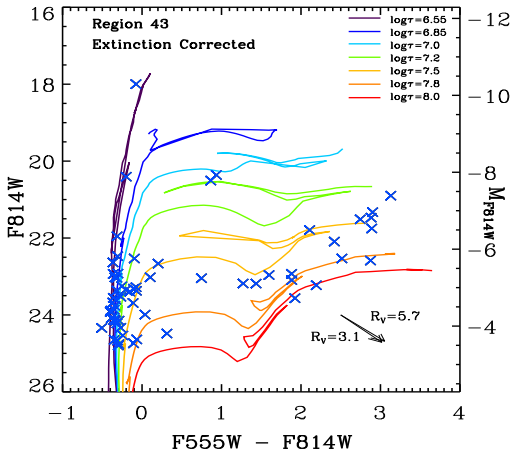
Region 43
Extinction Corrected
logτ=6.55
logτ=6.85
logτ=7.0
logτ=7.2
logτ=7.5
logτ=7.8
logτ=8.0
R_V=5.7
R_V=3.1
F814W
M_F814W
F555W − F814W

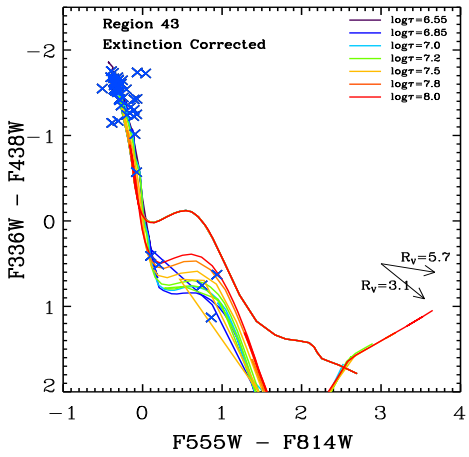
Region 43
Extinction Corrected
logτ=6.55
logτ=6.85
logτ=7.0
logτ=7.2
logτ=7.5
logτ=7.8
logτ=8.0
R_V=5.7
R_V=3.1
F336W − F438W
F555W − F814W

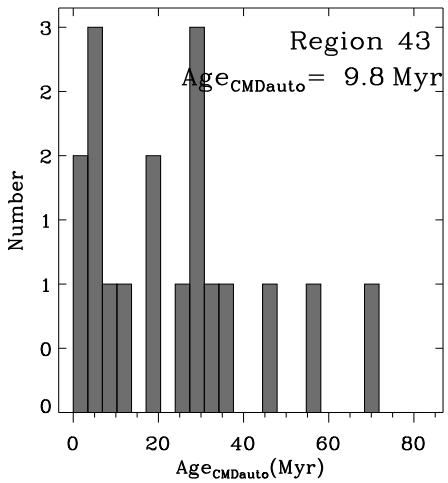
Region 43
Age_CMDauto= 9.8 Myr
Number
Age_CMDauto(Myr)

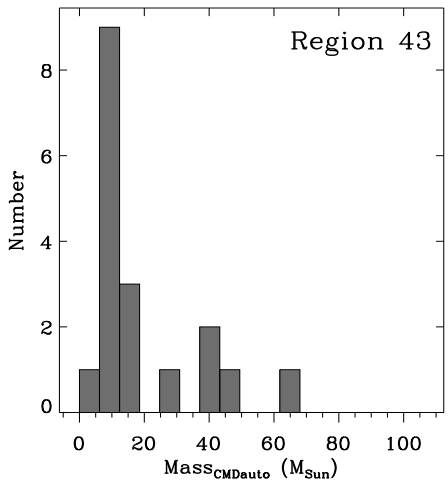
Region 43
Number
Mass_CMDauto (M_Sun)

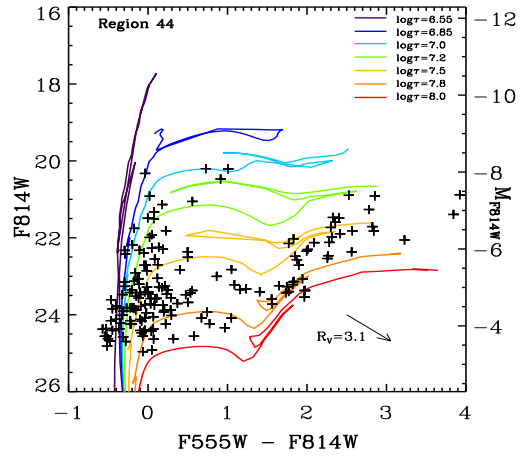
Region 44
logτ=6.55
logτ=6.85
logτ=7.0
logτ=7.2
logτ=7.5
logτ=7.8
logτ=8.0
R_V=3.1
F814W
M_F814W
F555W − F814W

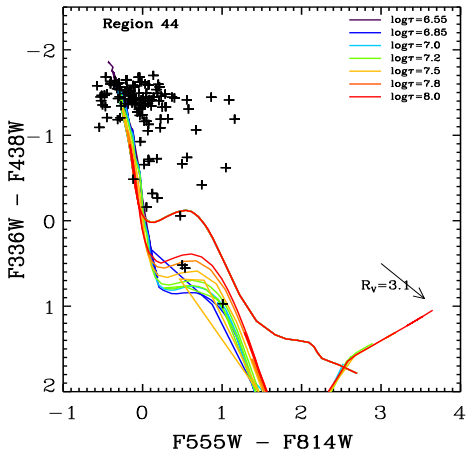
Region 44
logτ=6.55
logτ=6.85
logτ=7.0
logτ=7.2
logτ=7.5
logτ=7.8
logτ=8.0
R_V=3.1
F336W − F438W
F555W − F814W

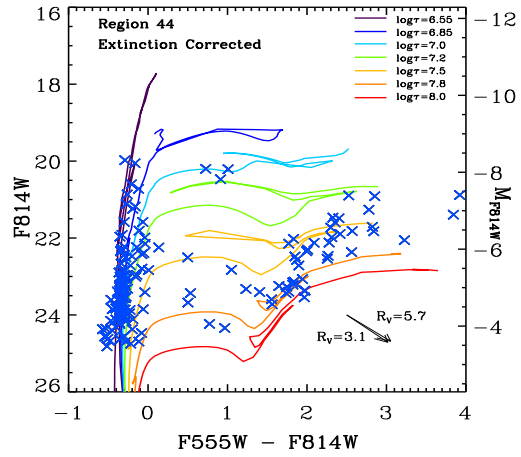
Region 44
Extinction Corrected
logτ=6.55
logτ=6.85
logτ=7.0
logτ=7.2
logτ=7.5
logτ=7.8
logτ=8.0
R_V=5.7
R_V=3.1
F814W
M_F814W
F555W − F814W

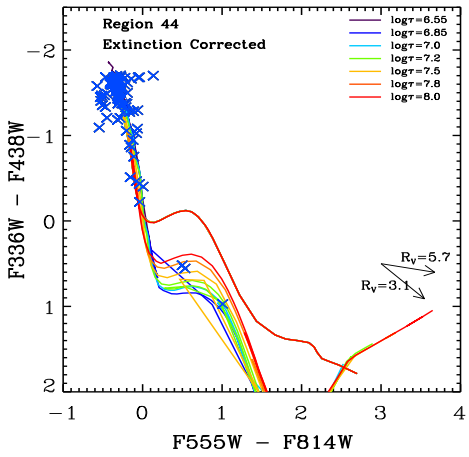
Region 44
Extinction Corrected
logτ=6.55
logτ=6.85
logτ=7.0
logτ=7.2
logτ=7.5
logτ=7.8
logτ=8.0
R_V=5.7
R_V=3.1
F336W − F438W
F555W − F814W

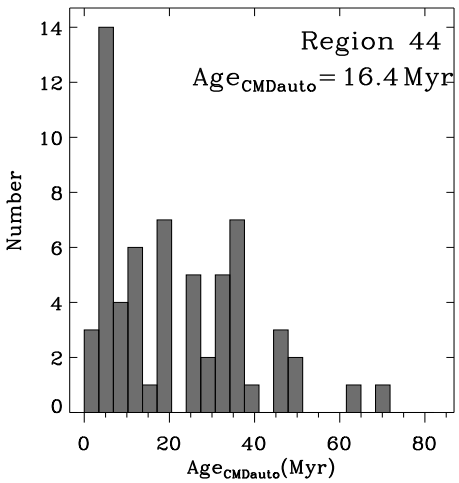
Region 44
Age_CMDauto = 16.4 Myr
Number
Age_CMDauto (Myr)

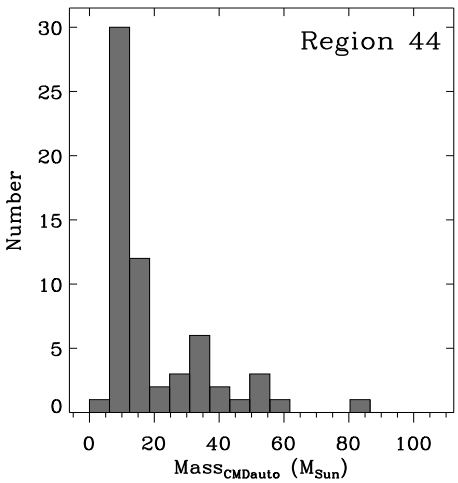
Region 44
Number
Mass_CMDauto (M_Sun)

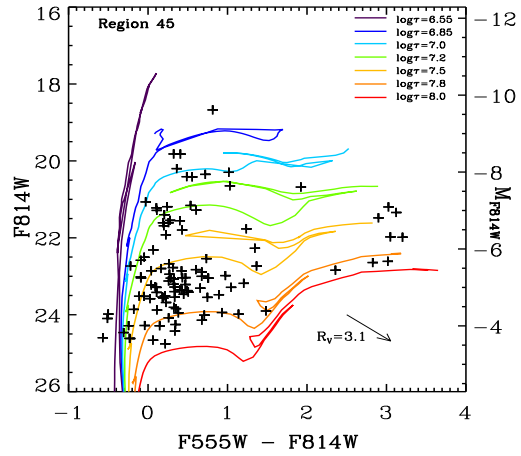
Region 45
logτ=6.55
logτ=6.85
logτ=7.0
logτ=7.2
logτ=7.5
logτ=7.8
logτ=8.0
R_V=3.1
F814W
M_F814W
F555W − F814W

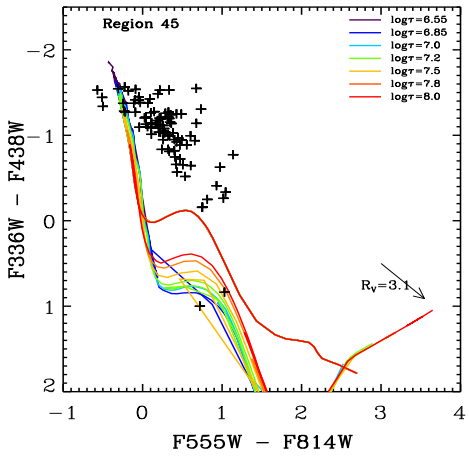
Region 45
logτ=6.55
logτ=6.85
logτ=7.0
logτ=7.2
logτ=7.5
logτ=7.8
logτ=8.0
R_V=3.1
F336W − F438W
F555W − F814W

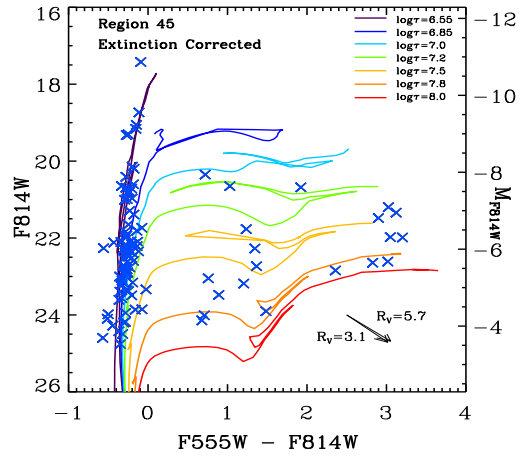
Region 45
Extinction Corrected
logτ=6.55
logτ=6.85
logτ=7.0
logτ=7.2
logτ=7.5
logτ=7.8
logτ=8.0
R_V=5.7
R_V=3.1
F814W
M_F814W
F555W − F814W

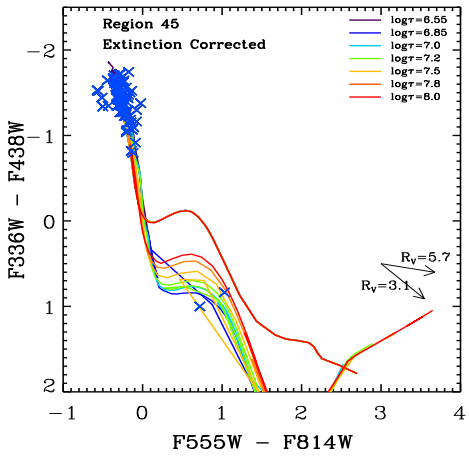
Region 45
Extinction Corrected
logτ=6.55
logτ=6.85
logτ=7.0
logτ=7.2
logτ=7.5
logτ=7.8
logτ=8.0
R_V=5.7
R_V=3.1
F336W − F438W
F555W − F814W

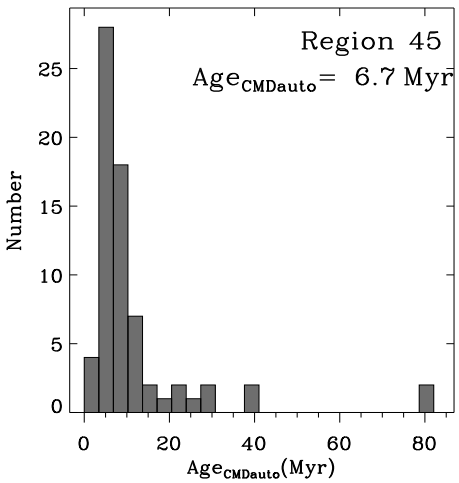
Region 45
Age_CMDauto= 6.7 Myr
Number
Age_CMDauto(Myr)

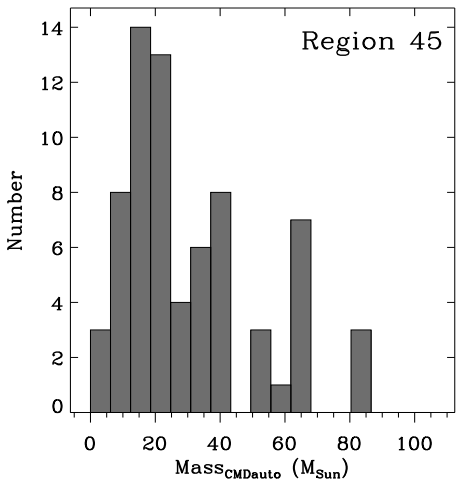
Region 45
Number
Mass_CMDauto (M_Sun)

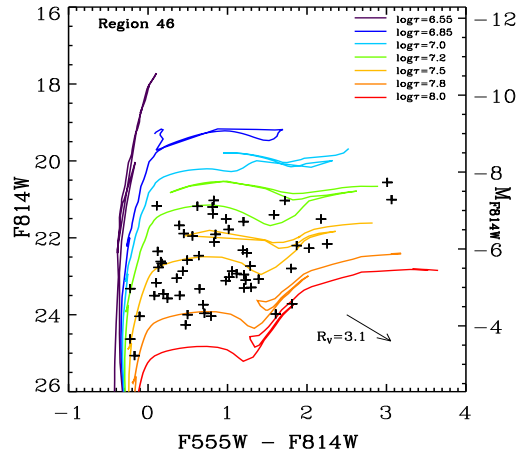
Region 46
logτ=6.55
logτ=6.85
logτ=7.0
logτ=7.2
logτ=7.5
logτ=7.8
logτ=8.0
R_V=3.1
F814W
M_F814W
F555W − F814W

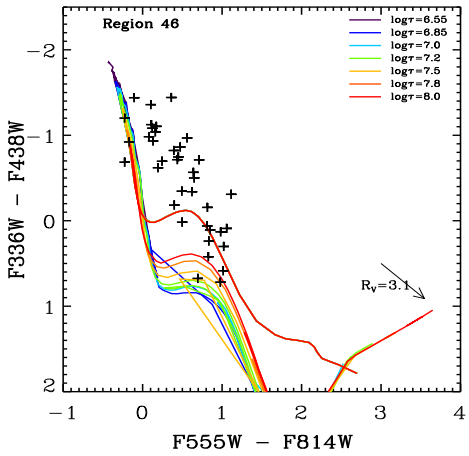
Region 46
logτ=6.55
logτ=6.85
logτ=7.0
logτ=7.2
logτ=7.5
logτ=7.8
logτ=8.0
R_V=3.1
F336W − F438W
F555W − F814W

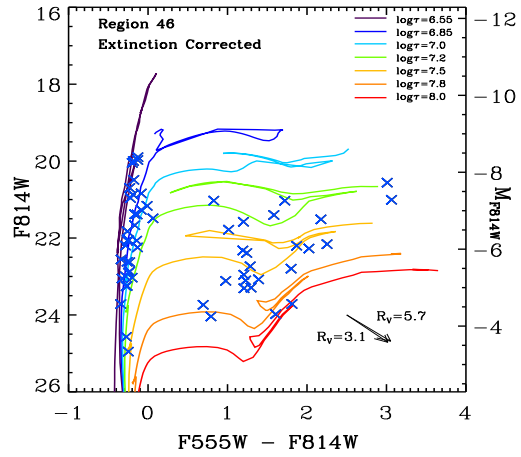
Region 46
Extinction Corrected
logτ=6.55
logτ=6.85
logτ=7.0
logτ=7.2
logτ=7.5
logτ=7.8
logτ=8.0
R_V=5.7
R_V=3.1
F814W
M_F814W
F555W − F814W

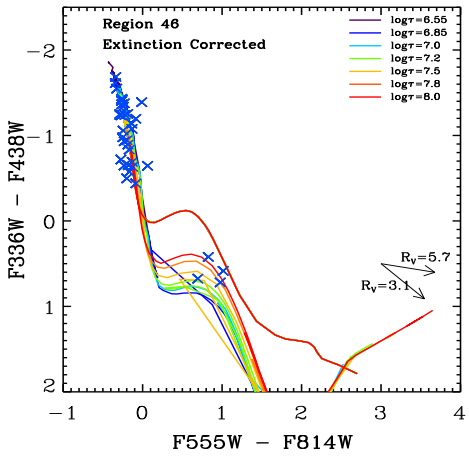
Region 46
Extinction Corrected
logτ=6.55
logτ=6.85
logτ=7.0
logτ=7.2
logτ=7.5
logτ=7.8
logτ=8.0
R_V=5.7
R_V=3.1
F336W − F438W
F555W − F814W

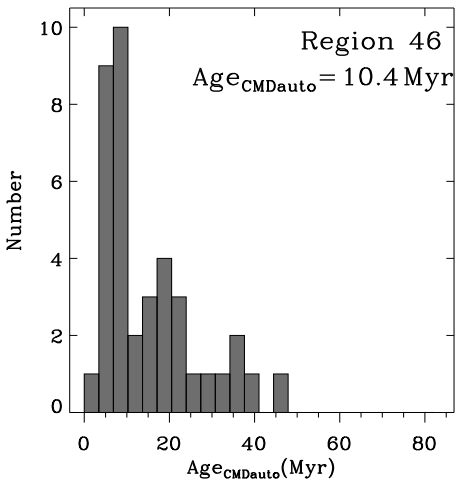
Region 46
Age_CMDauto = 10.4 Myr
Number
Age_CMDauto (Myr)

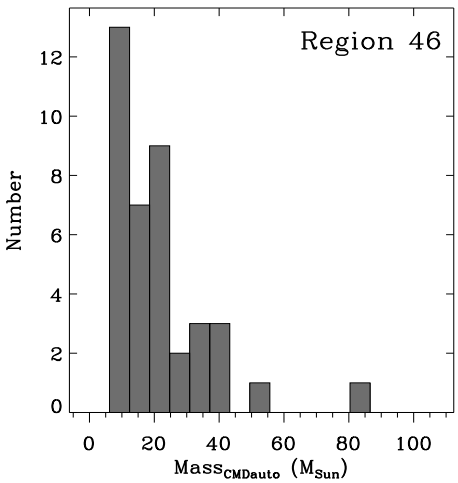
Region 46
Number
Mass_CMDauto (M_Sun)

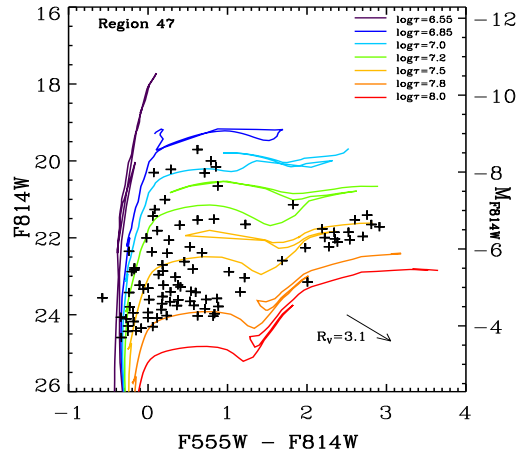
Region 47
logτ=6.55
logτ=6.85
logτ=7.0
logτ=7.2
logτ=7.5
logτ=7.8
logτ=8.0
R_V=3.1
F814W
M_F814W
F555W − F814W

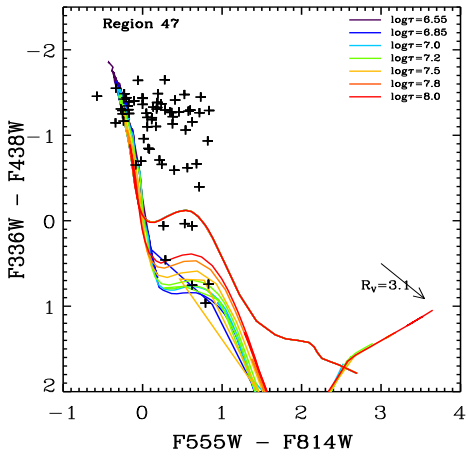
Region 47
logτ=6.55
logτ=6.85
logτ=7.0
logτ=7.2
logτ=7.5
logτ=7.8
logτ=8.0
R_V=3.1
F336W − F438W
F555W − F814W

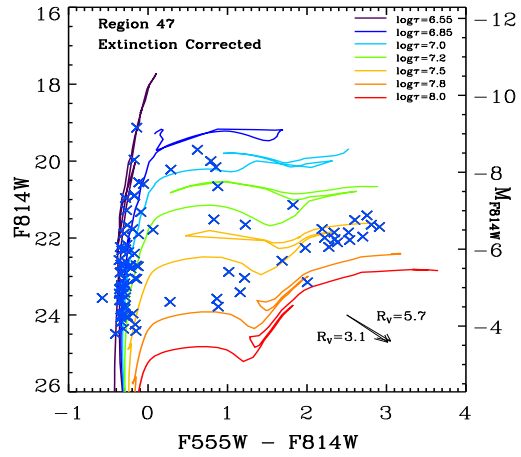
Region 47
Extinction Corrected
logτ=6.55
logτ=6.85
logτ=7.0
logτ=7.2
logτ=7.5
logτ=7.8
logτ=8.0
R_V=5.7
R_V=3.1
F814W
M_F814W
F555W − F814W

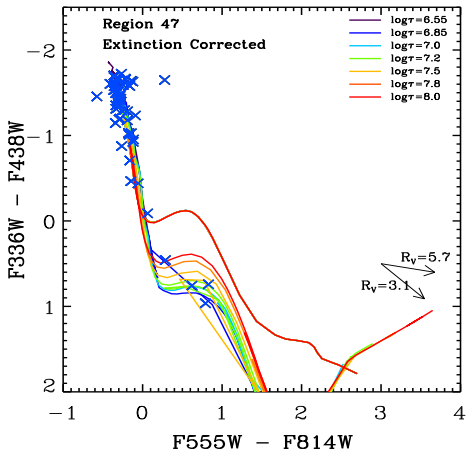
Region 47
Extinction Corrected
logτ=6.55
logτ=6.85
logτ=7.0
logτ=7.2
logτ=7.5
logτ=7.8
logτ=8.0
R_V=5.7
R_V=3.1
F336W − F438W
F555W − F814W

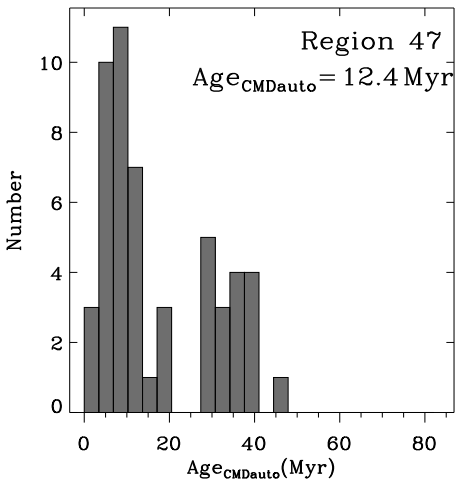
Region 47
Age_CMDauto = 12.4 Myr
Number
Age_CMDauto (Myr)

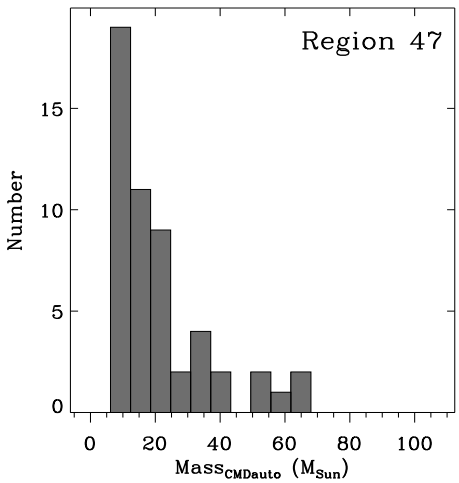
Region 47
Number
Mass_CMDauto (M_Sun)

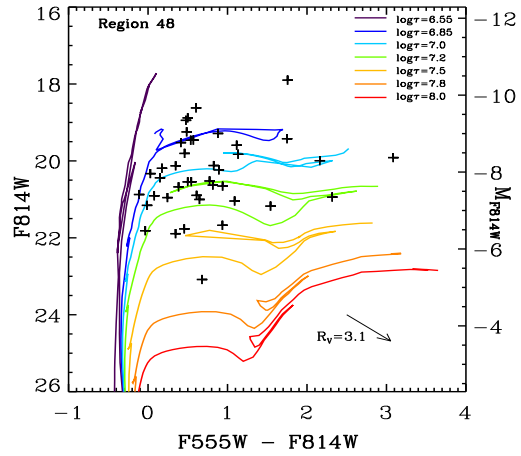
Region 48
logτ=6.55
logτ=6.85
logτ=7.0
logτ=7.2
logτ=7.5
logτ=7.8
logτ=8.0
R_V=3.1
F814W
M_F814W
F555W − F814W

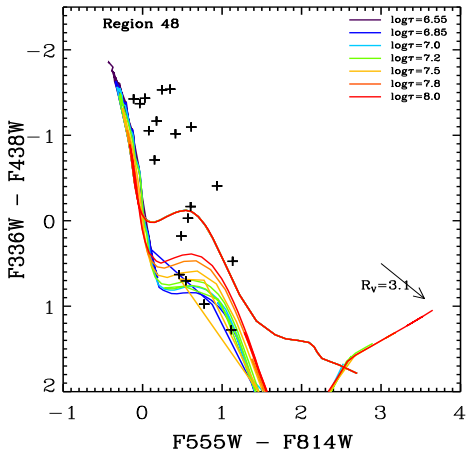
Region 48
logτ=6.55
logτ=6.85
logτ=7.0
logτ=7.2
logτ=7.5
logτ=7.8
logτ=8.0
R_V=3.1
F336W − F438W
F555W − F814W

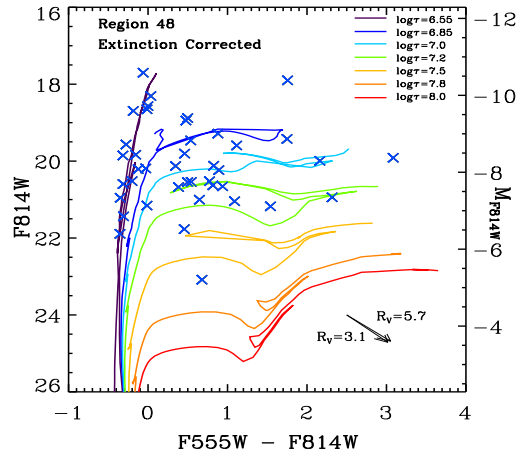
Region 48
Extinction Corrected
logτ=6.55
logτ=6.85
logτ=7.0
logτ=7.2
logτ=7.5
logτ=7.8
logτ=8.0
R_V=5.7
R_V=3.1
F814W
M_F814W
F555W − F814W

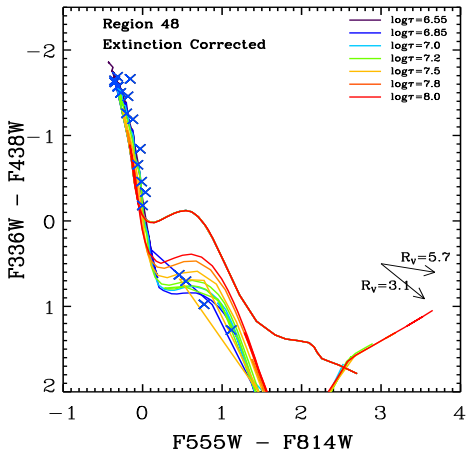
Region 48
Extinction Corrected
logτ=6.55
logτ=6.85
logτ=7.0
logτ=7.2
logτ=7.5
logτ=7.8
logτ=8.0
R_V=5.7
R_V=3.1
F336W − F438W
F555W − F814W

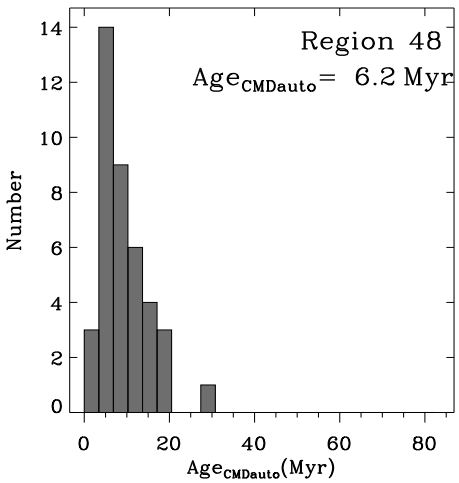
Region 48
Age_CMDauto= 6.2 Myr
Number
Age_CMDauto(Myr)

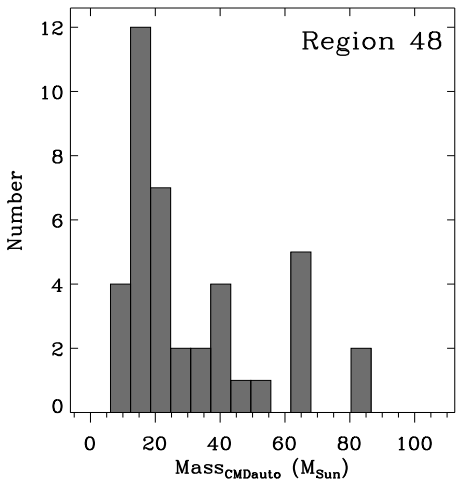
Region 48
Number
Mass_CMDauto (M_Sun)

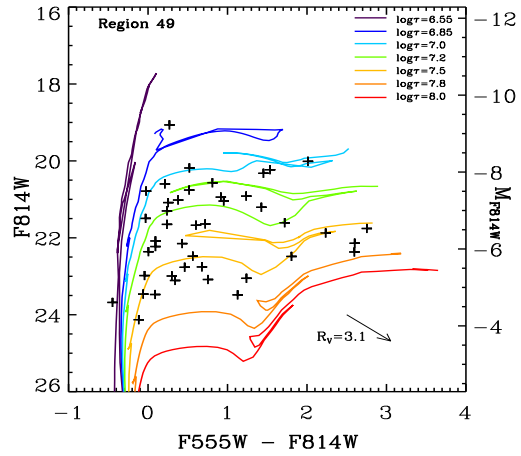
Region 49
logτ=6.55
logτ=6.85
logτ=7.0
logτ=7.2
logτ=7.5
logτ=7.8
logτ=8.0
R_V=3.1
F814W
M_F814W
F555W − F814W

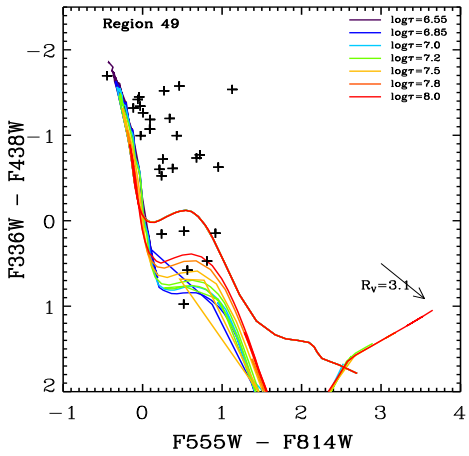
Region 49
logτ=6.55
logτ=6.85
logτ=7.0
logτ=7.2
logτ=7.5
logτ=7.8
logτ=8.0
R_V=3.1
F336W − F438W
F555W − F814W

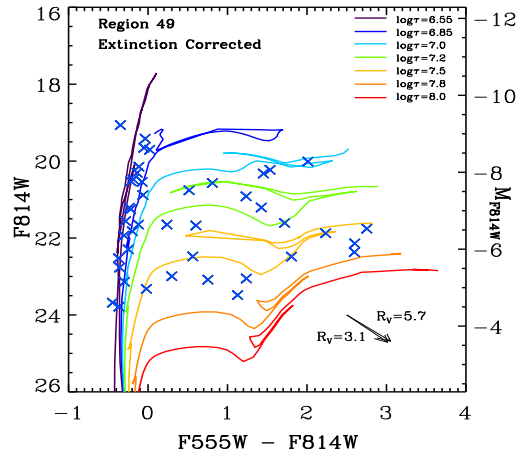
Region 49
Extinction Corrected
logτ=6.55
logτ=6.85
logτ=7.0
logτ=7.2
logτ=7.5
logτ=7.8
logτ=8.0
R_V=5.7
R_V=3.1
F814W
M_F814W
F555W − F814W

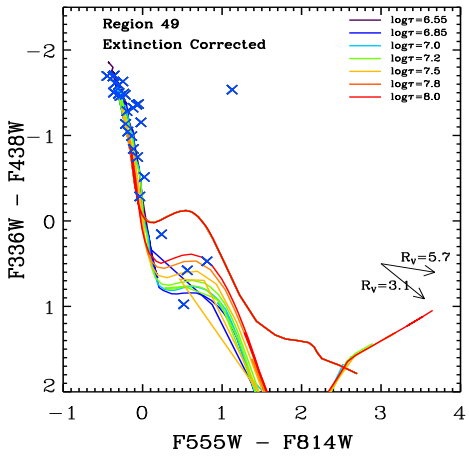
Region 49
Extinction Corrected
logτ=6.55
logτ=6.85
logτ=7.0
logτ=7.2
logτ=7.5
logτ=7.8
logτ=8.0
R_V=5.7
R_V=3.1
F336W − F438W
F555W − F814W

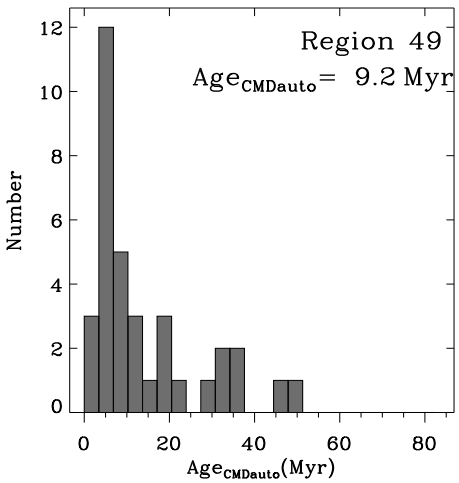
Region 49
Age_CMDauto= 9.2 Myr
Number
Age_CMDauto(Myr)

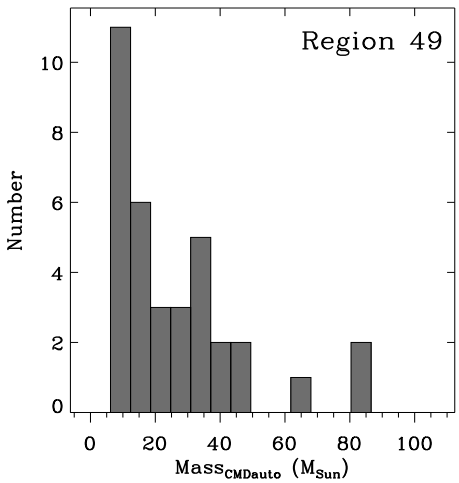
Region 49
Number
Mass_CMDauto (M_Sun)

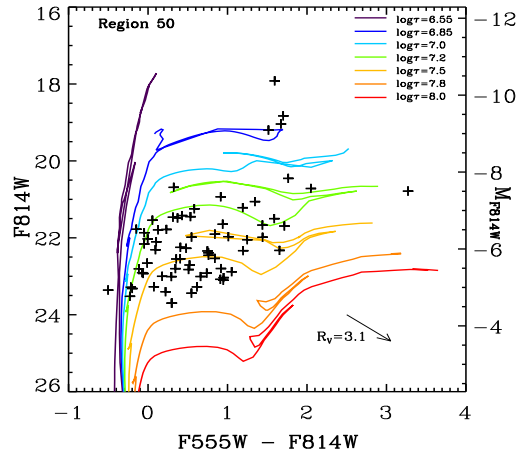
Region 50
logτ=6.55
logτ=6.85
logτ=7.0
logτ=7.2
logτ=7.5
logτ=7.8
logτ=8.0
R_V=3.1
F814W
M_F814W
F555W − F814W

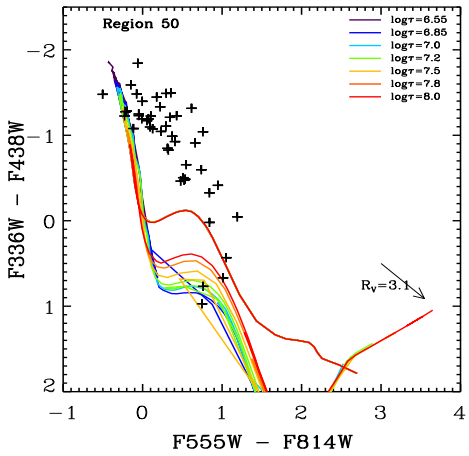
Region 50
logτ=6.55
logτ=6.85
logτ=7.0
logτ=7.2
logτ=7.5
logτ=7.8
logτ=8.0
R_V=3.1
F336W − F438W
F555W − F814W

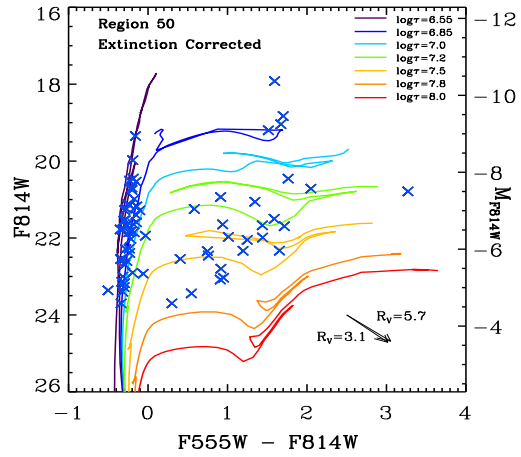
Region 50
Extinction Corrected
logτ=6.55
logτ=6.85
logτ=7.0
logτ=7.2
logτ=7.5
logτ=7.8
logτ=8.0
R_V=5.7
R_V=3.1
F814W
M_F814W
F555W − F814W

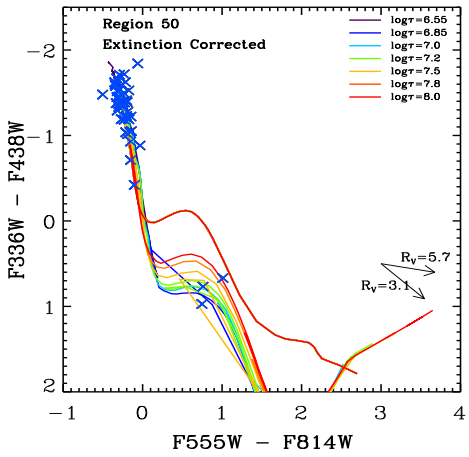
Region 50
Extinction Corrected
logτ=6.55
logτ=6.85
logτ=7.0
logτ=7.2
logτ=7.5
logτ=7.8
logτ=8.0
R_V=5.7
R_V=3.1
F336W − F438W
F555W − F814W

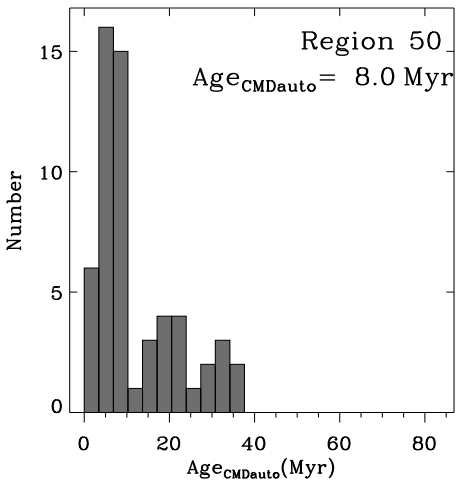
Region 50
Age_CMDauto= 8.0 Myr
Number
Age_CMDauto(Myr)

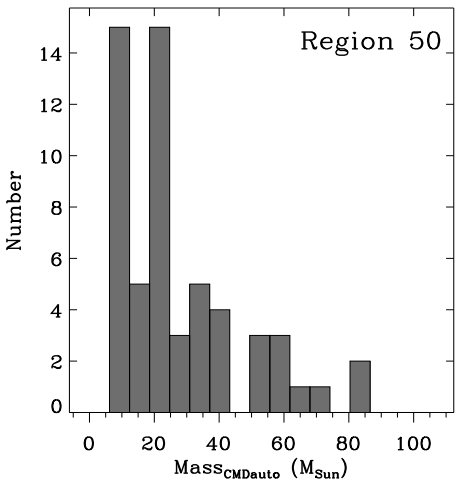
Region 50
Number
Mass_CMDauto (M_Sun)

Appendix B

SUPPLEMENTARY MATERIAL TO CHAPTER FOUR

B.1 Photometric Data Analysis

CGCG 269-049 was observed using the *HST*/ACS HRC instrument in the F330W ("u"), F550M ("v"), and F814W ("I") filters. Raw data was processed via the standard ACS OTFR pipeline. Total exposure times were 2,000 sec in F330W, 6,320 sec in F550M, and 2,120 sec in F814W.

PSF photometry was performed using the IRAF/DAOPHOT package (version 2.12.2 Jan 2004). A master catalog of the point sources in each image was created through a three-step process with progressively fainter detecting thresholds of 15, 10, and 5 σ, where σ is the standard deviation measured from the histogram of the sky background pixels. Detection thresholds below 5 σ were not used in this study because the stars in CGCG 269-049 are crowded and fainter thresholds did not reliably detect additional stars. In the second and the third steps, we used the residual images produced from the previous step after subtraction of the previously found brighter stars.

The PSFs used are a combination of an analytical base-function and an empirical image that describes the difference between a composite stellar image and the best-fit base-function. Since the sampling of the PSF differs in F330W, F550M, and F814W, we used different base-functions: Gaussian for F330W and F550M and Moffat15 for F814W. These choices minimized the residuals. The residual images show that most of the point sources had been cleanly subtracted out from the original images. After the third and final step, only a few stars that were affected by bad pixels or residuals from cosmic ray hits remain. Also, some light of an unresolved stellar population appears to be underlying resolved stars.

B.2 Construction of the CMD and the Color-color Diagram

We produced a CMD and color-color diagram using the cross-matched catalogs of F330W, F550M and F814W stellar photometry. We omitted all point sources detected near the edges of images and in the region around the coronagraphic finger. The magnitude and color are in the Vega magnitude system calculated using equation (4) in Sirianni et al. (2005), which is

ACSMAG(P) = -2.5 log (total count rate in electron per second) + Zpt(P).

The magnitude in the bandpass P (F330W, F550M or F814W in this study) is determined by the choice of the updated zero point magnitude (Zpt(P)) for the high-resolution camera given from the HST/ACS website [1]. In three filters we used, they are 22.907, 24.392 and 24.861 respectively. We only plot measurements with formal 1 σ errors less than 0.2 mag in F330W and F814W and less than 0.30 mag in F330W-F550M and F550M-F814W. We overlay theoretical isochrones in the HST/ACS HRC Vega magnitude system downloaded from the Padova database , where we adopted the distance of 4.96 Mpc for CGCG 269-049.

The zeropoints in Sirianni et al. (2005) assume an aperture of 5.5″, and hence we must apply aperture corrections that correspond to the flux lost outside our much smaller aperture used to fit our PSF-photometry. The aperture within which we fit the PSFs was 4 pixels in radius, which corresponds to ∼0.1″. This aperture captures most of the stellar light. The corrections from 0.1″ to 5.5″ made for each filter were 0.28 in F330W, 0.23 in F550M, and 0.43 in F814W in the sense that the corrections made the magnitude of each star brighter.

[1] http://www.stsci.edu/hst/acs/analysis/zeropoints

B.3 Completeness Level in Each Filter

To assess the completeness of the PSF-fitting, we inserted 100 artificial stars at a time at random positions into the actual images. For each filter, we repeated this task 32 times with different PSF functions such as Gaussian, Moffat15, Moffat25, and Auto defined in the IRAF task 'daopars'. The magnitude of the inserted PSFs was increased from 21 mag to 29 mag with the steps of 0.25 mag.

The recovery of artificial stars was performed with the same three-step process with which we measured the actual stars. The detections of the artificial stars dropped around the magnitudes fainter than 24.5, 27.0, and 26.5 for F330W, F550M, and F814W, respectively. The F330W image was not deep enough to recover stars to the faint limits reached in the F550M and F814W images. The F550M image effectively is the deepest with a completeness limit approaching 27 mag. The F814W photometry reaches ∼0.5 mag brighter. Before applying cuts on the formal photometric errors, we detect 1550 stars in F330W, 5993 in F550M, and 4164 in F814W. After requiring the error less than 0.2 mag, 309, 3128, and 4339 stars remain in F330W, F550M, and F814W, respectively. We plot matched photometry for 195 stars with F330W, F550M, and F814W, and for 2622 stars with both reliable F550M and F814W photometry.

B.4 Distance Calculation Using the RGB Tip Magnitude

We did not convert the F550M and F814W magnitudes to V and I magnitudes for all stars. However, to calculate the distance from the TRGB, we used the converted F814W magnitude (24.5 mag) of TRGB to I magnitude (24.4 mag) using Equation (12) and Table 23 in Sirianni et al. (2005), which is:

$$TMAG = SMAG + c_0 + c_1 \times TCOL + c_2 \times TCOL^2,$$

where $SMAG = 24.5$, $c_0 = 24.837 \pm 0.016$, $c_1 = 0.060 \pm 0.253$, $c_2 = -0.099 \pm 0.963$, and $TCOL = 1.15$.

$$m(I) - M(I) = 5log(d) - 5,$$

where $d = 10^{(m-M+5)/5} = 4.98\ Mpc$ with $M(I) = -4.05$ from Da Costa & Armandroff (1990).

B.5 Estimate of the Mass Fraction for Evolved Stars

We estimated the mass fraction of evolved stars using the initial mass functions (IMFs) of Scalo et al. (1986) and Miller & Scalo (1979) and the main-sequence (MS) lifetime based on the MS M-L relation. IMF parameters of Scalo et al. (1986) and Miller & Scalo (1979) laws for the IMF, parameterized as: $\xi(M) = \xi_0 \times M^{-(1+x)}$, where $M1$ and $M2$ are the lower and upper mass cutoffs (in units of solar mass), and x is the parameter of the power law. The mass fraction in each mass range can be obtained from the integration of the given function above and normalized to 1 over the whole mass range (see Table B.1).

To calculate the mass cut for 1 Gyr and 10 Gyr old stars, we used the MS lifetime : $t_{MS} =\sim 10^{10} \times M/{M_\odot}^{-2.5}$ yrs. The estimated MS turn-off masses are 2.51 $M_\odot$ for 1 Gyr old stars and 1 $M_\odot$ for 10 Gyr old stars. Since the time stars spend in evolved stages (RGB, Horizontal Branch, AGB) after leaving the MS depends strongly on their MS masses, this portion of the CMD is dominated by lower mass, older stars, with little contamination by massive stars that recently left the MS of a much younger stellar population. While 2.5 $M_\odot$, 1 Gyr old stars linger for no more than 10 Myr on the RGB, HB, and AGB, the more numerous (for any realistic IMF) stars with masses between $\sim$1.00 $M_\odot$ and $\sim$1.02 $M_\odot$ that linger for $\sim$500 Myr will constitute the majority of the evolved stars that we see in our CMD. We count 1372 stars with $0.4 <$ F550M-F814W < 1.5 mag and F814W

< 27 mag which implies that the total mass in these evolved stars is $\sim$1390 $M_{\odot}$. The F814W magnitude of a 10 Gyr MS turn-off is 31.3 mag which means that we detected approximately 1/3 of the evolved stars in the region covered by our ACS/HRC observations. We estimated the total population across this galaxy to be at least 3 times larger, which together with our computed mass fraction of 0.0032–0.0049 implies a total 10 Gyr ZAMS mass $>$ 2.52–3.87$\times 10^6$ $M_{\odot}$.

Table B.1: Mass Fraction of Evolved Stars in CGCG 269-049

IMF	$M1$	$M2$	x	Fraction
Scalo86	0.10	0.18	-2.60	0.1652
Scalo86	0.18	0.42	0.01	0.4629
Scalo86	0.42	0.62	1.75	0.1536
Scalo86	0.62	1.18	1.08	0.1615
Scalo86	1.18	3.50	2.50	0.0513
Scalo86	3.50	125.	1.63	0.0055
MillerScalo79	0.10	1.00	0.25	0.7828
MillerScalo79	1.00	2.00	1.00	0.1257
MillerScalo79	2.00	10.0	1.30	0.0848
MillerScalo79	10.0	125.	2.30	0.0067
IMF	$M1$	$M2$	Age (Gyr)	Fraction
Scalo86	0.10	2.51	1	0.9898
Scalo86	0.10	1.00	10	0.8845
Scalo86	1.00	1.02	10	0.0032
MillerScalo79	0.10	2.51	1	0.9332
MillerScalo79	0.10	1.00	10	0.7828
MillerScalo79	1.00	1.02	10	0.0049

B.6 Radial Change of Stellar Populations

We found the radial change of stellar populations in CGCG 269-049. Color-magnitude diagrams of resolved stars at progressively larger radial distance from the center show that the stellar content of CGCG 269-049 systematically varies with radius. We use the *HST*/ACS F550M and F814W images and construct (F550M-F814W) versus F814W CMDs of resolved stars within elliptical annuli. Figure B.1 shows the *HST* ACS/HRC F550M image of CGCG 269-049 with the elliptical annuli used in this analysis. The semi-major (semi-minor) axis of annuli (a)–(e) are 120 (90), 180 (130), 240 (180), 300 (220), 360 (270) parsecs, respectively. The annulus (f) covers the rest of the image outside of the annulus (e). The cross at the center of Figure B.1 indicate the flux-weighted center of the galaxy.

Six panels in Figure B.2 are the color-magnitude diagrams of resolved stars within the elliptical annuli shown in Figure B.1. The stellar model isochrones from Padova group with the ages from 10 Myr to 10 Gyr are overlaid. The grey dashed line is the 50% photometric completeness level described in Section B.3. The fraction of young ($\sim$10 Myr) and luminous (F814W$<$25.5 mag) main-sequence stars decreases with radius from 10% to 4%, while the fraction of the old ($>\sim$1 Gyr) populations stays relatively constant ($\sim$35%). The most recent star formation in CGCG 269-049 is concentrated in a star cluster ("Central Cluster") near, but offset from the flux-weighted galactic center (see the cross in Figure B.1). In the panel (d) of Figure B.2, the horizontal branch (HB) stars well-fitted with the 250 Myr isochrone are clearly separated from the sub-giant branch or HB stars of intermediate ages ($\sim$250–500 Myr).

To study star-formation history of CGCG 269-049, we investigate the spatial distribution of three major populations. We selected the MS, HB, and

RGB populations with the AGB stars based on the (F550M-F814W) color and F814W magnitude. Figure B.3 shows the color cuts used in the selection criteria: (F550M-F814W)<-0.3 (MS), $-0.3<$(F550M-F814W)<1.0 (HB), and (F550M-F814W)>1.0 (RGB+AGB) in grey dotted line. The magnitude cut is F814W<25.5 mag in grey dashed line shown in Figure B.3. The data points circled in red are stars with (F330W-F550M) color bluer than -1.3 and the majority of them are well-fitted with the young isochrones ($\sim$10–50 Myr). Using the selection criteria described in Figure B.3, we mapped the distribution of resolved stellar populations in CGCG 269-049. Figure B.4 is the maps of three selected populations (MS, HB, RGB+AGB). In Figure B.4 the MS stars are densely populated in the Central Cluster, which is so prominent in the ground-based images (see Figure 4.1). The *HST*ACS/HRC Hα image shows strong emission associated the OB stars in the Central Cluster (see Figure 4.5). The middle panel of Figure B.4 shows enhancement ($\sim$70%) of the HB population in the lower right half of the distribution map, but they are not strongly clustered compared to the map of MS stars. The RGB and AGB stars are evenly distributed over the entire region of the galaxy, as expected from the previous studies with M83 and NGC 4214 in Chapters 2 and 3.

To conclude this section, the CMDs of stellar populations within the annuli defined by their galactocentric distance show a deficit of blue luminous stars in the outer regions, while RGB and AGB stars can be found throughout. The most luminous blue stars are confined within the inner region within the annulus (a), which contains the Central Cluster of CGCG 269-049.

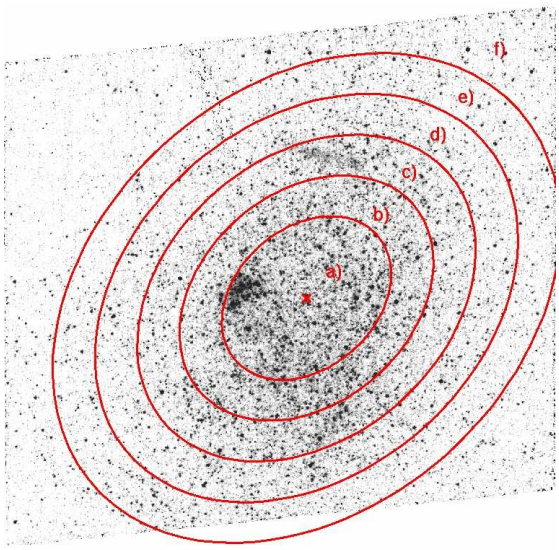

Figure B.1: *HST* ACS/HRC F550M image of CGCG 269-049 with the elliptical annuli used in our analysis overlaid. The ellipticity of the annuli is 0.2608. The cross indicates the flux-weighted center of the galaxy.

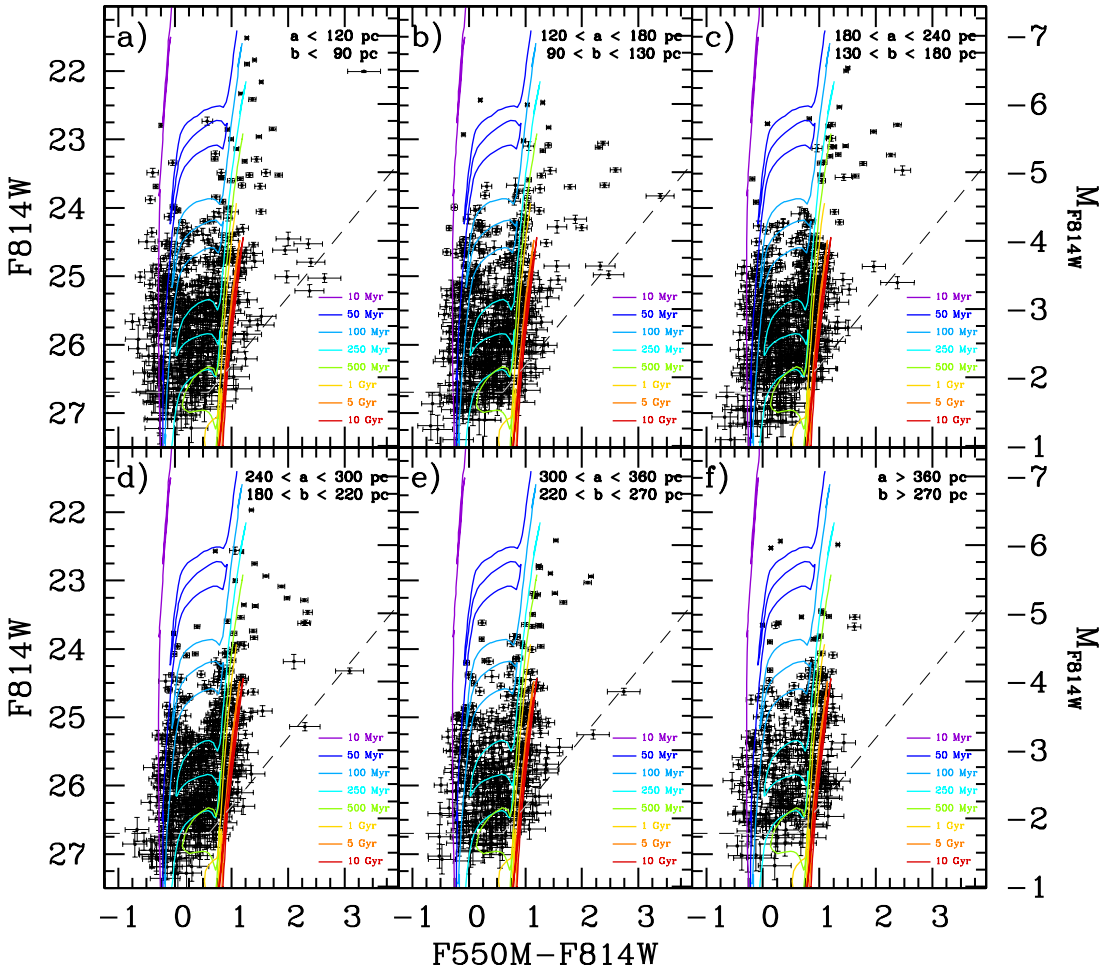

Figure B.2: (a)–(f) CMDs of resolved stars within annuli with the semi-major and -minor axis defined at the top right corner of each panel (also, see Figure B.1). The isochrones and dashed lines of 50% completeness level are the same as in Figure 4.6 (a).

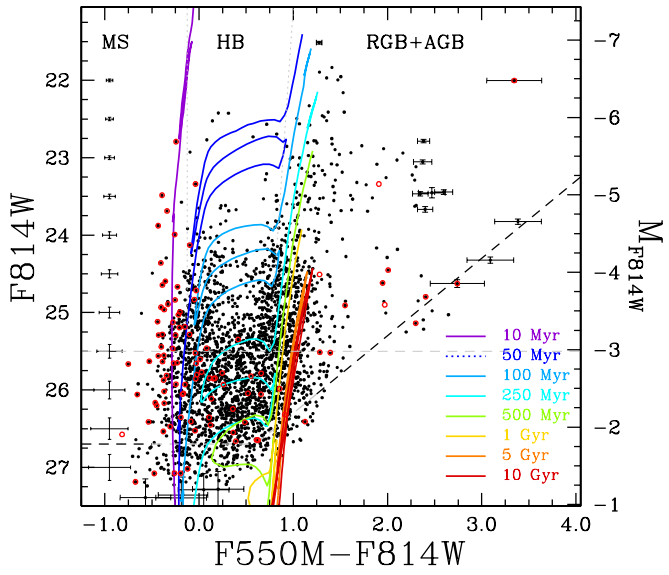

Figure B.3: Selection criteria (grey dotted line) of MS, HB, and RGB+AGB stars brighter than 25.5 mag (grey dashed line) in CMD. Data points circled in red are stars with (F330W-F550M)< -1.3.

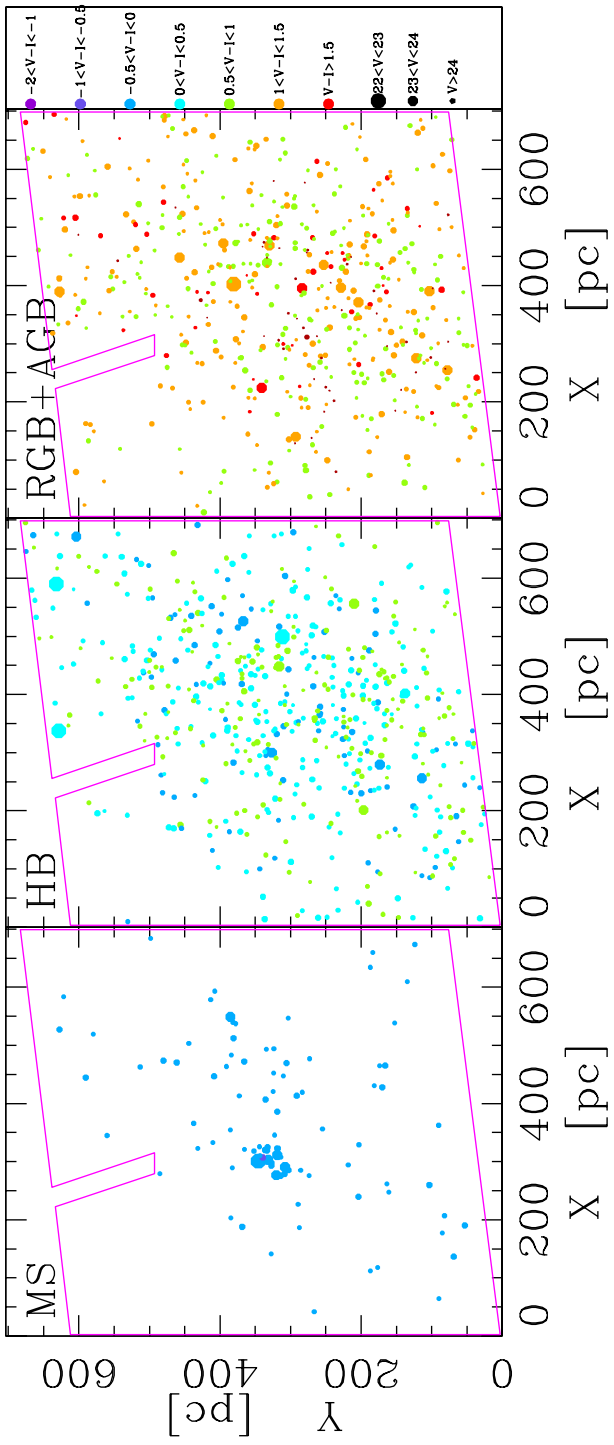

Figure B.4: Distribution of different stellar populations selected based on the criteria in Figure B.3 with the ACS/HRC footprint superposed. The color and the size of each data point are based on the (F550M-F814W) color and the F550M magnitude.